A COMPUTATIONAL INVESTIGATION OF RECEPTIVITY IN HIGH-SPEED FLOW NEAR A SWEPT LEADING-EDGE

A DISSERTATION

SUBMITTED TO THE DEPARTMENT OF MECHANICAL ENGINEERING

AND THE COMMITTEE ON GRADUATE STUDIES

OF STANFORD UNIVERSITY

IN PARTIAL FULFILLMENT OF THE REQUIREMENTS

FOR THE DEGREE OF

DOCTOR OF PHILOSOPHY

By

S. Scott Collis

March 1997

I certify that I have read this dissertation and that in my opinion it is fully adequate, in scope and in quality, as a dissertation for the degree of Doctor of Philosophy.

_____

Sanjiva K. Lele
(Principal Advisor)

I certify that I have read this dissertation and that in my opinion it is fully adequate, in scope and in quality, as a dissertation for the degree of Doctor of Philosophy.

_____

Parviz Moin

I certify that I have read this dissertation and that in my opinion it is fully adequate, in scope and in quality, as a dissertation for the degree of Doctor of Philosophy.

_____

William C. Reynolds

Approved for the University Committee on Graduate Studies:

_____

Abstract

Laminar-flow wings have the promise of reducing viscous drag forces in cruise for commercial aircraft. However, the success of a laminar-flow wing depends critically on the external disturbance environment and how these disturbances influence the transition from laminar to turbulent flow. The process by which external disturbances are converted into instability waves, which are the precursors to turbulence, is called receptivity.

The research described in this thesis focuses on the receptivity of the three-dimensional boundary layer near the leading edge of a high-speed swept wing. In particular, the influence of surface roughness near the leading edge is examined as it relates to the formation of stationary crossflow vortices in the boundary layer. Recent experiments indicate that surface roughness is the primary cause of stationary crossflow vortices which are observed to dominate the laminar to turbulent transition process on swept wings. Therefore, the mechanisms responsible for the formation of crossflow vortices and the accurate prediction of their initial amplitude are essential for the development of laminar-flow wings.

The receptivity and early evolution of stationary crossflow vortices is investigated through numerical solutions of the linearized Navier–Stokes equations for a swept leading-edge. Consistent with findings for other geometries, convex surface curvature stabilizes crossflow vortex growth while nonparallel effects are destabilizing. In contrast, the initial amplitude of crossflow vortices downstream of a localized surface roughness site is found to be greater in the presence of convex surface curvature, while the nonparallel meanflow near a leading-edge is found to strongly reduce the initial amplitude of crossflow vortices. These competing effects—curvature and nonparallelism—tend to counteract one another, but, for the conditions studied here, the nonparallel effect is dominant.

Comparisons between linearized Navier–Stokes solutions and recent theoretical receptivity analysis, based on the parallel-flow equations, show that the theoretical method over-predicts the initial amplitude of stationary crossflow vortices by as much as 77% for long wavelength disturbances. The error in the theoretical prediction is reduced for shorter wavelengths, since nonparallel effects are relatively less important, but remains as high as 30% near the leading-edge. Although the parallel

theory provides a conservative estimate of the initial amplitude of crossflow vortices, it is concluded that accurate theoretical prediction of crossflow receptivity near the leading-edge of a swept wing requires the inclusion of nonparallel effects.

Acknowledgments

I thank my advisor, Professor Sanjiva K. Lele, for his excellent technical advice and the fundamental background he has provided me through the courses he has taught. His experience and wisdom is greatly appreciated and I look forward to further collaborations.

I am also indebted to Professors Parviz Moin and William C. Reynolds for serving on my dissertation reading committee, and Professors Robert W. MacCormack and Stephen G. Monismith who served on my University examination committee.

Many people have contributed to my education at Stanford both in and out of the classroom. Certainly a large impact has come from my friends and office-mates: Ganyu Lu, Krishnan Mahesh, Keith Lucas, Steve Rennich, Ted Manning, Sungwon Bae, and Calvin Lui. Through countless conversations, they have offered their help and assistance and it is much appreciated.

Finally, I thank my parents for their constant support throughout my studies, and, for her understanding, encouragement and love, I dedicate this work to my wife, Emily.

Nomenclature

Roman Symbols

a Radius (Section 4.3)

A Amplitude

AR   Aspect ratio (Section 4.4)

c Sound speed

CFL   Courant–Friedrichs–Lewy number

c_p Specific heat at constant pressure

C_p Pressure coefficient, $C_p = \frac{p - p_r}{\frac{1}{2}\rho_r u_r{}^2}$

c_v Specific heat at constant volume

e Internal energy

E Total energy

E_k Kinetic energy

f Similarity variable for streamwise velocity (Appendix C)

F   Frequency parameter, $\mathsf{F} = \omega/\mathsf{Re} \times 10^6$

F   Nonlinear operator

g Similarity variable for spanwise velocity (Appendix C)

h Enthalpy

h_w Shape function for surface disturbance

H Boundary layer shape factor (Chapter 5), Total enthalpy (Appendix C)

i Square root of -1

J   Jacobian of the generalized coordinate mapping

k	Wavenumber vector
k	Wavenumber magnitude ($k = |\mathbf{k}|$)
k_x	Wavenumber component in chordwise direction
k_s	Wavenumber component along the surface
k_z	Wavenumber component in spanwise direction
K	Surface curvature
l	Similarity length scale (Appendix C)
L	Reference length scale
L	Matrix operator
$\mathcal{L}$	Linear operator in stability theory (Appendix D.3)
m	Falkner-Skan exponent (Appendix C), exponent for super-ellipse leading-edge (Section 4.4)
M	Mach number, $\mathsf{M} = u_r/c_r$
(n, s, z)	Body fitted coordinate system
N	Exponent in e^N transition prediction method, also the number of node points
p	Pressure
Pr	Prandtl number, $\mathsf{Pr} = c_p\mu_r/\kappa_r$
q_i	Heat flux vector
Q	Extended vector of primitive variables (see Appendix D.3)
(r, θ, z)	Cylindrical coordinates
$\bar{R}$	Attachment-line Reynolds number (Chapter 5)
$\mathcal{R}$	Gas constant

Re	Reynolds number, $\mathsf{Re} = \rho_r u_r L / \mu_r$
S	Strain-rate tensor
t	Time
T	Fluid temperature
(u, v, w)	Velocity components in the Cartesian coordinates
u_i	Cartesian components of the velocity
u_r	Reference velocity (typically the chordwise component of the freestream velocity)
U_∞	The magnitude of the freestream velocity
U	Vector of primitive variables
(x, y, z)	Cartesian coordinates
Z	Extended vector of adjoint variables (see Appendix D.3)

Greek Symbols

α	Angle of attack (Section 3.2); real component of the streamwise wavenumber (Chapter 5)
β	Real component of the spanwise wavenumber
β_h	Hartree pressure gradient parameter
χ	Crossflow Reynolds number (Chapter 5)
δ	The variation of a dependent variable
δ_1	Displacement thickness
δ_2	Momentum thickness
δ_g	Relative boundary layer growth parameter (Section 5.5)

δ_{ij}	Kronecker delta ($\delta_{ij} = 1$ when $i = j$, 0 otherwise)
δ_l	Attachment-line length-scale (Chapter 5)
Δ	Finite difference operator
γ	Ratio of specific heats
ε	Small parameter characterizing the nonparallelism of a boundary layer (Section D.3)
ε_d	Amplitude of the boundary damping term (Section 3.9.2)
ε_m	Parameter in the exact inviscid scattering solution for a circular cylinder (Section 4.3)
ε_w	Small parameter characterizing the height of surface roughness (Appendices E and F)
η	Wall normal direction in mapped space
η_b	Blasius boundary layer coordinate (Section 4.4.1)
κ	Thermal conductivity
Λ	Receptivity efficiency
λ	Second viscosity coefficient (Chapter 2); wavelength (Chapter 4)
μ	Dynamic viscosity coefficient
ν	Kinematic viscosity coefficient, $\nu = \mu/\rho$
ρ	Fluid density
τ	Pseudo-time (Chapter 3)
τ_{ij}	Shear stress tensor
ω	Angular frequency
ϕ	The velocity potential (Section 3.8); similarity variable for total Enthalpy (Appendix C)

ψ	Wave angle (Chaper 5)
Ψ	Factor used in FSC analysis (Appendix C)
σ	Growth rate of instability waves
θ	Wing sweep angle
θ_e	Sweep angle of the edge streamline
θ_p	Relative local sweep angle, $\theta_p = \theta_e - \theta$
Υ	Acoustic magnitude (Section 4.3)
ξ	Wall tangent direction in mapped space
(ξ, η, z)	Generalized coordinates
$(\tilde{\xi}, \tilde{\eta})$	Parabolic coordinates (Chapter 5)

Superscripts and Subscripts

$()_0$	Stagnation quantity
$()_\infty$	Value of quantity in the freestream
$()_{max}$	Maximum value
$()_{min}$	Minimum value
$()_r$	Reference quantity, often taken to be the freestream value
$()_w$	Wall quantity
$()^*$	Dimensional quantity
$()^\dagger$	Complex conjugate
$\overline{()}$	Mean quantity
$\widehat{()}$	Fourier transform
$\check{()}$	Denotes matrices in generalized coordinates

()′	Disturbance quantity or first derivative of a function of a single variable (Appendix C)
()″	Second derivative of a function of a single variable
Re()	Real part of a complex quantity
Im()	Imaginary part of a complex quantity
{}$^{\mathrm{T}}$	Transpose

Abbreviations

CF	Cross-Flow
CPU	Central Processing Unit
FRNT	Finite-Reynolds-Number-Theory
FSC	Falkner–Skan–Cooke
LFC	Laminar Flow Control
LHS	Left-Hand-Side
LNS	Linearized Navier-Stokes
LST	Linear-Stability-Theory
NLF	Natural Laminar Flow
NPWC	Non-Parallel With Curvature
NS	Navier–Stokes
PNS	Parabolized Navier-Stokes equations
PSE	Parabolized Stability Equations
QPNC	Quasi-Parallel, No Curvature
QPWC	Quasi-Parallel With Curvature
RHS	Right-Hand-Side
TS	Tollmien–Schlichting

Table of Contents

List of Tables

List of Figures

Chapter 1

Introduction

Receptivity is the process by which environmental disturbances are converted into instability waves in a boundary or shear layer. In this manner, receptivity provides the initial amplitudes of instability waves which eventually lead to transition from laminar to turbulent flow. An understanding of receptivity is fundamental to the development of reliable transition prediction schemes which, in turn, are necessary for the development of laminar-flow-wing technology.

The research described in this thesis focuses on the receptivity of the three-dimensional boundary layer near the leading-edge of a high-speed swept-wing. In particular, the influence of surface roughness near the leading-edge on the formation of crossflow (CF) vortices is examined. Recent experiments [90, 32] have demonstrated that surface roughness is the primary cause of stationary CF vortices and that stationary vortices dominate the transition process, near the leading-edge, in low-disturbance environments—such as the cruise condition for an aircraft in flight. Recently, the linear and nonlinear evolution of CF vortices has been well-predicted by analysis based on the Parabolized-Stability-Equations [50, 74]. However, the receptivity process for CF vortices remains an open issue mainly because experimental studies of receptivity due to surface roughness are hampered by several factors: (1) the complete disturbance environment is generally unknown, (2) the amplitudes of the crossflow vortices near the source of receptivity are not measurable, and (3) at downstream stations where measurements are possible, nonlinear effects may have already occurred. Through the numerical simulations presented here, each of these limitations are overcome and receptivity results are obtained that can be used to test recent theoretical predictions [17, 28].

This chapter begins with the general motivation for the study of receptivity along with a description of the laminar-to-turbulent transition process on a swept-wing and a summary of transition prediction techniques used in wing design. Included is a brief review of the voluminous literature on receptivity including theoretical, experimental, and computational studies. An attempt is made to focus the review on the receptivity

of three-dimensional boundary layers to surface roughness, and where appropriate, references are provided to the many review articles in the literature. The chapter closes with a summary of the accomplishments of this research and an overview of the material discussed herein.

1.1   Motivation: Laminar Flow Technology

Research on laminar-flow technology has been underway for over 50 years. However, as fuel resources become more scarce and manufacturing techniques improve, both the incentive and practicality of incorporating laminar-flow technology in new aircraft designs has increased. Possible applications of laminar-flow wings run the gamut of aircraft types—from general aviation to super-sonic passenger aircraft [9]. The primary incentive in applying laminar-flow technology stems from projections that maintaining laminar flow over a large portion of a wing can provide as much as a 25% to 30% fuel savings on long-range flights [89].

Laminar-flow wings can be broadly classified into two categories: Natural Laminar Flow (NLF) wings for which the pressure distribution is carefully tailored to delay transition, and Laminar Flow Control (LFC) wings which use surface suction to delay transition. Examples of both types of laminar-flow wings are shown in figure 1.1. The wing-type used depends on the particular application with NLF advocated for small, low-speed aircraft with small wing-sweep and LFC used for large, high-speed, swept-wing aircraft. For medium-sized aircraft with moderate wing-sweep ($\sim 20°$), recent designs take a hybrid approach by incorporating LFC near the leading-edge with NLF in the mid-chord region in an effort to achieve drag reduction more economically [9].

Regardless of the particular type, the success of a laminar-flow wing depends critically on the designer's ability to predict the location of laminar-to-turbulent transition. The transition process typically begins with the conversion of environmental disturbances into the instability waves of the flow by a process called receptivity [78]. This thesis is motivated by the need to increase the understanding of receptivity and to use this knowledge to improve transition prediction.

1.2   Transition Mechanisms on a Swept Wing

Transition in many practical situations can be modeled as a three-stage process: receptivity, linear amplification, and non-linear breakdown. Receptivity involves the conversion of environmental disturbances into the instability waves of the flow. The receptivity process typically occurs in the "subcritical" region, upstream of the location where instabilities begin to grow. Because of this, the waves excited in the receptivity phase often decay before undergoing amplification. Both the decay and subsequent amplification are generally linear processes that are well predicted by quasi-parallel Linear-Stability-Theory (LST). As the instability waves continue to amplify downstream, they eventually reach sufficiently large magnitudes such that nonlinear effects become important. These nonlinearities manifest themselves, at least initially, as secondary and tertiary instabilities. This final phase, non-linear breakdown, usually occurs rapidly, over a short streamwise length. In fact, the length of the linear amplification region is often an order-of-magnitude greater than the length of the nonlinear region (at least for two-dimensional instabilities). This fact is the rationale behind current transition prediction schemes which are based solely on the linear amplification stage, see section 1.3. Recently, a new transition prediction technique based on the Parabolized Stability Equations (PSE) [51] has been developed which yields accurate predictions for both the linear amplification and early nonlinear stages of transition. We will return to the topic of PSE methods in section 1.3. Transition phenomena which do not fit into this three-stage model are called by-pass transition and are characterized by nonlinearities from the onset. Examples of by-pass transition include attachment-line contamination and transition due to large surface protuberances or high-intensity free-stream turbulence.

The transition process in the three-dimensional boundary layer on a swept-wing typically involves one or more of the following phenomena:

1. Attachment-line instabilities and contamination

2. Crossflow vortices: stationary and non-stationary

3. Streamwise instabilities (*i.e.* Tollmien–Schlichting waves)

4. Görtler (centrifugal) instabilities

A schematic of possible transition routes for a swept-wing aircraft is given in figure 1.2.

Transition can begin on the attachment-line due to contamination from the turbulent fuselage boundary layer at the wing/fuselage junction. This by-pass mode of transition is due to a subcritical (*i.e.* finite amplitude) instability of the attachment-line flow which can be catastrophic since it results in a turbulent boundary layer over the entire wing surface. However, contamination can be prevented using a leading-edge notch or a Gaster bump [37] and, in the following discussion, we assume that such a device is employed.

In addition to contamination, the attachment-line boundary layer is susceptible to a viscous, Tollmien–Schlichting (TS) type, instability. Thus, on a laminar-flow wing, the attachment-line boundary-layer must be maintained subcritical by careful selection of the leading-edge radius or by surface suction. Assuming this to be the case, transition on the upper (convex) surface of a swept-wing is typically initiated by crossflow vortices in the favorable pressure gradient region near the leading-edge. The crossflow vortices result from an inviscid instability of the inflectional crossflow velocity profile (see figure 1.2), called the crossflow (CF) instability. If transition is delayed near the leading-edge (typically by surface suction) then transition typically occurs in the mid-chord region due to the TS instability. This fact motivates the Hybrid Laminar-Flow-Control (HLFC) approach, with suction used near the leading-edge to control the CF vortices and a favorable pressure gradient used in the mid-chord region to weaken the TS instability.

On the lower surface of the wing, an additional instability mechanism comes into play due to the concave curvature of the surface and streamlines. This centrifugal instability, called the Görtler instability, results in the formation of counter-rotating streamwise vortex pairs (in contrast to the crossflow instability which results in vortices with the same sense of rotation). Recently, there has been a number of investigations dealing with the combined effects of Görtler and CF vortices [5, 4, 115]. In the current investigation only convex surfaces are considered thereby avoiding the Görtler instability.

1.3   Transition Prediction Techniques

Current transition prediction schemes (e^N methods) are based solely on the linear instability phase of transition, ignoring both the external disturbance environment and nonlinear effects. Both Malik [75] and Redeker *et al.* [89] outline the origins of the e^N method (dating back to 1952) which has since been used extensively in laminar-flow-wing design.

The basic premise of the e^N method is that the transition location can be correlated with the amount of linear amplification of disturbances in the boundary layer. The N factor is given by the the integral of the spatial amplification rate, σ, from the point where disturbances first become unstable (Branch I, denoted by x_I) to the transition location x_{tr}:

$$N = \int_{x_I}^{x_{tr}} \sigma(x) \ dx. \tag{1.1}$$

Thus, the ratio of the amplitude of disturbances at transition to that at Branch I is given by e^N. By comparing experimental transition results in low disturbance environments with N-factors computed using LST, it was found for two-dimensional flows that transition occurs when $N = 10$ [56]. Because the N-factor represents a ratio of amplitudes, this method is insensitive to the external disturbance environment, thereby requiring different values of N for different levels and types of environmental disturbances. In addition, different values of N are expected for each type of instability mechanism: TS, CF, and Görtler instabilities. However, Malik [75], in providing a comprehensive review of the e^N results in the literature (as of 1990), finds that a value of $N = 10$ correlates reasonably well with the majority of the data, regardless of the instability mechanism. It is this "robustness" which helps make the method a useful design tool.

Given the apparent success of the e^N method, there is, however, a large amount of scatter in the values of N given in the literature. It is not unusual for N-factors to be reported in the range of $6 - 13$ depending on the instability mechanisms, test environment, and flow geometry. To put this in perspective, this range of N-factors corresponds to a three order-of-magnitude range of amplitude ratios. Thus, large safety factors are required in laminar flow wing design to account for this considerable uncertainty in the N-factor.

The success of the e^N method is hampered by the assumptions of linearity, parallel

flow, and by the exclusion of the receptivity process which determines the initial amplitude of disturbances within the boundary layer. By including only the linear amplification stage of transition, the e^N method tacitly assumes that disturbances are of sufficiently low amplitude so that there is a long region of linear growth which dominates the transition process. By ignoring the receptivity phase, the e^N method misses a fundamental characteristic of the transition process: the transition location moves upstream with increased disturbance levels. Furthermore, nonlinear effects in the form of nonlinear receptivity and nonlinear interactions are not accounted for. Thus, situations involving large initial disturbances and/or modal (*e.g.* TS and CF) interactions and mean flow modification are not captured in the e^N predictions.

There are currently numerous research efforts underway to address the limitations of the e^N method by developing an amplitude based transition criterion which uses the PSE approach developed by Herbert and coworkers [51]. These efforts include studies of both nonlinear effects and receptivity to address the deficiencies of the e^N method. The research discussed in this thesis focuses on the numerical simulation of the linear receptivity phase of transition with the hope that the results and methodology discussed here can be used toward the development of an amplitude-based transition prediction technique.

1.4   Synopsis of Previous Receptivity Results

Since 1969, when Morkovin [78] first coined the term "receptivity," there has been a tremendous amount of research to discover and identify the mechanisms which lead to the formation of instability waves in a boundary layer. In this section, salient receptivity and transition research is summarized including experimental, theoretical, and computational results. The discussion begins with a general overview of receptivity research and then specializes to research involving the generation of crossflow vortices in three-dimensional boundary layers.

Kerschen [57] has identified two categories of receptivity: forced and natural. In forced receptivity, the external disturbance has the appropriate length and time scales so that it can couple directly with an instability wave in the boundary layer. An early example of forced receptivity is the landmark experiment of Schubauer & Skramstad [97] in which TS waves were generated by a vibrating ribbon placed in the boundary

layer. Other examples include surface suction/blowing, surface heating/cooling, and surface roughness. We note in passing that both the length and time scales of the disturbance must match that of the instability wave such that surface roughness, which is generally regarded as steady, may only directly excite stationary modes such as stationary crossflow vortices or Görtler vortices.

In contrast to the forced case, natural receptivity involves external disturbances which have the correct time-scale but require some form of wavelength conversion to couple with an instability wave. Examples include freestream acoustic waves and freestream turbulence, which typically have longer wavelengths then boundary-layer instability waves at the same frequency. The wavelength reduction process was first clarified in the seminal work of Goldstein [40] who showed, using high Reynolds number asymptotic expansions, that the nonparallel mean flow near a leading-edge can lead to the transfer of energy from long wavelength freestream acoustic waves to Tollmien–Schlichting waves in the boundary layer. Since then, natural receptivity has been found to occur near other forms of nonparallel mean flows including: surface roughness [92, 41, 114, 19], marginal separation [44], sudden changes in surface curvature [42], and variations in surface admittance to pressure waves [16]. In general, the results of experiments and the asymptotic theory have been in good agreement [57,59]. Most importantly, both have demonstrated that regions of meanflow distortion which have a spatial spectrum consonant with an instability wave are the key to the transfer of energy from freestream disturbances to instability waves.

Readers interested in a more detailed view of receptivity research may wish to consult the many available review articles. In particular, the reviews by Goldstein & Hultgren [43] and Kerschen [57] provide excellent summaries of the high Reynolds number asymptotic theory results. The recently popular finite Reynolds number theory is reviewed by Choudhari & Streett [21] and Crouch [29], while, experimental research as of 1986 is reviewed by Nishioka & Morkovin [82] and includes a summary of the extensive Soviet receptivity research. The Soviet experimental and theoretical research is also discussed in the paper by Kozlov & Ryzhov [59]. More recent reviews of experimental research are given by Wlezien [112] and Saric *et al.* [96]. Several recent computational studies of natural receptivity have also been reported, including the work of Reed and her colleagues [94] and Corke & Haddad [26].

Although most flows of practical relevance contain three-dimensional boundary

layers, the majority of receptivity and transition research, including most of the work cited above, has been conducted for two-dimensional boundary layers. This restriction was made necessary by the complex physical phenomenon which occur during transition, even for two-dimensional boundary layers. Fortunately, many of the observations made for two-dimensional boundary layers also apply for three-dimensional boundary layers, including the importance of meanflow distortion on receptivity. As alluded to in section 1.1, the renewed interest in laminar-flow technology has prompted considerable research in the areas of receptivity, stability, and transition of three-dimensional boundary layers. Saric & Reed [95] provide a review of the research in stability and transition for three-dimensional boundary-layers up to 1989. Since then, considerable advances have been made both in the receptivity of three-dimensional boundary layers and in the nonlinear evolution of crossflow vortices. In the remainder of this section, the recent advances in the study of receptivity and transition for three-dimensional boundary layers are discussed.

The early experiments of Saric and coworkers [86] examined the effects of micronsized roughness elements on the transition location when the roughness is placed near the leading-edge of a 45° swept NLF(2)-0415 airfoil with a 1 m chord. Their experimental results show that the transition location is very sensitive to roughness near the leading-edge and that the crossflow vortex pattern formed downstream of the roughness is directly related to the applied surface roughness distribution. By placing artificial (6 μm) roughness at different chordwise locations, it was demonstrated that the transition location moved furthest upstream for roughness placed near the point of first instability of the stationary crossflow vortices. Variations in roughness height were also considered with the transition location further upstream for larger roughness sizes. Although these results showed a strong influence of surface roughness on the generated crossflow vortices, they did not provide a clear indication of the receptivity process since measurements of the transition location are not a particularly sensitive measure of the initial level of instability waves in the boundary layer.[1] In particular, there was no observed effect on the transition location when roughness was placed downstream of 4% chord. In subsequent work [87] measurement techniques were refined and the influence of artificial roughness was detected from the attachment

---

[1]The transition location depends on the linear and nonlinear evolution of instability waves in the boundary layer making it difficult to infer receptivity characteristics directly from measurements of the transition location.

line all the way to 20% chord. Their most recent experiments [90] demonstrate that the transition process is still dominated by stationary crossflow vortices for a surface that is polished to 0.25 μm RMS. However, the focus of these recent experiments has been to study the downstream evolution of crossflow vortices in order to document and explain the failure of linear theory to predict the growth rate. We return to this issue of early nonlinear development of crossflow vortices below.

Recently, Deyhle & Bippes [32] have performed a detailed experimental study of the receptivity characteristics of a three-dimensional boundary layer to roughness of varying shape, size, location, and distribution. By considering swept flat-plate models with different surface finishes, they find that the overall level of stationary CF vortices is directly related to the average peak-to-peak roughness amplitude. High levels of initial roughness lead to high initial amplitudes of the stationary crossflow vortices and to an earlier saturation at higher amplitudes. In comparison, the effect of roughness level on traveling crossflow vortices was minor with the primary effect related to earlier nonlinear interaction (see below) due to the enhanced stationary vortices at high roughness levels. For all roughness levels the crossflow vortices observed in the experiment had wavelengths corresponding to the most amplified linear mode.

Deyhle & Bippes [32] also considered the effect of discrete artificial roughness elements to ascertain whether different wavelengths could be excited. The discrete roughness elements had a circular planform with a height of 10 μm and were added to the polished surface (1.8 μm peak-to-peak) of the plate at fixed chordwise locations near the leading edge. Unfortunately, measurements where taken far downstream, well after the vortices had saturated so that the results are extensively influenced by nonlinearities. Given this, however, the greatest crossflow response was measured for roughness placed near the upstream neutral point and for roughness with a spanwise spacing close to the most amplified wavelength predicted by stability analysis. These results are consistent both with the experiments of Saric and coworkers [86,87,90] and with theoretical receptivity predictions [28], discussed in detail below. For roughness spacing of half the most unstable wavelength, enhanced crossflow vortices were still observed at the most unstable wavelength but with roughly half the amplitude.

The recent experiments by both Saric's group [90] and Bippe and coworkers [32] have established that surface roughness is of primary importance in the generation

of stationary CF vortices. These experiments, along with complementary PSE analyses [74, 50], have focused on the nonlinear evolution of CF vortices. The results of these investigations show that nonlinearity is primarily due to the interaction of stationary CF vortices with the meanflow. This interaction leads to meanflow distortion which alters the stability characteristics of the boundary layer, resulting in lower growth-rates and eventual saturation of the stationary crossflow modes. Deyhle & Bippes [32] have also shown that the nonlinear interaction of stationary and traveling modes can lead to an additional reduction in the growth-rate of the stationary modes. This nonlinearity is most pronounced for wind tunnel experiments with modest to high free-stream turbulence, indicating that the traveling modes are generated by a receptivity process which converts the freestream turbulence into traveling CF vortices. Most importantly, however, is the fact that freestream turbulence levels are generally much lower under flight conditions than in wind tunnels. Because of this, the stationary crossflow vortices are expected to be the dominant instability mechanism in low disturbance environments such as a wing in flight.

Comparisons of the experimental results [90, 32] with nonlinear PSE [50, 74] have shown that the nonlinear effects, including the saturation amplitude, are well predicted by PSE and, according to Deyhle & Bippes [32], it is the saturation amplitude that determines the transition location. In forming a complete amplitude-based transition prediction method, it remains to reliably predict the receptivity process for stationary crossflow modes due to surface roughness. It should be pointed out that in performing the PSE calculations which have been compared to experiments, the initial condition for the PSE marching procedure is based empirically on the experimental results at the furthest upstream station [50]. These comparisons are hampered by that fact that the disturbance environment is not completely known and that the flow evolution may already be nonlinear at the first measurement station. Recently there have been attempts to include the receptivity process in the PSE analysis [52]. However, this approach is still in its infancy and, due to the approximate nature involved in starting the PSE marching procedure, the current results are only qualitative and further refinement is required to incorporate quantitative receptivity predictions in PSE analysis.

In addition to the experimental work described above, there has also been considerable theoretical research on the prediction of receptivity in three-dimensional

boundary layers. A useful review of receptivity in three-dimensional and high-speed boundary layers is given by Choudhari & Streett [15]. In this article, the different receptivity mechanisms for the generation of stationary and traveling crossflow vortices are discussed. In particular it is suggested that although the traveling crossflow vortices have larger linear growth-rates then stationary modes, local receptivity mechanisms preferentially excite stationary vortices. This hypothesis has been recently verified by Choudhari [17] and Crouch [28] who have independently shown that the initial amplitude of traveling CF vortices due to the interaction of freestream acoustic waves with surface roughness is much smaller then that of stationary modes which are generated by the direct scattering of the meanflow by the roughness. This conclusion is directly related to the fact that the amplitude of unsteady freestream disturbances (both sound and turbulence) is very low under flight conditions. In passing, it should be noted that both the experiments of Radeztsky *et al.* [86] and Deyhle & Bippes [32] show that freestream acoustic disturbances have no measurable influence on the level of traveling crossflow modes or on the transition location.

The analysis used by both Choudhari [17] and Crouch [28] is done in the same framework as the asymptotic theories of Goldstein [41] and Ruban [92]. However, instead of approximating the Navier–Stokes equations using high Reynolds number expansions, the equations are replaced by the locally parallel equations in the vicinity of the surface disturbance. This approach was first used by Zavol'skii *et al.* [113] to study the generation of TS waves in the boundary layer over a wavy surface and several recent review articles [21, 29] summarize the various applications of this technique. The advantage of, what has been called Finite Reynolds Number Theory (FRNT), is that solutions can be more easily obtained for a wide range of physical problems at moderate Reynolds numbers. Furthermore, FRNT is not limited to the vicinity of the first neutral point as is the asymptotic theory. As indicated above, FRNT has been used to demonstrate that the initial amplitudes of traveling crossflow modes due to the interaction of sound with roughness is much smaller than that of stationary modes generated directly by surface roughness. Both of these studies where conducted for incompressible flow, with the mean boundary layer flow given by the family of Falkner–Skan–Cooke [25] swept-wedge flows. Consistent with the experimental results discussed above, the greatest effective receptivity is found to occur just upstream of the first neutral point. Although the receptivity increases upstream of the neutral

point, the actual amplitude of a generated instability wave in the unstable region is
reduced because the flow is highly damped upstream of the neutral point. As pointed
out by Choudhari [17], however, the results of the FRNT require numerical and/or
experimental verification in the vicinity of the first neutral point because nonparallel
effects may be important. Additionally, in practical situations, such as the leading-
edge of a wing, the first neutral point for stationary crossflow vortices will occur in
a region of large surface curvature. Recently the effects of both nonparallelism and
surface curvature on the stability characteristics of stationary crossflow vortices has
been examined by Malik and coworkers [76, 72, 73] using both PSE and perturbation
theory to account for the nonparallel effects. These results have generally shown
that while curvature effects are stabilizing, nonparallel effects are destabilizing for
crossflow modes. However, the impact of non-parallelism and curvature remain open
issues with regard to receptivity.

The present research aims to close the gap in transition prediction by predicting
the receptivity of crossflow vortices through numerical simulation of the linearized
Navier–Stokes equations. In this way, the disturbance environment can be carefully
controlled and both the physical mechanisms of the receptivity process and the success
and limitations of the theoretical approaches [17, 28] can be established. In particular,
both the effects of body curvature and nonparallel mean flow will be examined in the
context of a simplified model of a wing leading-edge. Although beyond the scope of
the current study, our results can also be compared to PSE receptivity predictions to
evaluate the viability of that approach.

1.5   Accomplishments and Overview

The accomplishments of this research include:

- A computational method for the simulation of receptivity phenomena near the
  leading-edge of a swept-wing at high subsonic speeds has been developed. To
  make the numerical simulation of receptivity problems more economical, only
  the region in the immediate vicinity of the leading-edge is included in the compu-
  tational domain. When computing mean-flow solutions, an outflow boundary
  condition based on the parabolized Navier–Stokes equations has been imple-
  mented which gives high-quality solutions up to the outflow boundary. For

disturbance calculations, extensive tests are reported on nonreflecting outflow boundary conditions for problems where instability waves exit the boundary. Conditions based on the damping sponge [55] are found to be adequate although more refined techniques are desirable.

- A suite of model problems which represent the physical phenomena expected in receptivity calculations have been solved. These problems include: unstable Tollmien–Schlichting waves in a two-dimensional boundary layer, unstable crossflow vortices in a three-dimensional boundary layer, and acoustic scattering from a circular cylinder. Results from each of these problems are in excellent agreement with exact solutions.

- As further validation, a limited investigation of acoustic leading-edge receptivity is performed for a flat-plate with a super-ellipse leading-edge. Results are compared to the incompressible calculation of Lin *et al.* [61] and the amplitude of the instability waves are predicted to within 10% of the incompressible solutions.

- A series of two- and three-dimensional meanflow solutions are obtained for a parabolic cylinder. Low Mach number, two-dimensional results compare favorably to a reference incompressible solution by Davis [31]. A three-dimensional, high-speed boundary-layer over a swept parabolic-cylinder is computed and thoroughly documented.

- The development of stationary crossflow vortices in the three-dimensional boundary layer on the swept parabolic-cylinder is compared to compressible, linear-stability-theory which incorporates the effects of curvature and nonparallelism. Curvature is included by writing the Navier–Stokes equations in a curvilinear coordinate system. Nonparallel effects are included using a perturbation approach where the solution is written in terms of a slowly varying chordwise coordinate.

- Stability results indicate that surface curvature and nonparallel flow are both important factors over the entire length of the unstable crossflow region. These results are in qualitative agreement with recent PSE and stability analysis for a swept circular cylinder [76, 72]. When measured by the integrated disturbance

kinetic energy, convex surface curvature is found to be stabilizing while non-parallel effects are destabilizing. Including both effects in the stability theory leads to growth-rate predictions which are in excellent agreement with linearized Navier–Stokes solutions for relatively short spanwise wavelengths. However, it is demonstrated for a longer spanwise wavelength that the perturbation approach is inadequate near the leading-edge. This is unfortunate since this longer wavelength mode has a larger N-factor making it considerably more "dangerous." An approximate criterion for the failure of the nonparallel perturbation approach is presented based on the normalized growth of the mean boundary layer.

• The impact of both curvature and nonparallel effects on the receptivity of this flow to surface roughness are established by solutions of the linearized Navier–Stokes equations. When the results are compared to Finite Reynolds Number Theory (FRNT), they indicate that curvature enhances receptivity while non-parallel flow attenuates receptivity. The net effect for the conditions of this study are that the nonparallel attenuation dominates. In a region near the leading-edge, the FRNT predictions are found to generally over-predict the crossflow amplitude, with errors as large as 77% when curvature is included. Although these predictions are conservative, additional refinement of the theory to include nonparallel effects is warranted.

We begin in Chapter 2 with a summary of the governing equations for an ideal, compressible fluid including nondimensionalization, and linearization suitable for receptivity problems. Chapter 3 details the numerical methods used to obtain high-accuracy meanflow solutions and linearized disturbance solutions. This chapter includes a discussion of the potential flow solver, used to compute initial conditions, and boundary conditions for both mean and disturbance equations. Extensive validation of the numerical method is performed in Chapter 4 using model problems based on the physical phenomena observed during the early phases of laminar-turbulent transition. As further validation, a limited study of leading-edge receptivity to sound is presented in section 4.4 including comparisons to previous incompressible solutions. The main focus of this research is detailed in Chapter 5 where an extensive study of instability and receptivity characteristics of the three-dimensional boundary layer on a swept parabolic cylinder is performed. Finally, the results of this thesis are summarized in Chapter 6 with conclusions and avenues for further investigation highlighted.

(a)

(b)

Transition

Cp

x/c

DLR-LV2
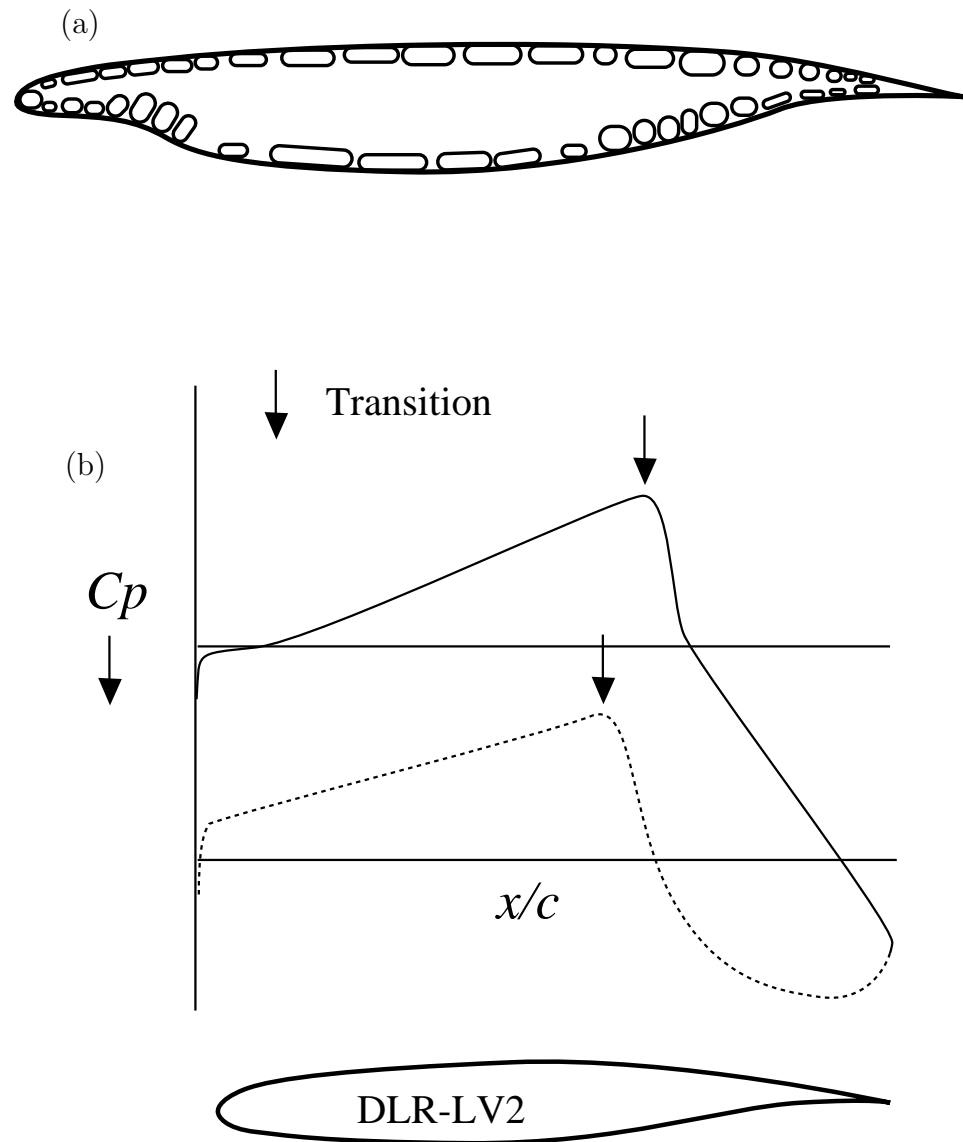
Figure 1.1: Laminar flow wing sections: (a) is a full chord Laminar-Flow-Control airfoil (after [49]) showing the ducting required to remove the suction air, while (b) is a Natural-Laminar-Flow airfoil (after [89]) with the predicted pressure distribution and transition locations on the upper and lower surfaces.

Growing 3D boundary layer
• TS instability
• Crossflow instability
• Centrifugal instability

TS instability
of the attachment
line boundary
layer

U W

Contamination
of the attachment
line flow

Contamination from
the turbulent fuselage
boundary layer

Turbulent
fuselage
boundary
layer
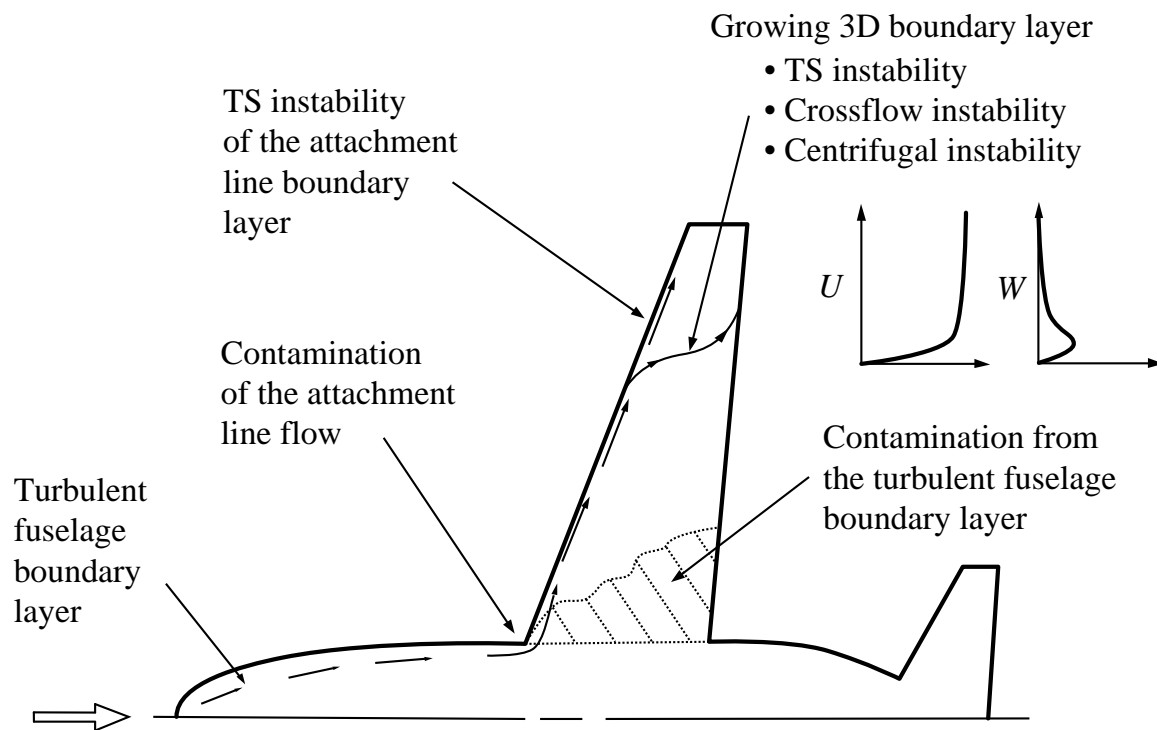
Figure 1.2: Routes to transition on a swept wing.

Chapter 2

Governing Equations

This chapter presents the compressible Navier–Stokes equations in a form amiable to the numerical simulation of receptivity phenomena. The equations are first discussed in dimensional form followed by a conversion to nondimensional variables and an introduction of the relevant nondimensional parameters. In the final section, the equations are linearized about a steady base flow, and these linearized Navier–Stokes equations form the basis for our receptivity study.

2.1 Compressible Navier–Stokes Equations

The compressible Navier–Stokes (NS) equations in primitive form using Cartesian tensor notation and dimensional variables can be written as

$$\rho^*_{,t^*} + \left(\rho^* u_i^*\right)_{,i} = 0, \tag{2.1}$$

$$\rho^* u^*_{i,t^*} + \rho^* u_j^* u^*_{i,j} = -p^*_{,i} + \tau^*_{ij}, \tag{2.2}$$

$$\rho^* h^*_{,t^*} + \rho^* u_j^* h^*_{,j} = \left(p^*_{,t^*} + u_j^* p^*_{,j}\right) + q^*_{j,j} + \tau^*_{ij} u^*_{i,j}, \tag{2.3}$$

where ρ^* is the density, u_i^* is the velocity vector, p^* is the thermodynamic pressure, τ^*_{ij} is the viscous stress tensor, q_j^* is the heat flux vector, and h^* is the fluid enthalpy defined by

$$h^* = e^* + p^*/\rho^*, \tag{2.4}$$

where e^* is the internal energy per unit mass. In the above equations, subscripts following a comma denote partial differentiation with respect to the subscript, and the Einstein summation convention is followed.

We assume a Newtonian fluid such that the viscous stress tensor and the heat flux vector are given by

$$\tau^*_{ij} = \lambda^* u^*_{k,k} \delta_{ij} + 2\mu^* S^*_{ij}, \tag{2.5}$$

17

$$q_j^* = -\kappa^* T_{,j}^*, \tag{2.6}$$

where μ^* is the first coefficient of viscosity, λ^* is the second coefficient of viscosity, κ^* is the thermal conductivity, $S_{ij}^* = \frac{1}{2}(u_{i,j}^* + u_{j,i}^*)$ is the rate-of-strain tensor, T^* is the absolute temperature, and δ_{ij} is the Kronecker delta.

The system of equations (2.1)–(2.3) is closed with an equation-of-state, relating the thermodynamic variables, and additional equations which relate the fluid properties to the thermodynamic variables. We use an ideal, calorically perfect gas with constant specific heats such that

$$p^* = \rho^* \mathcal{R}^* T^*, \tag{2.7}$$

where $\mathcal{R}^* = c_p^* - c_v^*$ is the gas constant, c_p^* is the specific heat at constant pressure, and c_v^* is the specific heat at constant volume. Both c_p^* and c_v^* are constant as is the ratio, $\gamma = c_p^*/c_v^*$. Under these conditions, the internal energy and enthalpy are related to the absolute temperature by

$$e^* = c_v^* T^*, \tag{2.8}$$

$$h^* = c_p^* T^*. \tag{2.9}$$

For a calorically perfect gas, the fluid properties (viscosity coefficients and conductivity) are functions of temperature only. For low-speed flows with small temperature variations, the fluid properties can be assumed constant with little loss of accuracy and this assumption is used for many of the low-speed results presented here. However, for high-speed flows the temperature dependence of the fluid properties becomes important. Before describing the relations used to determine the fluid properties, we will first convert the governing equations to nondimensional variables.

2.2   Nondimensional Navier–Stokes Equations

In equations (2.1)–(2.9), the superscript "$*$" indicates that the quantities are dimensional. In nondimensionalizing these equations the following relations have been used,

$$
\begin{aligned}
\rho &= \frac{\rho^*}{\rho_r^*}, & u_i &= \frac{u_i^*}{u_r^*}, & T &= \frac{T^*}{T_r^*}, \\
p &= \frac{p^*}{\rho_r^* u_r^{*2}}, & \mu &= \frac{\mu^*}{\mu_r^*}, & \lambda &= \frac{\lambda^*}{\mu_r^*}, \\
\kappa &= \frac{\kappa^*}{\kappa_r^*}, & x_i &= \frac{x_i^*}{L^*}, & t &= \frac{t^*}{L^*/u_r^*},
\end{aligned}
\tag{2.10}
$$

where L^* is some convenient reference length and quantities denoted with a subscript "r" are reference values typically taken to be far-field ambient conditions. The particular values of L^*, ρ_r^*, u_r^*, *etc.* are defined for each problem considered.

Using equations (2.10) in equations (2.1) through (2.7) yields the following non-dimensional equations

$$\rho_{,t} + (\rho u_i)_{,i} = 0, \tag{2.11}$$

$$\rho u_{i,t} + \rho u_j u_{i,j} = -p_{,i} + \frac{1}{\mathsf{Re}}\Big[(\lambda u_{j,j})_{,i} + (2\mu S_{ij})_{,j}\Big], \tag{2.12}$$

$$\begin{aligned}
\rho T_{,t} + \rho u_j T_{,j} + (\gamma - 1)\rho T u_{j,j} &= \frac{\gamma}{\mathsf{PrRe}}\Big[\kappa T_{,i}\Big]_{,i} + \\
&\quad \frac{\gamma(\gamma-1)\mathsf{M}^2}{\mathsf{Re}}\Big[\lambda S_{ii}S_{jj} + 2\mu S_{ij}S_{ij}\Big],
\end{aligned} \tag{2.13}$$

$$p = \frac{\rho T}{\gamma \mathsf{M}^2}, \tag{2.14}$$

where

$$\mathsf{M} = \frac{u_r^*}{c_r^*}, \qquad \mathsf{Re} = \frac{\rho_r^* u_r^* L^*}{\mu_r^*}, \qquad \mathsf{Pr} = \frac{\mu_r^* c_p^*}{\kappa_r^*}, \tag{2.15}$$

are the Mach number, Reynolds number, and Prandtl number respectively. In deriving the non-dimensional energy equation (2.13) from (2.3), use is made of equation (2.9) to convert enthalpy to temperature and the continuity equation (2.1) along with the equation-of-state (2.7) are used to remove the explicit pressure dependence.

For low-speed conditions where the dependence of fluid properties on temperature is negligible, $\mu = 1$. For cases where the temperature dependence of the fluid properties is important, μ is related to the temperature through Sutherland's law

$$\mu = T^{\frac{3}{2}}\frac{1+S}{T+S}, \tag{2.16}$$

where $S = S_0^*/T_r^*$ and $S_0^* = 111K$ for air [111]. The second coefficient of viscosity is computed using Stokes hypothesis, $\lambda = -\frac{2}{3}\mu$ (giving zero bulk viscosity), and the thermal conductivity is determined assuming constant Prandtl number, $\kappa = \mu$. Unless otherwise specified, the fluid is assumed to be air with a Prandtl number of 1.0 and a ratio of specific heats, $\gamma = 1.4$.

2.3   Linearized Navier–Stokes Equations

In determining receptivity or stability characteristics it is often convenient (where appropriate) to treat disturbances as linear perturbations about a steady base-flow. Thus, flow variables are written as

$$
\begin{aligned}
\rho &= \bar{\rho}(x_i) + \rho'(x_i,t), & u_j &= \bar{u}_j(x_i) + u'_j(x_i,t), \\
T &= \bar{T}(x_i) + T'(x_i,t), & \mu &= \bar{\mu}(x_i) + \mu'(x_i,t), \\
\lambda &= \bar{\lambda}(x_i) + \lambda'(x_i,t), & \kappa &= \bar{\kappa}(x_i) + \kappa'(x_i,t), \\
p &= \bar{p}(x_i) + p'(x_i,t),
\end{aligned}
\tag{2.17}
$$

where a bar denotes base-flow variables and primes denote (linear) perturbations about that base flow.

Substituting these expressions into equations (2.11)–(2.14) and dropping terms that are nonlinear in the perturbations leads to two sets of equations: one for the base flow and one for the perturbation flow. The base-flow equations are just the steady versions of equations (2.11)–(2.14).

$$
\left(\bar{\rho}\bar{u}_i\right)_{,i} = 0,
\tag{2.18}
$$

$$
\bar{\rho}\bar{u}_j\bar{u}_{i,j} = -\bar{p}_{,i} + \frac{1}{\mathsf{Re}}\Big[(\bar{\lambda}\bar{u}_{j,j})_{,i} + (2\bar{\mu}\bar{S}_{ij})_{,j}\Big],
\tag{2.19}
$$

$$
\begin{aligned}
\bar{\rho}\bar{u}_j\bar{T}_{,j} + (\gamma-1)\bar{\rho}\bar{T}\bar{u}_{j,j} &= \frac{\gamma}{\mathsf{Pr}\mathsf{Re}}\Big[\bar{\kappa}\bar{T}_{,i}\Big]_{,i} + \\
&\quad \frac{\gamma(\gamma-1)\mathsf{M}^2}{\mathsf{Re}}\Big[\bar{\lambda}\bar{S}_{ii}\bar{S}_{jj} + 2\bar{\mu}\bar{S}_{ij}\bar{S}_{ij}\Big],
\end{aligned}
\tag{2.20}
$$

$$
\bar{p} = \frac{\bar{\rho}\bar{T}}{\gamma\mathsf{M}^2},
\tag{2.21}
$$

while the perturbation equations are given by

$$
\rho'_{,t} + \left(\bar{\rho}u'_i\right)_{,i} + \left(\rho'\bar{u}_i\right)_{,i} = 0,
\tag{2.22}
$$

$$
\begin{aligned}
\bar{\rho}u'_{i,t} + \bar{\rho}\bar{u}_j u'_{i,j} + \bar{\rho}u'_j\bar{u}_{i,j} + \rho'\bar{u}_j\bar{u}_{i,j} &= -p'_{,i} + \\
\frac{1}{\mathsf{Re}}\Big[(\bar{\lambda}u'_{j,j})_{,i} + (\lambda'\bar{u}_{j,j})_{,i} + (2\bar{\mu}S'_{ij})_{,j} + (2\mu'\bar{S}_{ij})_{,j}\Big],
\end{aligned}
\tag{2.23}
$$

$$\bar{\rho}T'_{,t} + \bar{\rho}\bar{u}_j T'_{,j} + \bar{\rho}u'_j \bar{T}_{,j} + \rho'\bar{u}_j\bar{T}_{,j} =$$

$$(1-\gamma)\left[\rho'\bar{T}\bar{u}_{j,j} - \bar{\rho}_{,j}\bar{u}_j T' + \bar{\rho}\bar{T}u'_{j,j}\right] + \frac{\gamma}{\mathsf{PrRe}}\left[\bar{\kappa}T'_{,i} + \kappa'\bar{T}_{,i}\right]_{,i} +$$

$$\frac{\gamma(\gamma-1)\mathsf{M}^2}{\mathsf{Re}}\left[2\bar{\lambda}\bar{S}_{ii}S'_{jj} + \lambda'\bar{S}_{ii}\bar{S}_{jj} + 4\bar{\mu}\bar{S}_{ij}S'_{ij} + 2\mu'\bar{S}_{ij}\bar{S}_{ij}\right], \qquad (2.24)$$

$$p' = (\bar{\rho}T' + \bar{T}\rho')/(\gamma\mathsf{M}^2). \qquad (2.25)$$

Since the coefficients μ, λ, and κ are functions only of T, the linear perturbations of these coefficients and their derivatives are defined solely in terms of $\bar{T}$, T', and their derivatives. For example,

$$\mu' = \left(\frac{d\mu}{dT}\right)_{\bar{T}} T', \qquad (2.26)$$

and

$$\mu'_{,j} = \left(\frac{d^2\mu}{dT^2}\right)_{\bar{T}} \bar{T}_{,j}T' + \left(\frac{d\mu}{dT}\right)_{\bar{T}} T'_{,j}, \qquad (2.27)$$

where the derivatives of μ are zero for constant properties flow or are determined from Sutherland's law, equation (2.16). Similar expressions for λ' and κ' follow directly.

With these expressions for the fluid properties and by dividing through by $\bar{\rho}$, equations (2.22)–(2.24) can be rewritten using the more compact notation

$$\mathbf{U}'_{,t} + \mathbf{A}\mathbf{U}'_{,1} + \mathbf{B}\mathbf{U}'_{,2} + \mathbf{C}\mathbf{U}'_{,3} + \mathbf{D}\mathbf{U}' = \mathbf{V}_{11}\mathbf{U}'_{,11} + \mathbf{V}_{12}\mathbf{U}'_{,12} +$$

$$\mathbf{V}_{13}\mathbf{U}'_{,13} + \mathbf{V}_{22}\mathbf{U}'_{,22} + \mathbf{V}_{23}\mathbf{U}'_{,23} + \mathbf{V}_{33}\mathbf{U}'_{,33} \qquad (2.28)$$

where

$$\mathbf{U}' = \left\{\begin{array}{c} \rho' \\ u'_1 \\ u'_2 \\ u'_3 \\ T' \end{array}\right\} \qquad (2.29)$$

and the matrices $(\mathbf{A}, \mathbf{B}, \mathbf{C}, \mathbf{D}, \mathbf{V}_{ij})$, defined in Appendix A.1, depend only on the mean flow variables and their gradients.

The form of the linearized, compressible Navier–Stokes equations given in equation (2.28) is a suitable starting point for numerical simulation of receptivity (section 3.7), linear-stability analysis (Appendix D), and parabolized stability analysis [13].

Chapter 3

Numerical Method for Receptivity Calculations

This chapter presents the numerical methods developed to simulate receptivity phenomena near a swept leading-edge. We begin with a discussion of the issues and challenges faced when undertaking receptivity calculations.

3.1 Computational Issues and Challenges

The computational simulation of receptivity requires a numerical scheme capable of accurately and efficiently computing both the mean boundary-layer flow about an arbitrary leading-edge and the evolution of unsteady disturbances on that mean flow. The unsteady disturbances include inviscid (acoustic, entropy, vorticity) waves in the far-field and viscous instability waves in the boundary layer. The dispersion relations for all types of waves and the dynamics of their interaction (*i.e.* receptivity) must be accurately represented. Although accurate and efficient numerical methods have been developed to compute mean-flow and wave-propagation phenomena individually, there is no method readily available for the simultaneous solution of both types of problems in complex geometries.

For computing mean boundary-layer flows, there are a wide range of methods available [6,102,109,103,98] to name just a few. In general, these methods are second-order-accurate in space with second-order-accurate, implicit time-advancement and incorporate some form of (spatial) numerical dissipation to control spurious oscillations in the solution. These spurious oscillations arise for a host of reasons including, but not limited to, insufficient resolution, approximate boundary conditions, incomplete residual reduction when using iterative solvers, and mesh stretching. The type of numerical dissipation used depends on the particular scheme but can take the form of an artificial viscosity term, upwind differencing, or "least-squares" stabilization. In certain limiting cases each of these forms of numerical dissipation can be shown

to be equivalent. Although these flow solvers are generally found to converge rapidly to accurate mean-flow solutions, their use for unsteady, wave-propagation problems is relatively untested.

Recently Fenno *et al.* [36] used a second-order finite-volume scheme with artificial viscosity to study the receptivity of a two-dimensional parabolic-cylinder to freestream acoustic waves at low Mach numbers. They found that the numerical dissipation of the code damped the incoming acoustic waves by 56% before the waves struck the leading-edge, even when using a costly anisotropic dissipation technique. Furthermore, instability wave amplitudes and neutral point locations were in significant error when compared to previous incompressible results obtained using a spectral method. This was also the case when resolution was increased to over 50 points per instability wavelength—a value which resulted in prohibitively high CPU times.

Similar, although not as pessimistic, results were found when evaluating a finite-element flow solver using the "Galerkin Least-Squares" method [98] for computation of boundary layer instability waves [22]. When this method was properly formulated, by including the full residual of the Navier–Stokes equations in the Least-Squares term, it was found that 60 bilinear-elements per Tollmien–Schlichting wavelength and 250 elements normal to the wall are required to achieve sufficient accuracy in the growth-rate.[1] For comparison, the method presented below, achieves sufficient accuracy using 20 nodes per wavelength with 128 normal to the wall. To take full advantage of the finite-element method, an unstructured grid is desirable to cluster elements in regions of high gradients. However, the error in the growth-rate for linear triangles is 3.5 times greater than that of bilinear elements using the same node distribution. This loss in accuracy offsets the advantage of the unstructured grid. Investigations were also made using bi-quadratic and bi-cubic elements and, as expected, a significant reduction in the number elements was obtained with increasing order for the same level of accuracy. However, the greater expense in terms of code complexity and computer time renders these higher-order methods unsuitable for the present investigation.

In recent years, there has also been considerable method development for computing wave-propagation problems. These methods typically make use of high-order

---

[1]With reference to section 4.1 we have defined a growth-rate error of less than 0.2% as sufficient for the receptivity problems under consideration.

finite-difference spatial discretization with a high-order explicit time advancement scheme. Examples include the sixth-order-accurate compact scheme of Lele [60] with fourth-order Runge-Kutta time advancement used by Colonius *et al.* [23] and Mitchell *et al.* [77] and the DRP scheme of Tam and Webb [105] which uses an optimized 7-point finite-difference stencil in space with a multi-step, explicit time-advancement scheme. Although these schemes have excellent wave propagation characteristics, they typically suffer from poor convergence to steady-state since they rely on explicit time-advancement schemes with strict stability limits. Furthermore, converting to an implicit time-advancement scheme for computing steady-states is complicated by the large stencils used in computing spatial derivatives.

In an effort to develop a method suitable for both mean-flow and wave propagation problems, we have retained a fully implicit time-advancement scheme, but with a 5-point (up to 4th-order-accurate) finite difference stencil in space. With approximate factorization, this results in a series of block penta-diagonal matrices which must be solved at each time-step or iteration. We have found that even with the rather large, block penta-diagonal matrices, an efficient code results. Furthermore, when computing mean-flow solutions the block, penta-diagonal matrices can be approximated by block, tri-diagonal matrices, thereby reducing expense while retaining numerical stability.

In the following sections, details of the numerical method are presented including the generalized coordinate system, spatial discretization, time advancement, iterative solvers for both nonlinear and linearized equations, and boundary treatments for mean and disturbance solutions. But first, a brief description of the receptivity problem and computational domain is presented.

3.2   Problem Description

To render the discussion concrete, the numerical method is discussed in the context of the swept leading-edge, receptivity problem; although the method is generally applicable to a much wider set of problems. Figure 3.1 shows a schematic of the leading-edge geometry where the chordwise direction is denoted by x, the vertical direction by y, and the spanwise direction by z. The arc-length along the surface of the wing is given by s and the distance normal to the wing surface is n. The wing

has an angle-of-attack, α, and sweep angle, θ, and is idealized as having infinite span with no taper. This avoids fuselage and tip effects and renders all z-derivatives zero in the mean. The chordwise component of the freestream velocity is denoted as u_∞, the spanwise component as w_∞, and the magnitude of the freestream velocity is U_∞.

In constructing the computational domain, only the region in the immediate vicinity of the leading-edge is included. By truncating the downstream portion of the wing we avoid the unsteady and complicated flow features often present near the trailing-edge: shock waves, flow separation, and the unsteady wake. In a subsonic flow, pressure disturbances associated with these phenomena travel upstream and exert some influence on the flow near the leading-edge. To the extent that such upstream influence is important, the current solutions are only an approximation of the flow near an actual wing leading-edge. For the problems presented in this thesis, the impact of domain truncation will be assessed by comparing solutions computed with different domain lengths.

3.3   Generalized Coordinates

To represent the airfoil geometry and to cluster points in regions of high spatial gradients (such as the boundary layer and the attachment-line), a global, two-dimensional mapping is constructed from physical space (x, y, z) to a uniform, Cartesian computational space (ξ, η, z) with both ξ and η in the range $[0, 1]$.

Evaluation of first-derivatives in physical space in terms of derivatives in computational space utilizes the Jacobian of the mapping

$$\left\{ \begin{array}{c} \frac{\partial}{\partial x} \\[4pt] \frac{\partial}{\partial y} \end{array} \right\} = \mathbf{J} \left\{ \begin{array}{c} \frac{\partial}{\partial \xi} \\[4pt] \frac{\partial}{\partial \eta} \end{array} \right\}, \tag{3.1}$$

where the Jacobian, $\mathbf{J}$, is defined as

$$\mathbf{J} = \begin{bmatrix} \xi_{,x} & \eta_{,x} \\ \xi_{,y} & \eta_{,y} \end{bmatrix} \tag{3.2}$$

and $\xi_{,x}$, $\eta_{,x}$, $\xi_{,y}$, and $\eta_{,y}$ are the metrics of the mapping transformation. Similarly,

second-derivatives in physical space are computed using the Hessian of the mapping,

$$
\left\{ \begin{matrix} \frac{\partial^2}{\partial x^2} \\ \frac{\partial^2}{\partial x \partial y} \\ \frac{\partial^2}{\partial y^2} \end{matrix} \right\} = \begin{bmatrix} (\xi_{,x})^2 & \xi_{,x}\eta_{,x} & (\eta_{,x})^2 \\ \xi_{,x}\xi_{,y} & \xi_{,x}\eta_{,y} + \xi_{,y}\eta_{,x} & \eta_{,x}\eta_{,y} \\ (\xi_{,y})^2 & \xi_{,y}\eta_{,y} & (\eta_{,y})^2 \end{bmatrix} \left\{ \begin{matrix} \frac{\partial^2}{\partial \xi^2} \\ \frac{\partial^2}{\partial \xi \partial \eta} \\ \frac{\partial^2}{\partial \eta^2} \end{matrix} \right\} + \begin{bmatrix} \xi_{,xx} & \eta_{,xx} \\ \xi_{,xy} & \eta_{,xy} \\ \xi_{,yy} & \eta_{,yy} \end{bmatrix} \left\{ \begin{matrix} \frac{\partial}{\partial \xi} \\ \frac{\partial}{\partial \eta} \end{matrix} \right\}. \quad (3.3)
$$

The actual form of the mapping function depends on the particular problem under investigation.

Typically, in CFD applications, the governing equations are converted to a generalized coordinate space. In so doing, the mapping metrics ($\xi_{,x}$, $\eta_{,x}$, ...) are computed approximately using the same derivative scheme used for the flow variables. Errors in the mapping metrics can lead to an increase in numerical errors. To circumvent this, we use analytically defined metrics whenever possible, which includes all of the problems presented here. For geometries where analytical metrics are not possible, we have developed a preprocessing routine which uses a high resolution mesh to compute the mapping metrics. Although the preprocessor computes finite difference approximations to the metrics, the mesh spacing for the metric computation can be selected to virtually eliminate errors in the metric evaluation. These 'pseudo-analytical' metrics can then be used as input data to the flow solver.

It is important to note that the numerical method presented here is based on the primitive form of the governing equations (2.11)–(2.13). As such, the numerical method is not conservative and therefore is not appropriate for computations with shocks where shock-capturing is used. However, since the equations are in primitive form, we are guaranteed that the uniform freestream condition will be preserved regardless of the mesh metrics. Overall conservation with this type of approach is only approximate but the errors are small—on the order of the truncation error.

3.4   Spatial Discretization

Consider derivative operators in the uniform computational space (ξ, η) where ξ_i, η_j represent the nodal locations with $\xi_i = \Delta\xi(i - 1)$ for $1 \le i \le N_\xi$ and $\eta_j = \Delta\eta(j - 1)$ for $1 \le j \le N_\eta$. In presenting the spatial discretization, the difference operators are given only for the ξ direction since the η operators are completely analogous.

At interior nodes, the fourth-order-accurate central difference scheme is used for

first- and second-derivatives. First-derivatives are approximated by the expression

$$\left(\frac{\partial f}{\partial \xi}\right)_i \approx \frac{1}{12\Delta\xi}\Big[\left(f_{i-2} - f_{i+2}\right) - 8\left(f_{i-1} - f_{i+1}\right)\Big], \tag{3.4}$$

while second-derivatives are computed using

$$\left(\frac{\partial^2 f}{\partial \xi^2}\right)_i \approx \frac{1}{12(\Delta\xi)^2}\Big[-\left(f_{i-2} - 2f_i + f_{i+2}\right) + 16\left(f_{i-1} - 2f_i + f_{i+1}\right)\Big]. \tag{3.5}$$

Near the computational boundaries, finite difference operators that are biased toward the interior are required. Since the interior scheme uses a 5-point stencil, biased difference operators are required at the boundary point and at the first node in the interior, *i.e.* nodes $(1, 2, N_\xi - 1, N_\xi)$.

First derivatives at ξ_1 are computed using the 4th-order-accurate one-sided difference scheme

$$\left(\frac{\partial f}{\partial \xi}\right)_1 \approx \frac{1}{12\Delta\xi}\Big[-25f_1 + 48f_2 - 36f_3 + 16f_4 - 3f_5\Big], \tag{3.6}$$

while at node ξ_2 the 4th-order-accurate biased difference stencil is used

$$\left(\frac{\partial f}{\partial \xi}\right)_2 \approx \frac{1}{12\Delta\xi}\Big[-3f_1 - 10f_2 + 18f_3 - 6f_4 + f_5\Big]. \tag{3.7}$$

Second derivatives at ξ_1 are computed using the 3rd-order-accurate expression

$$\left(\frac{\partial^2 f}{\partial \xi^2}\right)_1 \approx \frac{1}{12(\Delta\xi)^2}\Big[11f_1 - 20f_2 + 6f_3 + 4f_4 - f_5\Big], \tag{3.8}$$

while a 3rd-order-accurate one-side expression is used at node ξ_2

$$\left(\frac{\partial^2 f}{\partial \xi^2}\right)_2 \approx \frac{1}{12(\Delta\xi)^2}\Big[35f_1 - 104f_2 + 114f_3 - 56f_4 + 11f_5\Big]. \tag{3.9}$$

Similar expressions hold for the derivatives at nodes $N_\xi - 1$ and N_ξ but with the stencils reversed and the signs switched on the coefficients for the first derivatives.

Notice that we have retained a 5-point stencil for all derivatives, even at the boundaries. This ensures that first-derivatives are computed to 4th-order-accuracy at every point in the domain, while second derivatives drop only one-order near the

boundary. Although retaining 4th-order-accurate first derivatives near the boundary is not required to obtain global 4th-order convergence [47], we have found, through numerical experimentation, that the added accuracy is desirable especially near the wall. The use of 5-point stencils near the boundary does alter the structure of the matrices used in the implicit solver and the impact of these changes is discussed in sections 3.6 and 3.7.

3.5   Temporal Discretization

For computing steady-state solutions (both nonlinear and linearized) we march the unsteady equations to the steady-state using the implicit Euler scheme, where the time derivative is approximated by

$$\left(\frac{\partial u}{\partial t}\right)^{(n+1)} = \frac{u^{(n+1)} - u^{(n)}}{\Delta t} + \mathcal{O}(\Delta t). \tag{3.10}$$

This first-order accurate scheme has significant temporal dissipation which helps speed the convergence to the steady-state solution. Since time-accuracy is not an issue for steady-state calculations, local-time-stepping is used to further accelerate convergence. With local-time-stepping, Δt in equation (3.10) is replaced by $\Delta t(x, y)$ which is a function of the (x, y) coordinates. The value of the time-step is chosen to be proportional to a measure of the local Courant–Friedrichs–Lewy (CFL) condition. The techniques for estimating the CFL for base flow and linearized calculations are presented in section 3.6 and section 3.7 respectively. It is important to remember that the CFL is only used to compute the local time-step as a means of enhancing convergence to the steady-state solution. In this context, the CFL has no relevance to numerical stability since the time-advancement scheme is unconditionally stable.

For unsteady calculations, we use the second-order accurate, two-step implicit scheme given by

$$\left(\frac{\partial u}{\partial t}\right)^{(n+1)} = \frac{3u^{(n+1)} - 4u^{(n)} + u^{(n-1)}}{2\Delta t} + \mathcal{O}(\Delta t^2) \tag{3.11}$$

Since this time-advancement scheme requires two previous time-levels, the integration is started at $t = 0$ with one step of implicit Euler, equation (3.10). The two-step

implicit scheme has been recently used to study transitional flows by Rai & Moin [88].
Unlike the Crank–Nicholson scheme which is the most accurate second-order accurate
implicit scheme, the two-step implicit scheme does introduce temporal dissipation
due to the biased stencil. When coupled with the central-difference operators used in
space, we have found that the Crank–Nicholson scheme eventually leads to numerical
oscillations in the solution which arise due to the variety of factors discussed in section
3.1. Using the two-step implicit scheme prevents the accumulation of these numerical
oscillations at the expense of slightly reduced accuracy for a given time-step.

3.6   Base Flow Solver

The base flow is given by solution of the steady, nonlinear Navier–Stokes equations
(2.18)–(2.21) subject to appropriate boundary conditions. Since the wing is idealized
as having infinite span the problem is reduced to a two-dimensional problem in the
(x, y) plane but with three nonzero components of velocity due to wing sweep.

   To solve (2.18)–(2.21) we retain the time terms and march the unsteady NS equa-
tions to the steady-state using the implicit-Euler time-integrator, equation (3.10).
With the time terms added, equations (2.18)–(2.21) can be written in the form

$$\bar{\mathbf{U}}_{,t} + \mathbf{F}(\bar{\mathbf{U}}) = 0, \tag{3.12}$$

where

$$\bar{\mathbf{U}} = \left\{ \begin{array}{c} \bar{\rho} \\ \bar{u}_1 \\ \bar{u}_2 \\ \bar{u}_3 \\ \bar{T} \end{array} \right\}. \tag{3.13}$$

Applying backward Euler time discretization yields

$$-\bar{\mathbf{U}}^{(n+1)} + \bar{\mathbf{U}}^{(n)} + \Delta t \bar{\mathbf{U}}_{,t}^{(n+1)} \equiv \mathbf{G}\left(\bar{\mathbf{U}}^{(n+1)}; \bar{\mathbf{U}}^{(n)}\right) = 0 \tag{3.14}$$

and applying Newton's method to solve this nonlinear problem leads to the iteration

$$\bar{\mathbf{U}}_1^{(n+1)} \;\; = \;\; \bar{\mathbf{U}}^{(n)} \tag{3.15}$$

$$\delta \bar{\mathbf{U}}_i = \bar{\mathbf{U}}_{i+1}^{(n+1)} - \bar{\mathbf{U}}_i^{(n+1)} \tag{3.16}$$

$$-\left(\frac{\partial \mathbf{G}}{\partial \bar{\mathbf{U}}}\right)_i \delta \bar{\mathbf{U}}_i = \mathbf{G}(\bar{\mathbf{U}}_i^{(n+1)}; \bar{\mathbf{U}}^{(n)}), \tag{3.17}$$

where (3.17) can be simplified to

$$\left[\mathbf{I} + \Delta t \frac{\partial \mathbf{F}}{\partial \bar{\mathbf{U}}}\right]_i \delta \bar{\mathbf{U}}_i = \mathbf{G}(\bar{\mathbf{U}}_i^{(n+1)}; \bar{\mathbf{U}}^{(n)}). \tag{3.18}$$

The process of linearization in the Newton iteration is nearly the same as that done in section 2 when deriving the disturbance equations. The only difference is that the linearization is now done about an unsteady field thus requiring a slight modification to the definitions of the matrices in equation (2.28). The required modifications are detailed in Appendix A.2. With the understanding that the matrices are modified to account for the unsteady flow, the tangent in the Newton iteration can be obtained from (2.28) by evaluating the matrices at the previous iteration.

Converting to the generalized coordinate system the tangent becomes

$$-\left(\frac{\partial \mathbf{G}}{\partial \bar{\mathbf{U}}}\right)_i = \left[\mathbf{I} + \Delta t\left(\check{\mathbf{A}}\Delta_\xi + \check{\mathbf{B}}\Delta_\eta + \check{\mathbf{D}} - \check{\mathbf{V}}_{\xi\xi}\Delta_{\xi\xi} - \check{\mathbf{V}}_{\xi\eta}\Delta_{\xi\eta} - \check{\mathbf{V}}_{\eta\eta}\Delta_{\eta\eta}\right)\right]_i. \tag{3.19}$$

In this equation the matrices are denoted with a check to indicate that the mapping metrics are included in their definitions, *e.g.*,

$$\check{\mathbf{A}} = \xi_{,x}\mathbf{A} + \xi_{,y}\mathbf{B} + \xi_{,xx}\mathbf{V}_{11} + \xi_{,xy}\mathbf{V}_{12} + \xi_{,yy}\mathbf{V}_{22}. \tag{3.20}$$

The symbols $(\Delta_\xi, \Delta_\eta, \dots)$ in equation (3.19) represent finite difference operators in computational space. In computing the mean flow, it is computationally attractive to approximate the tangent using second-order finite difference operators instead of the full fourth-order operators used to form the residual. This approximation decreases the bandwidth of the tangent, reducing memory storage and floating point operations. However, from computational experience we have found that convergence is degraded if the boundary differences are approximated in the tangent. So, in practice, second-order differences are used in the tangent only for interior nodes and 5-point stencils are retained at the three nodes nearest the boundaries. It should be noted that the approximation of the LHS finite difference operators with reduced-order finite-differences has been used previously by Rai & Moin [88] and Beaudan &

Moin [7]. However, in both these applications, the interior scheme used upwind biased differencing and the LHS was approximated by first-order upwind differencing with no report of poor convergence near the boundaries. However, it is well known that the use of biased differencing introduces numerical dissipation. The lack of numerical dissipation in the present scheme may contribute to the sensitivity of convergence on the boundary approximation in the LHS.

As a further approximation, (3.18) is approximately factored into

$$\left[\mathbf{I} + \Delta t\left(\check{\mathbf{A}}\Delta_\xi + \check{\mathbf{D}} - \check{\mathbf{V}}_{\xi\xi}\Delta_{\xi\xi}\right)\right]_i \mathbf{Z}_i = \mathbf{G}(\bar{\mathbf{U}}_i^{n+1}; \bar{\mathbf{U}}^n), \tag{3.21}$$

$$\left[\mathbf{I} + \Delta t\left(\check{\mathbf{B}}\Delta_\eta - \check{\mathbf{V}}_{\eta\eta}\Delta_{\eta\eta}\right)\right]_i \Delta\bar{\mathbf{U}}_i = \mathbf{Z}_i, \tag{3.22}$$

which greatly reduces the amount of memory required at the expense of introducing errors of $\mathcal{O}(\Delta t^2)$ in the tangent. The use of the higher-order boundary closure in the tangent spoils the block tri-diagonal structure of the approximately factored system near the boundaries resulting in a matrix with a profile as shown in figure 3.2. A special purpose routine based on Gaussian elimination [45] has been written to efficiently solve this, nearly, block tri-diagonal system on a vector supercomputer.

By introducing the approximations described above into the tangent, the quadratic convergence of the Newton iteration is sacrificed. Assuming that the iteration converges, the errors due to these approximations can be driven to zero. By analysis of the one-dimensional convection-diffusion equation and by computational experimentation of the full equations we have found that these approximations yield a stable and convergent scheme.

As discussed in section 3.5, local time-stepping, based on the local CFL, is used to speed convergence to the steady-state solution. To estimate the local CFL we use the following approximate expression [85] which follows from a physical argument of enclosing the physical domain of dependence within a computational cell [67]

$$\mathsf{CFL} = \frac{\Delta t}{\Delta\xi\Delta\eta}\Big\{|\mathbf{J}_{1i}\bar{u}_i|\Delta\eta + |\mathbf{J}_{2i}\bar{u}_i|\Delta\xi +$$
$$\bar{c}\left[(\mathbf{J}_{11}^2 + \mathbf{J}_{12}^2)\Delta\eta^2 + (\mathbf{J}_{21}^2 + \mathbf{J}_{22}^2)\Delta\xi^2\right]^{1/2}\Big\}. \tag{3.23}$$

In this expression, $\mathbf{J}$ is the Jacobian of the mapping and $\bar{c}$ is the local sound-speed. By specifying a value of CFL, equation (3.23) is solved for the local value of $\Delta t(x,y)$. The

CFL defined in equation (3.23) includes convective and acoustic phenomena but ignores viscous diffusion. A similar expression can be derived to include viscous effects, but we have found the current equation (3.23) adequate for accelerating convergence to steady-state.

3.7 Linear Disturbance Solver

Two approaches are used to obtain solutions to the linearized disturbance equations (2.28). In the first method, the unsteady equations are advanced in time using the second-order accurate, implicit, time-advancement scheme presented in section 3.5. This technique is suitable for the solution of problems in which the transient temporal evolution of disturbances is desired. In the second method, the equations are converted to the frequency domain and are marched to a steady-state solution using a technique similar to that used for the base-flow solution. This method is ideal when a time asymptotic solution is desired.

3.7.1 Unsteady Approach

In the unsteady approach, the disturbance equations are solved using a time-accurate technique to determine the transient evolution of disturbances. Given a mean flow solution, the solution to the disturbance equations follows using a combination of high-order finite difference and spectral schemes to accurately compute spatial derivatives. In the (x, y) plane, derivatives are computed in the same manner as for the base flow. Since the spanwise direction, z, is periodic, we write the solution as

$$\mathbf{U}' = \hat{\mathbf{U}}(x, y, t)\, e^{ik_z z} \tag{3.24}$$

where $k_z = 2\pi/\lambda_z$ is the spanwise wavenumber and the real-part convention is used. Substituting this expression into the linearized Navier–Stokes equation (2.28) one obtains

$$\hat{\mathbf{U}}_{,t} + \mathbf{A}\hat{\mathbf{U}}_{,1} + \mathbf{B}\hat{\mathbf{U}}_{,2} + ik_z\mathbf{C}\hat{\mathbf{U}} + \mathbf{D}\hat{\mathbf{U}} =$$

$$\mathbf{V}_{11}\hat{\mathbf{U}}_{,11} + \mathbf{V}_{12}\hat{\mathbf{U}}_{,12} + ik_z\mathbf{V}_{13}\hat{\mathbf{U}}_{,1} + \mathbf{V}_{22}\hat{\mathbf{U}}_{,22} + ik_z\mathbf{V}_{23}\hat{\mathbf{U}}_{,2} - k_z^2\mathbf{V}_{33}\hat{\mathbf{U}}. \tag{3.25}$$

Converting to computational space produces the equation

$$\hat{\mathbf{U}}_{,t} + \left[\check{\mathbf{A}}\Delta_\xi + \check{\mathbf{B}}\Delta_\eta + \check{\mathbf{D}} - \check{\mathbf{V}}_{\xi\xi}\Delta_{\xi\xi} - \check{\mathbf{V}}_{\xi\eta}\Delta_{\xi\eta} - \check{\mathbf{V}}_{\eta\eta}\Delta_{\eta\eta} \right]\hat{\mathbf{U}} = 0 \qquad (3.26)$$

where the check on the matrices indicates that they include the mapping metrics and contributions from the spanwise direction. In this equation, the derivative operators in computational space are given by the fourth-order interior scheme with fourth-order boundary closure for the first-derivatives and third-order boundary closure for second derivatives (see section 3.4). It is useful to rewrite this equation using operator notation as

$$\hat{\mathbf{U}}_{,t} + \mathbf{L}(\hat{\mathbf{U}}) = 0. \qquad (3.27)$$

The time derivative is discretized with the second-order, two-step implicit scheme, giving

$$-\hat{\mathbf{U}}^{n+1} + \frac{4}{3}\hat{\mathbf{U}}^n - \frac{1}{3}\hat{\mathbf{U}}^{n-1} + \frac{2\Delta t}{3}\hat{\mathbf{U}}_{,t}^{n+1} \equiv \mathbf{G}(\hat{\mathbf{U}}^{n+1}; \hat{\mathbf{U}}^n, \hat{\mathbf{U}}^{n-1}) = 0. \qquad (3.28)$$

Although (3.28) is a linear equation, we formally apply Newton's method to solve it, leading to the iteration

$$\hat{\mathbf{U}}_1^{n+1} = \hat{\mathbf{U}}^n \qquad (3.29)$$

$$\delta\hat{\mathbf{U}}_i = \hat{\mathbf{U}}_{i+1}^{n+1} - \hat{\mathbf{U}}_i^{n+1} \qquad (3.30)$$

$$\left[\mathbf{I} + \frac{2\Delta t}{3}\frac{\partial \mathbf{L}}{\partial \hat{\mathbf{U}}}\right]_i \delta\hat{\mathbf{U}}_i = \mathbf{G}(\hat{\mathbf{U}}_i^{n+1}; \hat{\mathbf{U}}^n, \hat{\mathbf{U}}^{n-1}). \qquad (3.31)$$

If (3.31) is solved exactly then only one iteration is required. However, for computational efficiency the disturbance equations are approximately factored to obtain

$$\left[\mathbf{I} + \frac{2\Delta t}{3}\left(\check{\mathbf{A}}\Delta_\xi + \check{\mathbf{D}} - \check{\mathbf{V}}_{\xi\xi}\Delta_{\xi\xi}\right)\right]_i \mathbf{Z}_i = \mathbf{G}(\hat{\mathbf{U}}_i^{n+1}; \hat{\mathbf{U}}^n, \hat{\mathbf{U}}^{n-1}) \qquad (3.32)$$

$$\left[\mathbf{I} + \frac{2\Delta t}{3}\left(\check{\mathbf{B}}\Delta_\eta - \check{\mathbf{V}}_{\eta\eta}\Delta_{\eta\eta}\right)\right]_i \delta\hat{\mathbf{U}}_i = \mathbf{Z}_i. \qquad (3.33)$$

The approximate factorization introduces an $\mathcal{O}(\Delta t^2)$ error in the tangent which is consistent with the second-order-accurate time advancement scheme. By taking additional iterations, the factorization error can be eliminated thus recovering the solution to equation (3.28).

In contrast to the base-flow solver, the fourth-order spatial differences for the interior nodes are retained in the tangent. This ensures second-order temporal accuracy in one iteration per time-step while also accelerating convergence when multiple iterations are used. With the exception of the boundaries, the approximate factorization of this system of equations results in a series of block, penta-diagonal linear systems. Near the boundaries the penta-diagonal structure is spoiled due to the high-order boundary closure (see figure 3.3) and a special solver has been developed to efficiently obtain solutions to this system on vector supercomputers. Since the matrices depend only on the mean-flow, a single LU factorization is performed for the first time-step and subsequent time-steps only require forward and backward substitutions. This renders the disturbance code roughly six times faster then the nonlinear base-flow solver.

3.7.2 Frequency-Domain Approach

The frequency-domain approach is used when only the time-asymptotic behavior of the solution is required. This includes cases when the disturbance solution is steady or when the solution is periodic with a single frequency, ω. In this case, the solution is assumed to be of the form

$$\mathbf{U}' = \hat{\mathbf{U}}(x, y)\, e^{i(k_z z - \omega t)}. \tag{3.34}$$

Substituting this expression into equation (2.28) yields

$$-i\omega\hat{\mathbf{U}} + \mathbf{A}\hat{\mathbf{U}}_{,1} + \mathbf{B}\hat{\mathbf{U}}_{,2} + ik_z\mathbf{C}\hat{\mathbf{U}} + \mathbf{D}\hat{\mathbf{U}} =$$
$$\mathbf{V}_{11}\hat{\mathbf{U}}_{,11} + \mathbf{V}_{12}\hat{\mathbf{U}}_{,12} + ik_z\mathbf{V}_{13}\hat{\mathbf{U}}_{,1} + \mathbf{V}_{22}\hat{\mathbf{U}}_{,22} + ik_z\mathbf{V}_{23}\hat{\mathbf{U}}_{,2} - k_z^2\mathbf{V}_{33}\hat{\mathbf{U}}. \tag{3.35}$$

When converted to computational space, this equation takes the form

$$\left[\check{\mathbf{A}}\Delta_\xi + \check{\mathbf{B}}\Delta_\eta + \check{\mathbf{D}} - \check{\mathbf{V}}_{\xi\xi}\Delta_{\xi\xi} - \check{\mathbf{V}}_{\xi\eta}\Delta_{\xi\eta} - \check{\mathbf{V}}_{\eta\eta}\Delta_{\eta\eta}\right]\hat{\mathbf{U}} = 0 \tag{3.36}$$

where the check on the matrices indicates that they include the mapping metrics and contributions from the spanwise direction and time-derivative. As in the unsteady approach, the derivative operators in computational space are given by the fourth-order interior scheme with fourth-order boundary closure for the first-derivatives and

third-order boundary closure for second derivatives. Rewriting this equation using operator notation and introducing a pseudo-time, τ-derivative leads to

$$\frac{\partial \hat{\mathbf{U}}}{\partial \tau} + \mathbf{L}_\omega(\hat{\mathbf{U}}) = 0. \tag{3.37}$$

The solution to this equation is obtained using the same technique described for the unsteady approach (see section 3.7.1) but with the second-order time advancement replaced with implicit Euler.

To speed convergence to the steady-state solution, local-time-stepping is used as discussed in section 3.5. In this case, we approximate the local CFL by the following expression

$$\begin{aligned}
\mathsf{CFL} \;=\; & \frac{\Delta\tau}{\Delta\xi\Delta\eta}\bigg\{|\mathbf{J}_{1i}\bar{u}_i|\Delta\eta + |\mathbf{J}_{2i}\bar{u}_i|\Delta\xi + \frac{\bar{w}}{\lambda_z}\Delta\xi\Delta\eta \\
& \bar{c}\left[(\mathbf{J}_{11}^2 + \mathbf{J}_{12}^2)\Delta\eta^2 + (\mathbf{J}_{21}^2 + \mathbf{J}_{22}^2)\Delta\xi^2 + \frac{\Delta\xi^2\Delta\eta^2}{\lambda_z^2}\right]^{1/2}\bigg\},
\end{aligned} \tag{3.38}$$

where the velocities and sound-speed are based on mean-flow quantities and $\lambda_z = 2\pi/k_z$ is the wavelength of disturbances in the z-direction. Letting $\lambda_z \to \infty$ yields the form appropriate for two-dimensional linear disturbances. By specifying a value of CFL, equation (3.38) is solved for the local value of $\Delta\tau(x,y)$. Although this estimate of CFL does not include viscous effects, we have found it to be adequate for accelerating convergence to steady-state.

3.8   Potential Flow Solutions

The initial conditions for the base-flow calculations can significantly influence the convergence to the steady state. For the base-flow computations presented here, a potential flow solution is used for the initial condition. Since we are considering only infinite-span wings, the spanwise component of velocity, w, is constant. Therefore the steady, three-dimensional potential equation in nonconservative form reduces to the two-dimensional equation

$$(1 - \mathsf{M}_x^2)\phi_{,xx} + (1 - \mathsf{M}_y^2)\phi_{,yy} - 2\mathsf{M}_x\mathsf{M}_y\phi_{,xy} = 0 \tag{3.39}$$

where ϕ is the velocity potential function defined as

$$u = \phi_{,x} \qquad v = \phi_{,y},$$ (3.40)

with $\mathsf{M}_x = u/c$, and $\mathsf{M}_y = v/c$. In these expressions, $c = \sqrt{T}/\mathsf{M}$ with T computed from the isentropic relation

$$T = 1 + \frac{(\gamma - 1)\mathsf{M}^2}{2}\left(1 - u^2 - v^2\right)$$ (3.41)

and with the reference Mach number given by $\mathsf{M} = u_\infty/c_\infty$ which corresponds to the chordwise Mach number. The freestream Mach number is related to the chordwise Mach number by $\mathsf{M}_\infty = \mathsf{M}\sqrt{1 + \tan^2(\theta)}$ where θ is the sweep angle. In these expressions, the reference velocity is $u_r^* = u_\infty^*$ such that the nondimensional spanwise component of velocity in the freestream is given by $w_\infty = \tan(\theta)$. The advantage of this approach is that an unswept potential solution at $\mathsf{M}_\infty = \mathsf{M}$ is identical to a swept solution at $\mathsf{M}_\infty = \mathsf{M}\sqrt{1 + \tan^2(\theta)}$ except with $w = \tan(\theta)$.

The method used to solve equation (3.39) is similar to that used for the Navier–Stokes equations above. Fourth-order accurate finite differences (see section 3.4) are used to approximate the spatial derivatives and the solution is marched to the steady-state using implicit Euler time-advancement. At each time-step the system of equations is approximately factored resulting in a series of (nearly) block, penta-diagonal systems.

On the wall and symmetry boundaries the normal derivative of the velocity potential function is enforced to be zero,

$$\frac{\partial \phi}{\partial n} = 0$$ (3.42)

corresponding to the no-penetration condition, $v_n = 0$, where n is the coordinate normal to the boundary under consideration. On the inflow and outflow boundaries, the potential function is set to the value corresponding to the freestream solution. Specific details on boundary conditions, mesh generation, and solution accuracy are given in section 5.2 for the parabolic-cylinder geometry. In addition to using the potential solution as an initial condition, we also use it to specify inflow and outflow boundary conditions for the base-flow NS calculation. Details are provided in section 3.9.2.

3.9   Boundary Treatments

In this section, the various boundary treatments used to obtain mean and disturbance solutions are discussed. Before doing so, however, the general framework used to implement boundary constraints in the implicit solver is presented. For this purpose, we adopt an approach which is based on a direct application of Newton's method to linearize the boundary constraints in terms of the primitive variables which results in linearized expressions for the boundary conditions that are compatible with Newton's method used to solve the Navier–Stokes equations [see equation (3.18) and (3.31)]. The advantage of this technique is that it provides a consistent framework for deriving the appropriate implicit boundary constraints given any desired boundary condition. Of course, the resulting constraints will be identical to those obtained using the so-called "delta-form" [53], however we feel that the present approach is easier to apply and more intuitive, especially for complicated boundary conditions.

3.9.1   Implicit Boundary Constraints

To preserve convergence of the implicit solver, linearized expressions for all boundary constraints are required in terms of $\delta \mathbf{U}$. Consider an arbitrary constraint,

$$g_k(\mathbf{U}^{(n+1)}) = 0 \,, \tag{3.43}$$

which is some function (possibly nonlinear) of the primitive variables at time-step, $n+1$. In this expression, k denotes the particular primitive variable under constraint and can take the values: ρ, u, v, w, T. Applying Newton's method to the constraint equation yields

$$\left(\frac{\partial g_k}{\partial \mathbf{U}}\right)_i \delta \mathbf{U}_i = -g_k(\mathbf{U}_i^{(n+1)}) \tag{3.44}$$

where $\delta \mathbf{U}_i = \mathbf{U}_{i+1}^{(n+1)} - \mathbf{U}_i^{(n+1)}$. When applying a boundary constraint, equation (3.44) is used in place of the discrete, linearized equations-of-motion for the constrained quantity. In presenting the boundary conditions, we define the constraints, g_k, and the variation of the constraints,

$$\delta g_k \equiv \left(\frac{\partial g_k}{\partial \mathbf{U}}\right)_i \delta \mathbf{U}_i \tag{3.45}$$

in terms of the primitive variables.

For example, consider the application of the no-slip condition on the first velocity component, $u = u_w$, where, for generality, the wall has velocity u_w. For this case

$$g_u(\mathbf{U}) = u - u_w = 0 \tag{3.46}$$

and

$$\delta g_u = \delta u . \tag{3.47}$$

Thus, equation (3.44) simply becomes

$$\delta g_u = -g_u , \tag{3.48}$$

which in terms of the primitive variables is just

$$\delta u = -(u - u_w) . \tag{3.49}$$

3.9.2 Base Flow Boundary Treatments

The base-flow solutions are obtained using no-slip boundary conditions on the wall with either isothermal or adiabatic temperature boundary conditions, symmetry conditions upstream of the leading edge, Riemann extrapolation on the inflow boundary, and a parabolic approximation on the outflow boundary. In the following, the detailed implementation of each of these boundary treatments is presented.

Wall boundary conditions

On the wall, $(n = \eta = 0)$, the no-slip boundary conditions are implemented by replacing the momentum equations with constraints on the velocities: $\bar{u}_i = 0$. Likewise, the energy equation is replaced by either the isothermal condition, $\bar{T} = \bar{T}_w$, or the adiabatic condition $\partial \bar{T}/\partial n = 0$. For the body orthogonal meshes used here, the adiabatic condition can be written in computational space as $\partial \bar{T}/\partial \eta (\eta = 0) = 0$ and the derivative is approximated by a fourth-order accurate one-sided difference (see section 3.4). In all cases the density at the wall is determined using the continuity equation.

For the implicit solver, the boundary constraints at the wall, $(\eta = 0)$, can be

written as:

$$g_{u_i} = \bar{u}_i = 0 \,, \tag{3.50}$$

$$g_T = \bar{T} - \bar{T}_w = 0 \,, \quad \text{or} \quad g_T = \Delta_\eta \bar{T} = 0 \tag{3.51}$$

and the variation of the constraints with the primitive variables are

$$\delta g_{u_i} = \delta \bar{u}_i \,, \tag{3.52}$$

$$\delta g_T = \delta \bar{T} \,, \quad \text{or} \quad \delta g_T = \Delta_\eta(\delta \bar{T}) \,. \tag{3.53}$$

Symmetry boundary

Near the symmetry boundary, $(\xi = 0)$, the finite difference stencil used in the interior is adjusted to account for the symmetry (or antisymmetry for the boundary normal velocity) of the variables at the boundary. Since a five-point stencil is used, modification is required for the three rows of nodes adjacent to the boundary when computing both the RHS and LHS.

Inflow boundary

On the inflow boundary, $(\eta = 1)$, the boundary conditions are based on the locally one-dimensional Riemann invariants. On a subsonic inflow, four quantities must be specified. Here we constrain the entropy, spanwise and tangential velocities, and the incoming Riemann invariant and each of these quantities are determined from the potential flow solution (see section 3.8).

The locally one-dimensional Riemann invariants are defined as

$$R_1 = v_n - \frac{2c}{\gamma - 1}, \quad R_2 = v_n + \frac{2c}{\gamma - 1} \tag{3.54}$$

where c is the local sound-speed and v_n is the velocity normal to the boundary. Then, on the inflow boundary

$$\frac{p}{\rho^\gamma} = \left(\frac{p}{\rho^\gamma}\right)_\infty \equiv \frac{1}{\gamma \mathsf{M}_\infty^2} \,, \quad w = w_p \,, \quad V_t = V_{t_p} \,, \quad R_1 = R_{1_p} \,, \quad R_2 = R_{2_{int}} \tag{3.55}$$

where V_t is the velocity tangent to the boundary, the subscript "p" refers to the potential flow solution, and the subscript "int" refers to a quantity extrapolated

from the interior.

The conditions (3.55) are used to form the following constraints on the primitive variables at the boundary:

$$g_\rho = \rho - \left(\frac{(\gamma-1)\mathsf{M}_\infty}{4}\left[R_{2int} - R_{1p}\right]\right)^{\frac{2}{\gamma-1}} = 0\,, \tag{3.56}$$

$$g_u = u - n_1\left(\frac{R_{1p} + R_{2int}}{2}\right) + n_2 V_{tp} = 0\,, \tag{3.57}$$

$$g_v = v - n_2\left(\frac{R_{1p} + R_{2int}}{2}\right) - n_1 V_{tp} = 0\,, \tag{3.58}$$

$$g_w = w - w_p = 0\,, \tag{3.59}$$

$$g_T = T - \left(\frac{(\gamma-1)\mathsf{M}_\infty}{4}\left[R_{2int} - R_{1p}\right]\right)^2 = 0\,, \tag{3.60}$$

where $\{n_1, n_2\}^{\mathrm{T}}$ is the unit, boundary-normal vector.

In Beaudan & Moin [7], zeroth-order extrapolation is used to determine R_{2int} from the interior values. We have found that first-order (*i.e.* linear) extrapolation yields an improved boundary approximation and, since we use a block penta-diagonal matrix structure, this is easily incorporated in the LHS. With the modified block penta-diagonal LHS discussed in section 3.6 we can actually implement up to cubic extrapolation. However, numerical experiments show that quadratic and cubic extrapolation are both highly unstable. Even linear extrapolation has been found to be slightly unstable for large CFL and techniques to remove this instability are discussed below. Assuming the boundary to be at node N, the outgoing Riemann invariant is given by

$$R_{2int} = 2R_{2N-1} - R_{2N-2}\,. \tag{3.61}$$

In constructing the implicit LHS operator at the boundary, the variation of the outgoing Riemann variable with-respect-to the primitive variables is required:

$$\delta R_2 = n_1\delta u + n_2\delta v + \frac{\delta T}{(\gamma-1)\mathsf{M}_\infty\sqrt{T}}\,. \tag{3.62}$$

With this expression, the variation of the boundary constraints becomes

$$\delta g_\rho = \delta\rho - \left(\frac{(\gamma-1)\mathsf{M}_\infty}{4}\right)^{\frac{2}{\gamma-1}} \left(\frac{2}{\gamma-1}\right) \left(R_{2int} - R_{1p}\right)^{\frac{3-\gamma}{\gamma-1}} \left(2\delta R_{2N-1} - \delta R_{2N-2}\right),$$

(3.63)

$$\delta g_u = \delta u - \frac{n_1}{2}\left(2\delta R_{2N-1} - \delta R_{2N-2}\right),$$

(3.64)

$$\delta g_v = \delta v - \frac{n_2}{2}\left(2\delta R_{2N-1} - \delta R_{2N-2}\right),$$

(3.65)

$$\delta g_w = \delta w,$$

(3.66)

$$\delta g_T = \delta T - 2\left(\frac{(\gamma-1)\mathsf{M}_\infty}{4}\right)^2 \left(R_{2int} - R_{1p}\right)\left(2\delta R_{2N-1} - \delta R_{2N-2}\right).$$

(3.67)

Boundary damping

As indicated in the previous section, the use of the Riemann extrapolation inflow condition results is a slight instability and the generation of numerical noise at the inflow boundary. This noise can eventually corrupt the entire solution, even near the wall. To control the instability and prevent numerical noise from affecting the rest of the field, a boundary damping term is added to the RHS of equation (3.12). This term takes the form of a fourth-derivative dissipation term in computational space and can be written as

$$\mathbf{D}_b = -\varepsilon_d\sigma_d(\eta)\left(\Delta_\xi^4\frac{\partial^4\mathbf{U}}{\partial\xi^4} + \Delta_\eta^4\frac{\partial^4\mathbf{U}}{\partial\eta^4}\right)$$

(3.68)

where ε_d controls the level of dissipation and $\sigma_d(\eta)$ takes the form [46]

$$\sigma_d(\eta) = 1 - 10^{-\left[a_d\left(\frac{\eta-\eta_s}{1-\eta_s}\right)\right]^{n_d}}$$

(3.69)

with $a_d = 2.57$, $n_d = 4$, and $\eta_s = 0.8$. Using these parameters, σ_d varies smoothly from one at the inflow boundary to zero at η_s such that the dissipation term acts over 20% of the domain in η. It is important to note that the σ_d term is constructed so that the dissipation term only affects the flow near the inflow, Riemann boundary. This guarantees that the dissipation term is zero inside the actual viscous boundary layer. A typically value of ε_d is 0.0125 and this is the value used for the mean-flow calculations described in Chapter 5.

Considering the η direction (analogous expressions hold for ξ), the fourth-derivative operator is approximated in the interior of the domain by the fourth-order accurate equation

$$(\Delta\eta)^4 \left(\frac{\partial^4 f}{\partial\eta^4}\right)_i \approx \frac{1}{6}\left[-(f_{i+3} + f_{i-3}) + 12(f_{i+2} + f_{i-2}) - 39(f_{i+1} + f_{i-1}) + 56f_i\right]. \quad (3.70)$$

This expression has a seven-point stencil which requires boundary closures for the boundary node and the two nodes adjacent to the boundary.

On the second node in from the boundary, the second-order accurate fourth-derivative is used:

$$(\Delta\eta)^4 \left(\frac{\partial^4 f}{\partial\eta^4}\right)_3 \approx \left[(f_5 + f_1) - 4(f_4 + f_2) + 6f_3\right]. \quad (3.71)$$

On the first node in from the boundary, the fourth-derivative dissipation term (3.68) is replaced, locally, with a second-derivative dissipation term of the form

$$\mathbf{D}_b = -\varepsilon_d\sigma_d(\eta)\left(\Delta_\xi^2\frac{\partial^2\mathbf{U}}{\partial\xi^2} + \Delta_\eta^2\frac{\partial^2\mathbf{U}}{\partial\eta^2}\right), \quad (3.72)$$

where ε_d and $\sigma_d(\eta)$ are the same as that used in equation (3.68). The second derivative operators are then approximated by second-order accurate differences, where, for example

$$(\Delta\eta)^2 \left(\frac{\partial^2 f}{\partial\eta^2}\right)_2 \approx \left[(f_3 - f_1) + 2f_2\right]. \quad (3.73)$$

Finally, on the actual boundary node, no dissipation term is used.

The seven-point stencil, used for the dissipation term (3.68) in the interior, is not compatible with the block penta-diagonal structure of the implicit LHS. Because of this, we use the the second-order, fourth-derivative stencil (3.71) for the interior nodes in the LHS and with this approximation, we have experienced no noticeable reduction in convergence of the iterative solver.

As an example of the success of the boundary damping term in stabilizing the Riemann extrapolation inflow boundary condition, figures 3.4 and 3.5 show contours of the pressure coefficient [see equation (5.6)] in the far-field and near the wall boundary for an unswept parabolic-cylinder at $\mathsf{M} = 0.1$ and $\mathsf{Re} = 1000$ (see section 5.4 for details) without boundary damping. For such low Mach number flows, the pressure field

is a sensitive indicator of numerical oscillations. Because of the approximate nature of the Riemann extrapolation used on the inflow boundary, numerical oscillations are generated that corrupt the entire solution. These oscillations are particularly acute near the wall, where the mesh is highly stretched and oscillations inside the boundary layer are particularly deleterious since first and second derivatives of the mean boundary-layer profiles are required for linear stability analysis. Figures 3.6 and 3.7 show the pressure field for the same conditions with boundary damping turned on [$\varepsilon_d = 0.0125$ and σ_d given by (3.69)]. The pressure field is now smooth in both regions with no sign of numerical oscillations. Figure 3.8 shows a streamwise velocity profile from the same simulation along with the derivatives needed for stability analysis. With boundary damping, both first and second derivatives are smooth.

In summary, the boundary damping term kills numerical oscillations at their source and prevents them from corrupting the solution near the wall. Since the boundary damping term is nonzero only near the inflow boundary, no noticeable effects on boundary-layer properties have been observed.

Parabolized outflow boundary

In constructing the computational domain for leading-edge receptivity problems, the computational expense can be significantly reduced by truncating the downstream portion of the domain (*e.g.* the trailing edge of a wing). Doing so, however, introduces difficulties in specifying accurate and stable boundary conditions on the downstream, outflow boundary. This difficulty is particularly acute, since the outflow boundary intersects not only a potential flow region, but also the viscously dominated boundary layer. Use of inviscid, nonreflecting boundary conditions, such those based on Riemann invariants (similar to section 3.9.2) or characteristics [83,38,106], work well for the outer potential flow; but cause large errors in the viscous layer even when viscous corrections [83] are employed. In a similar context, Fenno [36] recently used zeroth- and first-order extrapolation on an outflow boundary. However, numerical tests using these boundary conditions with the current low-dissipation numerical scheme show them to be highly unstable with large numerical errors generated.

These difficulties motived the development of a new, outflow boundary-condition (for steady-state flows) in which the Parabolized Navier–Stokes (PNS) equations are used to predict the flow on the outflow boundary. The PNS equations are derived from

the NS equations by removing the streamwise viscous derivatives and suppressing the upstream propagating acoustic waves in subsonic regions. The PNS were first used by Vigeron *et al.* [110] who modified the pressure gradient in the streamwise direction to remove the upstream propagating acoustic wave. More recently, [14] show that flux vector splitting naturally leads to a family of parabolized Navier–Stokes equations. Regardless of the approach, the PNS equations have been shown to yield accurate solutions for high Reynolds number flow as long as the freestream Mach number is supersonic [110]. However, when applied to fully subsonic flow, poor solutions can be obtained since the external inviscid field (which drives the boundary layer) is often inaccurate.[2]

The basic weakness of the PNS is that the streamwise pressure gradient is incorrectly predicted when the equations are parabolized. Thus, directly applying the PNS on the outflow boundary can lead to large errors since the local streamwise pressure gradient is incorrect. However, if the streamwise pressure gradient on the boundary can be reasonably estimated *a priori*, then it can be treated as a known source term in the equations. This is the technique used here to implement a parabolized outflow boundary condition. The streamwise pressure gradient is estimated from the potential solution about the body and used as a source term in the PNS at the outflow boundary.[3] This method is very successful in providing an accurate boundary treatment for both the inviscid and viscous regions of the flow.

This is demonstrated in figure 3.9 which shows contours of the pressure coefficient [see equation (5.6)] near the outflow boundary for a typical meanflow over a parabolic cylinder (see section 5.4 for more details). There is no indication of numerical oscillations in the far-field. Note that this solution does use boundary damping (discussed in the previous section) on the inflow boundary, but this does not affect the lower half of the outflow boundary. Figure 3.10 shows the evolution of the displacement thickness squared plotted as a function of the arc-length along the parabola. Eventually a nearly linear distribution is established downstream and there is no indication of

---

[2]The inaccuracies are greatest for geometries with curved walls where the streamwise pressure gradient is significant. Accurate solutions can be obtained for flat-plate, zero pressure-gradient boundary-layers since Vigeron's method naturally removes the streamwise pressure-gradient in subsonic flow.

[3]A better estimate of the pressure gradient would require viscous/inviscid interaction to be accounted for. However, for high Reynolds number flows with thin boundary layers, relative to a characteristic body length scale, the displacement thickness is small.

upstream influence due to the outflow boundary. This result is to be compared with figure 4.15 which shows a similar plot (although for a different geometry and nondimensionalization) which shows significant upstream influence when a characteristic based boundary condition [83] with viscous corrections is used.

For most of the computations reported here, we have noticed no instability or convergence problems associated with the parabolic outflow boundary treatment. However, for the high Reynolds number cases reported in Chapter 5, a slight instability was present when the residual approached 1×10^{-7} in magnitude. However, the solution at this point was judged to be sufficiently converged so that further investigation of the instability was not performed.

3.9.3   Disturbance Boundary Treatments

Disturbance-flow solutions are obtained using no-slip boundary conditions on the wall with either isothermal or adiabatic temperature boundary conditions, symmetry conditions upstream of the leading edge, and sponge layer boundary treatments on the inflow and outflow boundaries. The symmetry conditions are implemented in the finite-difference stencil in the same manner used for the base-flow. The detailed implementation of each of the other boundary treatments is presented below.

Wall boundary conditions

For disturbance calculations we consider both undisturbed surface boundaries and surface boundaries with small perturbations to model surface roughness. The undisturbed surface boundary conditions follow directly from the wall boundary conditions used for the mean-flow in section 3.9.2.

When the wall boundary is perturbed to model roughness, the no-slip and temperature boundary conditions must be applied on the perturbed surface. Denoting the smooth wall by $n(s, z) = 0$ the rough wall is obtained by adding a small, spanwise-periodic perturbation given by

$$\tilde{n}(s, z) = \varepsilon_w h_w(s) e^{i\beta_w z} \tag{3.74}$$

where $\varepsilon_w = \varepsilon_w^* / L^* \ll 1$ is the nondimensional roughness height, $h_w(s)$ is the streamwise shape of the bump, and $\beta_w = \beta_w L^*$ is the spanwise wavenumber of the bump.

Similar to the expansions used in section 2.3, the flow variables can be written as

$$u_j(x_i) = \bar{u}_j(x_i) + \varepsilon_w \tilde{u}_j(x_i) + \mathcal{O}(\varepsilon_w{}^2), \tag{3.75}$$

$$T(x_i) = \bar{T}(x_i) + \varepsilon_w \tilde{T}(x_i) + \mathcal{O}(\varepsilon_w{}^2), \tag{3.76}$$

where perturbations are denoted with a tilde. For all the cases considered here, we assume that ε_w is sufficiently small such that the $\mathcal{O}(\varepsilon_w{}^2)$ and higher terms can be neglected and that the surface boundary conditions can be transfered by Taylor series expansion to inhomogeneous boundary conditions on the undisturbed surface. The detailed derivation of these inhomogeneous boundary conditions is given in appendix F. Summarizing those results for an isothermal boundary, the appropriate linearized wall boundary conditions for both the mean and disturbances quantities are given by

$$\bar{u}_j(s,0,z) = 0, \tag{3.77}$$

$$\bar{T}(s,0,z) = T_w, \tag{3.78}$$

$$u'_j(s,0,z) = -h_w(s)e^{i\beta_w z}\frac{\partial \bar{u}_j}{\partial n}(s,0,z), \tag{3.79}$$

$$T'(s,0,z) = -h_w(s)e^{i\beta_w z}\frac{\partial \bar{T}}{\partial n}(s,0,z). \tag{3.80}$$

Not surprisingly, the mean boundary conditions are unchanged from the unperturbed case, while the disturbance boundary conditions are now inhomogeneous and depend on the wall-normal gradients of the mean flow. The linearized temperature boundary condition for an adiabatic wall is considerably more complicated then the isothermal condition and is given by equation (F.36) in Appendix F. The constraint equations for the implicit LHS are formed similar to section 3.9.2.

Sponge Boundary Treatment

When performing receptivity calculations one often encounters situations where waves of some type (inviscid and/or viscous) must pass through a computational boundary without producing significant reflections. Much work has been performed to develop nonreflecting boundary conditions for hyperbolic systems of equations such as the Euler equations, and the interested reader is referred to the review article by Givoli [39]

and the references therein for further information. However, these boundary conditions are typically only valid in regions where the mean flow is uniform. Furthermore, when used with the Navier–Stokes equations, these nonreflecting conditions are only useful away from viscous regions (like boundary layers and free-shear layers). For receptivity calculations the viscous layers typically contain instability waves which also must exit the computational domain.

For boundary layer instability waves, various outflow conditions have been used in the past with varying degree of effectiveness. Many of these conditions have been developed for incompressible flow. Recently Guo and Adams [46] have reported results for compressible flow in which they attempted a variety of outflow boundary conditions and determined the impact of these conditions on the growth of TS waves in a boundary layer. They find that the sponge-layer boundary treatment gives adequate results compared to buffer regions and characteristic-based conditions. Given this, and the fact that the sponge layer has proven to be rather robust, we have adopted the sponge layer as our primary outflow boundary treatment. We have also implemented the sponge layer on inflow boundaries and details are provided below.

Following Orszag & Israeli [55], the sponge layer is implemented by adding the following term to the RHS of the NS equations

$$\mathbf{F}_s = \sigma_s(x, y) \left[\mathbf{U}(x, y, z, t) - \mathbf{U}_{ref}(x, y, z, t) \right] \tag{3.81}$$

where $\mathbf{U}_{ref}$ is an arbitrary reference state which can be a function of the spatial coordinates and of time.

The sponge function is designed to vary smoothly from zero in the interior to a finite value, A_s, on the boundary. For this purpose, we use the following function which was suggested by Mahesh [69] as a simplification to the functions used by Adams [2]:

$$\sigma_s(x) = \begin{cases} A_s \left(\frac{x-x_s}{x_t-x_s} \right)^{N_s} & x \in (x_s, x_t] \\ 0 & \text{otherwise} \end{cases} . \tag{3.82}$$

In this expression, x_s denotes the start of the sponge, x_t the end of the sponge, and N_s is the exponent (generally taken to be 3) which determines the rate at which the function transitions from 0 to A_s. The effectiveness of this sponge is documented in section 4.1.2 for Tollmien–Schlichting waves, section 4.2.2 for cross-flow vortices, and section 4.3 for acoustic waves.

We note in passing that recent work by Colonius *et al.* [23] makes use of a "sponge-layer" outflow boundary treatment to damp reflections due to the passage of large vortical disturbances. Instead of adding a damping term to the equations, this technique uses an exit zone comprised of a stretched mesh combined with explicit filtering to damp disturbances before they reach the outflow boundary. Although shown to produce acceptable results, this method has the disadvantage of coupling the mesh point distribution to the boundary treatment. With the current method, the mesh can be constructed independent of the form of the sponge term, with the caveat that the spatial gradients which occur in the sponge region must be adequately resolved.
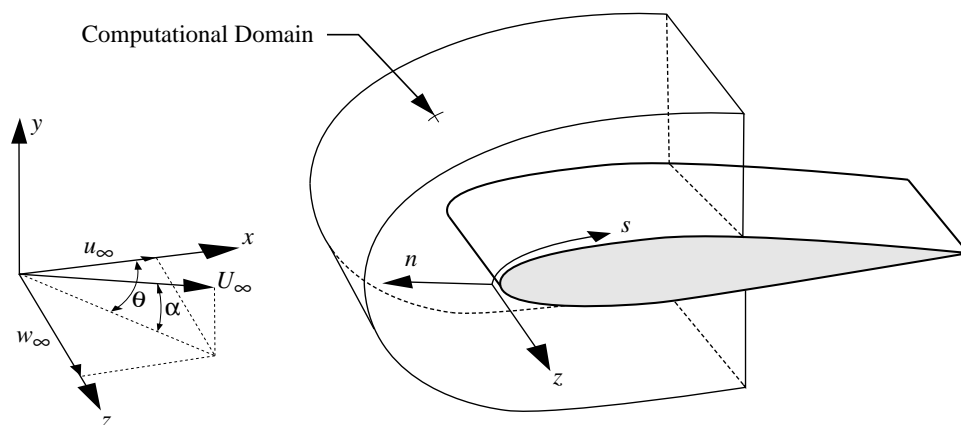
Figure 3.1: Generic geometry for leading-edge receptivity calculations.
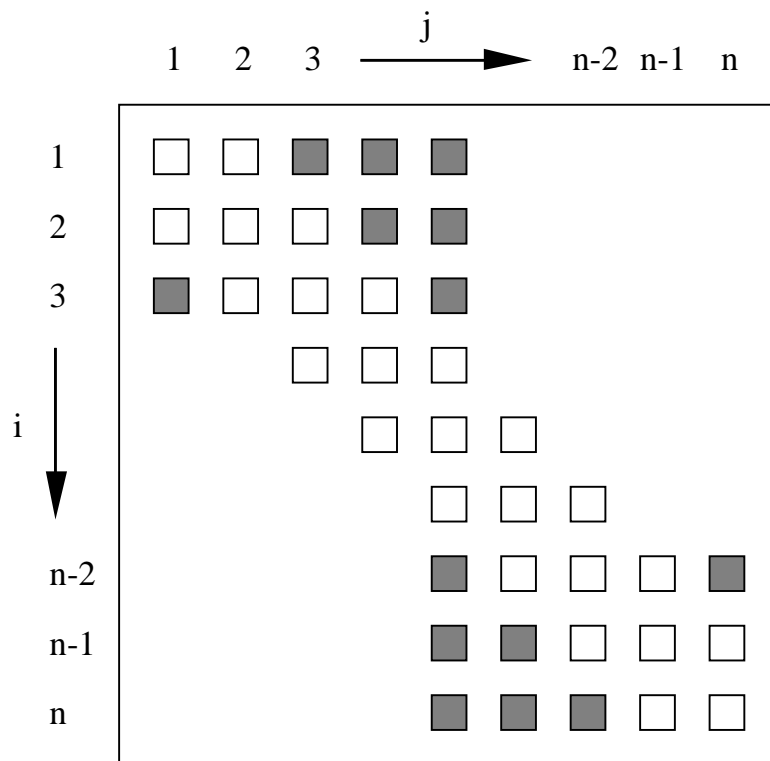
Figure 3.2: Modified, block tri-diagonal structure for mean-flow LHS matrix. Each block is a 5×5 dense matrix and the shaded blocks denote the boundary nodes which spoil the interior block, tri-diagonal structure.
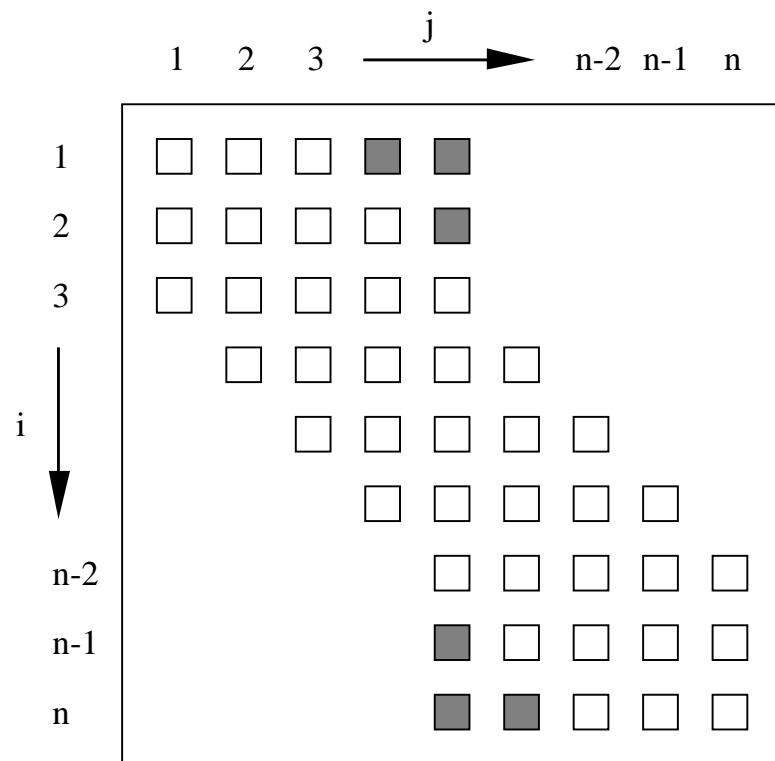
Figure 3.3: Modified block, penta-diagonal structure for disturbance-flow LHS matrix. Each block is a 5×5 dense matrix and the shaded blocks denote the boundary nodes which spoil the interior block, penta-diagonal structure.
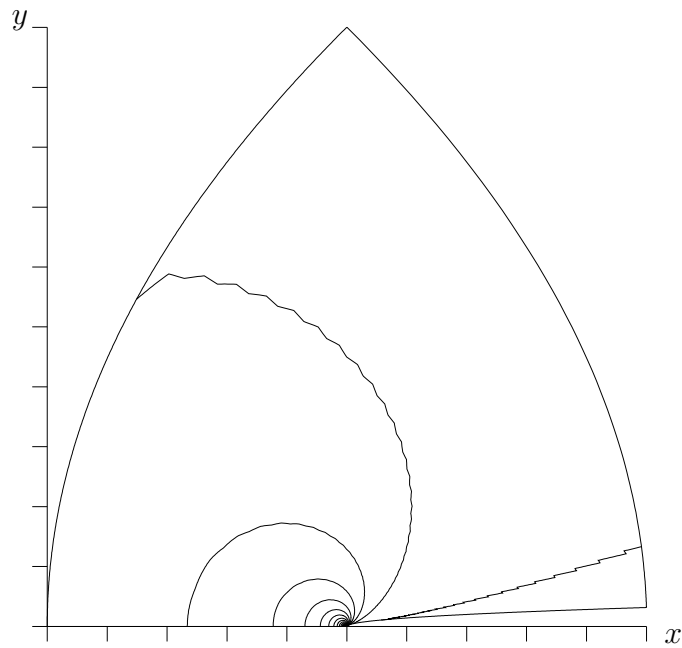
Figure 3.4: Contours of C_p for the unswept parabolic cylinder with no boundary damping at $\mathsf{M} = 0.1$, $\mathsf{Re} = 1000$, $\mathsf{Pr} = 0.7$. The contours range from 0 to 1.04 with increments of 0.04; tics every 100 nose radii.
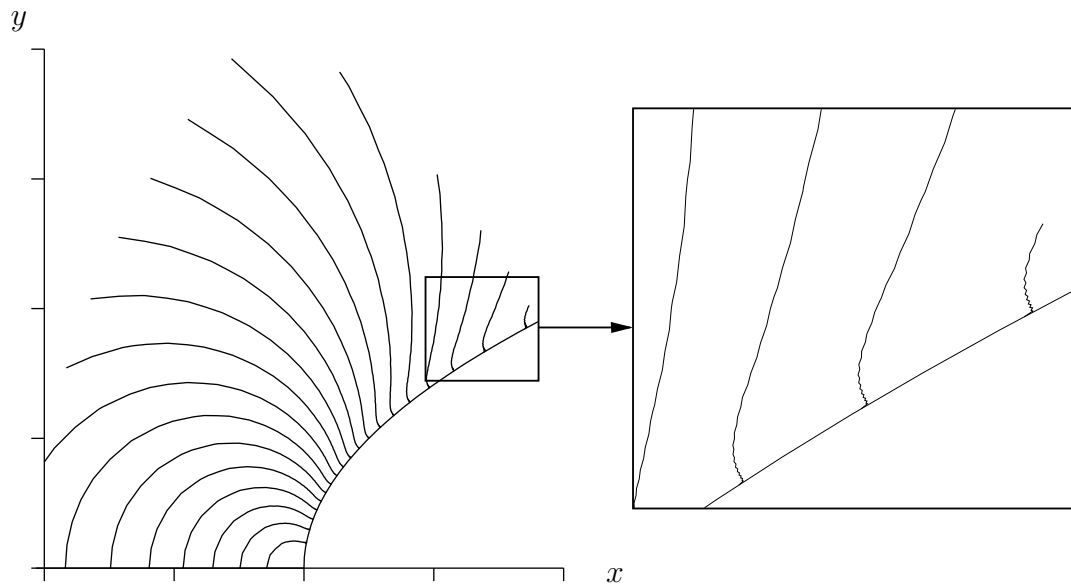
Figure 3.5: Contours of C_p near the leading-edge for the unswept parabolic cylinder without boundary damping at $\mathsf{M} = 0.1$, $\mathsf{Re} = 1000$, $\mathsf{Pr} = 0.7$. The contours range from 0 to 1.04 with increments of 0.04; tics every nose radii.
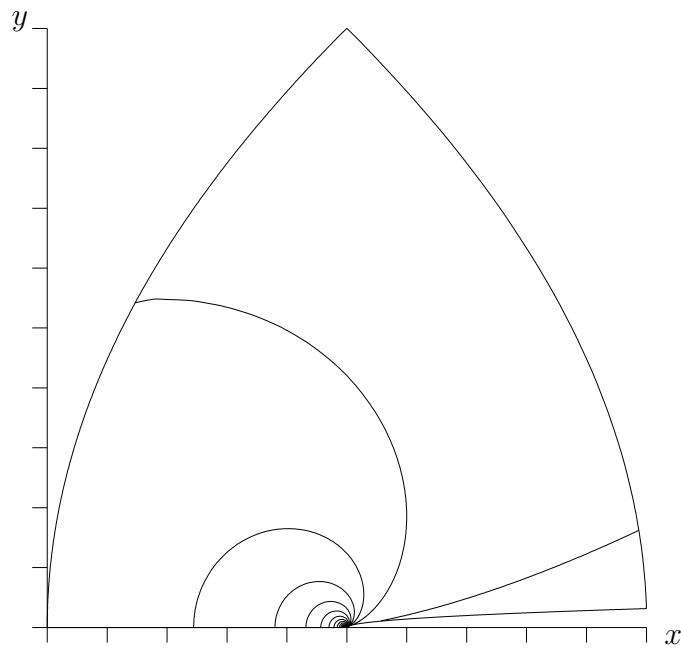
Figure 3.6: Contours of C_p for the unswept parabolic cylinder at $\mathsf{M} = 0.1$, $\mathsf{Re} = 1000$, $\mathsf{Pr} = 0.7$. The contours range from 0 to 1.04 with increments of 0.04; tics every 100 nose radii.
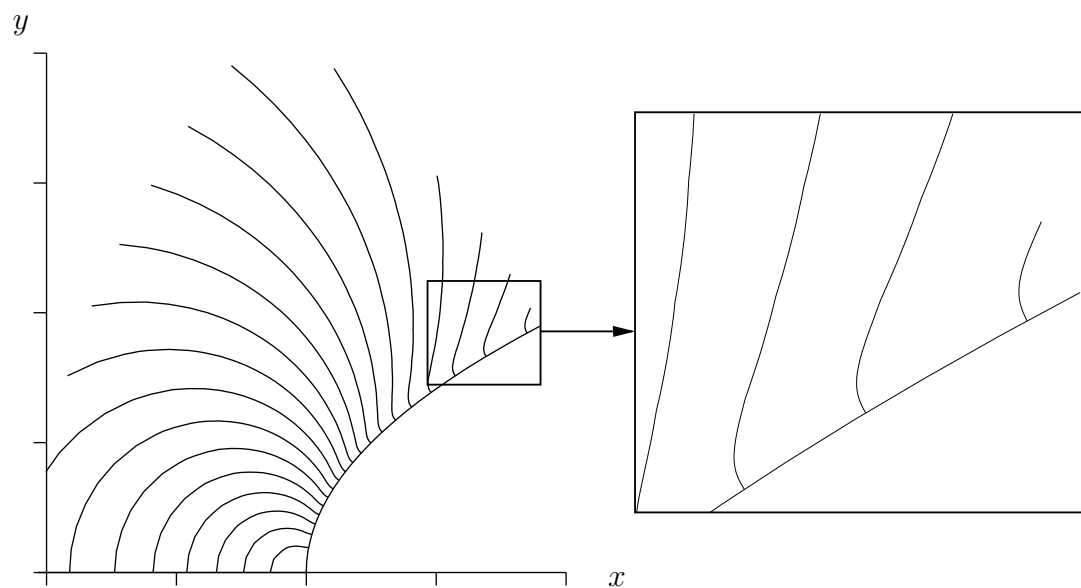
Figure 3.7: Contours of C_p near the leading-edge for the unswept parabolic cylinder at $\mathsf{M} = 0.1$, $\mathsf{Re} = 1000$, $\mathsf{Pr} = 0.7$. The contours range from 0 to 1.04 with increments of 0.04; tics every nose radii.
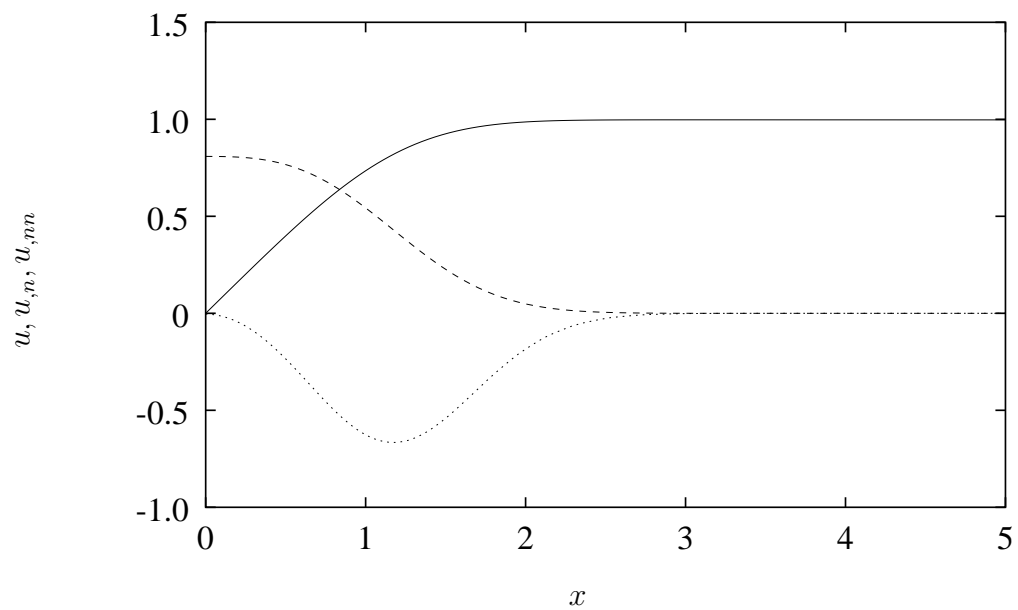
Figure 3.8: Derivatives of the streamwise velocity at $x = 172$ for the unswept parabolic cylinder with boundary damping at $\mathsf{M} = 0.1$, $\mathsf{Re} = 1000$, $\mathsf{Pr} = 0.7$: —— u, - - - - $u_{,n}$, ⋯⋯⋯ $u_{,nn}$.
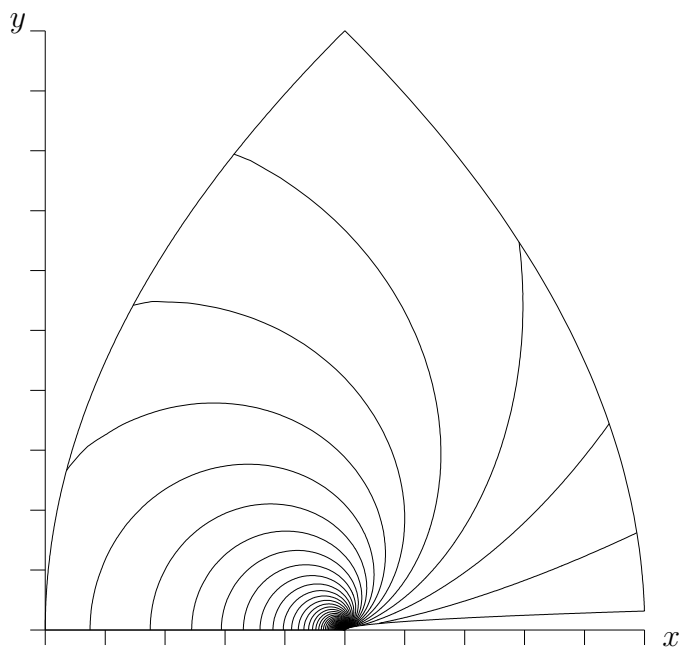
Figure 3.9: Contours of C_p for $\mathsf{M} = 0.1$, $\mathsf{Re} = 1000$ flow over a parabolic cylinder. Contours are from 0 to 1.2 in increments of 0.01; tics every 100 nose radii.
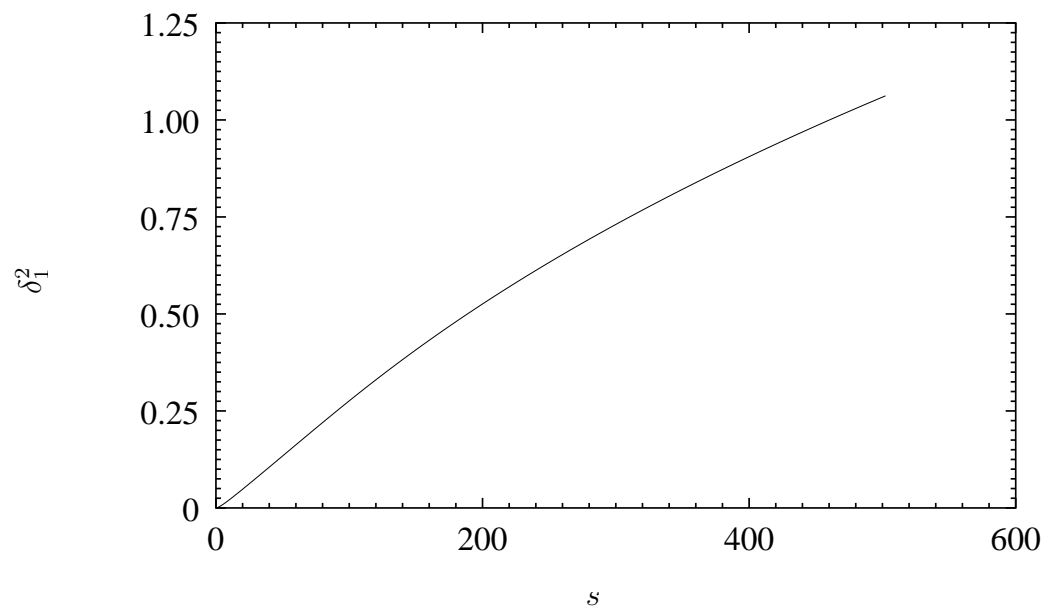
Figure 3.10: Evolution of the displacement thickness squared for a $\mathsf{M} = 0.1$ and $\mathsf{Re} = 1000$ boundary layer on a parabolic cylinder.

Chapter 4

Model Problems and
Code Validation

Although the numerical method is presented in Chapter 3 in the context of the swept, leading-edge receptivity problem, it is general enough to solve a variety of other problems. This chapter begins by presenting results for three model problems that contain many of the fundamental physical phenomena occurring in leading-edge receptivity problems: unstable Tollmien–Schlichting waves, growing crossflow vortices, and acoustic scattering. By isolating the physical phenomena, the viability of the method is evaluated and the resolution required to accurately represent each phenomenon is ascertained. As a final validation of the method, the last section of this chapter presents acoustic leading-edge receptivity results along with comparisons to a previous computation [63]. Readers, anxious for swept leading-edge receptivity results, may wish to bypass this chapter and go directly to Chapter 5 which discusses receptivity due to surface roughness on a swept parabolic-cylinder.

4.1 Viscous Instability Waves in a Parallel Boundary Layer

A major feature of the transitional flow near a leading-edge is the development of Tollmien–Schlichting (TS) waves in the boundary layer. Since TS waves have large gradients in the wall normal direction, it is computationally challenging to resolve them accurately while representing the mean flow variation on the scale of the airfoil. To determine the ability of our scheme to accurately compute the development of TS waves, we have performed a series of calculations using a parallel boundary layer as the base flow. In this way, the solutions can be compared directly to parallel, Linear Stability Theory (LST).

The base flow is computed from the compressible Falkner–Skan–Cooke equations

(see Appendix C) for an unswept ($\theta = 0$), zero-pressure-gradient ($\beta_h = 0$) boundary layer. The flow conditions are $\mathsf{M} = 0.3$, $\mathsf{Re} = 1000$, and $\mathsf{Pr} = 1.0$ with the reference length scale $L^* = \delta_1^*$ (δ_1^* is the displacement thickness) and all other reference quantities are based on edge values. The wall is assumed to be isothermal with $T_w = T_0$, where T_0 is the freestream stagnation temperature.[1] A linear stability solver (see Appendix D) using Chebyshev collocation with 96 points in the wall normal direction is used to provide the reference growth-rates for both temporally and spatially growing waves. For both the Linearized Navier–Stokes (LNS) and LST calculations, constant fluid properties are assumed.

4.1.1   Temporally Growing TS Waves

First, consider the temporal problem where the waves grow in time. In this case, the disturbance field is periodic in the streamwise direction. A computational domain containing only one wavelength of the TS wave is used with periodic boundary conditions on the left and right boundaries. For this calculation, the top boundary is placed at $y = 80$ which is sufficiently far away from the wall that a zero disturbance boundary condition can be used. At the wall, the no-slip and isothermal boundary conditions are enforced as described in section 3.9.3. Since we are interested in the temporal evolution of the disturbances, the unsteady solver is used with two-step implicit time-advancement.

The mesh is uniform in the streamwise direction, x, with an algebraic mapping function in the wall normal direction, y. The mapping function to computational space, $\eta \in [0, 1]$, is given by equation (D.20) with $y_{max} = 80$ and $y_s = 1$.

The LST eigenfunction for $k_x = 0.308620690$ is used as the initial condition with a theoretical frequency of

$$\omega_{LST} = 0.114678806 + 0.002384453i \tag{4.1}$$

and the growth-rate is given by the imaginary part, $\sigma_{LST} = 0.002384453$. In passing, we note that the eigenvalues from the LST calculation are believed to be accurate to the number of digits indicated. This has been verified by calculations with 128 Chebyshev points which show no change to 9 decimal places.

---

[1]Under these conditions, T_0 is also the adiabatic wall temperature.

Growth-rate results from the Navier–Stokes calculations are based on the integrated, disturbance kinetic-energy

$$E'_k \equiv \int_0^\infty \frac{1}{2} \left(|\hat{u}'|^2 + |\hat{v}'|^2 + |\hat{w}'|^2 \right) dy \,. \tag{4.2}$$

which is computed from the streamwise Fourier transform of the disturbance velocities for wavenumber k_x. Given E'_k the growth rate is given by

$$\sigma = \frac{1}{2} \frac{1}{E'_k} \frac{dE'_k}{dt} \tag{4.3}$$

where the factor $1/2$ is required since E'_k is a quadratic quantity.

Figure 4.1 shows the evolution of the growth-rate in the computed solution as a function of time for two spatial resolutions where each run was performed at a Δt corresponding to $N_t = 1150$ time-steps per period with two iterations of the implicit solver. For early times, the growth-rate undergoes a transient as the solution adjusts from the LST initial condition to the eigenfunction associated with the discrete finite difference equations. During the transient, additional acoustic modes are also generated and these modes lead to the high frequency modulation of the growth-rate seen in figure 4.1. As grid resolution is increased the severity of the initial transient and the amplitude of the resulting acoustic modes are reduced since the finite difference eigenfunction converges to the LST eigenfunction used for the initial condition.

To verify the rate of convergence, the relative error in the average growth rate is plotted in figure 4.2 over a range of mesh resolutions for $N_t = 1150$ with 2 iterations of the implicit solver. Fourth-order convergence is achieved in both spatial dimensions although the relative error begins to saturate at 10^{-4} due to the temporal error. If the CFL had been held constant instead of fixing N_t, then the saturation due to temporal errors would not have occurred [58]. However, the conclusion would have remained the same — the method is fourth-order accurate in space.

To confirm temporal convergence, figure 4.3 shows the relative error in the average growth-rate as a function of N_t, for an (80×127) mesh. Results are included for 1, 2, and 3 iterations of the implicit disturbance solver. In each case, (at least) second-order temporal convergence is obtained although the overall accuracy improves with the number of iterations. In fact, the rate of convergence for 2 and 3 iterations is

actually greater than second-order over the range of N_t considered. This is due to the fact that as N_t is increased, the additional iterations are more successful in removing the factorization error thus driving the solution to the exact, discrete solution. Eventually, however, as N_t is further increased the second-order error of the base time-advancement scheme will dominate regardless of the number of iterations.

With the convergence results presented above, it is possible to determine a spatial/temporal resolution required to resolve TS wave development to any desired accuracy. For the leading-edge receptivity problem a reasonable level of accuracy requires less than 1% error in the amplitude of the TS wave over the length of the computational domain. This level of accuracy can be achieved for a period of 40 oscillations in time with a resolution of $N_x = 20$, $N_y = 127$, $N_t = 1150$ with 2 iterations of the implicit solver. For this resolution, the error in the average growth-rate is 0.22%. In terms of a spatially growing wave, with 20 nodes per streamwise wavelength, 127 nodes normal to the wall, and 1150 time-steps per period with 2 iterations, a 1% error in the amplitude will not occur until a domain length of 40 wavelengths which should be adequate for the leading-edge receptivity problems under consideration.

4.1.2   Spatially Growing TS Waves

Now consider the case where the TS waves grow in space on the same parallel, mean boundary-layer profile. For a frequency $\omega = 0.08$ the spatial wavenumber predicted by LST is

$$k_{xLST} = 0.228047394 - 0.006516315i \qquad (4.4)$$

where the growth-rate is given by the negative imaginary part of the wavenumber, $\sigma_{LST} = 0.006516315$.

For the spatial calculations the same wall-normal grid is used as in section 4.1.1. However, the streamwise length of the domain is increased to allow the TS waves to grow in space. Two domain sizes are considered: $5\lambda_{TS}$ and $10\lambda_{TS}$. Based on the temporal convergence results, 20 nodes are used per TS wavelength resulting in an overall mesh size of (101×127) for the $5\lambda_{TS}$ case and (201×127) for the $10\lambda_{TS}$ case.

Unlike the temporal problem, both inflow and outflow boundary conditions are required. On the inflow boundary, the eigenfunction from LST is enforced by specifying the incoming inviscid characteristics [38]. On the outflow, a sponge is used

over the last wavelength of the domain (see section 3.9.3). The sponge function is given by equation (3.82) with $A_s = 2$, $N_s = 3$, and the reference state corresponds to zero disturbances. The top and wall boundaries are treated in the same manner as in section 4.1.1. Since we are interested in the time asymptotic solution, the frequency domain approach is used with $\omega = 0.08$.

Growth-rate results for both domains are presented in figure 4.4 based on the integrated, disturbance kinetic-energy using

$$\sigma = \frac{1}{2} \frac{1}{E'_k} \frac{dE'_k}{dx} \,.$$
(4.5)

In the figure, the sponge regions have been truncated so that the right boundary is coincident with the start of the sponge. From the inflow boundary to the location $1\lambda_{TS}$ upstream of the sponge the growth-rates from both domains are in reasonable agreement with LST. To quantify this, the average growth-rate in this region gives a relative error of 2.9×10^{-3} (for both domains) which is consistent with the error in the temporal problem (2.2×10^{-3}) for the same resolution. However, the introduction of inflow/outflow boundaries causes several important differences between the spatial and temporal results discussed above. The most obvious difference occurs near the outflow sponge where the spatial growth-rate undergoes a large fluctuation that appears to be limited to about $1\lambda_{TS}$ upstream of the start of the sponge for both domain lengths. This upstream influence is likely due to the elliptic nature of the streamwise viscous terms in the boundary layer. The nature and extent of the upstream influence are consistent with the results of previous authors [46, 2] who used a similar sponge term.

Another difference between the spatial and temporal results is that the magnitude of the oscillations in growth rate about the mean value are much higher, $\approx 2\%$, for the spatial simulation as compared to $\approx 0.1\%$ for the temporal simulation. There are several potential sources for these oscillations. First, similar to the temporal problem, there is a mismatch between the LST eigenfunction forced on the inflow and the discrete eigenfunction of the finite difference scheme. Second, the one-dimensional, inviscid boundary condition used to force the eigenfunction at the inflow is only an approximation. Third, the outflow sponge may cause reflections (both numerical waves and physical waves) which could travel upstream.

To isolate the cause of these oscillations, a third simulation was performed using

the $10\lambda_x$ domain but with the outflow sponge set to use the LST solution as the reference state. This ensures that the transient in the sponge will be less severe since the sponge only has to correct for the errors in the discrete finite difference solution instead of damping the disturbances to zero. Figure 4.5 shows the growth-rate results from this simulation. By comparison to figure 4.4, the extent of the direct upstream influence of the sponge is similar to the previous results, although the magnitude of the influence is much less. The amplitude of the oscillations in the interior of the domain are also reduced—they are on the order of 0.1% instead of 2%. From this, we conclude that the majority of the errors in the previous solutions are due to reflections from the strong sponge, not errors due to inflow forcing. In constructing the sponge term, these results suggest that it is advantageous to devise the reference state so that the transient in the sponge is minimized. Unlike the current case, however, in receptivity calculations the solution in the sponge is not known *a priori* so that different means of improving the solution must be sought.

Returning to the zero reference state sponge, another way of reducing the influence of the sponge is to increase the length of the sponge while keeping the sponge function (*i.e.* A_s and N_s) constant. Figure 4.6 shows growth-rate results for sponge lengths of 1, 2, and 5 λ_{TS}. As the sponge length is increased the magnitude of the upstream influence is reduced for both the fluctuation directly upstream of the sponge and the oscillations in the interior. Note: the fluctuation directly upstream of the sponge can only be seen for the 5 λ_{TS} sponge since this portion of the domain is not shown for the shorter sponges. However, by comparison to the results of figure 4.4 the direct upstream influence of the sponge has been significantly reduced by increasing the length of the sponge. A similar, although smaller, reduction is obtained for the $2.5\lambda_{TS}$ case. Comparing the solution with a $5\lambda_{TS}$ sponge to the solution with a λ_{TS} sponge using the LST reference state (figure 4.5) shows that the solutions are of comparable quality with errors on the order of 0.2%.

To summarize the results of this section, the resolution estimates made for the temporal problem in section 4.1.1 are verified for the spatial problem. Furthermore, the outflow sponge is found to be successful in damping TS waves before they interact with the outflow boundary, although not without some level of upstream influence. Two types of upstream influence are observed. The first is a spatially damped oscillation of approximate length λ_{TS} directly upstream of the start of the sponge. The

second type of upstream influence is due to reflections (both numerical and physical) which lead to oscillations of the growth-rate in the interior. Both forms of upstream influence can be reduced by either improving the sponge reference state or by increasing the length of the sponge. In either case, the effect is to reduce the strength of the transition in the sponge. Acceptable solutions are obtained using a sponge length of $5\lambda_{TS}$ with a zero disturbance reference state. For this case, the errors due to upstream influence are comparable in magnitude to the error in the average growth-rate and the maximum error in the growth-rate is less than 0.4%.

4.2 Crossflow Vortices in a Parallel Boundary Layer

In addition to TS waves, the transitional flow near a swept leading-edge may also include crossflow (CF) vortices. To evaluate the ability of our numerical method to predict the growth of CF vortices we have performed a series of calculations using a parallel boundary layer as the base flow. Similar to the TS wave study above, the solutions can be compared directly to parallel, Linear Stability Theory (LST).

The base flow is computed from the compressible Falkner–Skan–Cooke equations (see Appendix C). However, we now consider profiles with sweep and favorable pressure gradient ($\theta = 45°$, $\beta_h = 1$) such that the crossflow component of velocity is maximized [68]. The flow conditions are $M = 0.3$, $Re = 400$, and $Pr = 1.0$. The reference length for this calculation is the displacement thickness of the chordwise velocity profile and all other reference quantities are based on edge values. The wall is isothermal at the adiabatic wall temperature, $T_w = T_0$, and constant fluid properties are assumed. The reference growth rates are obtained from the linear stability solver (see Appendix D) with 96 Chebyshev collocation points.

4.2.1 Temporally Growing CF Vortices

As in the case of TS waves, we begin by considering the growth of CF vortices in time. For this test, a stationary mode with $k_x = -0.287436451$ and $k_z = 0.35$ is simulated and for these wavenumbers LST predicts a purely imaginary frequency of

$$\omega_{LST} = 0.006533585i \tag{4.6}$$

so that the growth rate is given by $\sigma = 0.006533585$. The LNS calculations use the same wall normal mapping used for the temporally growing TS waves in section 4.1.1. The unsteady disturbance code is used with $\Delta t = 0.047643$ (the nominal time-step in the TS wave study) and with 2 iterations per time-step.

Figure 4.7 shows the evolution of the growth-rate of disturbance kinetic energy from the LNS calculation compared to LST. The results for two spatial resolutions, (20×127) and (80×127), are presented and clearly demonstrate that the LNS solution converges to the LST solution as resolution is increased. Consistent with the TS wave study, the relative error in the growth-rate for a resolution of (20×127) is 0.28% which should be adequate for the present investigation.

4.2.2   Spatially Growing CF Vortices

Now consider the spatial growth of a stationary, $\omega = 0$, CF vortex mode with $k_z = 0.35$. LST predicts the chordwise wavenumber to be

$$k_{xLST} = -0.288319629 - 0.013854663i \qquad (4.7)$$

so that the spatial growth rate is given by $\sigma_{LST} = 0.013854663$.

Similar to the spatial TS wave investigation, a domain is constructed that is $10\lambda_x$ long and uses 20 nodes per streamwise wavelength. The wall normal mesh is identical to that used in the temporal investigation in section 4.2.1. On the inflow boundary the LST eigenfunction is enforced by setting the incoming characteristics [38]. Zero disturbance conditions are used on the top boundary and a sponge of length λ_x is used on the outflow boundary. The sponge parameters are $A_s = 2$, $N_s = 3$, and the reference state is zero.

The computed growth-rate, based on the disturbance kinetic energy, is shown in figure 4.8 compared to the value from LST where the sponge region has again been truncated. Computing the average growth-rate in the domain yields a value within 0.3% of the LST result. Similar to the spatial TS wave results using a similar sponge, the sponge causes a fluctuation in the growth-rate that appears limited to $1\lambda_{CF}$ upstream of the start of the sponge. However, unlike the spatial TS wave results, the overall level of the oscillations in the interior are much smaller indicating that the upstream influence of the sponge is more benign.

Given these results, we conclude that the outflow sponge, relative to the TS wave problem, has relatively little impact on the CF vortex solution. This fact allows the use of much shorter sponges, on the order of λ for CF vortices, compared to 5λ for TS waves.

4.3 Acoustic Scattering from a Circular Cylinder

A fundamental aspect of the acoustic receptivity problem is the interaction of free-stream acoustic waves with the leading-edge. This interaction results in a scattered acoustic wave which propagates away from the body. To ensure that our simulations accurately represent this phenomenon, we have validated our code for the simple case of acoustic scattering from a stationary circular cylinder of radius a^* subject to a plane acoustic-wave traveling perpendicular to the cylinder axis. For this calculation, the reference length is the cylinder radius $L^* = a^*$, the reference velocity is the far-field acoustic speed $u_r^* = c_\infty^*$, and all other reference quantities are based on far-field values.

The incident, plane acoustic-wave with nondimensional wavelength λ is given by

$$p_i = P_0 e^{ik(x-t)}, \quad k = \frac{2\pi}{\lambda} \tag{4.8}$$

where the direction of propagation is along the positive x-axis and P_0 is the incident pressure amplitude, taken to be 0.5.

Under these conditions, the scattered pressure wave can be expressed by the following Bessel function expansion [79]

$$p_s = \sum_{m=0}^{\infty} A_m \cos(m\theta)[J_m(kr) + iN_m(kr)]e^{-i\omega t} \tag{4.9}$$

where (r, θ) are the the usual cylindrical coordinates, $\omega = k$, and

$$A_m = -\varepsilon_m P_0 i^{m+1} e^{-i\gamma_m} \sin \gamma_m, \tag{4.10}$$

$$\tan \gamma_0 = -\frac{J_1(k)}{N_1(k)}, \tag{4.11}$$

$$\tan \gamma_m = \frac{J_{m-1}(k) - J_{m+1}(k)}{N_{m+1}(k) - N_{m-1}(k)} \tag{4.12}$$

with $\varepsilon_0 = 1$ and $\varepsilon_m = 2$ for all m larger than zero. In these expressions, J_m and N_m are Bessel functions of the first- and second-kind, respectively. This solution is exact in the inviscid limit and is used to evaluate the accuracy of our numerical scheme.

An inviscid simulation is conducted for an incident acoustic wave with $\lambda = 2.5$. A circular mesh with dimensions (256×241) is used with the far-field boundary placed at $r_o = 13.5$. The mesh is uniform in θ and in r and provides a minimum of 18 nodes per incident wavelength in θ and 48 nodes per scattered wavelength in r. Since the flow is symmetric about the x-axis, we solve for the solution only on the upper half-plane with symmetry conditions used on the x-axis.

Before proceeding, we note that the rather high resolution in r is used to reduce the accumulation of phase errors in the calculation since the acoustic waves propagate over 10 wavelengths within the domain. Compared to our acoustic receptivity calculations (see Chapter 4.4), this scattering test is a severe test of our method.

Since only viscous wall boundary conditions were discussed in section 3.9.3, the appropriate inviscid wall boundary conditions are presented here. For an inviscid wall the only boundary condition required is the no-penetration condition, $v_n = 0$. Since the wall boundaries are curved, in general, the equations and velocity unknowns on the wall boundary must be locally rotated to a body-normal coordinate system. Defining the unit, body normal as $\{n_1, n_2\}^{\mathrm{T}}$, the primitive variables in the body-normal coordinate system are given by

$$
\begin{Bmatrix} \rho \\ v_s \\ v_n \\ w \\ T \end{Bmatrix} = \begin{bmatrix} 1 & & & & \\ & n_2 & -n_1 & & \\ & n_1 & n_2 & & \\ & & & 1 & \\ & & & & 1 \end{bmatrix} \begin{Bmatrix} \rho \\ u \\ v \\ w \\ T \end{Bmatrix}
\tag{4.13}
$$

which can be written as

$$
\mathbf{U}_s = \mathbf{R}\mathbf{U} .
\tag{4.14}
$$

The matrix, $\mathbf{R}$ is used to rotate the equations and unknowns at the boundary to the body-normal coordinate system. In particular, let $\mathbf{R}_i$ be the rotation matrix at node i on the boundary $j = 1$.

Before approximate factorization, the linear system that must be solved every

iteration can be written compactly as

$$\mathbf{M}\delta\mathbf{U} = \mathbf{G} \,. \tag{4.15}$$

A block-diagonal matrix is constructed with the rotation matrix on the diagonal for nodes on the boundary and the identity matrix elsewhere;

$$\mathbf{S} = \text{diag}(\mathbf{R}_1, \ldots, \mathbf{R}_{N_\xi}, \mathbf{I}, \ldots, \mathbf{I}) \tag{4.16}$$

where the first N_ξ nodes are on the boundary $j = 1$. Then the equations and unknowns can be rotated to the new coordinate system

$$[\mathbf{SMS}^{\mathrm{T}}](\mathbf{S}\delta\mathbf{U}) = (\mathbf{SG}) \tag{4.17}$$

which can be written as

$$\mathbf{M}_s\mathbf{U}_s = \mathbf{G}_s \,. \tag{4.18}$$

Thus, on the boundary $j = 1$, the velocity unknowns are (v_s, v_n, w) and the x- and y-momentum equations have been replaced with the s- and n-momentum equations. In practice, this system of equations is approximately factored before solving, as discussed in section 3.12.

In body normal coordinates at the wall, the impermeable boundary constraint can be written simply as

$$g_{v_n} = v_n = 0 \tag{4.19}$$

which is used to replace the normal momentum equation at the boundary (Note that the tangential momentum-equation is solved as is). The variation of this constraint required to form the LHS is simply

$$\delta g_{v_n} = \delta v_n \,. \tag{4.20}$$

At the far-field boundary, locally one-dimensional characteristic boundary conditions [38] are used to force the plane acoustic wave. In addition, over the region $r_s = 8.5$ to $r_o = 13.5$ a sponge term is added to damp the scattered field while leaving the incident wave unaffected. This is accomplished by using the sponge term defined

in equation (3.81) with the reference state, $\mathbf{U}_{ref}$, equal to the incident, plane acoustic wave. The sponge function is defined by equation (3.82) with x replaced by r, $A_s = 10$, and $N_s = 3$.

The simulation is conducted using the frequency domain approach with $\omega = k = 2.513$. Figure 4.9 shows contours of the instantaneous, scattered pressure field from the simulation demonstrating the damping of the scattered field in the sponge region. The acoustic intensity, $\Upsilon = r|p_s|^2$, for the scattered wave along the ray $\theta = \pi$ is shown in figure 4.10 compared to inviscid theory. As expected, the acoustic intensity approaches a constant far from the cylinder which confirms the expected $1/r$ decay of the scattered wave. In the sponge, the intensity of the scattered wave is smoothly damped to zero and there are no noticeable reflections on this scale. Often in acoustics the directionality of the scattered sound is of importance. Figure 4.11 shows a polar plot of the acoustic intensity at three radial locations. The top frame, at $r = 3.45$, shows excellent agreement between theory and calculation with the RMS relative error equal to 0.07% and similar results are obtained for all $r < r_s$. The middle frame is slightly outside the sponge at $r = 8.45$ and we see that even here the agreement with theory is good with an RMS error of 1%. Note that most of these errors occur around $\theta = 90°$ which is the location of minimum resolution for the incoming acoustic wave. The bottom frame, at $r = 11.16$, is well within the sponge and, as expected, the scattered intensity is significantly reduced at this location.

To assess the level of reflections in the sponge, figure 4.12 shows the relative error in the computed acoustic intensity along the ray $\theta = \pi$. Results are shown for both the original calculation, and a second calculation in which $r_o = 11$ and $N_r = 201$ with all other parameters the same. Thus, the second calculation has a sponge that is only one wavelength long and the number of nodes in r is reduced to keep the number of points per wavelength constant. For the original sponge, the RMS error in the interior region is 8.8×10^{-4} while for the shorter sponge, the RMS error is an order-of-magnitude greater, 8.3×10^{-3}. The oscillations in the error are indicative of both phase errors and reflections, while the mean error is entirely due to reflections since the spatial scheme has no inherent amplitude error. As the sponge is lengthened, both the level of oscillations, and the mean error are reduced indicating that reflections are weaker for the longer sponge.

Another means of reducing reflections caused by the sponge is to reduce the sponge

amplitude A_s while keeping the sponge length constant. Figure 4.13 shows the relative error in acoustic intensity along the ray $\theta = \pi$ for the original calculation, and a third calculation where $A_s = 5$ with all other quantities the same as the original calculation. For this case, decreasing A_s, reduces the average error with little effect on the level of oscillations in the error. The remaining oscillations are due to the phase error of the finite difference scheme. We have found for this case, that further reduction of A_s has negative impact on the solution, because the sponge is unable to reduce the amplitude of the scattered wave sufficiently to make it consistent with the far-field boundary condition.

In summary, we conclude that our numerical method can accurately predict the intensity and directionality of acoustic waves scattered from a solid body. Furthermore, we have found that an inflow sponge, where the reference state corresponds to an incoming acoustic wave, is a viable technique for enforcing incoming disturbances while reducing reflections of outgoing disturbances. For the current problem, a sponge two acoustic wavelengths long is required to reduce the error due to reflections to the level of the truncation error of the numerical scheme.

4.4   Two-Dimensional Leading-Edge Receptivity to Sound

In this section, results from two-dimensional calculations are presented for a flat-plate with a super-ellipse leading-edge. For this calculation, the reference length scale is the plate half-thickness, L^*, and the reference velocity is the freestream speed, $u_r^* = u_\infty^*$. All other reference quantities are based on their freestream values. The plate is smooth, unswept and at zero angle-of-attack. The super-ellipse geometry is given by

$$\left(1 - \frac{x}{\mathsf{AR}}\right)^m + y^2 = 1 \tag{4.21}$$

where $\mathsf{AR} = x_j^*/L^*$ is the aspect-ratio of the leading edge (LE) with x_j^* the location of the junction between the LE and plate; and m determines the level of continuity at the junction.

To assess the ability of our method to predict LE receptivity, we have chosen the geometry and flow conditions so that our results can be compared to the previous

incompressible results of Lin [63]. We therefore use an $\mathsf{AR} = 6$, $m = 4$ super-ellipse LE with $\mathsf{Re} = 2400$ and $\mathsf{M} = 0.1$ where M is selected based on mean flow comparisons (shown below) with the incompressible results.

Figure 4.14 shows the computational mesh for this geometry where symmetry has been used to limit the domain to only the upper surface of the plate. A plate length of 40 is used and the farfield boundary is placed 40 units above the plate. The mesh dimensions are (384×127) and hyperbolic tangent mapping functions, similar to those used by Lin [63], are used to cluster points near the LE and near the wall. This mesh provides at least 30 points in the mean boundary-layer and 18-22 points per TS wavelength for the receptivity calculation.

4.4.1   Mean Flow Computation

The first step in performing a receptivity calculation is to determine the mean flow. In computing the mean flow, the nonlinear solver discussed in section 3.6 is employed. Adiabatic, no-slip boundary conditions are used on the plate surface with symmetry enforced directly in the finite-difference stencil on the boundary upstream of the leading-edge. On the outflow boundary, a characteristic based nonreflecting boundary condition with viscous corrections [83] is used while on the inflow boundary first-order Riemann Extrapolation (see section 3.9.2) is performed. Each of these boundary conditions is treated fully implicitly to improve convergence to the steady-state. Note that after performing the current calculation, an improved outflow boundary treatment was developed utilizing the parabolized Navier–Stokes equations (*e.g.* section 3.9.2). The current calculations were not rerun, since the outflow boundary treatment is not expected to have a large impact on the meanflow near the leading-edge.

The evolution of the displacement thickness, δ_1, along the plate is shown in figure 4.15. The computed result is compared to the Blasius solution where the virtual origin is set to match the computed solution. The computed solution quickly evolves to the Blasius curve downstream of the junction at $x = 6$ and by $x = 10$ the development is indistinguishable from the Blasius curve. At $x = 30$ the solution begins to diverge from the Blasius curve as the approximate outflow boundary condition begins to influence the development. This region of upstream influence does not affect the unsteady receptivity calculation since this region is inside the outflow sponge (see section 4.4.2).

In comparing our results to those of Lin [63], we must verify that our $\mathsf{M} = 0.1$ mean flow is a reasonable approximation to an incompressible flow. Figure 4.16 shows the pressure gradient with respect to arc-length, s, along the plate for a range of Mach numbers. As M is decreased, the curves converge to the incompressible result [63] and for $\mathsf{M} = 0.1$ the pressure gradient is indistinguishable from the incompressible curve. This excellent agreement between our mean flow solution and Lin's [63] is also observed in other wall quantities such as the pressure coefficient (figure 4.17) and the wall vorticity (figure 4.18). Based on these comparisons we believe that our solutions at $\mathsf{M} = 0.1$ are a good approximation to the incompressible solution. Figure 4.19 shows a streamwise velocity profile, plotted versus the Blasius variable $\eta_b \equiv y\sqrt{\mathsf{Re}/x}$, in the flat plate region compared to Lin's results. Again the comparison is excellent. However, to confidently conclude that the stability properties of our mean flow match those of Lin requires that first- and second-derivatives of the boundary layer profiles agree. Unfortunately Lin does not provide these data, but this comparison can be inferred from comparing the neutral point predictions of local, parallel LST. For his mean flow, Lin reports the first neutral point location to be $x = 5.7$ while our analysis yields $x = 6.2$ using the parallel LST solver discussed in Appendix D. Given the extreme sensitivity of the neutral point location we judge this roughly 9% difference to be acceptable. Although only parallel LST theory has been applied to this flow, it is noted that the current results could be refined using the nonparallel theory developed in Appendix D.3.

4.4.2 Receptivity Computation

With the mean flow computed in section 4.4.1, the linear disturbance solver discussed in section 3.7 is used to solve for the response of the boundary layer to a forced, plane acoustic wave striking the leading edge at normal incidence. For comparison to Lin's [63] results, a nondimensional forcing frequency $\omega = 0.552$ is used, which equates to a frequency parameter of $\mathsf{F} \equiv \omega/\mathsf{Re} \times 10^6 = 230$. At $\mathsf{M} = 0.1$ this frequency corresponds to a downstream propagating acoustic wave with wavelength $\lambda = 125$.

When this calculation was performed the more efficient frequency-domain approach (see section 3.7.2) was not complete. So, instead, the unsteady approach was employed as described in section 3.7.1. The time-step is selected to provide $N_t = 2400$

time-steps per period of the acoustic forcing and 2 iterations of the implicit solver are taken at each step. Based on the resolution study of section 4.1.1, the spatial and temporal resolution used should be sufficient to yield TS growth-rates to within 0.2%.

The wall, symmetry, and outflow boundary conditions for the receptivity calculation are the same as those used to compute the mean flow in section 4.4.1. However, the farfield boundary condition is changed to a locally one-dimensional characteristic boundary condition [38] which forces the plane acoustic wave while allowing boundary normal waves to exit. This is the same farfield boundary condition used for the cylinder scattering problem in section 4.3. See section 3.9.3 for a detailed discussion of boundary condition implementation for the linear disturbance solver.

To reduce reflections, two sponge terms are added to the NS equations: an inflow sponge and an outflow sponge. Figure 4.20 is a schematic of the computational domain showing the boundary conditions and sponge regions. For the inflow sponge, the same sponge used in the cylinder scattering problem is utilized with $r_s = 10$ and $r_0 = 40$ where r is the normal distance from the plate. By construction, this sponge damps all disturbances except the plane acoustic wave forced on the farfield boundary. Near the outflow, a sponge similar to that used in the spatial TS wave problem is utilized with $x_s = 20$ and $x_o = 40$. This sponge damps all disturbances, including the plane acoustic wave, before they hit the outflow boundary. Linear stability theory predicts the wavelength of the TS waves in the boundary layer to be about $4L^*$ so that the outflow sponge is approximately $5\lambda_{TS}$ long. Based on the results of the spatial TS model problem in section 4.1.2, this sponge should provide sufficient damping with negligible reflection of the TS wave. However, both the inflow and outflow sponge are only about 16% of an acoustic wavelength in length. Based the scattering for a circular cylinder (*e.g.* section 4.3), this sponge is very likely to cause reflections. However, experience has shown these reflections to be acceptably small for this problem as demonstrated by the clean instability wave shown in figure 4.23 below. Based on this, further increases in the sponge region were deemed unnecessary for this problem.

The region in figure 4.20 where the two sponges overlap requires special attention. To prevent incompatibility between the two sponges and the top boundary condition, the acoustic wave forced at the top boundary and the wave subtracted off in the inflow

sponge must account for the decay of the plane acoustic wave in the outflow sponge. This is accomplished by performing a one-dimensional acoustic wave simulation over the length of the domain [-40,40] using the same outflow sponge and the same flow conditions. The solution to this problem, which now includes the damping in the outflow sponge, is then forced on the top boundary and subtracted off in the inflow sponge.

To begin the calculation, the acoustic forcing on the boundary is smoothly ramped up over one period of the forcing. The success of the boundary treatments is evident in instantaneous contours of velocity shown in figures 4.21 and 4.22. The data in these figures are given for $t = 65.45$ which corresponds to 5.75 periods of the acoustic forcing. By this time in the simulation, TS waves formed at the leading-edge have entered the outflow sponge so that a full train of TS waves exists on the plate surface. The long wavelength acoustic wave is clearly visible in the u' contours of figure 4.21 with no noticeable distortion in the inflow sponge. Included above the contour plot, is the distribution of the Fourier amplitude of u' specified on the top boundary, showing the decay of the forcing wave in the outflow sponge. Returning to the contours of u', the solution takes the form of a Stokes-wave near the plate which obscures the development of instability waves. However, since the Stokes-wave has nearly zero velocity component in y, contours of v' in figure 4.22 shows the development and growth of an instability wave on the plate. Also visible is the decay of the instability waves in the outflow sponge and the decay of the scattered acoustic field in the inflow sponge.

Figure 4.23 again shows contours of v' at $t = 65.45$ but with the sponge regions removed for clarity. At this particular phase of the forcing, the amplitude of the scattered acoustic wave and Stokes-wave near the LE region is negligible so that the development of the instability wave is clearly observed even close to the LE. However, taking the Fourier transform in time (denoted by $\hat{v}'$) and plotting the amplitude in figure 4.24 shows the large scattered acoustic field and the Stokes-wave near the LE. Also observed in this figure is the initial decay and then growth of the instability wave in the boundary layer.

To extract the amplitude of the instability wave from the total disturbance signal requires some form of post-processing. For incompressible calculations this is typically accomplished by performing a separate, no-flow, scattering calculation for

the same geometry. After taking the Fourier transform in time, the Fourier coeffi-
cients of the scattering solution are subtracted from the Fourier coefficients of the
receptivity solution leaving only the instability wave component [63]. However, for
compressible flows there is a change in the acoustic wavelength between no-flow and
finite flow conditions and this change increases with Mach number. For our $M = 0.1$
calculation, this amounts to a 10% difference in the wavelengths between flow and no-
flow conditions. Even for this modest difference, we have found that subtracting the
Fourier coefficients from a no-flow scattering calculation does not adequately remove
the acoustic component.

To analyze the present results, we use the complex plane decomposition developed
by Wlezien [112]. As an example of this technique, figure 4.25 shows the trajectory
of the Fourier coefficient of the vertical component of disturbance velocity plotted in
the complex plane. The large spiral curve shown in the figure is parameterized by
x and represents the Fourier coefficient at each x taken at the y location where the
magnitude is maximum. Each symbol on the curve represents data from a different x
location in the grid starting at $x = 6$ and going to $x = 20$. If the disturbance consisted
solely of a TS wave, the curve would spiral around a fixed center, first spiraling inward
from $x = 6$ to $x = 9$ (corresponding to the initial decay of the TS wave) followed
an outward spiral due to the growth of the instability wave. However, as seen in the
figure, the center of the spiral is not fixed, but appears to move as one follows the
curve. The changes in the center of the spiral are due to the presence of the scattered
acoustic field resulting from the interaction of the incoming acoustic wave and the
leading edge. To separate the TS and acoustic components, Wlezien [112] suggests
that three consecutive samples along the spiral can be used to, locally, define a circle as
shown schematically in figure 4.26. The center of this circle approximates the acoustic
component, while the radius approximates the TS component of the total disturbance.
Clearly, the success of this techniques depends on a large wavelength disparity between
the TS wave and the acoustic wave which for our calculation is roughly 1:30. The
amplitude of the TS wave must also be on the order of, or greater than that of the
acoustic wave for this technique to be useful. Using the complex plane decomposition,
the TS and acoustic components of the disturbance have been extracted and their
amplitudes are shown in figure 4.27 compared to the total disturbance amplitude.
Clearly, the modulation in the total amplitude was due to interference between the

two wave types. The extracted TS wave amplitude has significantly less oscillations while the acoustic amplitude is of small amplitude and roughly constant in the flat plate region, as expected.

Figure 4.28 shows the extracted TS wave Fourier amplitude compared to the results of Lin [63]. Recall that these results are taken at the local maximum in y of $|\hat{v}'|$ for each x location. From the figure we see that our results are in excellent qualitative agreement with the incompressible results. The Branch I locations (different from those of LST due to nonparallel effects) are in excellent agreement, although our calculation predicts the TS wave amplitude at Branch I to be 10% higher than that predicted by Lin. The source for this difference is not apparent, however the difference is of the same order as the difference in the LST predicted Branch I locations discussed in section 4.4.1. Although, not performed here, it would be interesting to compare the current results to predicts based on the nonparallel linear stability theory of Appendix D.3.

To verify that the signal extracted by the complex plane decomposition is in fact a TS wave, figure 4.29 shows the extracted $\hat{v}'$ variation in the y-direction compared to the v'-eigenfunction from parallel LST, both at $x = 12$. The agreement is excellent, confirming that the decomposition has extracted a TS wave from the full disturbance solution. Ideally, one would like to perform a similar decomposition for other variables such as ρ', u', and T'. However, since the TS wave amplitude is small compared to the forced/scattered acoustic wave, the complex plane decomposition is unable to extract the TS component for these variables.

The final results in this section are for the same super-ellipse geometry but with the Mach number increased to 0.8. Although this problem is somewhat academic since the pressure distribution is unrealistic for a wing in flight, it does serve as an introduction to high-speed acoustic receptivity calculations. The mean pressure gradient along the plate for $\mathsf{M} = 0.8$ is shown in figure 4.16. The most important observation from this plot is that both the magnitude and the streamwise extent of the adverse pressure gradient are significantly larger compared to the $\mathsf{M} = 0.1$ case. This suggests that the flow will be more unstable as is verified by LST which predicts the Branch I location to be $x = 3.0$ and the maximum growth rate to be an order of magnitude greater than the $\mathsf{M} = 0.1$ case for the same frequency, $\mathsf{F} = 230$.

The receptivity calculation is conducted in the same manner as the $\mathsf{M} = 0.1$

case with $F = 230$ and figure 4.30 shows the evolution of the local maximum of the instability wave amplitude along the plate. These results are again computed using the complex plane decomposition [112] where the instability to acoustic wavelength ratio is now only 1:6.5. However, due to the large amplitude of the instability wave relative to the acoustic wave, nearly identical results are obtained by plotting the total disturbance amplitude without performing the complex plane decomposition. Because of this, we can obtain disturbance mode-shapes for all the primitive variables for this case. These curves are compared in figure 4.31 to the LST eigenfunction demonstrating conclusively that the primary response of the boundary layer is a TS wave.

4.5   Summary

For all three model problems—unstable TS wave, growing CF vortices, and acoustic scattering—the numerical method presented in Chapter 3 produces accurate solutions when compared to exact theoretical results. From these studies we have determined that for 20 points per wavelength and 128 points in the wall normal direction (with suitable non-uniform mesh distribution away from the wall), both TS and CF average growth-rates can be predicted to within 0.2%. Given the domain lengths anticipated for receptivity studies this level of accuracy ensures that the amplitude errors are less than 1% over the entire domain. To achieve this level of accuracy for spatially growing TS waves requires a sponge outflow region of approximately five instability wavelengths. In contrast, this same level of accuracy can be achieved for CF vortices with a sponge length of only one wavelength. We believe that the inviscid character of the CF instability makes it less susceptible to upstream influence caused by the sponge. For the case of acoustic scattering from a circular cylinder, we have shown that an inflow sponge term can also be used to enforce an incoming acoustic disturbance while damping outgoing scattered waves. This capability is vital to the study of acoustic receptivity which is the subject of the final validation study in which an incoming plane acoustic wave strikes a flat-plate with a super-ellipse leading-edge. The geometry and flow conditions are modeled after an incompressible calculation performed by Lin [63] and the mean flow at Mach number 0.1 is shown to be in

excellent agreement with Lin's incompressible mean solution. For the receptivity calculation, acoustic waves with $\mathsf{F} = 230$ are forced on the far-field boundary using the "inflow" sponge treatment developed for the cylinder scattering problem. Performing a complex plane decomposition [112] on the solution yields a TS wave amplitude that qualitatively agrees with Lin's results and compares to within 10% at the first neutral point. The y-variation of the v'-component of the decomposed solution is shown to match the eigenfunction shape predicted from local, parallel, linear stability theory— verifying that the boundary layer response is indeed a TS wave. Increasing the Mach number to $\mathsf{M} = 0.8$ for this geometry results in a mean boundary-layer with a severe adverse pressure gradient leading to large TS growth rates which are verified in the receptivity results.
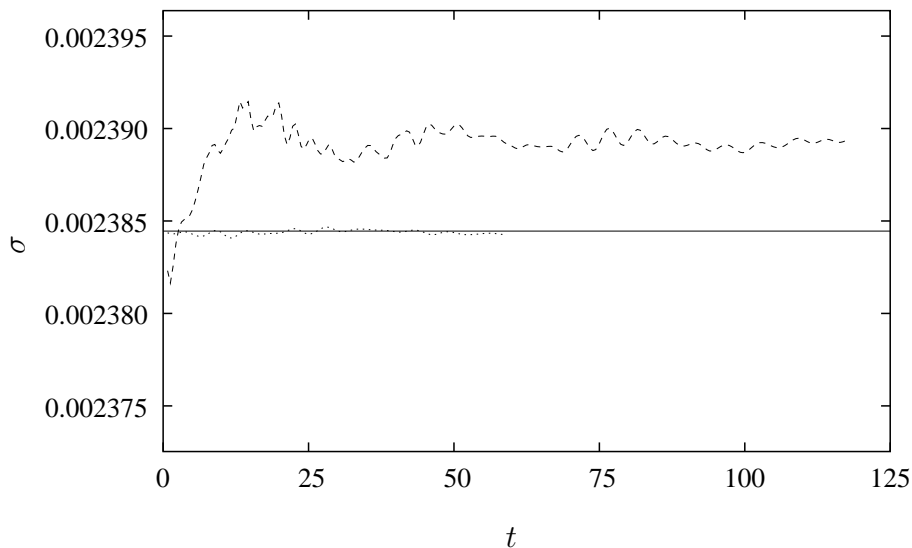
Figure 4.1: Evolution of the temporal growth-rate for a TS wave with $N_t = 1150$: —— is LST, - - - - is a computed solution with $N_x = 20$ and $N_y = 127$, and ········· is a computed solution with $N_x = 80$ and $N_y = 127$.
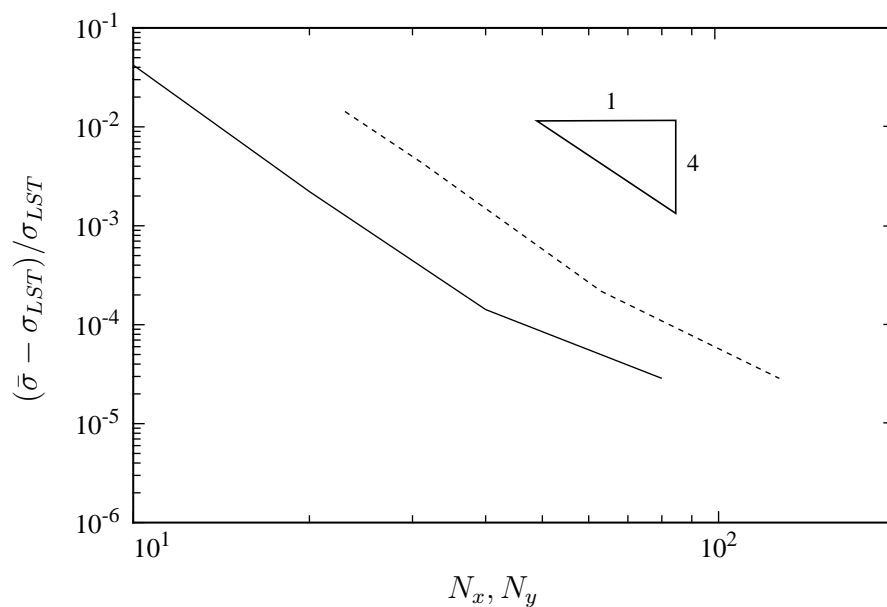

Figure 4.2: Spatial convergence of the temporal growth-rate for a TS wave with $N_t = 1150$. The —— line denotes grid refinement in x with $N_y = 127$, while the - - - - line denotes grid refinement in y with $N_x = 80$.
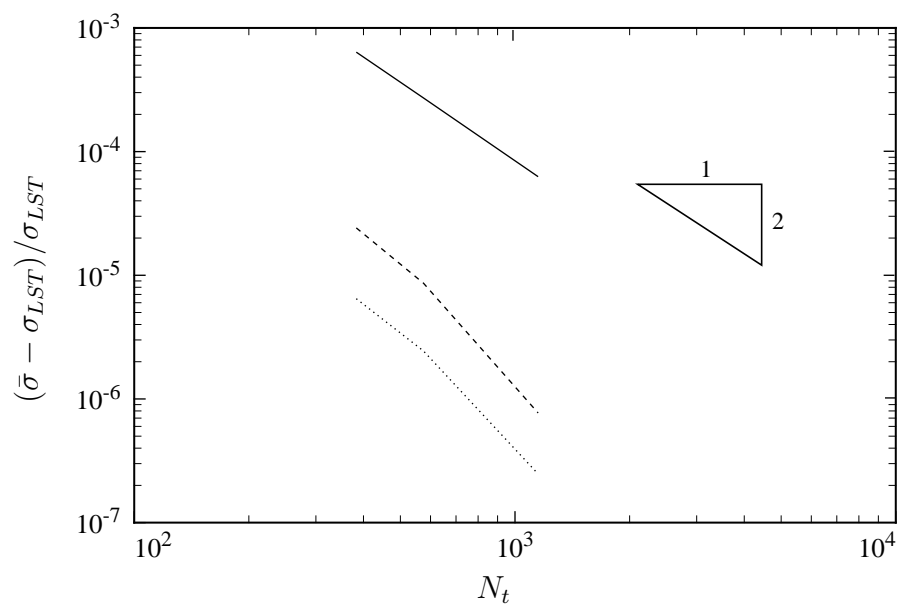
Figure 4.3: Temporal convergence of the temporal growth-rate for a TS wave with $N_x = 80$ and $N_y = 127$. The —— line is for 1 iteration, the ---- line for 2 iterations, and the ······ line for 3 iterations.
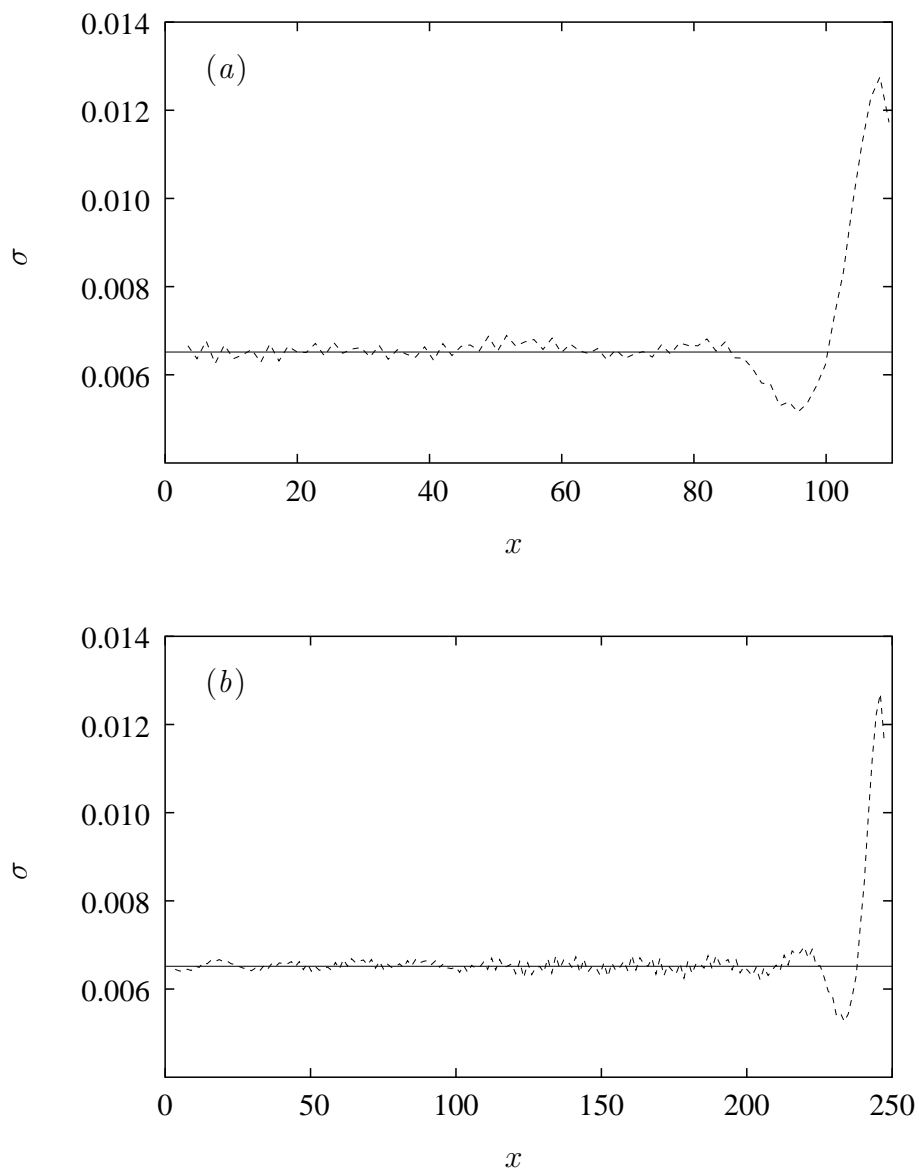
Figure 4.4: Evolution of the spatial growth-rate for a TS wave with sponge to zero: —— is LST and ---- are the computed results. Frame (a) shows results from the $5\lambda_{TS}$ domain while the $10\lambda_{TS}$ results are shown in frame (b).
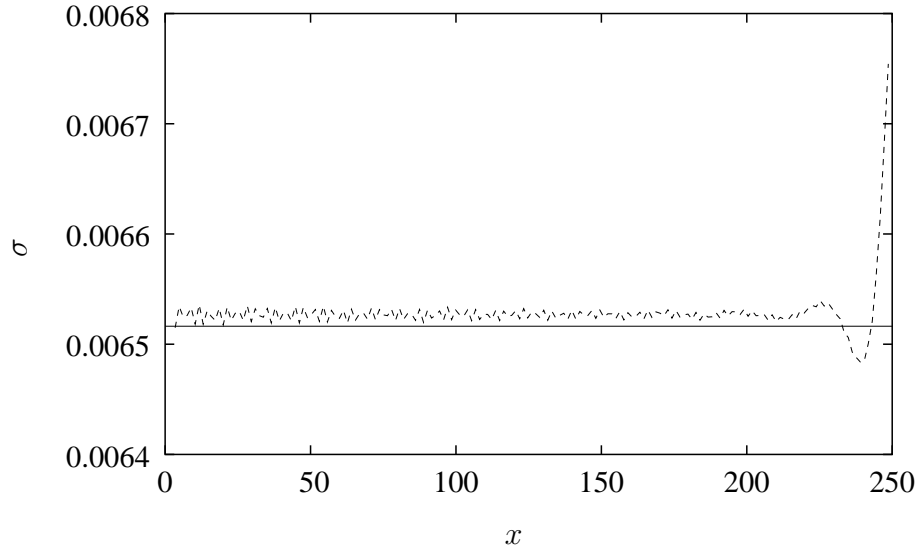
Figure 4.5: Evolution of the spatial growth-rate for a TS wave using a sponge to the LST solution: ―― is LST and – – – – is the computed result.
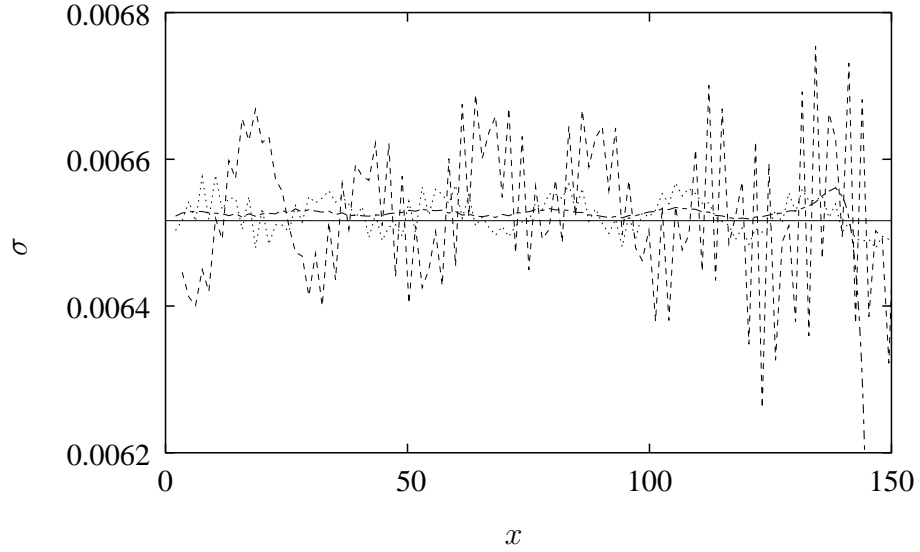

Figure 4.6: Effect of sponge length on the spatial growth-rate of a TS wave: ―― is LST, – – – – uses a λ_{TS} sponge, ⋯⋯ a $2.5\lambda_{TS}$ sponge, and —·— a $5\lambda_{TS}$ sponge.
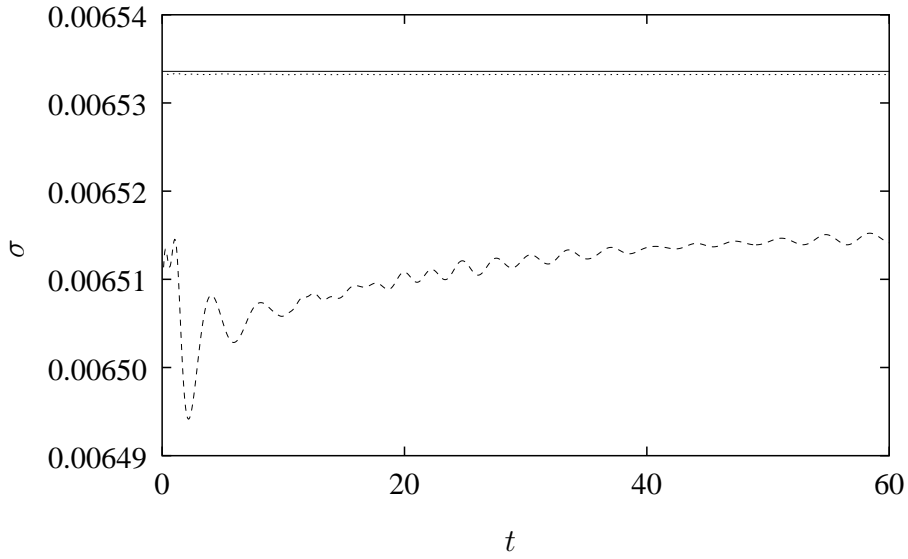
Figure 4.7: Evolution of the temporal growth-rate for a CF vortex: —— is LST, - - - - is a computed solution with $N_x = 20$ and $N_y = 127$, and ······· is a computed solution with $N_x = 80$ and $N_y = 127$.
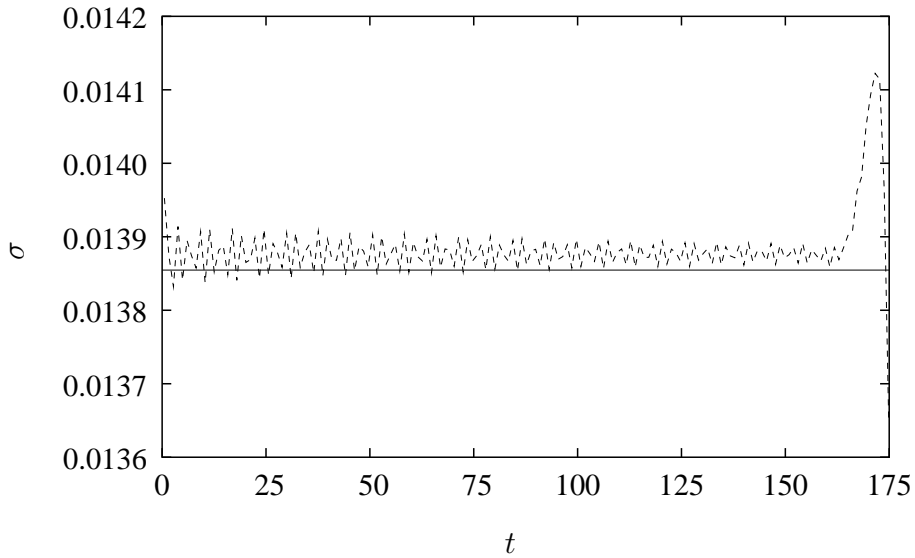

Figure 4.8: Evolution of the spatial growth-rate for a CF vortex: —— is LST, - - - - is a computed solution with $N_x = 201$ and $N_y = 127$.
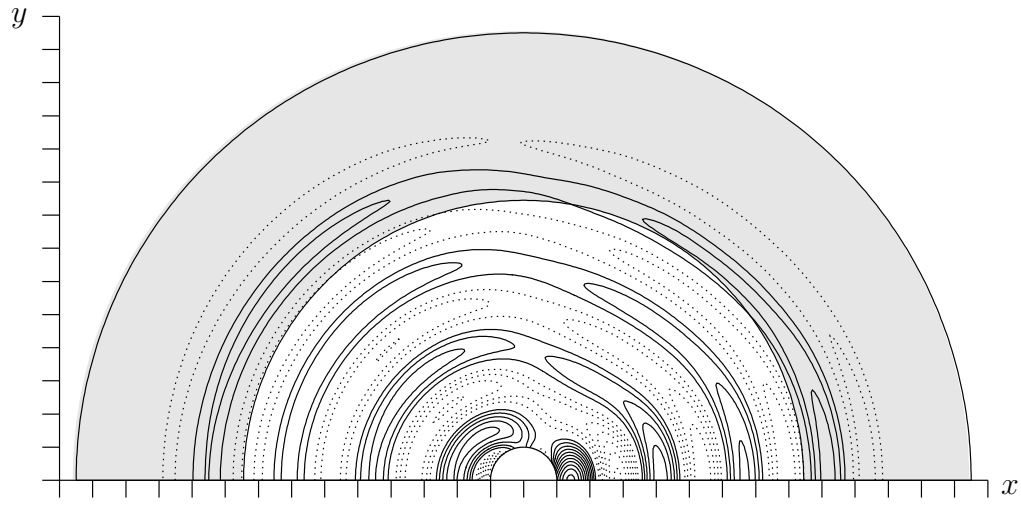
Figure 4.9: Real component of the scattered pressure field. Contour are from -0.5 to 0.5 with increment 0.05. Solid contours denote positive pressure perturbations, dotted contours denote negative pressure perturbations and the shaded region is the sponge; tics every cylinder radii.

Figure 4.10: Comparison of acoustic intensity along the ray $\theta = \pi$ for a circular cylinder subject to an incoming planar acoustic wave with $\lambda = 2.5$. The —— line is inviscid theory while the - - - - line is from the simulation.
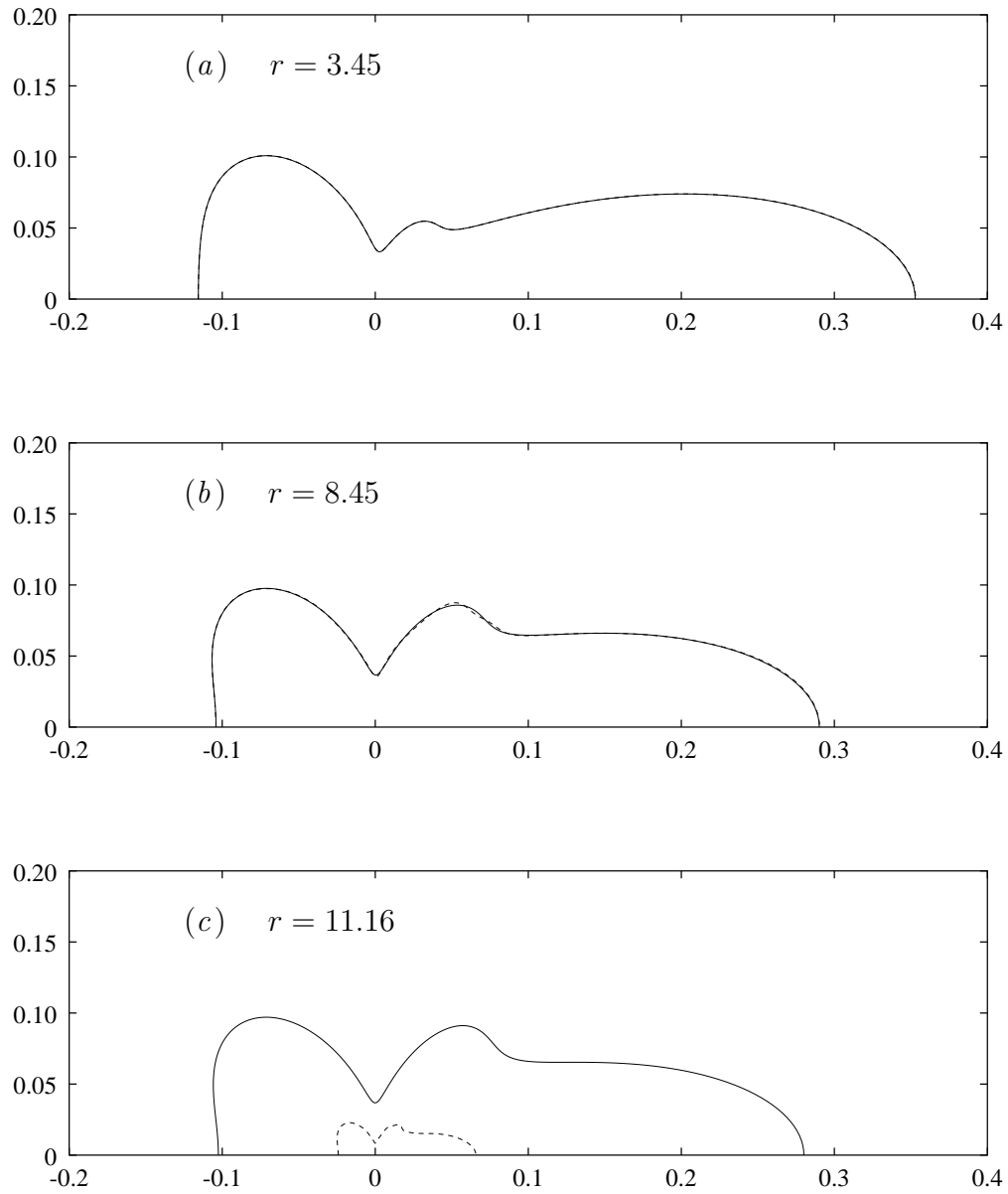
Figure 4.11: Polar plot of scattered acoustic intensity, Υ, for an incoming planar acoustic wave with $\lambda = 2.5$. The ——— line is inviscid theory while the - - - - line is from the simulation.
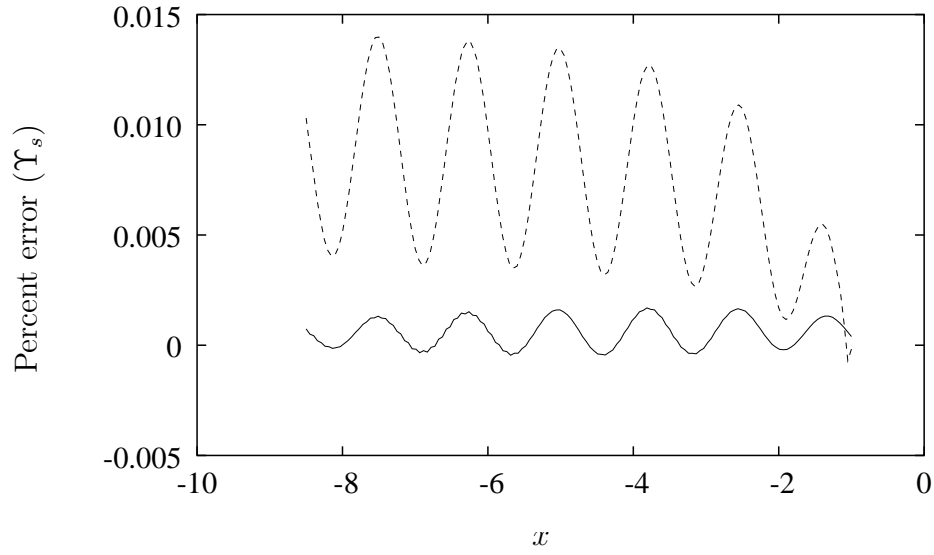
Figure 4.12: Effect of sponge-length on the relative-error in scattered acoustic intensity along the ray $\theta = \pi$ for a circular cylinder subject to an incoming planar acoustic wave with $\lambda = 2.5$.

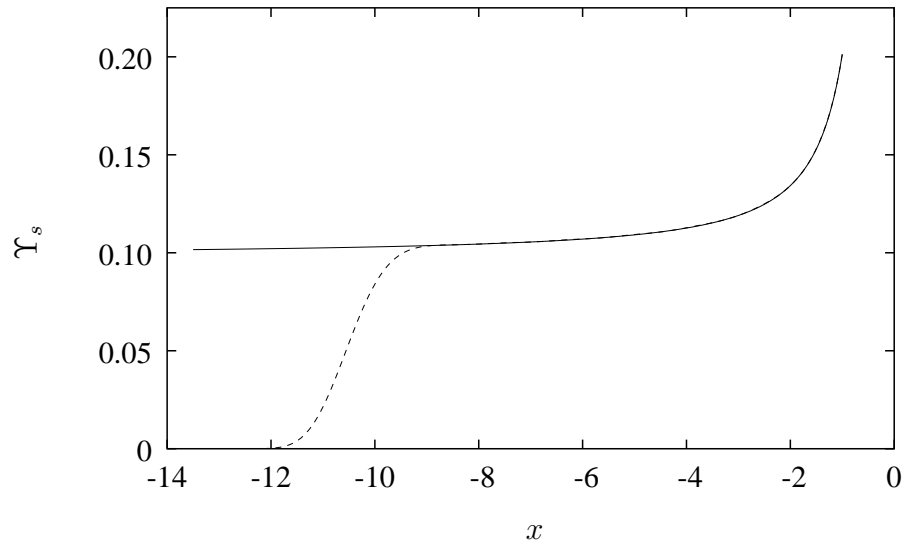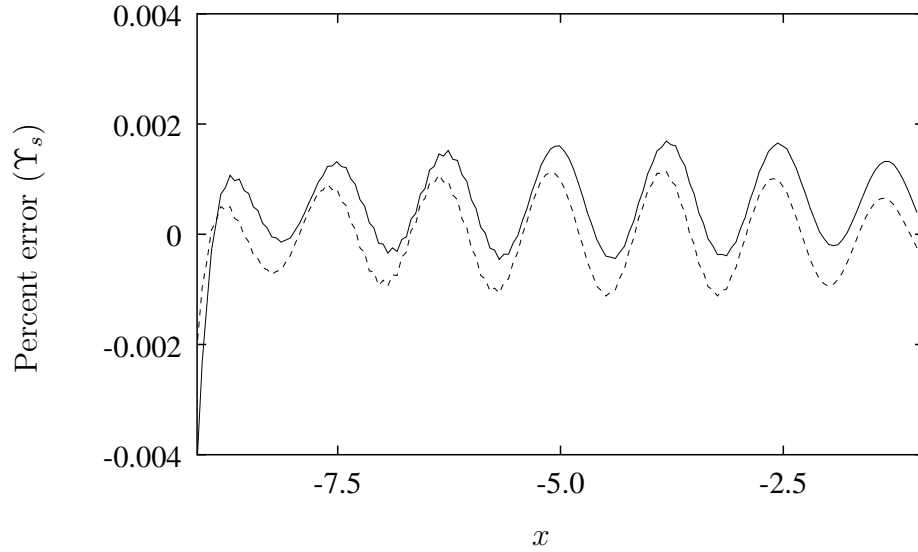**Figure 4.13:** Effect of sponge-amplitude on the relative-error in scattered acoustic intensity along the ray $\theta = \pi$ for a circular cylinder subject to an incoming planar acoustic wave with $\lambda = 2.5$.
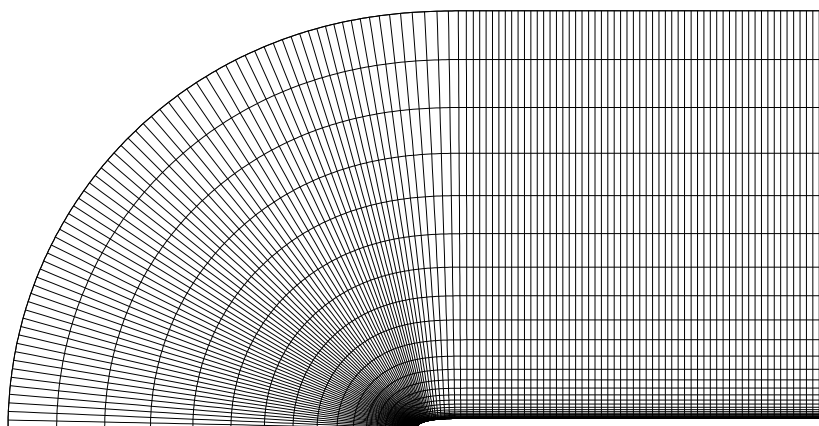
Figure 4.14: Computational mesh for the flat-plate with $\mathsf{AR} = 6$, $m = 4$ super-ellipse leading-edge. Total resolution is [384,127] however, only every third line is shown for clarity.
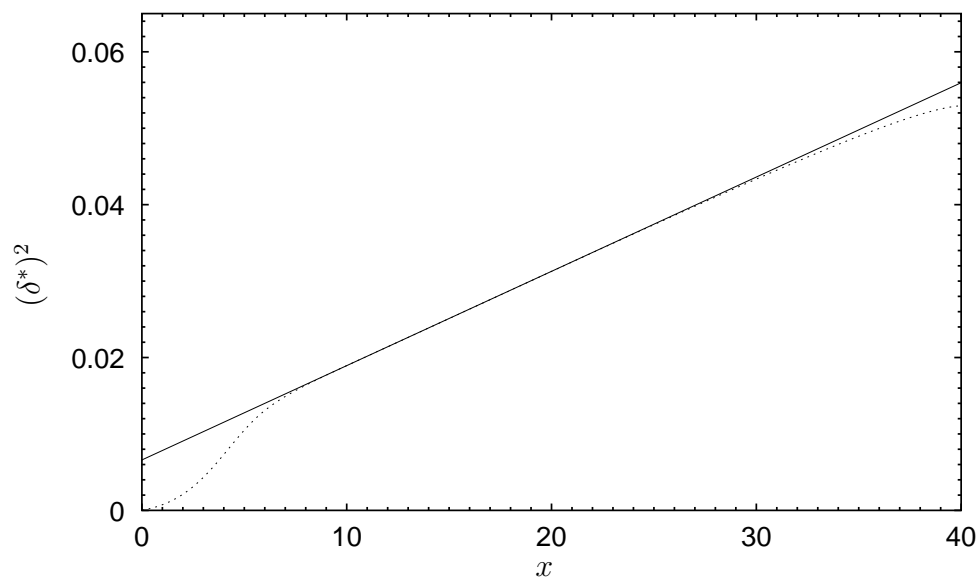
Figure 4.15: Evolution of displacement thickness squared over the plate. The ——— line denotes the Blasius solution and the ········ line is the computed solution.
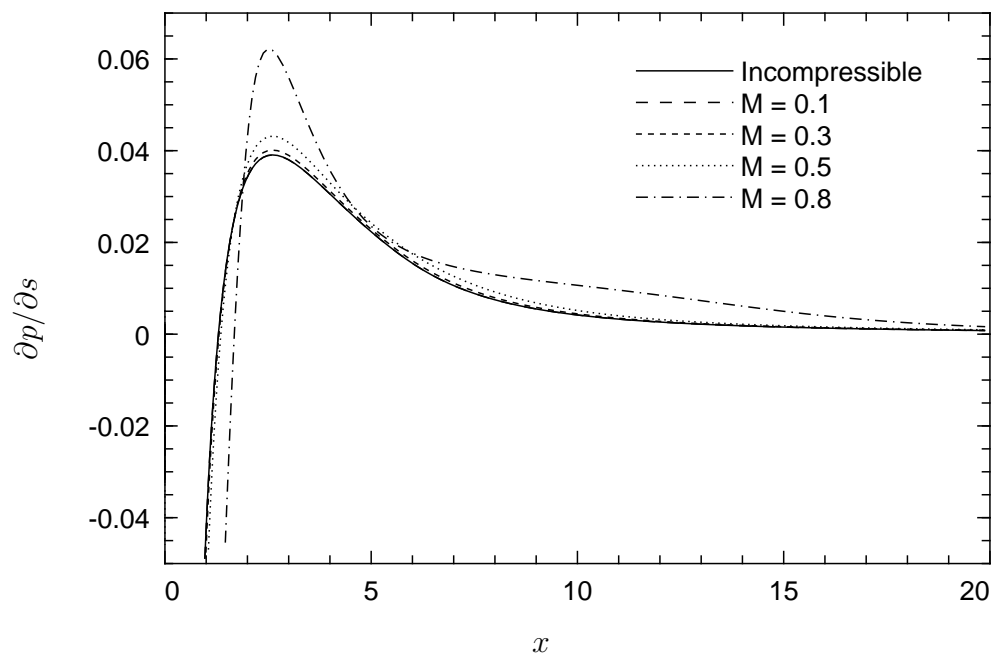
Figure 4.16: Pressure gradient along the plate for several Mach numbers. The incompressible result is taken from [63].
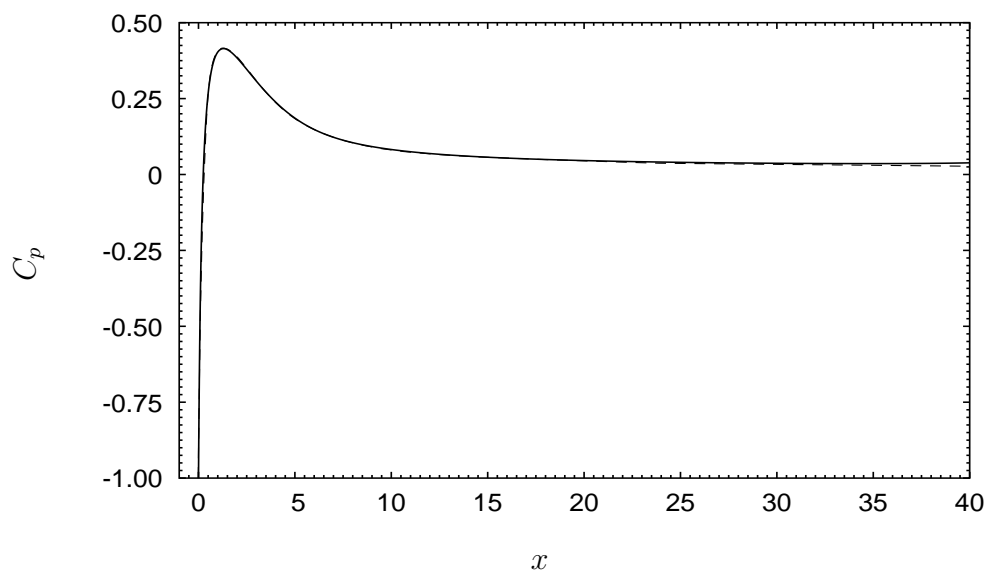
Figure 4.17: Comparison of the pressure coefficient, C_p: —— is the M $= 0.1$ result and ---- is the incompressible result [63].
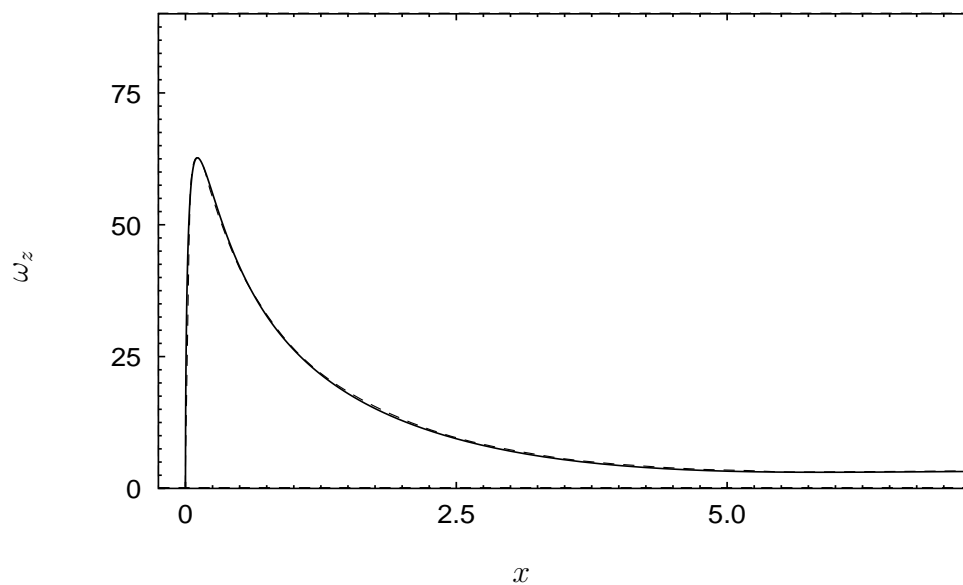
Figure 4.18: Comparison of the wall vorticity, ω_z: ⎯⎯ is the $M = 0.1$ result and ⎯⎯⎯⎯ is the incompressible result [63].
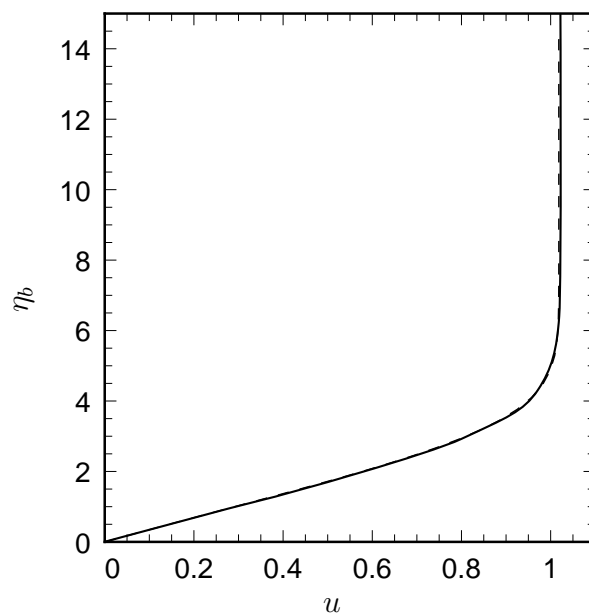
Figure 4.19: Streamwise velocity profile at $x = 22.7$ for $M = 0.1$. The ⎯⎯ line is the incompressible result [63], the −−− line is the $M = 0.1$ result.
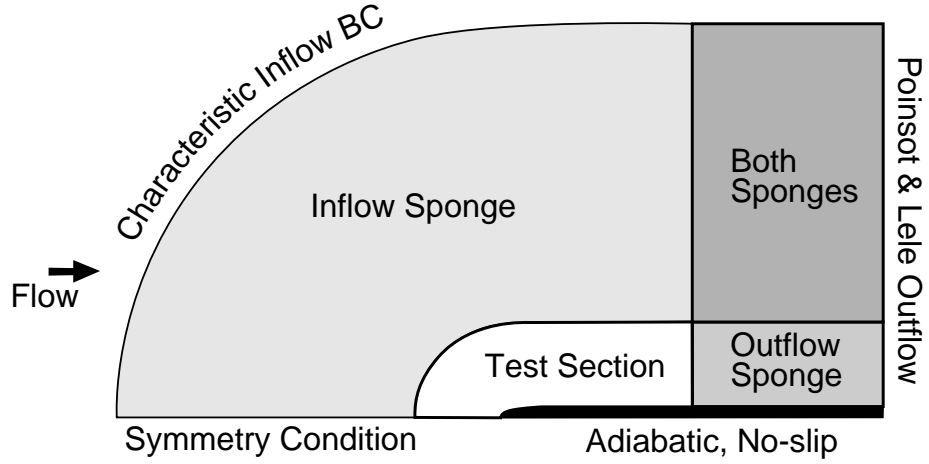
Figure 4.20: Schematic of the computational domain showing boundary conditions for unsteady receptivity calculations.
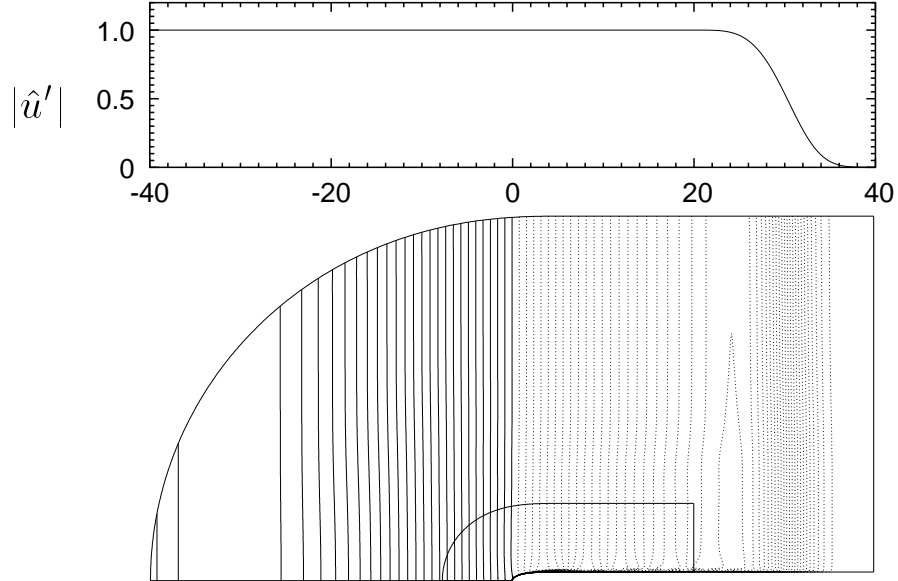
Figure 4.21: Contours of instantaneous streamwise velocity at $t = 65.45$. Contours from -0.05 to 0.05 with increment 0.002. Solid contours indicate positive velocity while dotted contours indicate negative velocity. Included above the contour plot is the Fourier amplitude of u' specified on the top boundary.
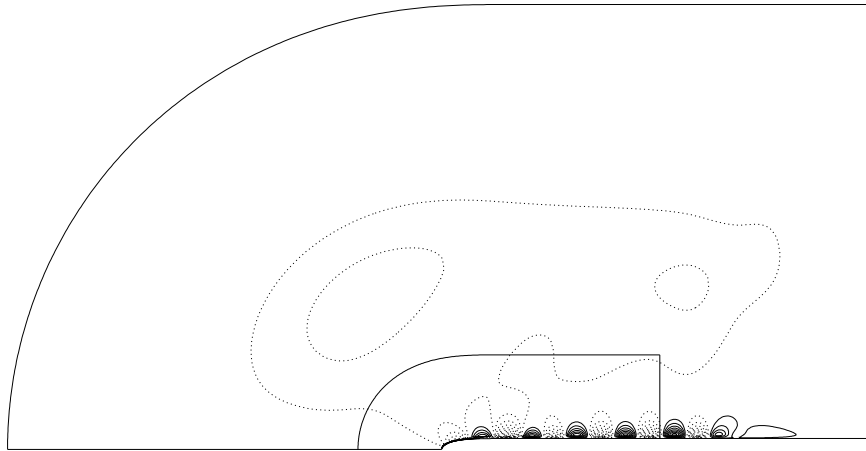
Figure 4.22: Contours of vertical velocity at $t = 65.45$. Contours from -0.002 to 0.002 with increment 0.0002. Solid lines indicate positive velocity while dotted lines indicate negative velocity.
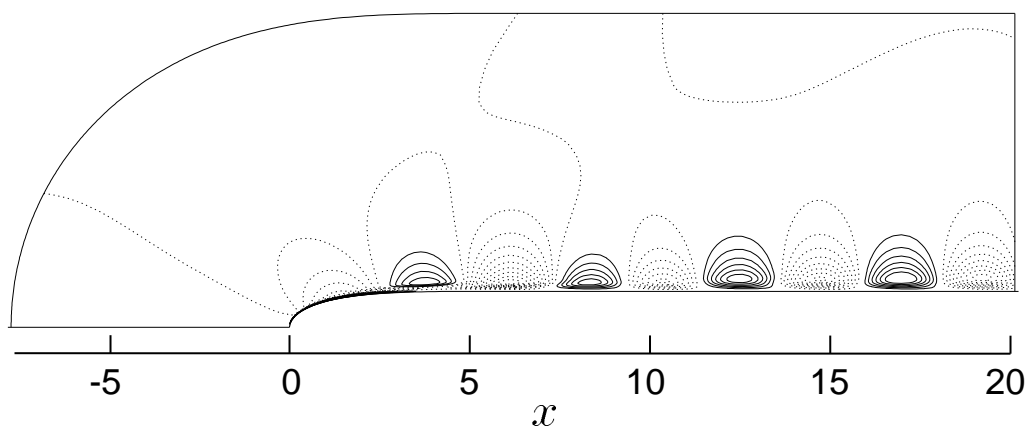
Figure 4.23: Closeup of the vertical disturbance velocity contours at $t = 65.45$. Contours from -0.002 to 0.002 with increment 0.0002. Solid lines indicate positive velocity while dotted lines indicate negative velocity.
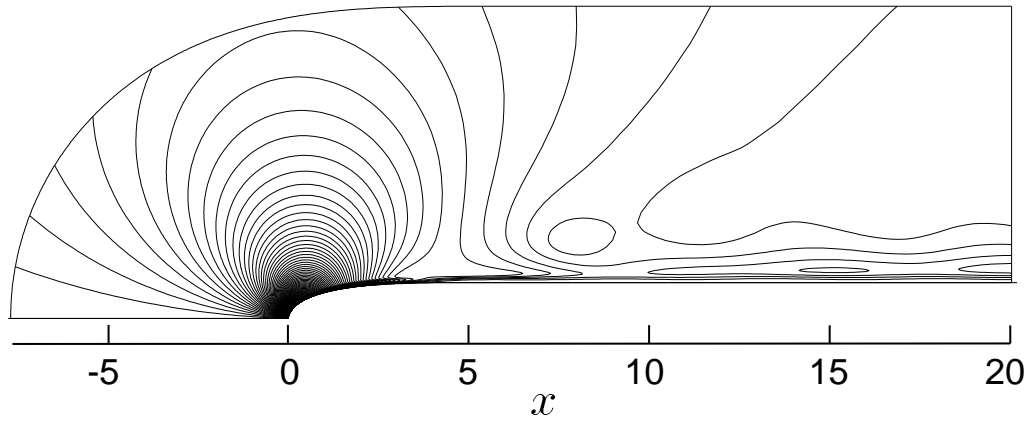
Figure 4.24: Contours of the Fourier amplitude of the vertical disturbance velocity. Transform taken over the sixth period of the forcing. Contours from 0 to 0.02 with increment 0.0002.
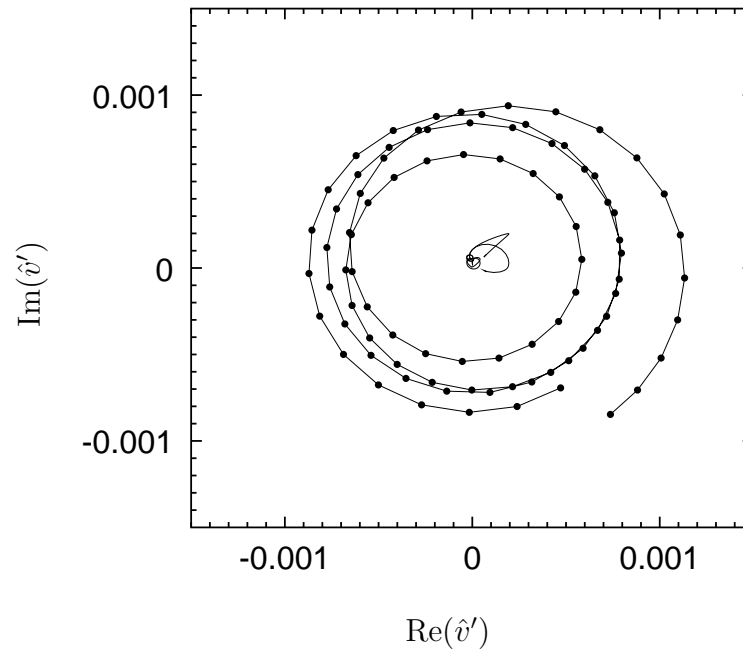
Figure 4.25: Trajectory of the Fourier coefficient, $\hat{v}'$, in the complex plane. —●— denotes the trajectory in x of the maximum in y of $|\hat{v}'|$. The —— line in the center of the figure denotes the acoustic component obtained after using the complex-plane decomposition.
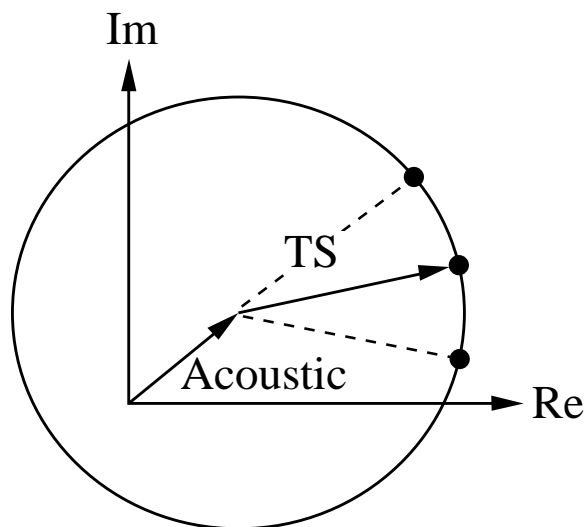
Figure 4.26: Schematic of the complex plane decomposition.
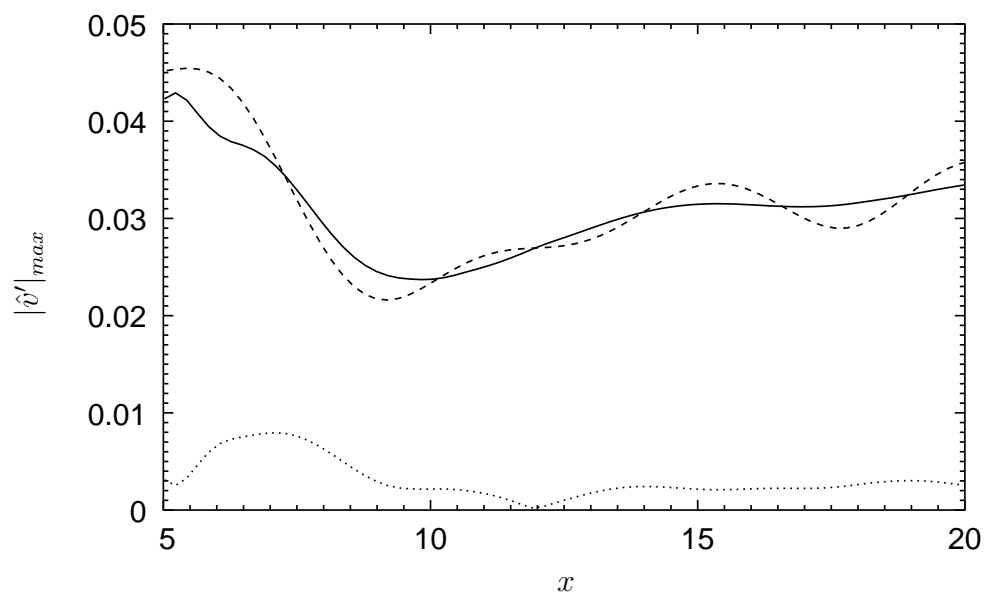
Figure 4.27: Decomposition of the local maximum of the amplitude of vertical component of disturbance velocity, —— is the TS wave amplitude, - - - - is the total amplitude, and ······· is the amplitude of the acoustic component.
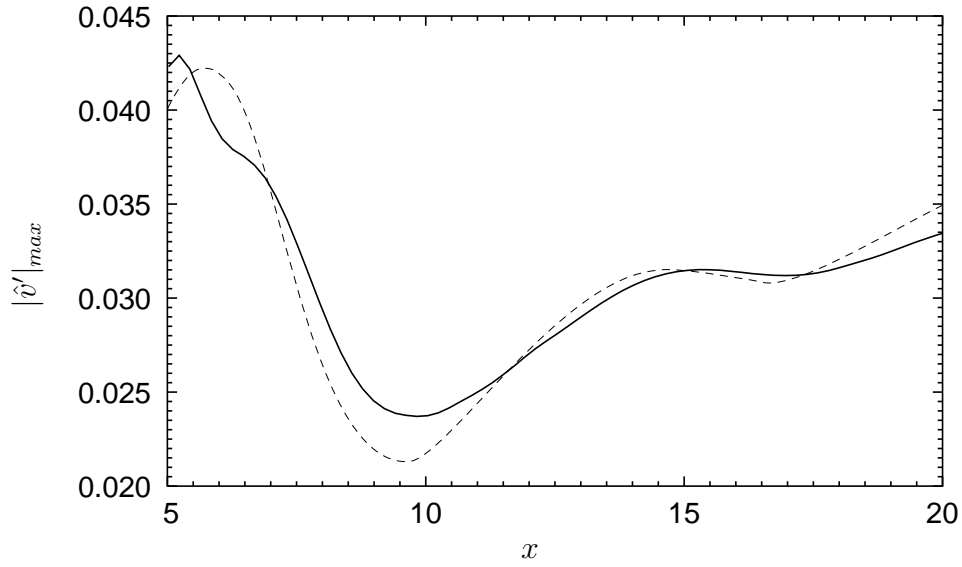
Figure 4.28: Comparison of the local maximum of the TS wave amplitude based on the vertical component of disturbance velocity along the plate. The ——— line denotes the $M = 0.1$ result and the - - - - line denotes the incompressible result [63].
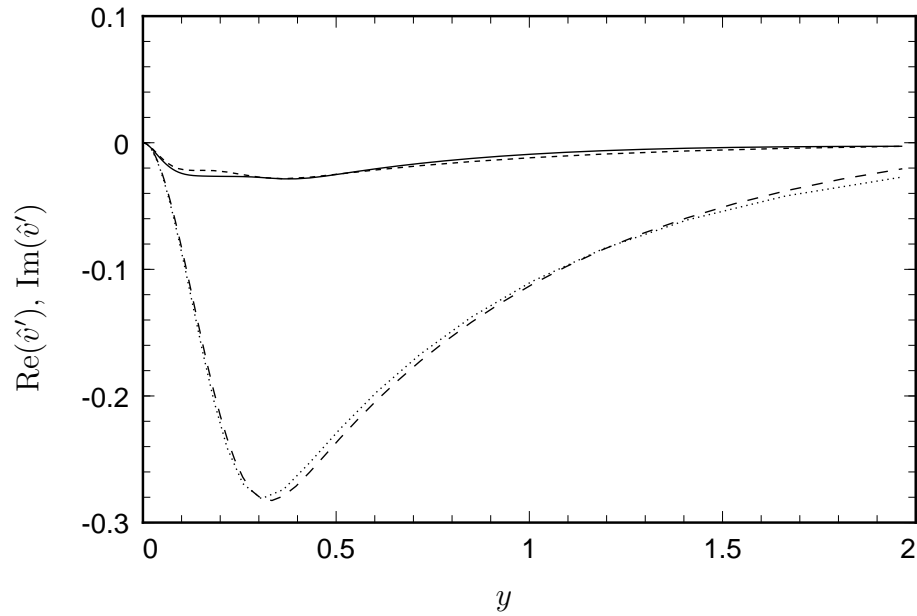
Figure 4.29: Extracted wave amplitude for the vertical component of disturbance velocity compared to LST at $x = 12$ for $M = 0.1$. ——— is the real component of the computed solution, $---$ is the imaginary component of the computed solution, - - - - is the real component of the LST solution, and $\cdots\cdots$ is the imaginary component of the LST solution.
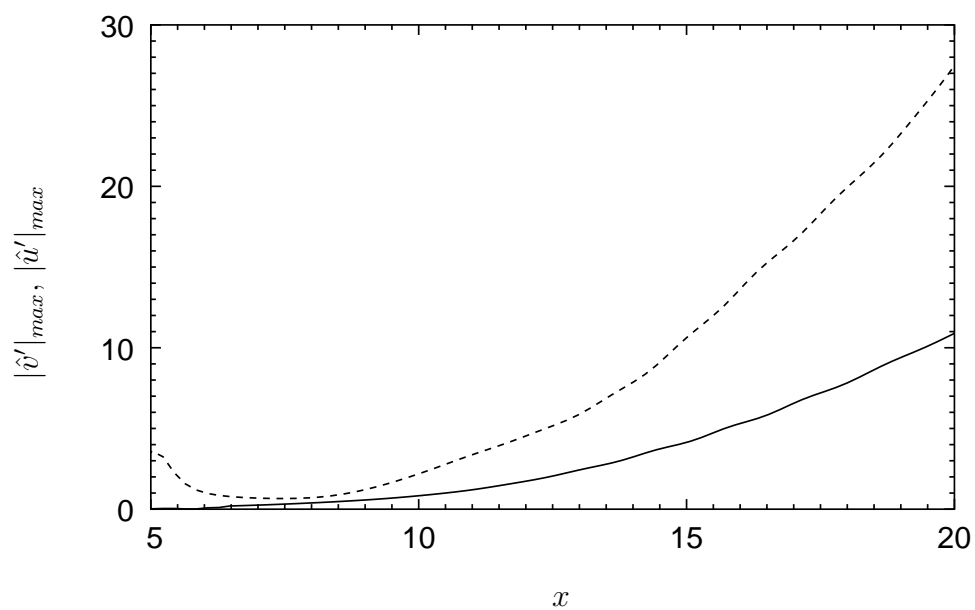
Figure 4.30: Comparison of the local maximum of the TS wave amplitude along the plate for $M = 0.8$. The ——— line denotes the $|\hat{v}'|_{max}$ result and the $----$ line denotes the $|\hat{u}'|_{max}$ result.
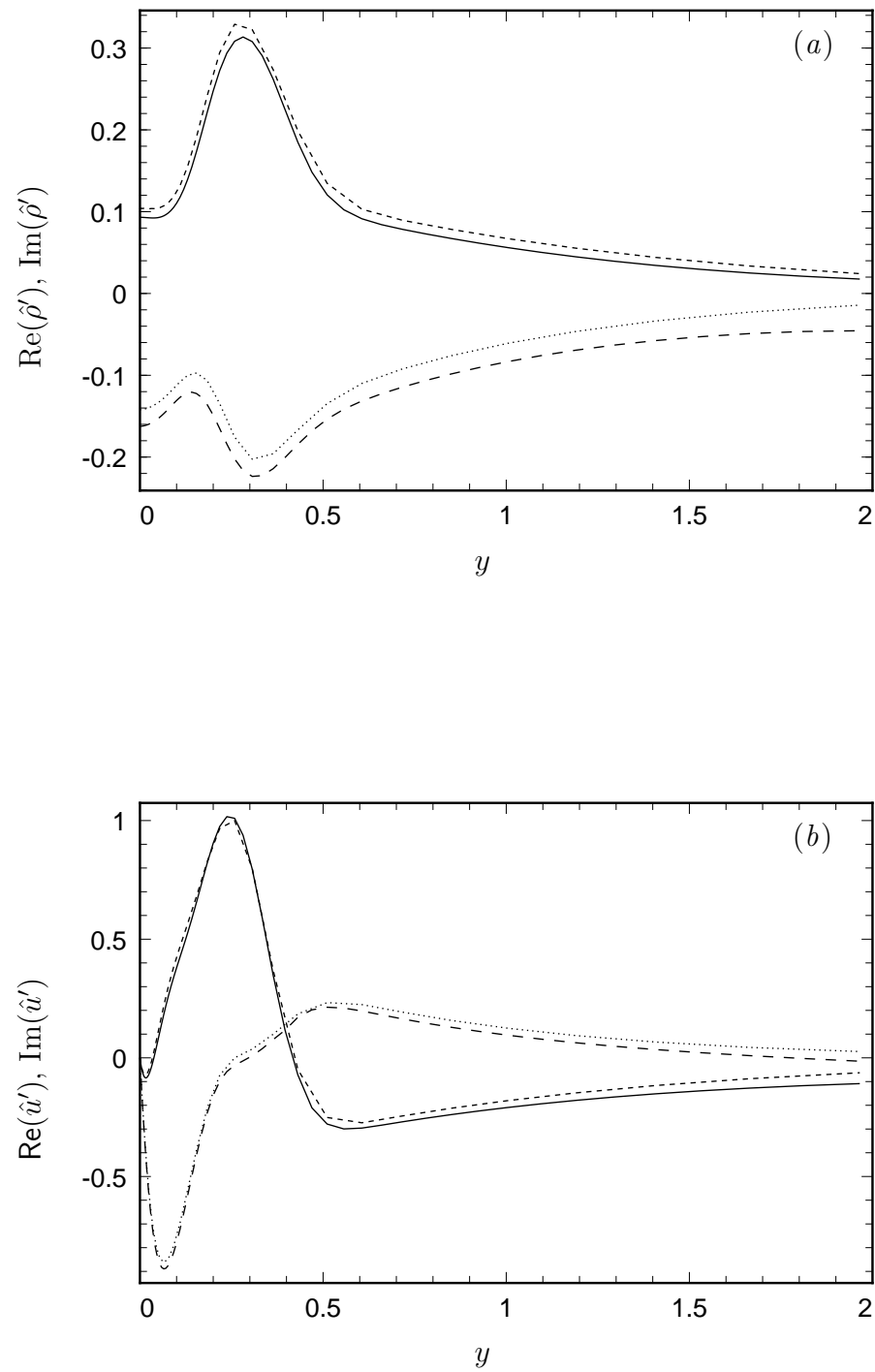
Figure 4.31: See following page for caption.
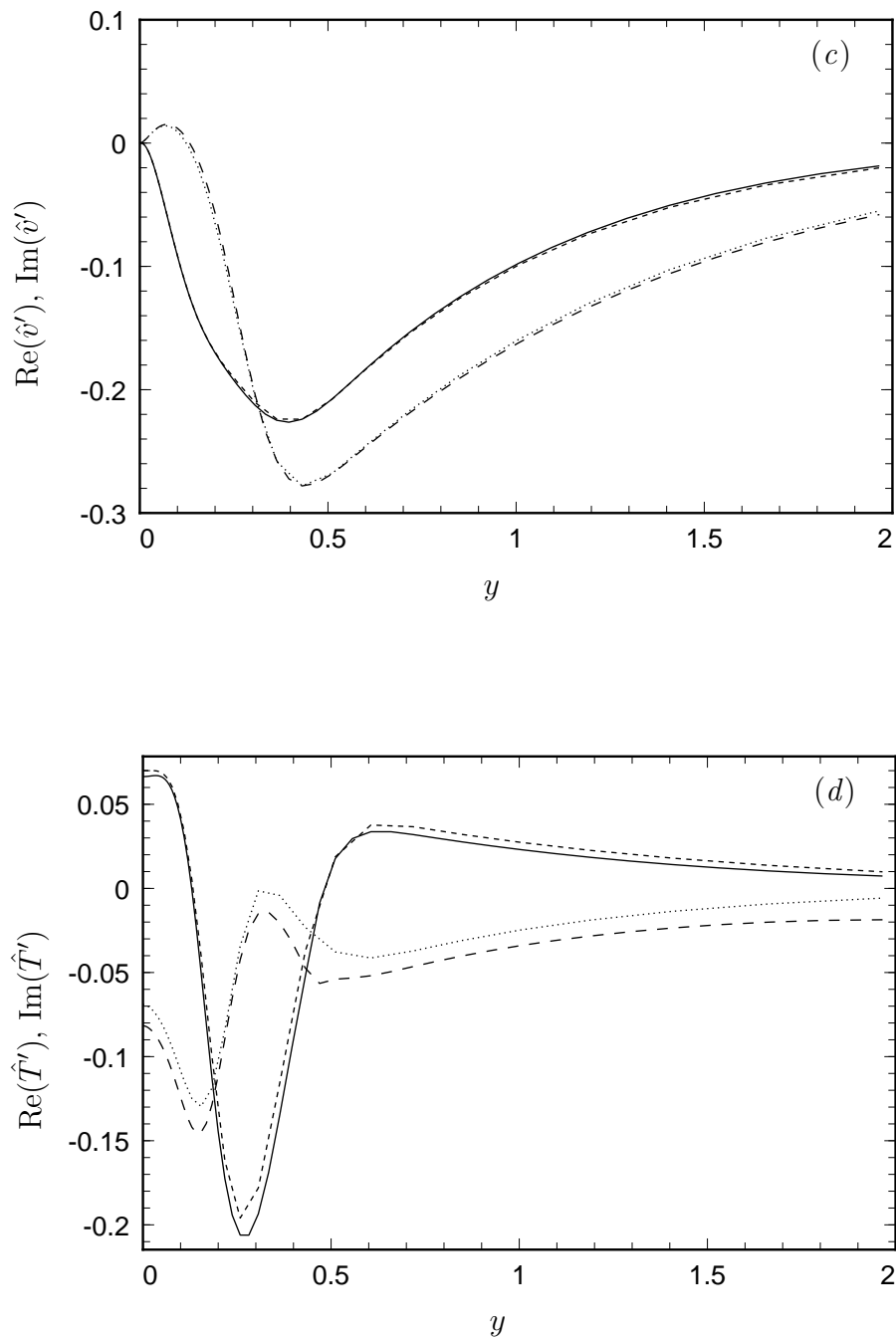
Figure 4.31: Extracted wave amplitudes compared to LST at $x = 12$ for $\mathsf{M} = 0.8$: —— is the real component of the computed solution, $---$ is the imaginary component of the computed solution, ---- is the real component of the LST solution, and ······· is the imaginary component of the LST solution. Frame (a) shows density, (b) streamwise velocity, (c) vertical velocity, and (d) temperature.

Chapter 5

Receptivity on a Swept Parabolic-Cylinder

This chapter focuses on the receptivity of the three-dimensional boundary-layer on a swept parabolic-cylinder subject to surface roughness. The discussion begins with a description of the geometry followed by the potential flow solution, mesh generation for Navier–Stokes calculations, and mean boundary-layer flow characteristics—both for two-dimensional and three-dimensional boundary layers. The linear stability characteristics are then documented for a three-dimensional boundary-layer which serves as a model of the flow near the leading-edge of a swept-wing in flight. Finally, forced receptivity calculations are presented for surface roughness located near the leading-edge including results from Linearized Navier–Stokes (LNS) calculations and comparisons to receptivity predictions based on Finite Reynolds Number Theory (FRNT).

5.1   Geometry: the Parabolic Cylinder

The leading-edge geometry is given by a swept parabolic-cylinder shown in figure 5.1. The reference length-scale is the leading-edge radius, $L^* = r_n^*$ and the reference velocity is the chordwise component of the freestream velocity, $u_r^* = u_\infty^*$ where the total magnitude of the freestream velocity is denoted by U_∞. Unless otherwise indicated, free-stream values are used for all other reference quantities.

In many previous experimental and computational investigations of receptivity, the geometry consists of a flat-plate with some type of smooth leading-edge attached in front. The parabolic cylinder has several advantages over these types of geometries: (1) the surface is continuous and infinitely differentiable, (2) a conformal map to a rectangular domain exists, (3) a theoretical investigation [48] of two-dimensional, acoustic receptivity is available, and (4) the pressure gradient is everywhere favorable and relatively insensitive to Mach number (see section 5.4).

For hybrid flat-plate/leading-edge geometries, there is often a lack of continuity

(*i.e.* smoothness) between the plate and leading-edge. This can lead to an additional source of receptivity [42] which may cloud the receptivity mechanisms actually under investigation. Attempts to rectify this situation have been made [62] including polynomial smoothing at the junction and the so-called Modified-Super-Ellipse which can be designed to mimic the pressure distribution of an elliptical leading-edge while retained higher continuity at the junction. The parabolic cylinder avoids these difficulties by providing a continuous geometry (with no arbitrary junction) that serves as a first-order approximation [108] to the leading-edge of an airfoil. Use of this geometry for receptivity investigations dates back to the work of Murdock [80] who performed two-dimensional, acoustic receptivity computations. More recently, Hammerton and Kerschen [48] have investigated the same problem using high Reynolds number asymptotic theory. Their results show that TS-wave response is reduced as the nose radius becomes more blunt. These results have been qualitatively validated by the recent numerical simulations of Corke & Haddad [26].

Here, we investigate receptivity of the three-dimensional boundary-layer on a swept parabolic-cylinder due to surface roughness and our discussion begins with the computation of potential flow solutions.

5.2   Potential Flow Solutions

Before computing the base-flow solutions, a potential flow solution is required both as an initial condition to the NS solver and to supply information for the farfield boundary conditions as described in section 3.9.2. The potential flow solution is determined using the method presented in section 3.8. The no-penetration condition is used on the wall and on the symmetry boundary upstream of the leading-edge. On the inflow and outflow boundaries, the velocity potential function is set to the value corresponding to the exact incompressible solution given by van Dyke [108]

$$\tilde{\eta} = \left(\frac{1}{2} - x + \frac{1}{2}\sqrt{(2x - 1)^2 + 4y^2} \right)^{1/2}, \tag{5.1}$$

$$\tilde{\xi} = \frac{y}{\sqrt{2}\tilde{\eta}}, \tag{5.2}$$

$$\phi = \tilde{\xi}^2 - \frac{1}{2}\tilde{\eta}^2 + \tilde{\eta}, \tag{5.3}$$

where $(\tilde{\xi}, \tilde{\eta})$ are the parabolic coordinates and ϕ is the velocity potential. Use of this solution on the inflow and outflow boundaries is obviously only an approximation for $\mathsf{M} \neq 0$. To overcome this, we typically solve for the potential flow solution on a mesh that is much larger than the mesh used in our receptivity calculations.

In constructing the mesh for the potential flow solution, an exponential mapping of the conformal coordinates to the uniform coordinates (ξ, η) is used to place the inflow/outflow boundaries far away from the leading-edge. Given the minimum mesh spacing, $\Delta\tilde{\xi}_{min}$ and the number of node points, N_ξ, the exponential mapping is given by

$$\tilde{\xi} = \frac{1}{c_1} \exp\left(c_1\xi + c_2\right) - \exp\left(c_2\right), \tag{5.4}$$

where $c_2 = \log\left(\Delta\tilde{\xi}_{min}(N_\xi - 1)\right)$ and

$$c_1 = (N_\xi - 1)\left[\log\left(s_\xi\Delta\tilde{\xi}_{min}(N_\xi - 1)\right) - c_2\right]. \tag{5.5}$$

The stretching factor, s_ξ, is determined from equation (5.4) by requiring that $\tilde{\xi} = \tilde{\xi}_{max}$ at $\xi = 1$. A detailed derivation of the metrics required by the potential flow solver is provided in Appendix B. With this mapping, we have constructed meshes for potential flow solutions that extend to $x = \pm 10^8$ which prevents the boundary approximation from corrupting the solution near the body.

To demonstrate this, figure 5.2 shows contours of the pressure coefficient, C_p, defined as

$$C_p \equiv \frac{p^* - p^*_\infty}{\frac{1}{2}\rho^*_\infty u^{*\,2}_\infty} = 2\left(p - \frac{1}{\gamma\mathsf{M}^2}\right), \tag{5.6}$$

for the potential flow over a parabolic cylinder at $\mathsf{M} = 0.8$, $\theta = 0°$ in the region $x \in [-500, 500]$. Solutions from three domains are shown: $x \in \pm 10^8$, $x \in \pm 10^7$, and $x \in \pm 10^6$. The results for the two larger domains are identical, to graphical accuracy, indicating that the solution is independent of the farfield boundary. In figure 5.3, the pressure gradient along the wall is plotted for the solutions from the two largest meshes and, again, the results are in excellent agreement. It is important to point out that the domain size required to obtain a converged solution is quite large. This is, of course, due to the approximate boundary-condition imposed on the farfield boundary. Compared to a closed body with a similar nose radius (*e.g.* an airfoil or circular cylinder) the parabolic cylinder requires a much larger domain to

obtain a mesh independent potential flow solution given a similar farfield boundary-condition. This is due to the fact that domain truncation at some finite location results in a disregard of the upstream influence associated with the ever expanding parabola downstream.

To convert the potential flow solutions to a mesh suitable for NS calculations we use fourth-order accurate B-splines [54] to interpolate the solutions in computational space. Then using the mapping functions, the interpolated solution is converted to physical space on the new grid. After interpolating to a typical NS mesh, we have re-plotted the pressure contours from the original and interpolated fields in figure 5.4 demonstrating excellent agreement.

5.3   Mesh Generation for Navier–Stokes Solutions

The conformal mapping of the parabolic-cylinder to the half-plane is also used in forming a mesh suitable for Navier–Stokes solutions. The conformal mapping can be written as

$$x = \tilde{\xi}^2 + \frac{1 - \tilde{\eta}^2}{2}\,, \tag{5.7}$$

$$y = \sqrt{2}\tilde{\xi}\tilde{\eta}\,, \tag{5.8}$$

where (x, y) are the nondimensional physical coordinates and $(\tilde{\xi}, \tilde{\eta})$ are the nondimensional conformal coordinates. In this expression, the body is given by the curve $\tilde{\eta} = 1$. The conformal coordinates are further transformed to computational coordinates (ξ, η) using hyperbolic mapping functions [70] designed to cluster points near the leading-edge and in the boundary layer. An example of a typical mesh that results from these transformations is shown in figure 5.5.

The same mapping function is used for both the ξ- and η directions. Considering the ξ-direction, the transformation takes the form

$$\tilde{\xi} = \frac{\tilde{\xi}_{max}}{\Xi} \left\{ c_m \xi + \log \left(\frac{\cosh[b(\xi - \xi_c)]}{\cosh[b(\xi + \xi_c)]} \right) \right\}, \tag{5.9}$$

where

$$\Xi = c_m + \log\left(\frac{\cosh[b(1-\xi_c)]}{\cosh[b(1+\xi_c)]}\right), \tag{5.10}$$

and

$$c_m = \frac{2b\tanh(b\xi_c) + \frac{(N_\xi-1)\Delta\tilde{\xi}_{min}}{\tilde{\xi}_{max}}\log\left(\frac{\cosh[b(1-\xi_c)]}{\cosh[b(1+\xi_c)]}\right)}{1 - \frac{(N_\xi-1)\Delta\tilde{\xi}_{min}}{\tilde{\xi}_{max}}}. \tag{5.11}$$

In these equations, $\Delta\tilde{\xi}_{min}$ is the minimum desired mesh spacing in $\tilde{\xi}$, N_ξ is the number of nodes in the ξ-direction, $\tilde{\xi}_{max}$ is the maximum $\tilde{\xi}$ node location, ξ_c is the location of the transition point in computational space, and b controls the rate of stretching at the transition. The derivatives of the mapping function which are required to compute the mesh metrics (see Appendix B) are given by

$$\frac{\partial\tilde{\xi}}{\partial\xi} = \frac{\tilde{\xi}_{max}}{\Xi}\left(c_m + b\tanh[b(\xi-\xi_c)] - b\tanh[b(\xi+\xi_c)]\right) \tag{5.12}$$

and

$$\frac{\partial^2\tilde{\xi}}{\partial\xi^2} = \frac{\tilde{\xi}_{max}}{\Xi}\left(-b^2\tanh^2[b(\xi-\xi_c)] + b^2\tanh^2[b(\xi+\xi_c)]\right) \tag{5.13}$$

Figure 5.6 shows the mapping function and its derivatives for parameters typical of those used in the wall-tangent direction (see the figure caption for the parameter values). The node spacing near the leading-edge is small to resolve the viscously dominated stagnation region. The first derivative of the mapping, which is proportional to the local mesh spacing, is approximately constant at the leading-edge, indicating that the mesh is nearly uniform there. The second derivative at the leading-edge is exactly zero which ensures that the mesh metrics are symmetric about the $(-x)$-axis. Downstream of the leading-edge, the mesh transitions smoothly to a second region of uniform spacing, but with a spacing roughly 32 times larger than that at the leading-edge. Note that a uniform spacing in the conformal coordinate, $\tilde{\xi}$, still grows like $\sqrt{s}$ in the chordwise direction so that the mesh spacing in the physical space continues to grow downstream in a manner consistent with the growing boundary layer. As indicated above, the same mapping function is also used in the wall-normal direction. For this application, the transition point, η_c, is set to 3/4 instead of 1/4. For an appropriate value of $\Delta\eta_{min}$, this has the effect of shifting approximately half of the mesh points into the boundary layer. Using the mapping functions presented above, the metrics required by the Navier–Stokes solver can be determined using the equations

in Appendix B.

Before closing this section, we point out that the mapping function given by equation (5.9) has several advantages over the algebraic, hyperbolic tangent [63], and exponential [35,36] mappings used previously. In particular, the first derivative of the mapping function approaches a constant at the boundaries implying that the mesh is nearly uniform there. This ensures that the mesh and its metrics are smooth at the boundaries and that the mesh has the proper symmetry characteristics for both solid walls and symmetry boundaries. With a region of nearly uniform mesh near the boundaries, second derivative metrics are also better scaled in these regions. In our applications, this is important at both the wall and in the stagnation region on the symmetry-line boundary where viscous effects are important.

5.4   Base Flow Results

Mean-flow results for the parabolic cylinder have been obtained for a variety of conditions. For unswept cases at low Mach numbers, the results are compared to the reference incompressible solutions of Davis [31]. After doing so, the influence of compressibility and wing sweep are examined.

5.4.1   Two-Dimensional Solutions

Our discussion begins with the mean-flow solution at $\mathsf{M} = 0.1$, $\mathsf{Re} = 1000$, and $\mathsf{Pr} = 0.7$ using constant fluid-properties with an adiabatic wall-temperature boundary-condition. A Mach number of 0.1 was selected to mimic the reference incompressible solutions, and the appropriateness of this choice will be assessed below. The mean flow is computed using the method discussed in section 3.6 with the boundary conditions of section 3.9.2. Figure 5.7 shows the convergence history for a steady-state calculation on a (384×127) mesh with a potential flow solution as the initial condition. Points where a rapid change in the residual occurs correspond to times during the computation when the timestep was altered to improve convergence. The norm of the residual at the end of the computation is approximately 1.4×10^{-7} and this is typical of the convergence achieved for all the mean-flow computations presented here. The computation required 4234 iterations using 1.15 hr of CPU time on a single Cray C-90 processor which corresponds to 20 μ-sec/node/iteration.

To assess accuracy, the mean solutions are compared to the incompressible results of Davis [31]. Davis solves for the mean flow over an infinitely long parabolic cylinder by mapping the infinite conformal space to a finite domain. In this manner, his method treats the farfield boundaries exactly. The equations are cast in stream-function/vorticity form and solutions are obtained with a iterative scheme based on a parabolic approximation. Davis' results are presented using a scaled wall vorticity defined as

$$\omega_D \equiv -\frac{(2x+1)}{\sqrt{2x\mathsf{Re}}}\omega_w \tag{5.14}$$

where ω_w is the wall vorticity. This quantity is plotted versus a viscously-scaled, streamwise, conformal-coordinate defined as

$$\xi_D \equiv \sqrt{2x\mathsf{Re}}\,. \tag{5.15}$$

By scaling the wall vorticity by the factor in equation (5.14), the first-order variation of the incompressible solution near the leading-edge and far downstream is accounted for. Thus ω_D approaches a constant both near the leading-edge and far downstream, making it a very sensitive measure of solution accuracy. Figure 5.8 shows a comparison of results using the current method, at $\mathsf{M} = 0.1$ and $\mathsf{Pr} = 0.7$, compared to Davis' incompressible solutions for $\mathsf{Re} = 100$ and 1000. The current results agree well with the incompressible solutions for both Reynolds numbers. This indicates that both the inflow and outflow boundary conditions are quite successful even for very thick viscous layers. That this isn't surprising is demonstrated by Davis' figure 3 which shows that for $\xi_d > 50$ the parabolized Navier–Stokes equations are a good approximation to the full Navier–Stokes equations (also see figure 5.11 discussed below).

A close examination of the vorticity function near the leading-edge shows that the current results slightly under-predict the incompressible results. To determine if this difference is due to compressibility, mean flow solutions have been obtained over a range of subsonic Mach numbers at $\mathsf{Re} = 1000$, $\mathsf{Pr} = 0.7$, again using constant fluid-properties and an adiabatic wall temperature condition. The use of constant fluid properties at high subsonic Mach numbers is obviously an approximation, but doing so is not expected to have a qualitative impact on the present results. The scaled wall vorticity from these solutions is shown in figure 5.9 which gives results

for Mach numbers of 0.1, 0.5 and 0.8 along with Davis' incompressible solution. As the Mach number is decreased, ω_D near the leading-edge increases, approaching the incompressible solution. In figure 5.10, ω_D at the attachment-line is plotted as a function of Mach number squared. The relationship is linear and extrapolating to zero Mach number gives a value 1.146, which is in very good agreement with Davis' value of 1.15.

Returning to figure 5.9, we see that ω_D also approaches the incompressible solution over the entire domain as Mach number is lowered. But, near the end of the computational domain, there is a slight difference between the current solution at $M = 0.1$ and Davis' incompressible solution. However, the symbols plotted corresponding to Davis' solution were extracted from a rather small and crowded graph in [31] so that there could be some error in the deduced incompressible values. This is particularly the case for high ξ_D where many solutions overlap on Davis' plot. However, Davis demonstrated that beyond $\xi_D \approx 50$ a fully parabolic approximation to the governing equations agrees very well with the full Navier–Stokes solutions. In figure 5.11 the incompressible parabolic solution is compared to our $\mathsf{M} = 0.1$ solution. The parabolic result was obtained using a method identical to that presented by Davis. Our solution compares very well with the parabolic solution downstream of $\xi_D = 50$, but, as expected, the parabolic solution near the leading-edge is poor [31].

As the final result for two-dimensional boundary layers, figure 5.12 shows the evolution of the wall-tangent pressure gradient, evaluated at the wall, for a range of Mach numbers. As Mach number is increased, the favorable pressure gradient, which exists over the entire surface, increases slightly over most of the chordwise extent. This is in contrast to the results presented in section 4.4.2 for the super-ellipse which showed a dramatic increase in the magnitude and length of the region of adverse pressure gradient, associated with the leading-edge/plate junction, as Mach number was increased. As alluded to earlier, the more benign influence of Mach number on the pressure gradient (and therefore stability characteristics) for the parabolic cylinder makes it a more useful geometry for the study of receptivity at high subsonic Mach numbers.

To summarize the two-dimensional results, it is concluded that the current mean-flow solutions converge to the reference incompressible solution of Davis as Mach number is reduced. Furthermore, at $\mathsf{M} = 0.1$ the current solution is in good agreement

with the incompressible solution over the full length of the parabolic-cylinder, and, as Mach number is increased, the vorticity at the leading-edge varies like $\omega_D(0) = 1.146 - 0.248\mathsf{M}^2$.

5.4.2 Three-Dimensional Solutions

To create a three-dimensional boundary layer, the parabolic-cylinder is swept with respect to the incoming uniform flow. The conditions are selected to generate a flow which, in the vicinity of the leading-edge, roughly models that of a subsonic transport-aircraft in cruise. For this purpose, we use a sweep-angle of $\theta = 35°$ with $\mathsf{M}_\infty = 0.977$ and $\mathsf{Pr} = 1$. Using the chordwise component of the freestream velocity as the reference velocity gives a Mach number of $\mathsf{M} = 0.8$ and Reynolds number of $\mathsf{Re} = 1 \times 10^5$, where the nose radius is the reference length-scale. Assuming that the nose radius of a typical airfoil section is approximately 1% chord [1], these conditions correspond to a chord Reynolds number of approximately 1×10^7, which is in the realm of flight Reynolds numbers.

Unlike the two-dimensional results presented above, an isothermal wall-temperature boundary-condition of the form $T_w = T_0$ is now used, where

$$T_0 = 1 + \frac{\gamma - 1}{2}\mathsf{M}^2(1 + \tan^2(\theta)) \tag{5.16}$$

is the freestream stagnation temperature. For $\mathsf{Pr} = 1$, this corresponds to the adiabatic wall temperature for a flat-plate boundary layer. Since the boundary layer flow over a parabolic cylinder approaches a flat-plat boundary layer downstream, the wall temperature boundary condition asymptotically approaches an adiabatic condition downstream. The use of the isothermal boundary-condition greatly simplifies the wall-roughness boundary condition (see below), while using $\mathsf{Pr} = 1$ allows more direct comparisons to available similarity solutions (see Appendix C). As before, the mean-flow is computed using constant fluid properties since variations in fluid properties are not expected to cause qualitative differences in receptivity results.

To extract boundary layer profiles and non-dimensional parameters characteristic of its state from the Navier–Stokes solution, the original solution on the conformal mesh, described in section 5.3, is interpolated onto a body-fitted coordinate system. Recall that the body-fitted coordinate system is denoted by (s, n, z) where s is the

arc-length in the chordwise direction, n is the distance normal to the body, and z is the spanwise direction. The body-fitted mesh is constructed by forming level-sets off the parabolic body. To cluster points near the leading-edge and in the viscous layer, the mesh mapping presented in equation (5.9) is used in both the body normal and tangent directions. Since the body-fitted mesh is used only for analysis, the top boundary can be placed much closer to the wall to reduce the number of points in the far-field. To interpolate the solution from the conformal to body-fitted mesh, fourth-order accurate B-spline interpolation is used in computational space. Each point, in the body-fitted mesh, is converted using the mapping of section 5.3 to the uniform computational space where the IMSL B-spline routines [54] are used to determine the interpolated value for each of the primitive variables. This interpolation procedure, which is similar to that used to interpolate the potential flow solution, has been found to yield excellent results and is also used to convert solutions to different grids when performing mesh resolution studies and when computing local quantities such as $\delta_{0.999}$ and local profile maxima.

Given the meanflow solution on a body-fitted mesh, the first step in analyzing the boundary layer is to determine the edge conditions. Conceptually, the edge conditions are given by the local inviscid-flow outside of the boundary layer. Figure 5.13 is a schematic of a three-dimensional boundary layer near a swept leading-edge which aids in the definition of the various boundary layer parameters. In this study, the boundary-layer edge is defined as the point where the spanwise, w, component of velocity reaches 99.9% of its freestream value. Since the wing has infinite span, the w-velocity profile increases monotonically from zero at the wall to its freestream value, $\tan(\theta)$. This is in contrast to the more traditionally used v_s velocity. Recall that v_s is the velocity locally tangent to the body at a given station while v_n is the body-normal velocity. These velocity components are related to the global Cartesian velocity components by

$$v_s = n_2 u - n_1 v \,, \tag{5.17}$$

$$v_n = n_1 u + n_2 v \,, \tag{5.18}$$

where the outward unit-normal to the body is $\mathbf{n} = \{n_1, n_2, 0\}^{\mathrm{T}}$. Since the flow is accelerated in the chordwise direction, the v_s velocity over-accelerates near the leading-edge making an unambiguous definition of the boundary-layer edge difficult.

Although the particular choice of edge-conditions does have an influence on the re-
ported boundary-layer parameters, the effects are minor and the current approach
yields adequate results. Throughout the following discussion, the reader may wish to
consult table 5.1 which itemizes the boundary-layer edge-conditions and parameters
for selected stations near the leading-edge.

The magnitude of the edge-velocity, projected to the plane tangent to the body,
is given by $U_e = \sqrt{v_{s_e}^2 + w_e^2}$. In practice, U_e is referred to as the total edge-velocity
since v_n is negligible except in the immediate vicinity of the attachment-line. The
edge-velocity makes an angle θ_e with respect to the x-axis and this angle is called the
local sweep-angle. When presenting boundary-layer profiles, it is useful to convert the
velocity to a coordinate system that is locally aligned with the edge-velocity. Velocity
components in this "streamwise" coordinate system are denoted by (u_s, v_n, w_s), where
u_s is the local, streamwise velocity; v_n is the body-normal velocity; and w_s is the
crossflow velocity. These components are related to the velocities in the boundary-
fitted coordinate system by

$$u_s = \cos(\theta_e)v_s + \sin(\theta_e)w\,, \tag{5.19}$$

$$w_s = -\sin(\theta_e)v_s + \cos(\theta_e)w\,. \tag{5.20}$$

With these definitions we can begin to examine the characteristics of this three-
dimensional boundary-layer. Figures 5.14–5.16 show streamwise, u_s, and crossflow,
w_s, velocity profiles at three stations near the leading-edge where the profiles have
been nondimensionalized by U_e. The streamwise profile is "Blasius-like" while the
crossflow profile is inflectional with a maximum, crossflow velocity of $\approx 11\%$ of the
local edge velocity at $s = 0.802$. The inflectional crossflow profile gives rise to the
inviscid, crossflow instability.

For this flow, the standard attachment-line length-scale $\delta_l^* \equiv \sqrt{\nu_e^*/(\partial U_e^*/\partial s^*)}$ is
$0.00353\,r_n^*$ and this yields an attachment-line Reynolds number $\bar{R} \equiv \delta_l^* w_\infty^*/\nu_\infty^*$ of 247.
This value of $\bar{R}$ is less than the critical value of $\bar{R}_{crit} = 583$, which ensures that the
flow is linearly stable along the attachment-line [100].

Figure 5.17 shows the chordwise evolution of the maximum crossflow component
of velocity normalized relative the local edge-velocity. The crossflow component is
everywhere negative and reaches its greatest magnitude of -0.107 at $s = 0.802$. At

the point of maximum crossflow, the crossflow Reynolds number

$$\chi \equiv \delta^*_{0.999} w^*_{s\,max}/\nu^* \tag{5.21}$$

is 161. The results of Poll [84] for a swept circular-cylinder indicate that the critical crossflow Reynolds number is 125 and our value of 161 suggests that significant crossflow instability will be present. Table 5.1 shows the crossflow Reynolds number reaches a maximum of 256 at $s \approx 20.3$.

The variation of the local sweep-angle, θ_e, of the edge-velocity is shown in figure 5.18. At the point of maximum crossflow, the local sweep-angle is 54.5° relative to the chord compared to a value of 90° at the attachment-line. Downstream, the local sweep-angle asymptotes to the global sweep-angle $\theta = 35°$ as the chordwise pressure gradient decays. The pressure gradient along the parabola is documented using the Hartree pressure-gradient parameter which is defined as

$$\beta_h = \frac{2m}{m+1} \tag{5.22}$$

where

$$m = \frac{s}{u_s} \frac{\partial u_s}{\partial s} . \tag{5.23}$$

Figure 5.19 shows the evolution of β_h along the length of the plate. At the attachment line, $\beta_h = 1$ corresponding to a stagnation region while downstream of the leading edge, β_h decays monotonically to zero. At the point of maximum crossflow, $\beta_h = 0.765$ and by 30 nose radii downstream β_h is reduced to 0.042 indicating that the flow is approaching a zero-pressure gradient boundary layer.

Figure 5.20 shows the displacement and momentum thickness evolution for the local streamwise velocity profile. The displacement thickness is defined by

$$\delta_1 \equiv \int_0^{\delta_{0.999}} \left(1 - \frac{\rho u_s}{\rho_e U_e}\right) dn \tag{5.24}$$

while the momentum thickness is given by

$$\delta_2 \equiv \int_0^{\delta_{0.999}} \frac{\rho u_s}{\rho_e U_e} \left(1 - \frac{u_s}{U_e}\right) dn . \tag{5.25}$$

For incompressible flow at the attachment-line, Spalart gives a value of $\delta_2/\delta_l = 0.404$

[100]. From the current data, we get a value of 0.337 which suggests that this quantity decreases with Mach number. To verify this, a separate calculation at $\mathsf{M} = 0.73$, with all other conditions the same, was performed which gives a value of $\delta_2/\delta_l = 0.349$. Linearly extrapolating these results against the *freestream* Mach number squared gives a value of 0.407 at $\mathsf{M}_\infty = 0$ which is in good agreement with the incompressible value. The evolution of the boundary-layer shape-factor, defined as $H = \delta_2/\delta_1$, is shown in figure 5.21. At the attachment-line $H = 0.368$ and quickly increases to a maximum of $H = 0.377$ at $s = 0.63$ before beginning a slow decay, eventually asymptoting to $H = 0.317$.

5.5 Linear Stability Analysis

Before performing receptivity calculations, it is necessary to determine the stability characteristics of the mean flow. This is accomplished by using the spatial, Linear Stability Theory (LST) solver described in Appendix D in conjunction with several LNS stability calculations. Recent investigations [76, 72] have shown that the growth of stationary crossflow vortices is significantly influenced by nonparallel and curvature effects. The boundary-layer over a parabolic cylinder is an ideal flow for studying these effects since both curvature and nonparallelism occur naturally and are attenuated downstream. In this section, we examine the influence of curvature and nonparallel flow on the stability characteristics of stationary crossflow vortices, since these effects are also likely to impact the receptivity characteristics.

Our discussion begins by considering the boundary-layer profiles at the location of maximum crossflow velocity, $s = 0.802$. These profiles are shown in figure 5.22 and are extracted using a body-fitted mesh as described in section 5.4. Since we are interested in comparing the LST results with LNS calculations, we break with the traditional nondimensionalization of LST and instead retain the global nondimensionalization used in the LNS solutions. In particular, the reference velocity is the chordwise component of the freestream velocity and the reference length is the leading-edge nose radius. Use of the global nondimensionalization makes comparison of results at different stations more convenient. However, our results can be easily converted to the local nondimensionalization based on the displacement thickness and edge-velocity using the data supplied in Table 5.1.

Growth-rate predictions from quasi-parallel LST at $s = 0.802$ are given in figure 5.23 for zero-frequency crossflow vortices. The range of amplified spanwise wavenumbers is from roughly 32 to 160 and the maximum predicted growth-rate at this station occurs for $\beta = 90$. The predicted chordwise wavenumber for stationary modes is shown in figure 5.24 where it is seen that α varies almost linearly with β in the unstable range. In figure 5.25, the wave-angle, ψ, with respect to the body-fixed coordinate system is shown as a function of the spanwise wavenumber, demonstrating that across the unstable range the wave-angle is nearly fixed at 140°. This means that the axis of the crossflow vortices is at approximately 50° and remains within 6° of the local streamwise direction.

Considering the spanwise wavenumber, $\beta = 35$, figure 5.26 shows the variation in the LST growth-rate and wavenumber as a function of the distance along the plate. The growth-rate of this crossflow mode quickly increases from the first neutral-point at $s = 0.65$ reaching a maximum at $s = 2.05$ before slowly decaying to zero with the second neutral-point located at $s = 27.7$. This extended region (about 27 nose radii) of crossflow amplification is due to the slowly decaying favorable pressure gradient (see figure 5.19) of the meanflow. We note that typical airfoil sections have a pressure minimum on the upper surface followed by an adverse pressure gradient that destabilizes TS waves. The relatively simpler situation here, combined with the extended region of crossflow amplification, makes the parabolic-cylinder an ideal geometry for the study of crossflow vortex receptivity. For a discussion of combined crossflow/TS instability modes for a flow with both favorable and adverse pressure gradients, the reader is referred to the recent computations by Spalart *et al.* [101].

To verify the accuracy of the quasi-parallel LST prediction, several LNS calculations have been performed in order to determine the actual stability characteristics including nonparallel and curvature effects. These stability calculations are performed using the techniques introduced in section 4.2. To decrease the cost of the calculations, conformal grids are constructed that truncate the extensive inviscid region used in the meanflow calculations. The steady-state meanflow is then interpolated using fourth-order-accurate B-splines to the new mesh. Consistent with the findings of section 4.2, the chordwise mesh spacing is chosen to ensure at least 20 node points per wavelength based on the chordwise wavenumber predicted by LST. The LST eigenfunction is forced on the inflow boundary using the same technique discussed in

section 4.2.2. This eigenfunction is only an approximation, since curvature and non-parallelism are not accounted for, and we therefore expect a small transient before a dominant mode is established. The nonparallel meanflow introduces another complication since the growth-rate is now a function of both the quantity measured and the wall normal location, n. In general, the growth-rate for any linear disturbance quantity, $\hat{f}$, is given by

$$\sigma = \mathrm{Re}\left[\frac{d\ln(\hat{f}(s,n))}{ds}\right] \qquad (5.26)$$

while the wavenumber is determined from

$$\alpha = \mathrm{Im}\left[\frac{d\ln(\hat{f}(s,n))}{ds}\right] . \qquad (5.27)$$

To remove the n dependence from the growth-rate, experimental investigations often define the growth-rate based on the (first) maximum, in n, of the chordwise velocity, v_s. Similar quantities can be computed based on other disturbance variables. Another way to remove the variation in the wall-normal location is to base the growth-rate on the integrated disturbance kinetic energy, defined as

$$E_k' \equiv \int_0^{n_{max}} \frac{1}{2}\left(|\hat{u}|^2 + |\hat{v}|^2 + |\hat{w}|^2\right) dn \qquad (5.28)$$

where n_{max} is sufficiently large so that additional contributions to the integral are negligible. Here, n_{max} is taken to be the the maximum wall-normal location in the computational domain. The growth-rate, based on E_k', is obtained from

$$\sigma = \frac{1}{2}\frac{d\ln(E_k')}{ds} . \qquad (5.29)$$

The first LNS calculation is performed for a domain starting at $s = 5.6$ and extending to $s = 25.8$. This domain covers the later portion of the unstable region, and, since it is located far from the leading-edge, offers the best chance that curvature and nonparallel effects will be small. Figure 5.27 shows the growth-rate extracted from the calculation, based on E_k', compared to the quasi-parallel LST prediction. As expected, there is a slight transient in the LNS solution since the function forced on the inflow is only an approximation to the actual eigenfunction. After approximately two nose radii downstream, the transient is no longer noticeable and a single instability

wave dominates the flow. Interestingly, the LNS and LST growth-rates cross-over at $s = 13$ and the errors in the LST prediction increase upstream and downstream of this point. This implies that there may be competing errors in the quasi-parallel LST prediction.

To identify the source of this discrepancy, we have incorporated both surface curvature and nonparallel effects in the LST predictions. Surface curvature is accounted for by solving the stability equations in a general orthogonal coordinate system that is coincident with a body-fitted mesh. Nonparallel effects are included through a perturbation approach where the meanflow, chordwise wavenumber, and eigenfunction are allowed to vary slowly in the chordwise direction. The detailed implementation of curvature and nonparallel effects is discussed in Appendix D.

Figure 5.28 compares the growth-rate for $\beta = 35$ from the LNS calculation with two predictions from LST. These two LST predictions are denoted by QPNC, which stands for Quasi-Parallel with No Curvature, and QPWC, which is short for Quasi-Parallel With Curvature. The growth-rate for the QPWC case shows that curvature is stabilizing which is consistent with recent analysis of the flow over a circular cylinder [76]. However the stabilization due to curvature leads to a greater discrepancy between LST and LNS, as compared to QPNC. As expected, the effect of curvature increases upstream as the surface curvature increases. Figure 5.29 shows the normalized curvature $K\delta_1$, where K is the surface curvature, which demonstrates that the curvature decays as $1/s$ downstream of $s = 1$. Upstream of $s = 1$, the normalized curvature plateaus at a value of $K\delta_1 = 3.23 \times 10^{-3}$. This behavior is in contrast to results using a circular cylinder where the normalized curvature increases downstream of the leading-edge since the radius of curvature for that geometry remains constant. However, based on the results from QPNC, even a very small normalized curvature on the order of 10^{-4} still has a significant effect on the predicted growth-rates. This result is qualitatively consistent with recent PSE analysis [50] of the crossflow experiments performed by Saric's group [90] which indicate that curvature continues to influence the growth-rate of stationary CF vortices over the entire upper surface of an airfoil up to transition.

The influence of nonparallel effects are shown in figure 5.30 which includes the nonparallel correction with curvature (NPWC) in addition to the previous results. It is obvious from the figure that including both nonparallel and curvature effects leads

to growth-rate predictions that are in excellent agreement with the LNS solution. This level of agreement gives further confidence that both the LNS and LST implementations are free of errors. In general, nonparallelism is seen to destabilize the flow, returning the growth-rate to a level similar to quasi-parallel theory over most of the plate. Near the leading-edge, the flow becomes highly nonparallel causing a qualitative change in the shape of the NPWC growth-rate distribution when compared to the quasi-parallel results. This difference is in the form of a local maxima in the NPWC growth-rate which occurs at $s = 0.7$.

Based on the analysis in Appendix D, there are three contributions to the nonparallel growth-rate: the quasi-parallel growth-rate with curvature (QPWC), the eigenfunction distortion term, and the nonparallel meanflow term. These contributions are shown in figure 5.31 both in an expanded view near the leading-edge and over the entire unstable region. Downstream of $13r_n^*$, the nonparallel meanflow term becomes negligible in comparison to the other contributions indicating that the meanflow is, for all practical purposes, parallel. However, the eigenfunction distortion term remains significant beyond the second neutral-point resulting in a downstream shift of the neutral-point (relative to QPWC) to $s = 30.54$. As shown in Appendix D, the eigenfunction distortion term can be computed directly from the quasi-parallel eigenfunctions so that it can be accounted for without resorting to the full perturbation approach. However, the small influence of the nonparallel meanflow term at the second neutral-point is not a general result, and conditions (either β or Re) could be selected such that this is not the case. The second frame of figure 5.31 shows the contributions to the nonparallel growth-rate near the leading-edge. Upstream of $s \approx 5$, the eigenfunction distortion term begins to increase slowly to a maximum at $s = 1$; decaying further upstream. Upstream of $s \approx 1$, (which, coincidently, is the approximate location of the first neutral-point for QPWC) the nonparallel meanflow term undergoes a sudden increase, quickly dominating the other terms. The increase in both nonparallel terms causes the local maxima in the total NPWC growth-rate and results in an upstream shift (relative to QP theory) in the first neutral-point to $s = 0.471$. Since the nonparallel correction is based on a perturbation expansion, the results near the leading-edge may be inaccurate. This is addressed below by comparison to LNS calculations.

But first, the effect of curvature and nonparallelism on the chordwise wavenumber

is shown in figure 5.32 (note that a log scale is used in s to more clearly show the leading-edge behavior). The NPWC wavenumber is computed based on the maximum in the wall-normal direction of the $|\hat{v}_s|$ velocity. As seen in the figure, both QPNC and QPWC give almost identical results, indicating that curvature has little influence on the wavenumber. However, NPWC shows that nonparallel effects tend to decrease the wavenumber magnitude—when based on $|\hat{v}_s|_{max}$. This effect is most pronounced near the leading-edge, but it also occurs to a lesser degree over the entire unstable range. This is demonstrated in figure 5.33 which shows a comparison of the wavenumber extracted from LNS (also based on $|\hat{v}_s|_{max}$) with the QPWC and NPWC predictions. After a brief transient in the LNS solution, the NPWC wavenumber is in good agreement with LNS while QPWC slightly over-predicts the wavenumber magnitude.

As indicated above, nonparallel effects in the LST are accounted for using a perturbation expansion so that the results may become inaccurate near the leading-edge where the meanflow is highly nonparallel. To evaluate this, a second LNS calculation is performed on a domain from $s = 0.2$ to $s = 5.25$ in which the QPWC eigenfunction is forced on the inflow. The measured growth-rate from this calculation is shown in figure 5.34 compared to the NPWC prediction where both are based on E'_k. Clearly, the NPWC results do not agree with the LNS solution near the leading-edge indicating that the perturbation approach is inaccurate under these conditions. However, by $s = 3$ the two approaches are in excellent agreement. The failure of the nonparallel perturbation approach leads to both qualitative and quantitative errors in the predicted growth-rate near the leading-edge. The peak growth-rate is grossly under-predicted and there is the appearance of a spurious local maxima. In addition, the first neutral point is also in error with a predicted value of 0.471 compared to the actual value of 0.395.

The failure of the perturbation approach, at first, appears at odds with recent stability analysis which have shown the nonparallel perturbation results to be in good agreement with PSE for a swept circular cylinder [76]. Likewise, PSE has been demonstrated to compare well with LNS calculations [74] for the swept Hiemenz flow. Compared to the current results, the stability characteristics in these studies are, by necessity, limited to the immediate vicinity of the attachment-line. For this reason, the spanwise wavenumbers used were large compared to the present value of $\beta = 35$

in order to limit the chordwise extent of the unstable region. In particular, Masad & Malik [76], in their investigation of the stability characteristics of the boundary layer on a swept circular-cylinder under conditions similar to those studied here ($\mathsf{Re} = 1.675 \times 10^5$, $\Lambda = 60°$) used $\beta^* r_n^* = 150$ compared to the current value of 35. For large β, the downstream extent of the region of instability is reduced and nonparallel effects are weakened since the chordwise instability wavelength is reduced. To demonstrate this effect, Figure 5.35 compares the predicted growth-rate from NPWC and LNS for $\beta = 100$ computed on a domain from $s = 0.32$ to $s = 3.18$. The agreement of the perturbation theory with LNS is much better for this higher spanwise wavenumber. There is no indication of a local maxima and both the neutral point and the maximum growth-rate are well predicted. Figure 5.36 shows the contributions to the nonparallel growth-rate and comparing these results to figure 5.31 shows that both the meanflow and eigenfunction corrections are considerably more benign for the higher spanwise wavenumber. For $\beta = 100$ strong nonparallel effects occur considerably upstream of the first neutral point so that the perturbation approach is adequate in the unstable region.

To determine the stability characteristics over the entire unstable region in s with both curvature and nonparallel effects accounted for, a series of six LNS calculations, four runs for $\beta = 35$ and two runs for $\beta = 100$, have been performed. The runs for each wavenumber consist of partially overlapping domains each with a locally optimized mesh to provide at least 20 nodes per crossflow wavelength in the chordwise direction. Using this "multidomain" approach allows for an efficient account of the wide variance in the chordwise wavenumber over the full unstable region (recall figure 5.32) while limiting each individual domain to a reasonable size, $\leq (1024 \times 63)$ node points. On the inflow to each domain, the local eigenfunction from LST (with curvature) is forced which causes a mild inflow transient before the actual instability wave is established. On the outflow boundary a sponge term is used which has been shown to damp stationary crossflow vortices with only minor upstream influence (see section 4.2.2). The use of overlapping domains allows us to evaluate the agreement in the growth-rate predictions to ensure accuracy. An example of the typical level of agreement is shown in figure 5.37 for two overlapping domains with $\beta = 100$. In this figure, the complete inflow transient is shown for each domain, however, the outflow sponge regions have been partially truncated. The agreement in the overlap region is excellent downstream

of the second inflow transient and a similar level of agreement is achieved on all the overlap regions. After truncating the inflow and outflow regions, the growth-rate and wavenumber results from each run are combined and shown in figure 5.38 for the growth-rate, and figure 5.39 for the wavenumber. These figures include results for both spanwise wavenumbers along with the corresponding NPWC predictions. For $\beta = 100$, both the wavenumber and growth-rate from NPWC are in good agreement with LNS. The only noticeable discrepancy occurs in the growth-rate for $s > 2$ where the NPWC prediction begins to deviate slightly from the LNS result. As noted above, both the NPWC growth-rate and wavenumber for $\beta = 35$ are in poor agreement with LNS near the leading-edge ($s < 3$) due to a breakdown of the perturbation approach used to compute the NPWC results. For $s > 3$, the wavenumber and growth-rate from NPWC are in good agreement with LNS; although, similar to the $\beta = 100$ case, the NPWC growth-rate deviates slightly from the LNS for large s. Thus, for both spanwise wavenumbers considered, the error in the NPWC growth-rate increases near the second neutral point, and this error takes the form of a slight under-prediction of the growth-rate.

The N-factor is extracted from the LNS solutions and is given in figure 5.40 which shows results for both spanwise wavenumbers. Recall that the N-factor is defined as $N = \ln(A(s)/A_0)$ where A is the amplitude at a given station s, and A_0 is the amplitude at a reference location, s_0. As is typically done, the reference location used for figure 5.40 is the first neutral point so that N is defined to be zero there. As expected, the higher growth-rate for the $\beta = 100$ case leads to a quicker initial rise in N-factor; however, the very long region of unstable flow for $\beta = 35$ makes this wavenumber considerably more dangerous, with $N > 10$ beyond $s = 10$.

The N-factors computed from the LNS solutions are compared to those computed from the NPWC predictions in figure 5.41 for $\beta = 35$ and figure 5.42 for $\beta = 100$. The error in the NPWC growth-rate near the leading-edge for $\beta = 35$ leads to significant errors ($\approx 6\%$) in the N-factor predicted downstream. For $\beta = 100$, the N-factor from NPWC is in much better agreement with the LNS value. However, the slight errors in the NPWC growth-rate lead to an accumulation of error in the N-factor. At the second neutral point, the error in the NPWC N-factor is 2.5% for $\beta = 100$. In the following section the N-factor is used to extrapolate the measured amplitude from receptivity calculations back to the source location. Given the error in the NPWC

stability results, we use the "exact" LNS N-factors to perform this extrapolation.

Before concluding this section, we point out that the linear stability results presented here can be used to develop an approximate criteria for the failure of the nonparallel linear stability theory. Toward this goal, we introduce the quantity

$$\delta_g = \frac{\lambda_s}{\delta_1} \left(\frac{\partial \delta_1}{\partial s} \right) \tag{5.30}$$

which can be interpreted as the relative growth of the boundary layer over one wavelength of the instability wave. This quantity is plotted as a function of arclength along the parabolic cylinder in figure 5.43. From figure 5.38a for $\beta = 35$, the NPWC growth-rate is seen to depart significantly from the LNS growth-rate for $s < 3$. With reference to figure 5.43, we see that at $s = 3$ the relative boundary layer growth is $\delta_g = 0.22\%$ for $\beta = 35$. In comparison, δ_g for $\beta = 100$ reaches a maximum of approximately 0.15% which is well below 0.22%. Based on this result, we suggest the value of $\delta_g > 0.22\%$ as an approximate criterion for the failure of the nonparallel linear stability theory for this flow. For some value of $35 < \beta_{crit} < 100$, the maximum value of δ_g will be exactly 0.22%. For any $\beta < \beta_{crit}$ the nonparallel linear stability results are likely to be inaccurate. Care must, of course, be used in generalizing this result, since the critical value of δ_g depends (to some degree) on Re, M, the geometry, and the particular instability mode under consideration.

In summary, the results presented above indicate that both curvature and nonparallelism have a significant quantitative effect on the growth of stationary crossflow vortices in the three-dimensional boundary layer on a swept parabolic-cylinder. Comparison of LST growth-rate predictions with LNS calculations are generally in good agreement when both curvature and nonparallel effects are accounted for in the theory. Unlike previous investigations, we have considered longer wavelength disturbances which, for this geometry, are unstable over an extended chordwise region. In this sense, the current results are similar to the experiments of Saric *et al.* [90] and Bippes *et al.* [32] where there is a long region of crossflow vortex growth. For this long wavelength mode, nonparallel effects are enhanced to such a degree that the nonparallel perturbation approach is inadequate near the leading-edge.

5.6   Receptivity to Surface Roughness

Receptivity to surface roughness is investigated by modeling an array of roughness elements near the leading edge. The roughness elements are assumed to be periodic in the z-direction with wavenumber β. In the chordwise direction a Gaussian distribution is used in the arc-length,

$$h_w(s) = \exp\left[\frac{-(s - s_w)^2}{2\sigma_w^2}\right] , \tag{5.31}$$

where the roughness is centered about s_w and σ_w is the standard deviation (*i.e.* width) of the Gaussian distribution. The roughness is modeled as a small perturbation of the wall and, under the linear assumption, the wall boundary conditions on the perturbed wall are converted to an inhomogeneous set of boundary conditions enforced at the unperturbed wall location. The detailed derivation of such linearized boundary conditions is presented in Appendix F for both isothermal and constant heat-flux wall-temperature boundary-conditions. In computing the theoretical receptivity predictions, the Fourier transform of the bump is required in the chordwise direction. For a Gaussian distribution, the Fourier transform is also Gaussian and is given by

$$\hat{h}_w(\alpha) = \sigma_w \exp\left[\frac{-\alpha^2\sigma_w^2}{2}\right] . \tag{5.32}$$

The primary objective in this section is to evaluate the accuracy and range of validity of the recently developed Finite Reynolds Number Theory for the prediction of receptivity. This theory is summarized in Appendix E in the context of surface roughness on an infinite swept wing.

5.6.1   Parallel Boundary-Layer Without Curvature

To evaluate the Finite Reynolds Number Theory (FRNT) for the prediction of crossflow vortex receptivity, it is instructive to first investigate the receptivity of stationary crossflow vortices for a parallel meanflow with no curvature. In this way, all the assumptions of the theory are satisfied and the amplitudes from LNS and FRNT should agree to a high degree of precision. For this purpose, consider the boundary-layer profile from the swept parabolic-cylinder at the point of maximum crossflow

velocity, $s = 0.802$, as given in figure 5.22. In order to make this comparison easily reproducible, a compressible Falkner–Skan–Cooke (FSC) boundary-layer is fit to the profile taken from the Navier–Stokes solution. The methods used to compute and fit the profile are given in Appendix C and a comparison of the NS and FSC velocity profiles is shown in figure C.1. The FSC profile is placed on a LNS mesh using the parallel flow assumption and, to simplify the comparison with the parabolic cylinder results, the global nondimensionalization is retained. The information required to convert to a local nondimensionalization is provided in Appendix C.

The domain for the receptivity calculation extends from $x = 0$ to $x = 5$ in the chordwise direction and from $y = 0$ to $y = 0.3$ in the wall-normal direction which places the top boundary $78\delta_1$ above the wall. (Since the wall is flat for this geometry, s and x are equivalent.) The solutions are obtained using the techniques introduced in section 4.2.2. The grid is uniform in x with 512 nodes and the standard mapping, equation (5.9), is used in y with 63 nodes. An outflow sponge is employed over the last 20% of the domain to damp the crossflow vortices and a zero disturbance condition is imposed on the top boundary. A Gaussian bump is placed at $x_w = 0.7$ with a standard deviation of $\sigma_w = 0.05$ and a spanwise wavenumber of $\beta = 35$. For this spanwise wavenumber, LST predicts a chordwise wavenumber of $\alpha = -37.39$ and a growth-rate of $\sigma = 0.3043$. Figure 5.44 shows the evolution of the square-root of the integrated disturbance kinetic energy from the LNS solution. Near the roughness site, $E_k'^{1/2}$ has roughly the shape of the imposed Gaussian bump. Downstream, there is a mild transient as the spatially damped modes excited by the bump quickly decay. By $x = 1.2$ the response is dominated by the most unstable crossflow vortex and this continues to $x = 4$ where the outflow sponge begins to damp the crossflow mode. Also included in figure 5.44 is the FRNT prediction where the LST growth-rate has been used to extrapolate the amplitude upstream and downstream of the center of the bump. The FRNT prediction is computed using the methods presented in Appendix E. Downstream of the transient, the extrapolated FRNT and LNS solution are in excellent agreement.

To better observe the transient behavior downstream of the bump, results have also been obtained at $\beta = 30$ which is predicted by LST to have a chordwise wavenumber of $\alpha = -31.30$ and a stable growth-rate of $\sigma = 0.3781$. Figure 5.45 shows the evolution of $E_k'^{1/2}$ for this case including the extrapolated FRNT prediction. Again

the agreement between FRNT and LNS is excellent. In this case, the transient is more clearly observed since the solution decays for large x. The transient results in a local maximum in $E_k'^{1/2}$ at $x = 1.2$ before the asymptotic decay begins. The overall transient growth (measured at the local maximum) is small, about a factor of 1.5 when measured by $E_k'^{1/2}$. This modest amount of transient growth is not surprising given the nature of the surface roughness disturbance. By examining the linearized roughness boundary conditions in Appendix F, it is seen that (linearized) roughness leads to a direct perturbation of the wall tangent velocities u' and w' which are proportional to the wall-normal gradients of the mean velocities. However, for a parallel boundary layer (and, to a good approximation, all boundary layers) the perturbation of the wall-normal velocity is zero at the wall. This is because the wall-normal gradient of the mean normal-velocity is zero (approximately zero for nonparallel flow). Thus, the wall-normal velocity is perturbed only in an indirect manner through the equations of motion. Research on temporal instabilities in an incompressible FSC boundary layer [10] has shown that transient growth is most pronounced for initial disturbances composed primarily of wall-normal velocity. Compared with surface roughness, one would therefore expect greater transient growth associated with wall suction/blowing since this boundary condition directly perturbs the normal velocity.

Figure 5.46 shows the growth-rate based on E_k' extracted from the LNS solutions for both $\beta = 35$ and $\beta = 30$ compared to the LST predictions. The growth-rate is a very sensitive indicator of both errors in the solution and transient behavior. As seen in the figure, the transient behavior downstream of the bump is complete by $x = 2$ for both wavenumbers, with the growth-rate from the LNS solutions in excellent agreement with LST. The slight oscillations in the growth-rate downstream of $x = 2$ (more noticeable for $\beta = 30$) are caused by the presence of damped modes which are generated by the bump. These modes have sufficiently small amplitudes that they are not visible on the amplitude plots shown in figures 5.44 and 5.45. When extracting receptivity results for the parabolic cylinder, growth-rate results similar to those presented here are used to ensure that the crossflow amplitude is measured downstream of the transient (see section 5.6.3).

In summary, the amplitude predictions from FRNT are in excellent agreement with LNS calculations for a parallel boundary layer with no curvature. Since the

conditions of the LNS calculation have been constructed to satisfy all the assumptions in the FRNT, the agreement is not surprising. However, the consistency of the results does suggest that both the LNS and FRNT implementations are free of errors. Furthermore, the transient associated with local surface roughness is observed to be small even for an asymptotically stable mode. This fact greatly simplifies the receptivity calculations presented in section 5.6.3 for the parabolic cylinder since a relatively short domain size can be used.

5.6.2 Finite Reynolds Number Receptivity Theory for the Parabolic Cylinder

Having established agreement between LNS and FRNT for an idealized, parallel boundary-layer with no curvature, we now consider the FRNT predictions for the meanflow about the parabolic cylinder. Since the FRNT is based on quasi-parallel flow, nonparallel effects are obviously not included. However, curvature can be accounted for by forming the FRNT equations in body-fitted curvilinear coordinates. Therefore, in presenting the FRNT predictions, results are given both with and without curvature to determine its influence. In addition, FRNT results are given for both of the spanwise wavenumbers used in the stability analysis of section 5.5.

Applying FRNT to the mean boundary-layer profiles on the parabolic cylinder yields the complex valued efficiency factor, Λ, as discussed in Appendix E. The expression for the initial amplitude and phase of the crossflow vortex is given by equation (E.15) which is repeated here as

$$A_{cf} = \varepsilon_w \, \hat{h}_w(\alpha_{cf}) \, \Lambda(\beta, \mathsf{Re}, \mathsf{Pr}, \mathsf{M}) \qquad (5.33)$$

where $\varepsilon_w = \varepsilon_w{}^*/L^*$ is the normalized roughness height and α_{cf} is the chordwise wavenumber of the local crossflow eigenmode with spanwise wavenumber, β. Notice that the Fourier transform of the roughness distribution is required at the chordwise wavenumber resonant with the crossflow mode and this is obtained for the Gaussian bump using equation (5.32).

Figures 5.47 and 5.48 show the magnitude of Λ for $\beta = 35$ and $\beta = 100$ as a function of arc-length along the parabolic-cylinder. An interesting, and previously undocumented, result that is immediately obvious is that convex curvature increases

the efficiency of the receptivity process for this flow. This result holds true over the full range of unstable spanwise wavenumbers as seen in figure 5.49 which shows the variation of $|\Lambda|$ with β at the point of maximum crossflow velocity, $s = 0.802$, both with and without curvature. The increase in receptivity efficiency due to curvature is most pronounced near the first neutral-point ($\beta \approx 40$) where there is a local maxima in the receptivity efficiency. A similar local maxima has been observed by Crouch [28] for an incompressible FSC boundary layer on a flat-plate. With the exception of the region immediately surrounding the lower neutral point, curvature causes a relatively uniform increase of 10% in the receptivity efficiency factor at this station. In interpreting the results in figures 5.47 and 5.48, it is important to realize that $|\Lambda|$ is the response for a Dirac delta function bump in s (*i.e.* it is the Green's function response). This explains why $|\Lambda|$ increases without bound as s is decreased since the delta function has a unit spectrum for all α. The actual amplitude, as given by equation (5.33), is modulated by the Fourier spectrum in s of the bump shape, h_w, which limits the amplitude for a fixed bump width as s is decreased.

The increase in receptivity efficiency due to convex curvature is particularly interesting given the fact that convex curvature has a stabilizing effect on the growth of crossflow vortices. The stabilizing effect of convex curvature follows from Rayleigh's centrifugal stability criterion [33] which states that for axisymmetric, inviscid flows with curved streamlines, the flow is stabilized if the square of the angular momentum about the center of curvature increases with the radius. This is the case for the three-dimensional boundary layer on a convex surface in which the instability mechanism is the inviscid crossflow instability. In fact, the correspondence between the crossflow and Görtler instabilities has been recently examined by Bossom & Hall [5] who show that Görtler vortices smoothly transition to crossflow vortices as the mean three-dimensionality is increased. However, the effect of curvature on crossflow vortex receptivity has not been previously reported. The reduced growth-rate with convex curvature is offset, to some degree, by a greater initial amplitude. Of course, the net impact of curvature depends on the particular conditions. In the following section, the combined effects of nonparallel flow and curvature on receptivity are examined using LNS calculations.

5.6.3   Linearized Navier–Stokes Receptivity Predictions

For comparison with the FRNT predictions presented in the previous section, a series of LNS calculations have been performed. The methods used to do so have already been discussed in section 4.2.2 and section 5.6.1. We first consider the short spanwise wavelength, $\beta = 100$, since nonparallel effects are expected to be less severe for this case. Similar to the LNS stability calculations performed above, a multidomain approach is employed with two domains used to cover the unstable region. The first domain includes the region from $s = 0.32$ to 1.80 while the second domain covers $s = 1.80$ to 5.12. In each of these domains, a series of calculations are performed using different bump locations, s_w, but all using that same bump width, $\sigma_w = 0.01$. The bump locations and associated receptivity results are presented in table 5.2. Figure 5.50 shows the evolution of $E_k'^{1/2}$ for case 3 of table 5.2. For this case, the bump is placed at $s_w = 0.5$ and the resulting transient and subsequent exponential growth are qualitatively similar to that obtained for the parallel FSC profile in section 5.6.1. The growth-rate computed from this solution is shown in figure 5.51 compared to the LNS stability result from section 5.5. Downstream of $s = 1.2$, and until the start of the sponge at $s = 1.5$, the two growth-rates are in excellent agreement. As a general procedure for extracting the amplitude of the dominant crossflow mode, we compare the growth-rate from the receptivity calculation with the LNS stability result. Since the growth-rate is a very sensitive indication of transient behavior, this comparison allows us to determine a location, s_l, where the transient is negligible. For case 3 we selected $s_l = 1.4$ and measured the amplitude of the response at this location, A_l, based on $E_k'^{1/2}(s_l)$. These results are shown for each bump location in table 5.2.

To compare the results to FRNT, the crossflow amplitudes must be extrapolated to the location of the bump, s_w, since this is the value given by the theory. For this purpose, we use the N-factors based on the LNS calculations discussed in section 5.5. The amplitude at s_w is then given by

$$A_w = A_l e^{(N_w - N_l)} \tag{5.34}$$

where N_w is the N-factor at the bump location, and N_l is the N-factor at the measurement station. Another useful measure of receptivity is the effective amplitude at

the upstream neutral point. This amplitude is simply given by

$$A_{np} = A_l e^{-N_l} \tag{5.35}$$

since the N-factor is defined relative to the neutral point. Both A_w and A_{np} are also reported in table 5.2.

The amplitude at the bump location is compared to the FRNT predictions, both with and without curvature, in figure 5.52. The FRNT predictions are computed using equation (5.33) with the receptivity efficiency factors found in figure 5.48. The amplitude, A_w, generally follows the same trend as the efficiency factor for large s, with A_w increasing as s is reduced. At about $s = 0.65$, there is a maximum in A_w which is associated with the Fourier spectrum of the roughness distribution with $\sigma_w = 0.01$. When comparing the LNS results to the FRNT predictions, the first observation is that FRNT over-predicts the amplitude, by as much as 29% with curvature and 21% without curvature. Based on these results, it is obvious that nonparallel effects tend to reduce the amplitude of crossflow vortices generated by roughness. Similar to curvature, this result is opposite to that observed for stability characteristics, where nonparallel flow, generally speaking, destabilizes crossflow vortices. Downstream of the maximum, the FRNT predictions approach the LNS solution with the no-curvature prediction in slightly better agreement than the prediction with curvature. The fact that the FRNT prediction without curvature is in better agreement with the LNS solution is similar to the stability results where the growth-rate with curvature is a worse approximation to the actual growth-rate compared with the local flat-plate prediction. Since nonparallel and curvature effects are competing, including only one of the effects results in a prediction which is in greater error than the original parallel, flat-plate value.

Similar results have been obtained for $\beta = 35$ using a bump with a standard deviation of $\sigma_w = 0.05$. The results from these calculations are summarized in table 5.3. Figure 5.53 shows the effective amplitude of the crossflow vortex at the bump location for LNS and FRNT. Similar to the $\beta = 100$ case, both FRNT results significantly over-predict the crossflow amplitude near $s = 1$. The greater nonparallel effects for this long spanwise wavelength are evident in the maximum error which is 77% with curvature and 45% without. Beyond approximately $s = 5$, the FRNT amplitudes are in reasonably good agreement with LNS. However, upstream of the neutral point,

$s = 0.40$, the FRNT amplitudes are slightly lower than the LNS values. This is more clear in figure 5.54 which also shows A_w, but plotted on a log-log scale. A similar plot (figure 5.55) for $\beta = 100$ indicates that LNS and FRNT amplitudes will likely cross over upstream of the neutral point ($s = 0.465$).

The effect of the width of the Gaussian bump, as predicted by FRNT with no-curvature, is shown in figures 5.56 and 5.57 for $\beta = 100$ and 35 respectively. With reference to equation (5.33) we see that the influence of the bump width on $|\Lambda|$ is through the amplitude of the Fourier coefficient of the Gaussian at the chordwise wavenumber which is locally resonant with the crossflow mode. For a fixed value of σ_w (and β), there is a variation of $|\hat{h}_w|$ in the chordwise direction since the local wavenumber of the dominant crossflow mode changes (see figure 5.39). Thus, as σ_w is increased the Fourier magnitude of the Gaussian bump is reduced for the high wavenumbers near the leading-edge resulting, eventually, in a drop-off of the amplitude that moves downstream. From this result, it is clear that the drop-off in the response for both $\beta = 35$ and $\beta = 100$ cases above, is due to the choice of σ_w. We note in passing that the σ_w used in the LNS calculations were selected to ease the resolution requirements near the bump. The actual value of σ_w is not expected to alter the qualitative comparison to FRNT. This is demonstrated in figure 5.58 which shows the effect of σ_w on the initial crossflow amplitude with the bump placed at $s = 0.6$ and with $\beta = 100$. As expected, the FRNT prediction overestimates the amplitude for all σ_w. However, the functional dependence of A_w on σ_w is correctly predicted by FRNT. This is demonstrated by setting $\alpha = -141.5$, which is the value based on $|\hat{v}_s|_{max}$ from the LNS stability calculation (see figure 5.39), and adjusting $|\Lambda|$ in equation 5.33 to generate a curve that fits the LNS data. Excellent agreement is achieved for $|\Lambda| = 193$ and this curve is also shown in figure 5.58. We point out, that estimating $|\Lambda|$ in this manner is only an approximation, since the value of α used to evaluate $|\hat{h}_w|$ is not necessarily the "correct" value. A better fit could be obtained by optimizing both α and $|\Lambda|$, however the improvement is slight.

Given the success of the current method, we have used the same procedure to estimate the value of $|\Lambda|$ from the LNS solutions at other chordwise stations. Using α, based on $|\hat{v}_s|_{max}$ from the LNS stability calculation, equation (5.32) is used to compute the local value of $|\hat{h}_w|$ and equation (5.33) is then solved for $|\Lambda|$. The results, for both values of β, are shown in figure 5.59 along with the FRNT predictions.

For both spanwise wavenumbers, the receptivity efficiencies from LNS and FRNT approach one another for large s. This is consistent with the reduction in nonparallel effects with increasing s observed in the stability analysis. Near the leading-edge (*i.e.* upstream of $s = 1$), nonparallel effects increase causing FRNT to over-predict the receptivity efficiency. The influence of nonparallel effects is more pronounced for $\beta = 35$ which is also consistent with the linear stability results. At the upstream neutral point, $s = 0.395$ for $\beta = 35$, the FRNT result with curvature has an error of 264% while the prediction without curvature has a 182% error. For $\beta = 100$ the errors in the FRNT are reduced considerably to 32.2% for FRNT with curvature, and 24.5% without curvature. For both spanwise wavenumbers, nonparallel effects decrease the receptivity efficiency over the entire unstable region. Based on these results, we conclude that the crossover in A_w observed for small s in figures 5.54 is primarily due to errors in the LST prediction of α used in the FRNT to compute $|\hat{h}_w|$. In general, the receptivity efficiency is consistently reduced by nonparallel effects for this flow as shown in figure 5.59.

5.7   Discussion of Results

The results presented in the previous sections have identified curvature and nonparallel effects as having a significant quantitative impact on the initial amplitude of stationary crossflow vortices downstream of a localized roughness element. Given the previously documented [76, 72] effect of both curvature and nonparallelism on the growth characteristics of crossflow vortices, their impact on receptivity is not surprising. What is interesting, however, is that curvature, known to stabilize crossflow vortices, actually enhances receptivity; while nonparallel effects, which typically destabilize crossflow modes, are found to attenuate the initial crossflow amplitude. For the limited range of parameters investigated here, the attenuation due to nonparallel effects is greater than the enhancement due to convex surface curvature. Progressing downstream on the parabolic-cylinder, curvature and nonparallel effects are naturally reduced so that the FRNT predictions approach the LNS solution for large s. However, the effect of nonparallelism is still evident at the furthest downstream stations investigated and the amplitudes predicted by FRNT are consistently greater than the NS solution. For both wavenumbers investigated, the error in the theory for

the farthest downstream location is still approximately 5%. The fact that nonparallel effects are so significant for this flow stems from the fact that the first neutral point for crossflow vortices typically lies very close to the leading-edge. Choudhari [17], when presenting FRNT results for FSC profiles, cautions that since the neutral point for crossflow vortices occurs near the leading-edge for realistic geometries, nonparallel effects may be important. This hypothesis is clearly substantiated by the current results where the error in the predicted amplitude (with curvature) is as high as 77% shortly downstream of the neutral point.

The current results are in contrast to the recent study by Crouch & Spalart [30] who investigated the influence of nonparallel effects on the receptivity of a two-dimensional boundary layer with localized suction subjected to a freestream acoustic wave. Comparing numerical simulations with FRNT predictions, they found that the theory is in very good agreement with simulations downstream of the first neutral point for the prediction of Tollmien–Schlichting wave amplitudes. At the neutral point, the theory under-predicts the amplitude by 4% and this difference increases further upstream to a value between 6.5% and 11.2%. Based on these results, they conclude that neglecting the weak boundary-layer growth in the receptivity theory is an acceptable approximation for this flow.

Based on the current results, the conclusion of Crouch & Spalart obviously does not apply for crossflow vortices. It is particularly interesting to note that they found nonparallel effects to slightly increase the receptivity amplitude for TS waves, while we find that initial crossflow vortex amplitudes are generally attenuated by nonparallel effects. This is in contrast with the influence of nonparallel flow on stability characteristics. Fasel & Konzelmann [34], in comparisons of Navier–Stokes solutions and stability analysis, show that for TS waves in a Blasius boundary layer nonparallel effects lead to an increase in the growth-rate. Similarly, we have shown that nonparallel flow also destabilizes crossflow vortices. Thus, there is no apparent trend linking stability and receptivity results concerning nonparallel effects. However, we note that the receptivity and stability processes under consideration are quite different, and this statement must be considered in this light.

s	δ_1 $\times 100$	δ_2 $\times 100$	U_e	T_e	θ_e (deg.)	$\frac{w_{s_{max}}}{U_e}$	χ	M_e	β_h
0.020	0.324	0.119	0.700	1.128	88.7	-0.006	7	0.527	1.000
0.041	0.324	0.119	0.700	1.128	87.3	-0.012	14	0.527	0.999
0.085	0.324	0.120	0.703	1.128	84.5	-0.024	28	0.529	0.996
0.109	0.325	0.120	0.705	1.127	82.9	-0.031	36	0.531	0.993
0.136	0.325	0.120	0.708	1.127	81.2	-0.038	45	0.533	0.989
0.197	0.326	0.121	0.717	1.125	77.5	-0.053	63	0.540	0.978
0.233	0.328	0.122	0.723	1.124	75.4	-0.061	73	0.545	0.970
0.273	0.329	0.123	0.731	1.122	73.2	-0.069	84	0.552	0.960
0.368	0.334	0.125	0.752	1.118	68.5	-0.084	105	0.569	0.931
0.423	0.338	0.127	0.766	1.116	66.0	-0.090	116	0.580	0.912
0.485	0.344	0.129	0.781	1.113	63.6	-0.096	126	0.592	0.890
0.553	0.351	0.132	0.799	1.109	61.1	-0.101	136	0.607	0.864
0.712	0.371	0.140	0.838	1.101	56.5	-0.106	153	0.639	0.801
0.802	0.384	0.144	0.860	1.096	54.5	-0.107	161	0.657	0.765
0.904	0.400	0.150	0.881	1.091	52.5	-0.106	168	0.675	0.727
1.014	0.419	0.156	0.903	1.086	50.8	-0.105	174	0.693	0.688
2.091	0.618	0.221	1.030	1.055	42.8	-0.087	208	0.803	0.425
4.098	0.953	0.326	1.111	1.033	39.0	-0.066	232	0.874	0.241
6.167	1.239	0.415	1.143	1.024	37.7	-0.055	242	0.904	0.168
8.210	1.483	0.491	1.159	1.019	37.1	-0.048	248	0.919	0.131
10.013	1.676	0.550	1.169	1.016	36.8	-0.043	251	0.928	0.110
15.479	2.175	0.705	1.185	1.011	36.2	-0.034	255	0.943	0.075
20.261	2.544	0.818	1.192	1.009	35.9	-0.030	256	0.949	0.060
25.164	2.879	0.922	1.197	1.007	35.8	-0.027	255	0.954	0.049
30.121	3.185	1.016	1.200	1.006	35.7	-0.024	254	0.957	0.042
40.092	3.733	1.186	1.204	1.005	35.5	-0.021	251	0.961	0.033
50.083	4.216	1.335	1.207	1.004	35.4	-0.018	249	0.964	0.027

Table 5.1: Swept parabolic-cylinder boundary-layer characteristics for $\mathsf{M} = 0.8$, $\mathsf{Re} = 1 \times 10^5$, $\mathsf{Pr} = 1$, and $T_w = T_0$. Crossflow Reynolds number, χ, is defined in equation (5.21) and the Hartree parameter, β_h, is defined by equation (5.22).

Case	s_w	s_l	A_l	N_w	N_l	A_w	A_{np}
1	0.40	1.3997	4.0933	0.0709	2.3166	0.4333	0.4036
2	0.45	1.2014	3.2454	0.0043	1.7999	0.5388	0.5365
3	0.50	1.3997	6.2504	0.0097	2.3166	0.6224	0.6163
4	0.55	1.3997	6.4534	0.0611	2.3166	0.6764	0.6364
5	0.60	1.3997	6.2156	0.1457	2.3166	0.7090	0.6129
6	0.70	1.3997	5.0748	0.3754	2.3166	0.7284	0.5004
7	0.80	1.3997	3.7751	0.6475	2.3166	0.7113	0.3723
8	0.90	1.3997	2.6939	0.9369	2.3166	0.6779	0.2656
9	2.00	4.0036	1.3979	3.5579	4.9883	0.3344	0.0095
10	2.50	4.0036	0.5357	4.2538	4.9883	0.2570	0.0037
11	3.00	4.1999	0.2706	4.7009	4.9639	0.2080	0.0019

Table 5.2: Crossflow receptivity results for $\beta = 100$. Flow conditions are $\mathsf{M} = 0.8$, $\mathsf{Re} = 1 \times 10^5$, and $\theta = 35°$.

Case	s_w	s_l	A_l	N_w	N_l	A_w	A_{np}
1	0.30	2.0012	0.6041	0.1262	2.4554	0.0588	0.0518
2	0.40	2.0012	2.4038	0.0001	2.4554	0.2063	0.2063
3	0.50	2.0012	4.9201	0.0490	2.4554	0.4435	0.4223
4	0.60	2.0012	6.8010	0.1528	2.4555	0.6800	0.5837
5	0.70	2.0028	7.5289	0.2849	2.4579	0.8571	0.6446
6	0.80	2.0012	7.3646	0.4354	2.4555	0.9769	0.6320
7	1.00	2.5094	12.4113	0.7680	3.2134	1.0760	0.4992
8	1.20	2.5094	8.6871	1.1172	3.2134	1.0679	0.3494
9	1.50	2.5000	4.6284	1.6377	3.2000	0.9703	0.1887
10	2.50	6.0009	27.6655	3.2000	7.0173	0.6083	0.0248
11	4.00	7.0056	5.0805	5.1042	7.7820	0.3491	0.0021
12	5.00	7.0056	1.3736	6.1357	7.7820	0.2648	0.0006
13	7.00	12.0000	2.4094	7.7780	10.4235	0.1710	0.0001

Table 5.3: Crossflow receptivity results for $\beta = 35$. Flow conditions are $\mathsf{M} = 0.8$, $\mathsf{Re} = 1 \times 10^5$, and $\theta = 35°$.
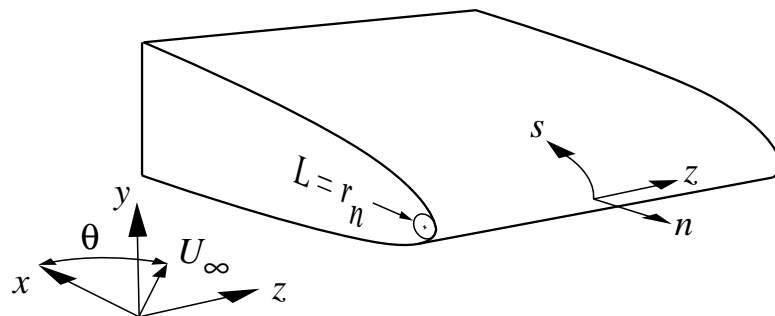
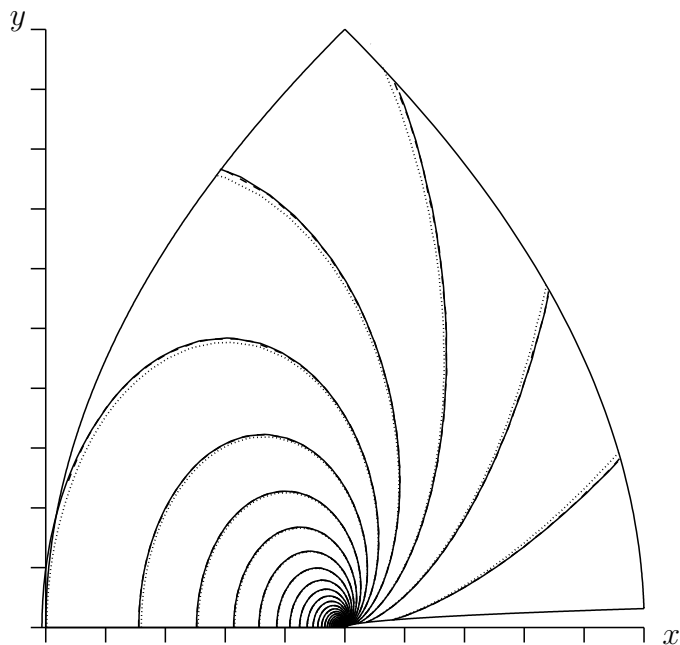**Figure 5.1:** Swept parabolic-cylinder geometry.

Figure 5.2: Contours of C_p for $\mathsf{M} = 0.8$, $\mathsf{Re} = 1000$ flow over a parabolic cylinder. Results from three domain sizes are shown: —— $x^*/r_n^* \in \pm 1 \times 10^8$, ---- $\pm 1 \times 10^7$, and ⋯⋯ $\pm 1 \times 10^6$. Contours are from 0 to 1.2 in increments of 0.02; tics every $100 r_n$. Note that 10^8 and 10^7 contours over-lie each other.
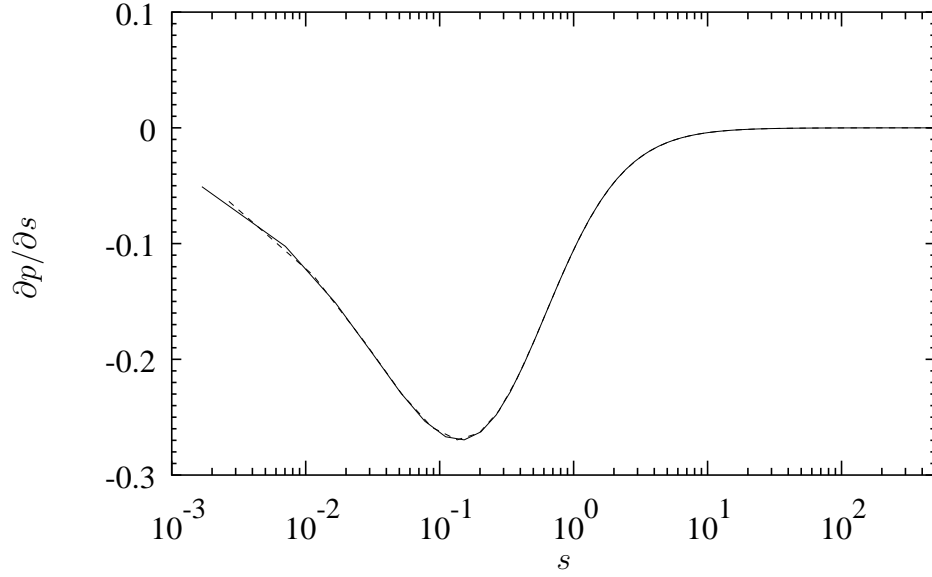
Figure 5.3: Pressure gradient along the wall for two domain sizes: —— $x^*/r_n^* \in \pm 1 \times 10^8$ and ---- $\pm 1 \times 10^7$.
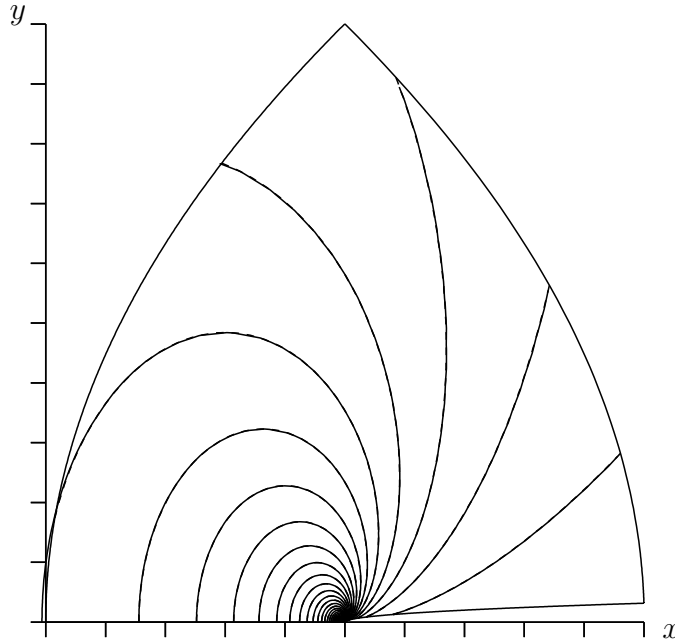
Figure 5.4: Contours of C_p from the potential solution at $M = 0.8$, $Re = 1000$ after interpolation to a Navier–Stokes mesh. The —— lines are the $x^*/r_n^* \in \pm 1 \times 10^8$ potential solution while the ---- lines are the interpolated solution. Note that they are very nearly identical. Contours are from 0 to 1.2 in increments of 0.02; tics every $100 r_n$.
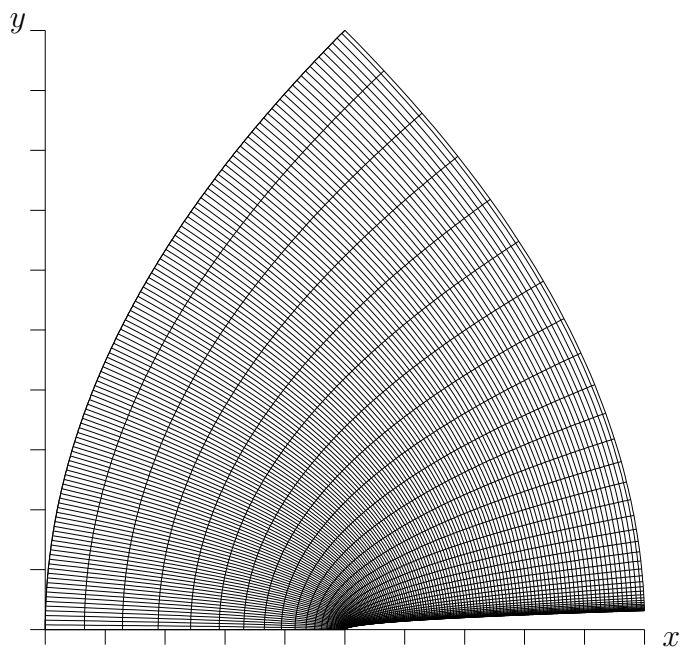
Figure 5.5: Typical Parabolic cylinder mesh: $x_{min} = -500$, $x_{max} = 500$. Tic marks are at every $100r_n$. (This particular mesh uses the same distribution but with fewer points than that used in the $\mathsf{Re} = 1000$ calculations.)
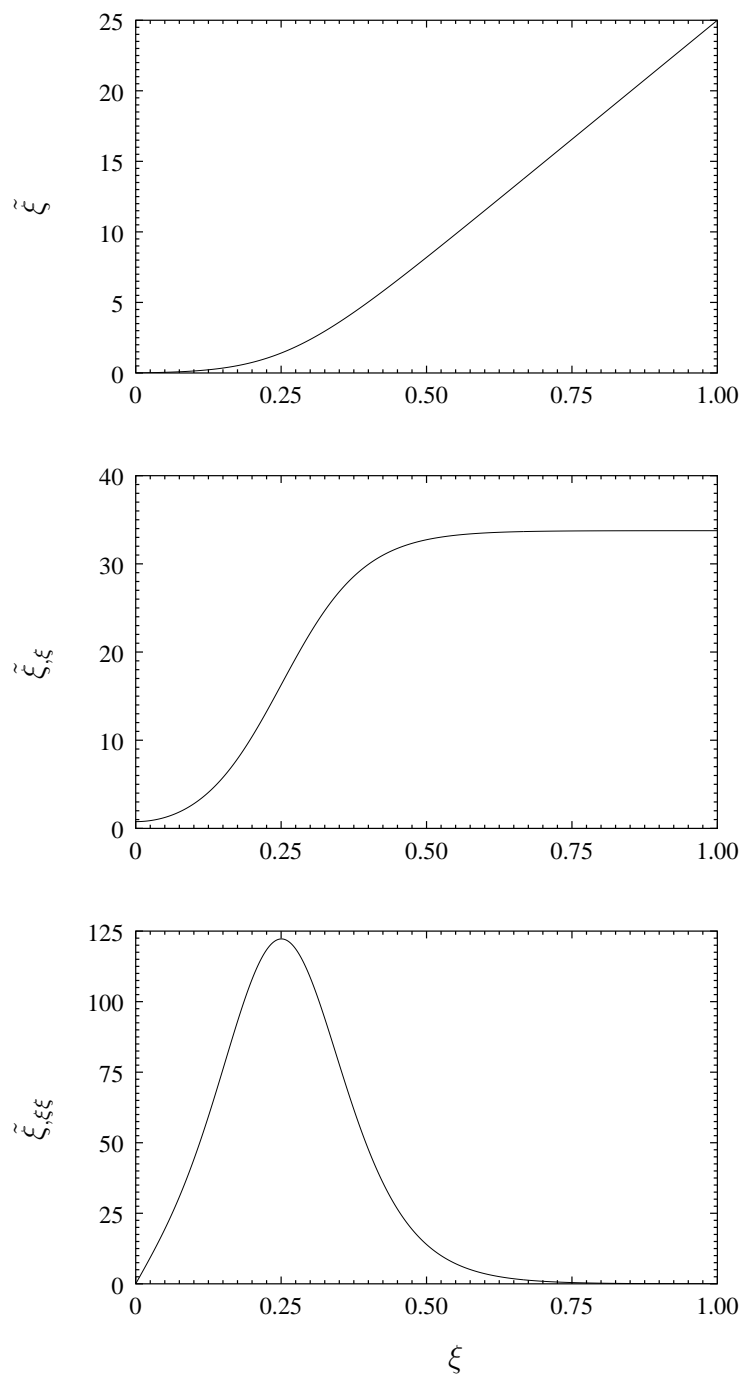
Figure 5.6: Mapping function and its derivatives for parameters typical of those used in the wall-tangent direction: $\Delta\tilde{\xi}_{min} = 0.001$, $N_\xi = 768$, $\tilde{\xi}_{max} = 25$, $\xi_c = 0.25$, $b = 7$.
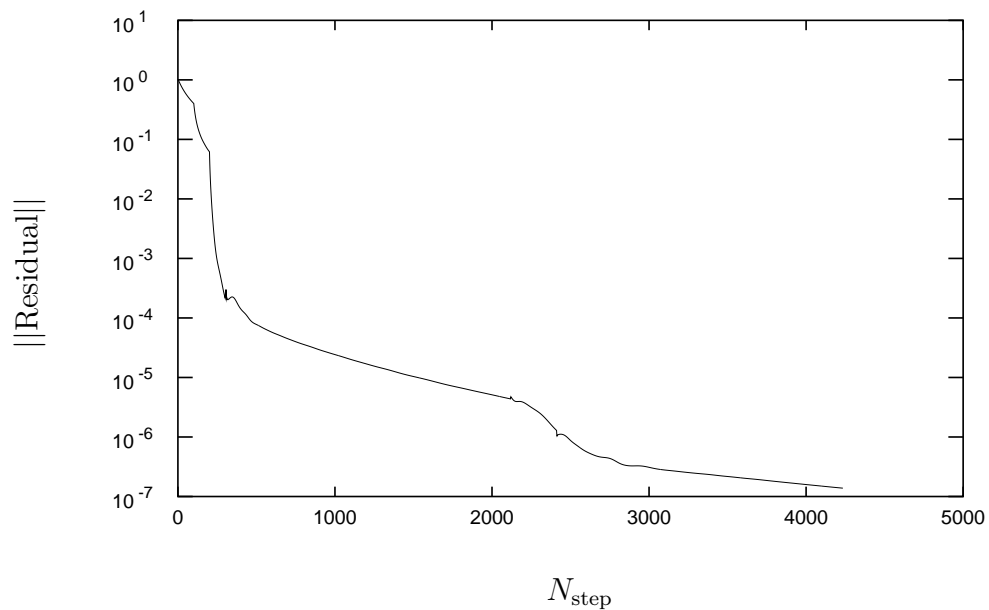
Figure 5.7: Convergence history for $M = 0.1$, $Re = 1000$ mean flow calculation.
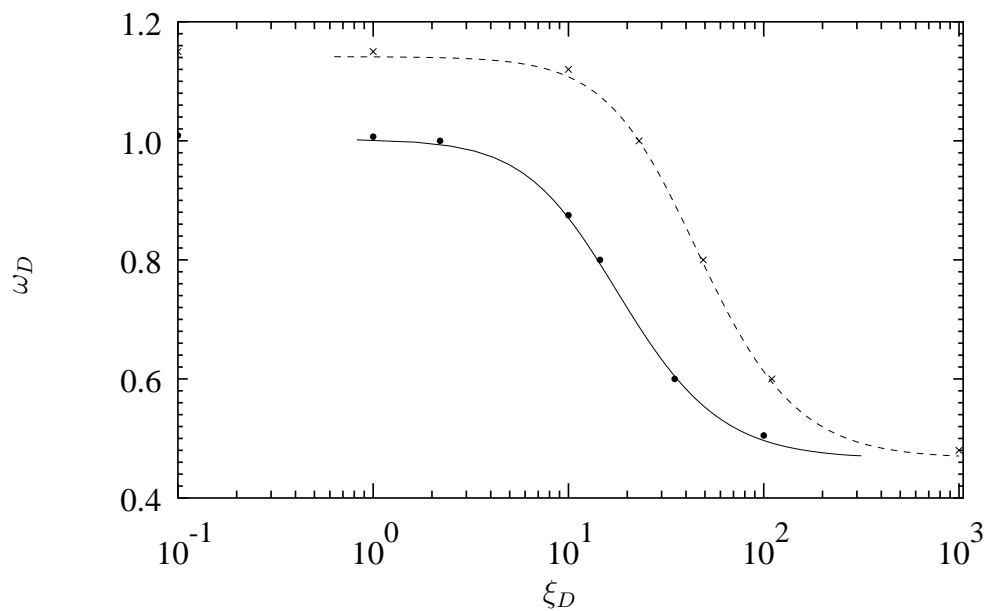
Figure 5.8: Vorticity along the surface of the parabolic cylinder plotted in the coordinates of Davis [31]. Lines denote the current solution at $M = 0.1$ while symbols are taken from Davis' incompressible solutions: —— , • are at $Re = 100$ and ········ , × are at $Re = 1000$.
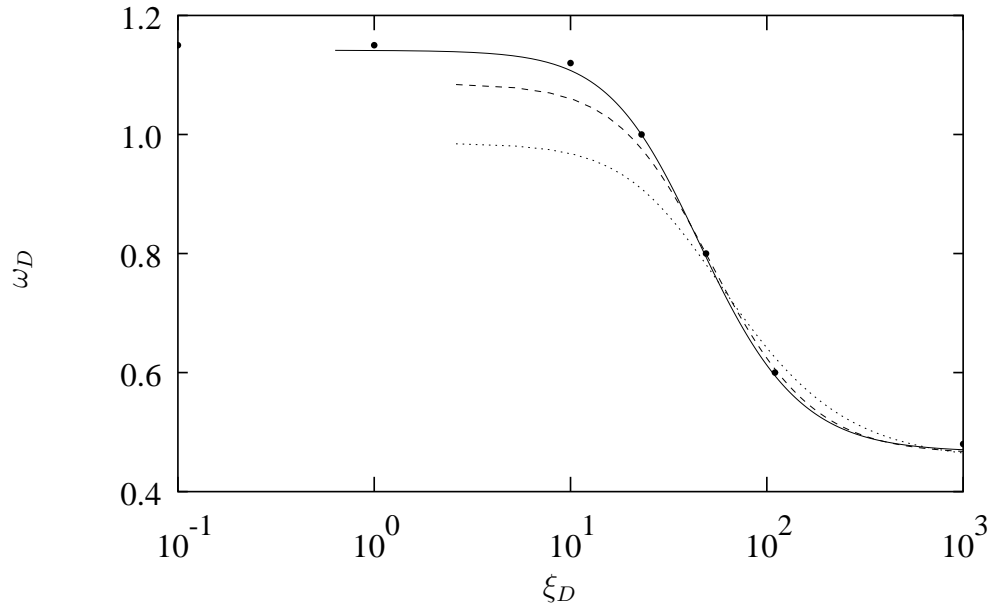
Figure 5.9: Effect of compressibility on the scaled wall-vorticity at $Re = 1000$, $Pr = 0.7$: $\bullet$ incompressible, —— $M = 0.1$, - - - - $M = 0.5$, and ········ $M = 0.8$
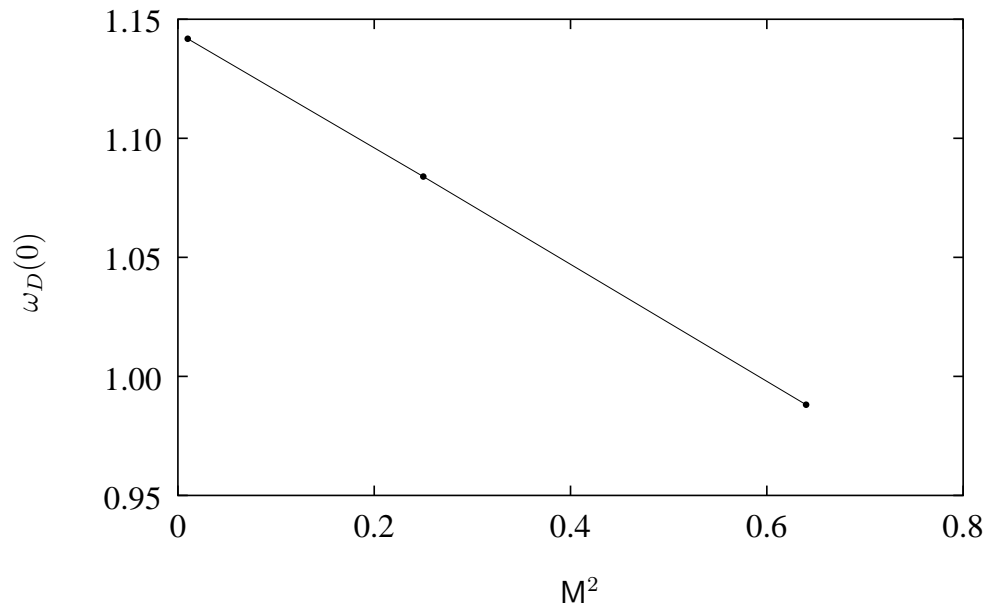
Figure 5.10: Variation of the scaled wall-vorticity at the attachment line with the Mach number squared: $Re = 1000$, $Pr = 0.7$.
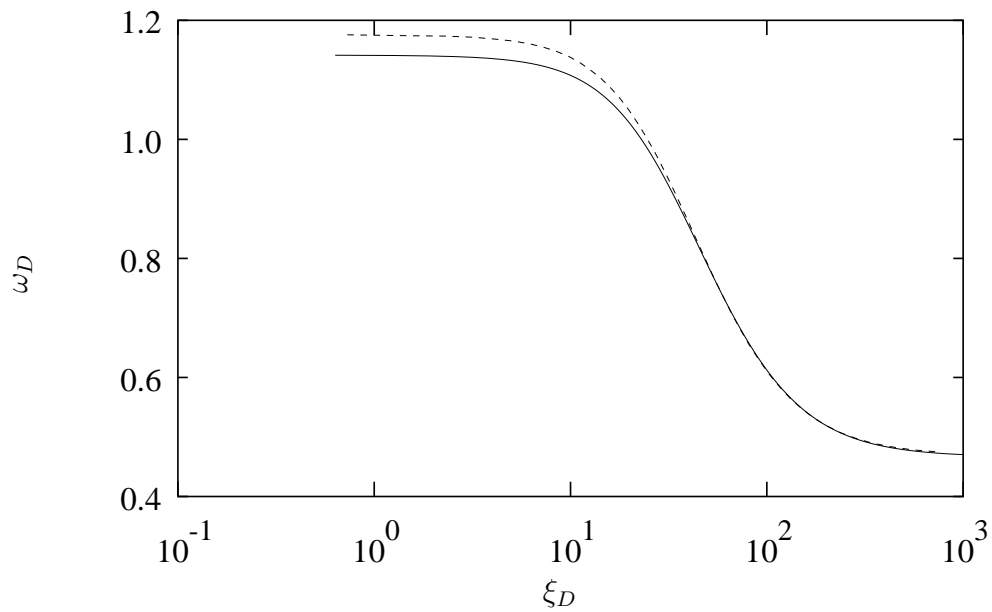
Figure 5.11: Comparison of wall vorticity with incompressible parabolized solution, Re = 1000, Pr = 0.7: ——— M = 0.1 and ---- M = 0 parabolized.
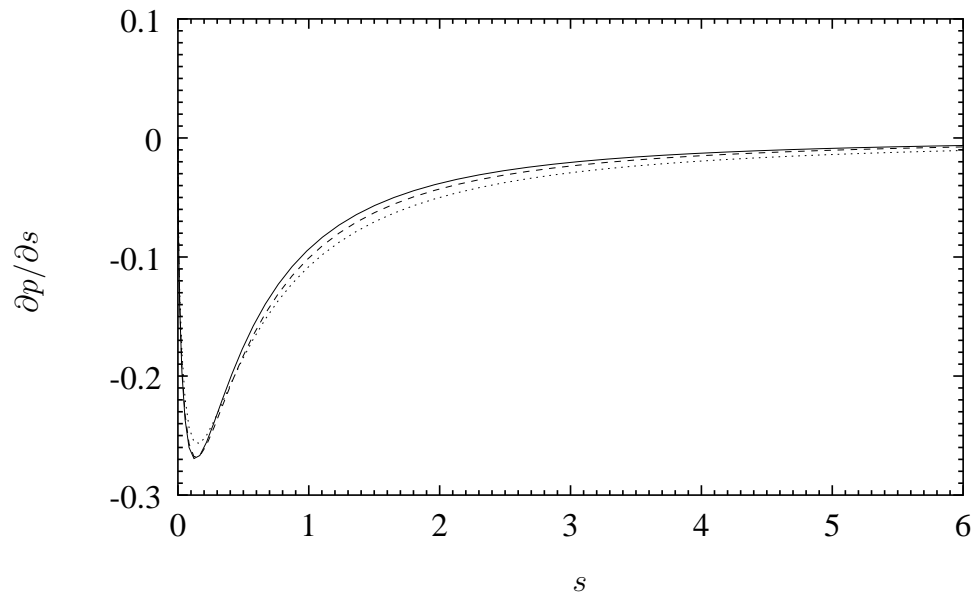

Figure 5.12: Effect of Mach number on the pressure gradient, $\partial p/\partial s$, at the wall for Re = 1000, Pr = 0.7: ——— M = 0.1, ---- M = 0.5, ········ M = 0.8.
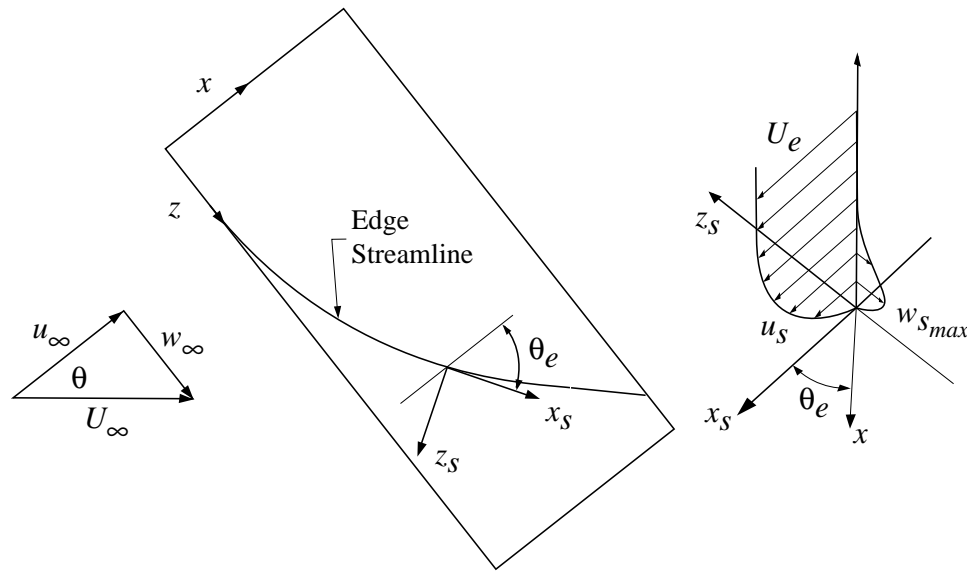
Figure 5.13: Schematic of a three-dimensional boundary layer near a swept leading-edge. Surface curvature is not explicitly shown in order to simplify the presentation.
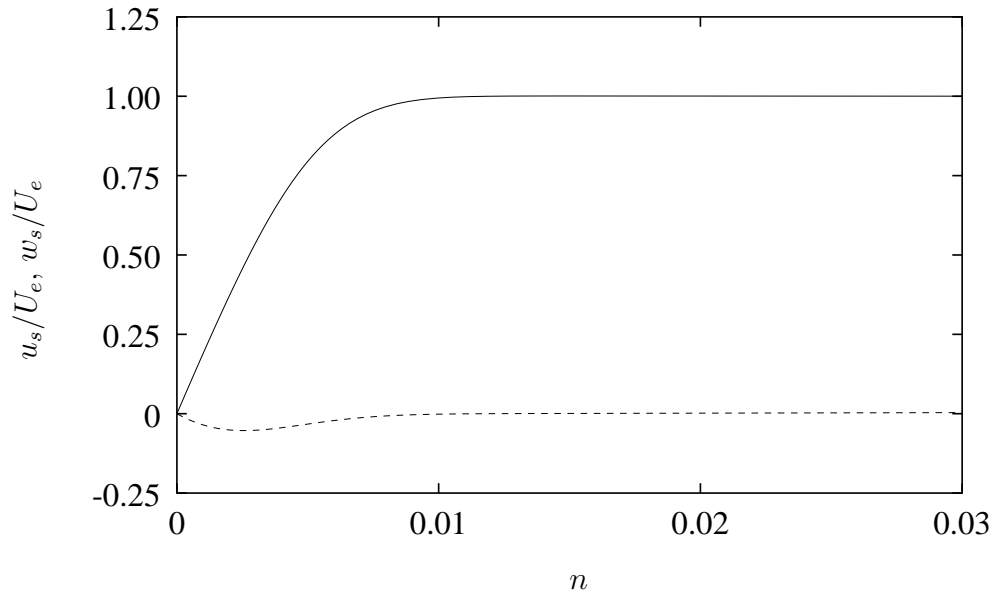

Figure 5.14: Velocity profiles at $s = 0.197$ in local streamwise coordinates: —— u_s/U_e, - - - - w_s/U_e. Flow conditions are $\mathsf{M} = 0.8$, $\mathsf{Re} = 1 \times 10^5$, $\theta = 35°$.

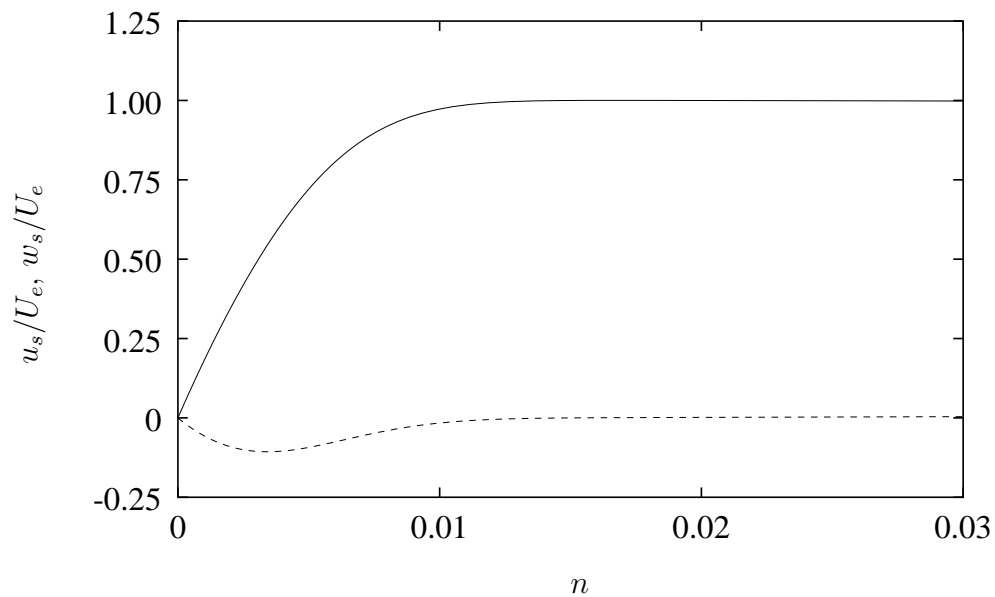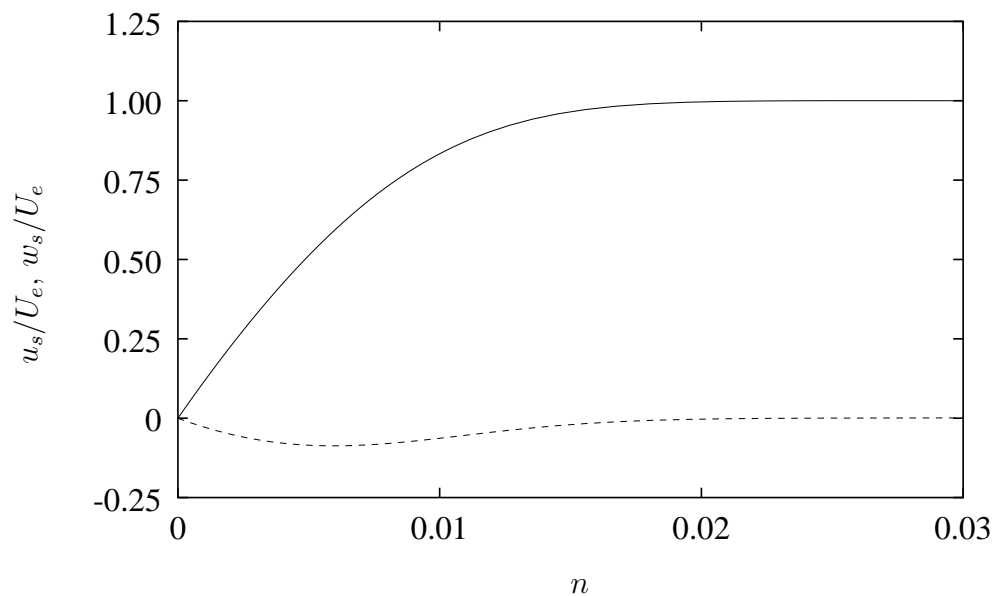**Figure 5.15:** Velocity profiles at $s = 0.802$ in local streamwise coordinates: ——— u_s/U_e, - - - - w_s/U_e. Flow conditions are $\mathsf{M} = 0.8$, $\mathsf{Re} = 1 \times 10^5$, $\theta = 35°$.

Figure 5.16: Velocity profiles at $s = 2.09$ in local streamwise coordinates: ——— u_s/U_e, - - - - w_s/U_e. Flow conditions are $\mathsf{M} = 0.8$, $\mathsf{Re} = 1 \times 10^5$, $\theta = 35°$.
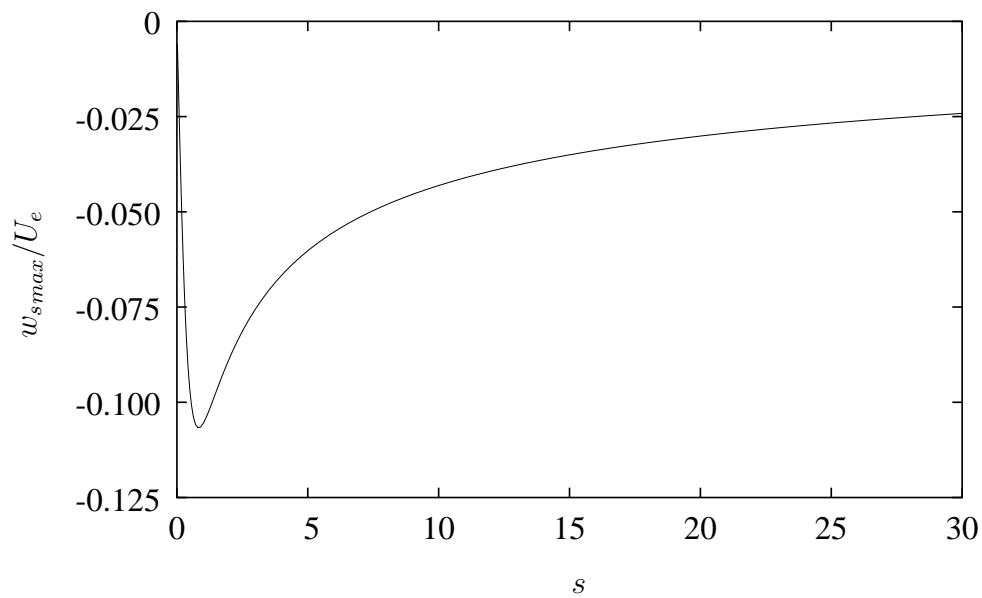
Figure 5.17: Maximum, in the transverse direction, of the crossflow component of velocity normalized by the local edge velocity for the flow conditions: $\mathsf{M} = 0.8$, $\mathsf{Re} = 1 \times 10^5$, $\theta = 35°$.
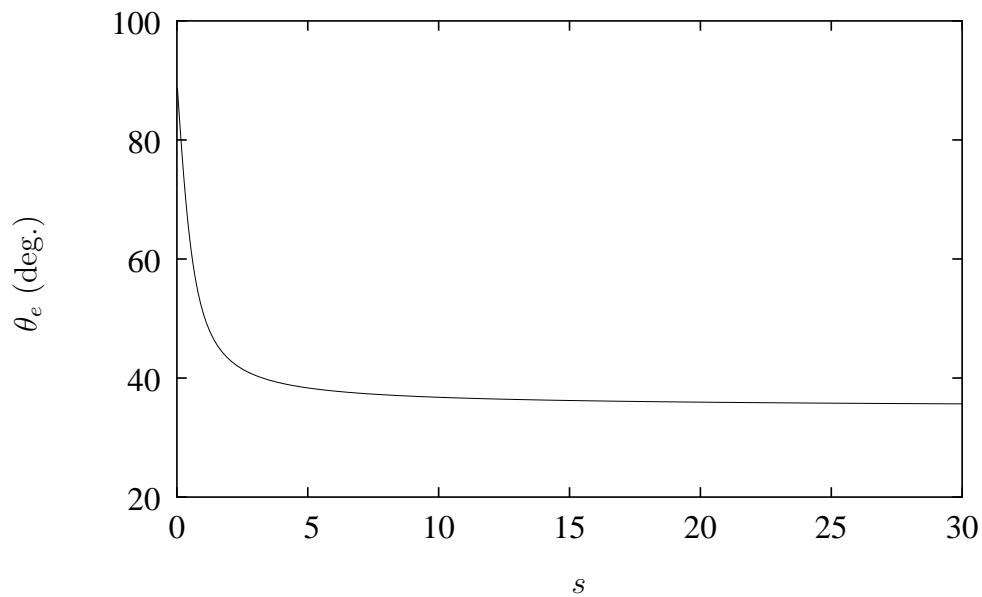

Figure 5.18: Evolution of the local sweep angle for the conditions $\mathsf{M} = 0.8$, $\mathsf{Re} = 1 \times 10^5$, $\theta = 35°$.
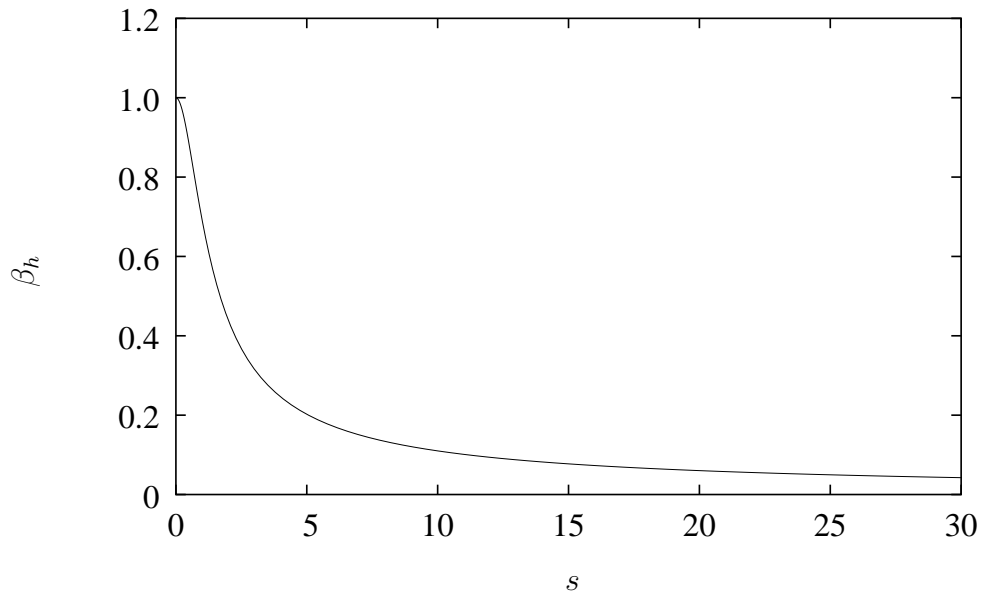
Figure 5.19: Evolution of the Hartree parameter for the flow conditions: $\mathsf{M} = 0.8$, $\mathsf{Re} = 1 \times 10^5$, $\theta = 35°$.
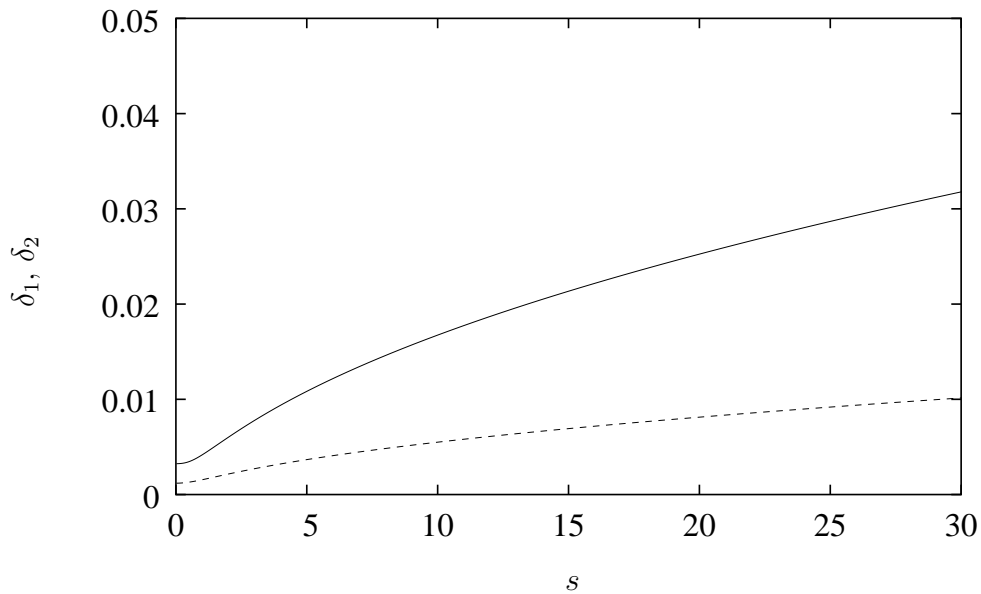

Figure 5.20: Boundary layer displacement thickness and momentum thickness: ——— is the displacement thickness, - - - - denotes the momentum thickness. The flow conditions are $\mathsf{M} = 0.8$, $\mathsf{Re} = 1 \times 10^5$, $\theta = 35°$.
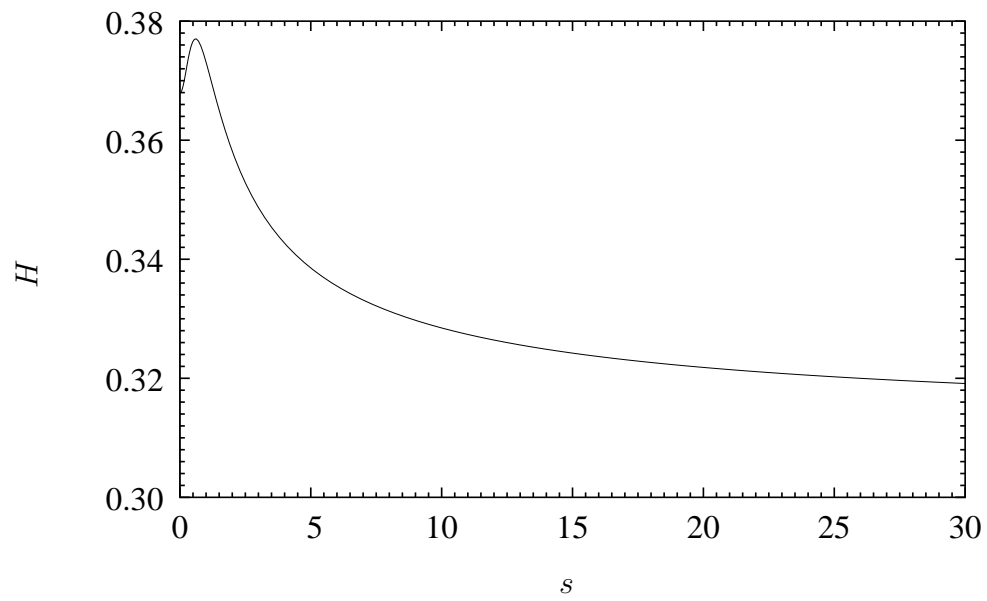
Figure 5.21: Boundary layer shape factor for the conditions: $\mathsf{M} = 0.8$, $\mathsf{Re} = 1 \times 10^5$, $\theta = 35°$.
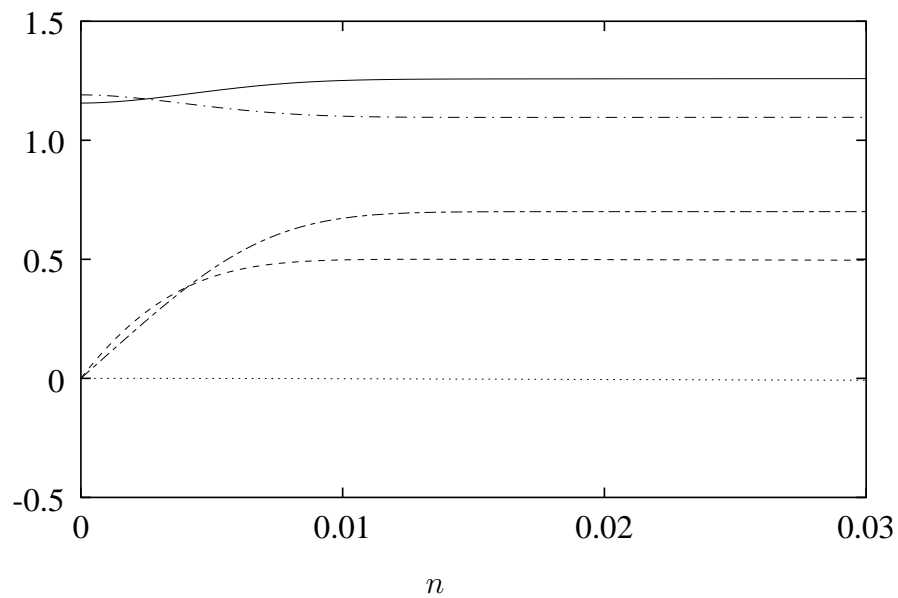
Figure 5.22: Boundary layer profiles at the point of maximum crossflow: —— ρ, - - - - v_s, ········· v_n, —--—w, and —·— T. Conditions: $s = 0.802$, $\mathsf{M} = 0.8$, $\mathsf{Re} = 1 \times 10^5$, $\theta = 35°$.
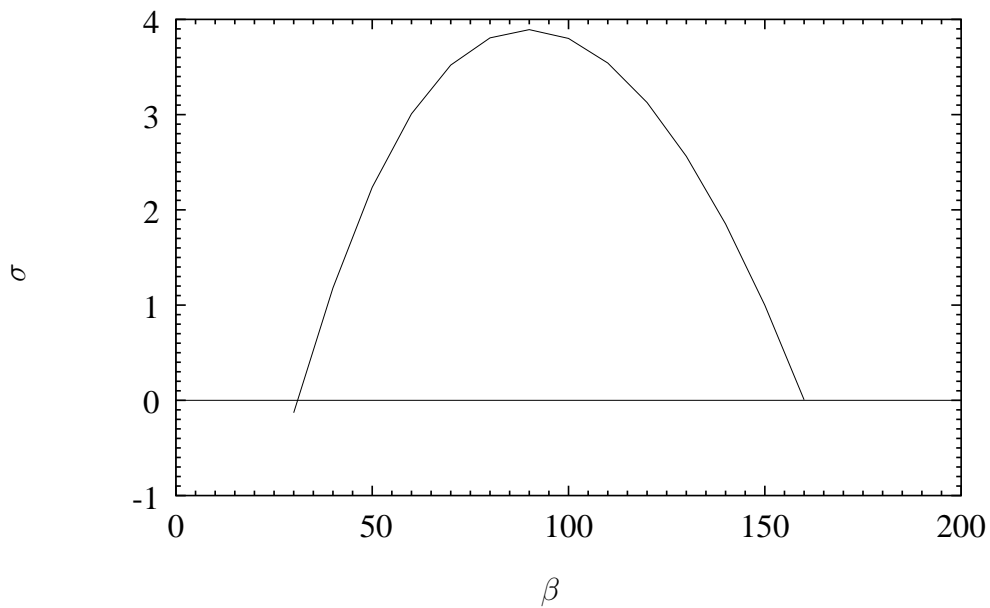
Figure 5.23: Quasi-parallel LST spatial growth-rate: $s = 0.802$, $\beta = 35$, $\mathsf{M} = 0.8$, $\mathsf{Re} = 1 \times 10^5$, $\theta = 35°$.
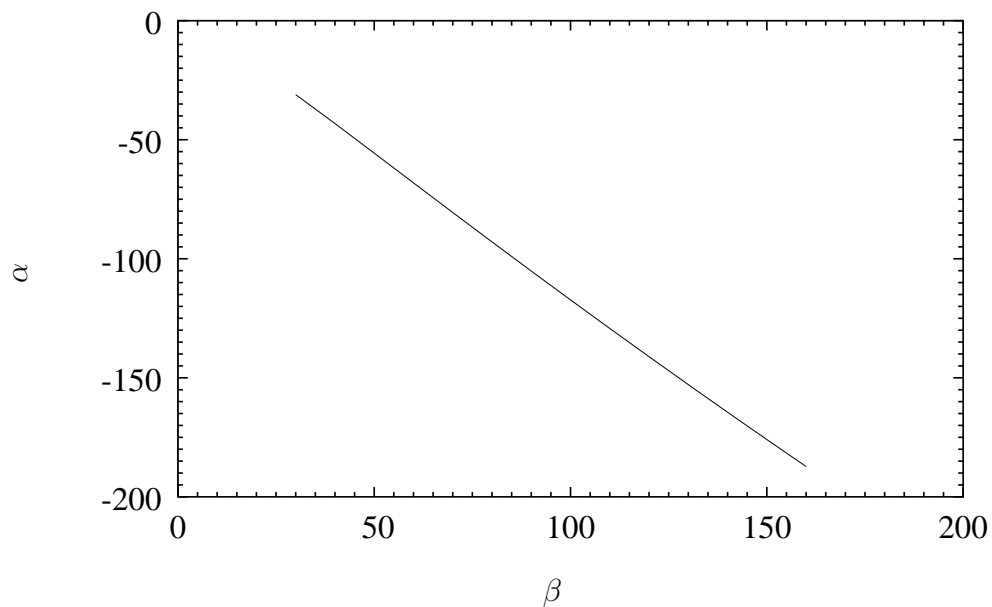
Figure 5.24: Quasi-parallel LST chordwise wavenumber: $s = 0.802$, $\beta = 35$, $\mathsf{M} = 0.8$, $\mathsf{Re} = 1 \times 10^5$, $\theta = 35°$.
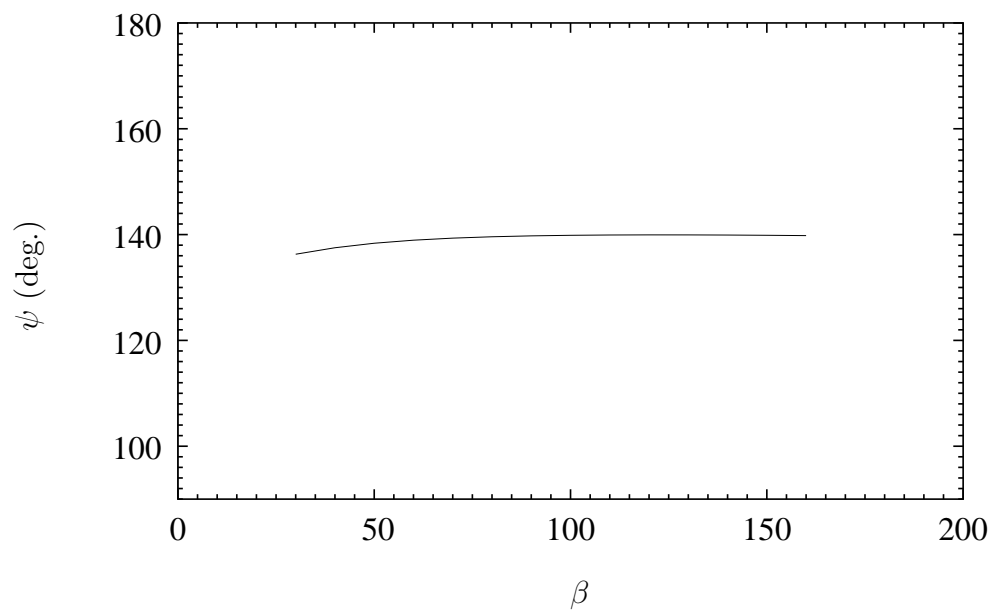
Figure 5.25: Wave-angle variation predicted from quasi-parallel LST: $s = 0.802$, $\beta = 35$, $\mathsf{M} = 0.8$, $\mathsf{Re} = 1 \times 10^5$, $\theta = 35°$.
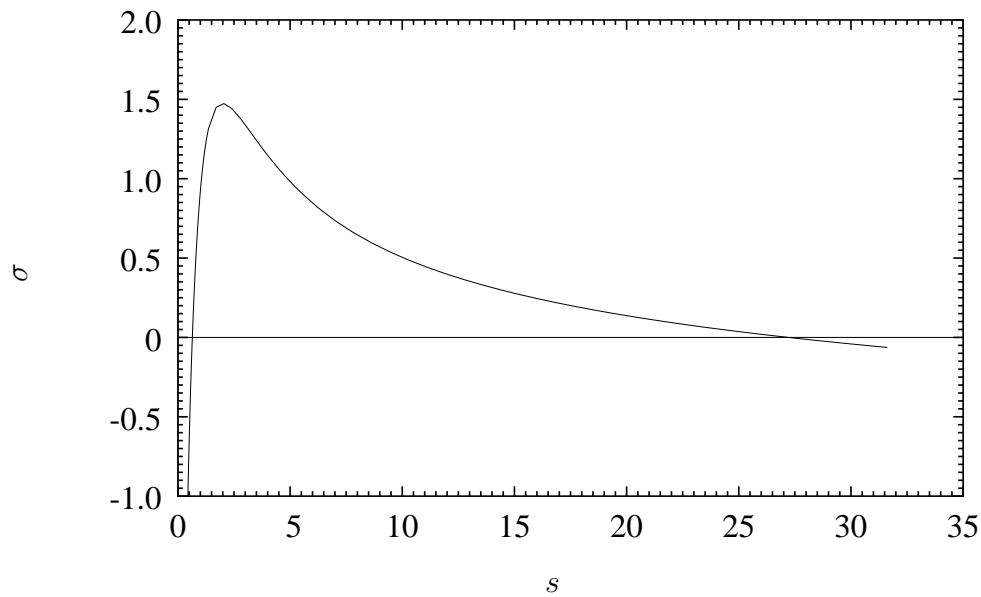
Figure 5.26: Quasi-parallel growth-rate without curvature for $\beta = 35$, $\mathsf{M} = 0.8$, $\mathsf{Re} = 1 \times 10^5$, $\theta = 35°$.
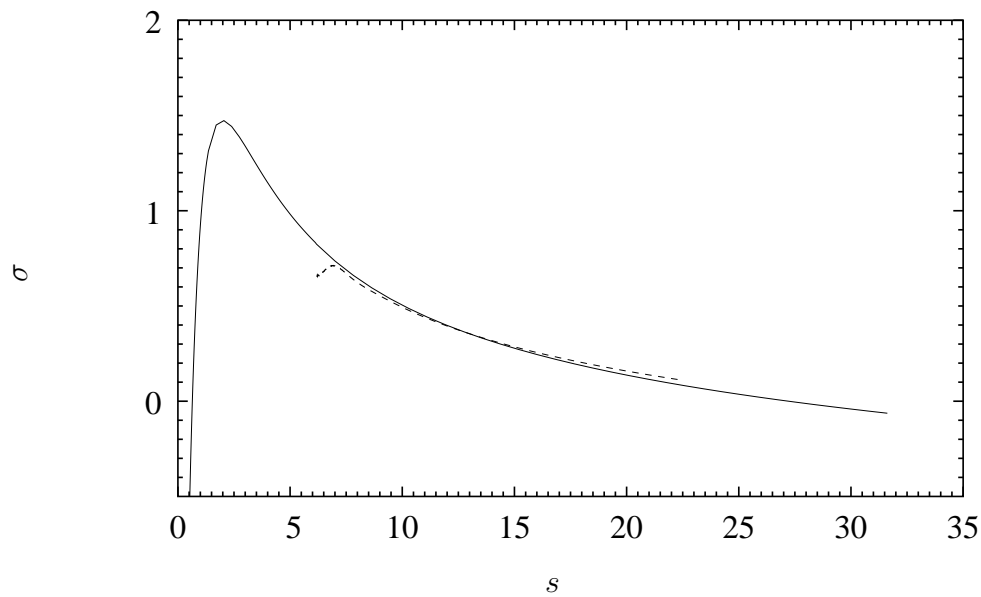
Figure 5.27: Comparison of growth-rate from QPNC —— and LNS ---- : $\beta = 35$, $\mathsf{M} = 0.8$, $\mathsf{Re} = 1 \times 10^5$, $\theta = 35°$.
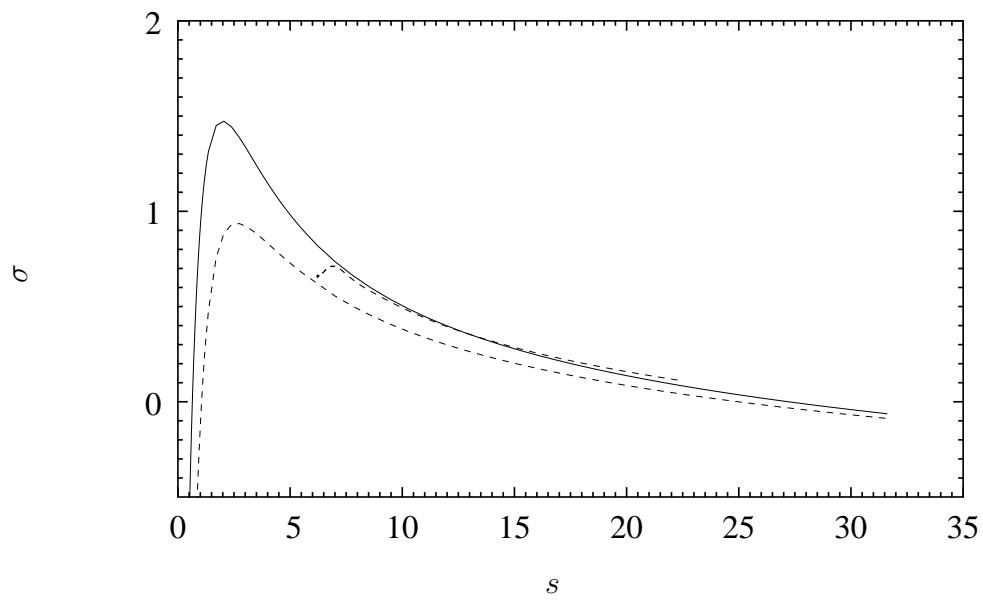
Figure 5.28: Comparison of growth-rate from QPNC ——— , LNS ---- , and ⋯⋯
QPWC: $\beta = 35$, $\mathsf{M} = 0.8$, $\mathsf{Re} = 1 \times 10^5$, $\theta = 35°$.
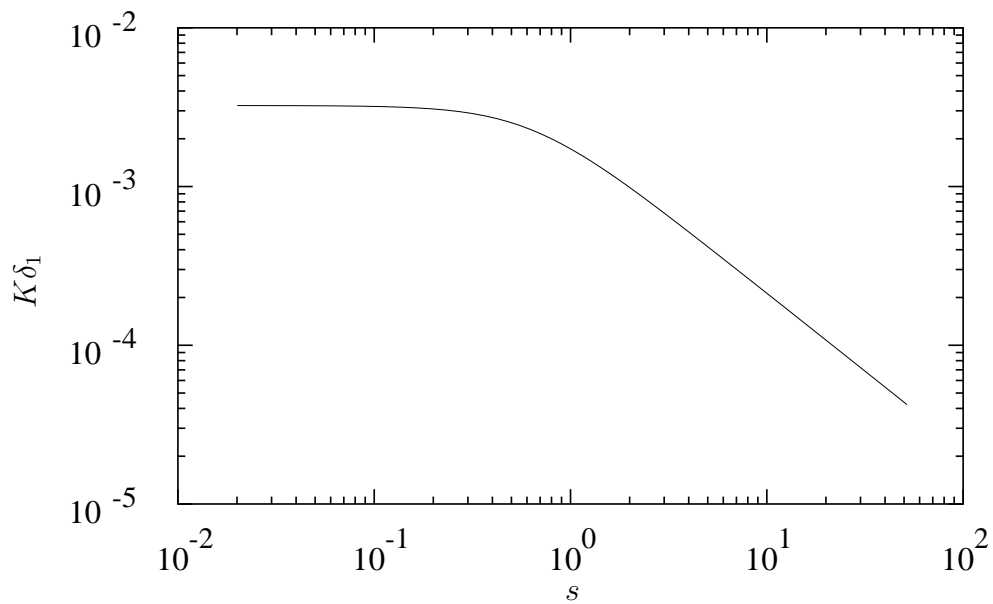
Figure 5.29: Normalized surface curvature for $\mathsf{M} = 0.8$, $\mathsf{Re} = 1 \times 10^5$, $\theta = 35°$.
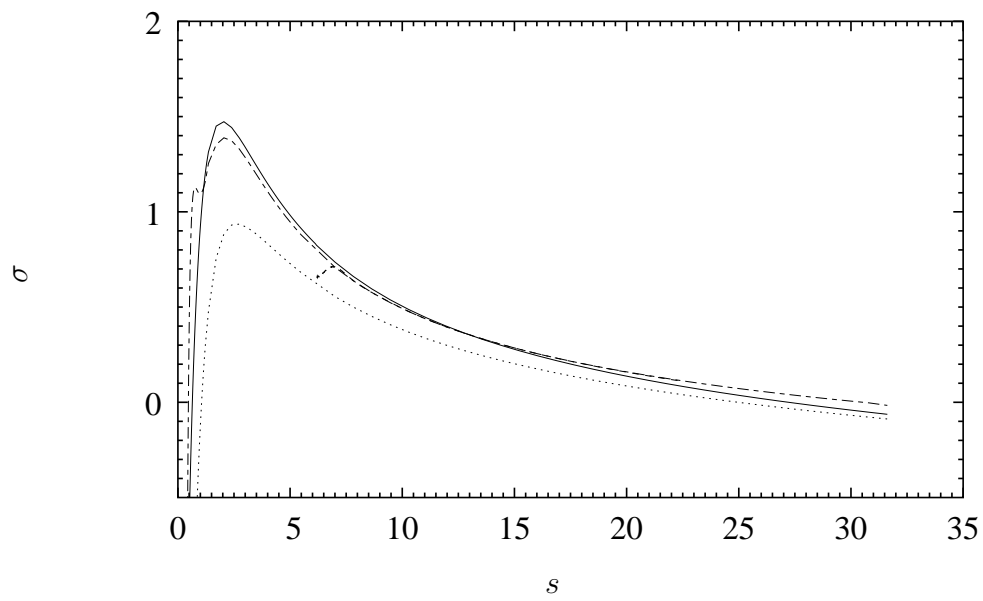
Figure 5.30: Comparison of growth-rate predictions: —— QPNC, - - - - LNS, ········· QPWC, —·—— NPWC. Flow parameters: $\beta = 35$, $\mathsf{M} = 0.8$, $\mathsf{Re} = 1 \times 10^5$, $\theta = 35°$. Note that LNS and NPWC curves overlap.
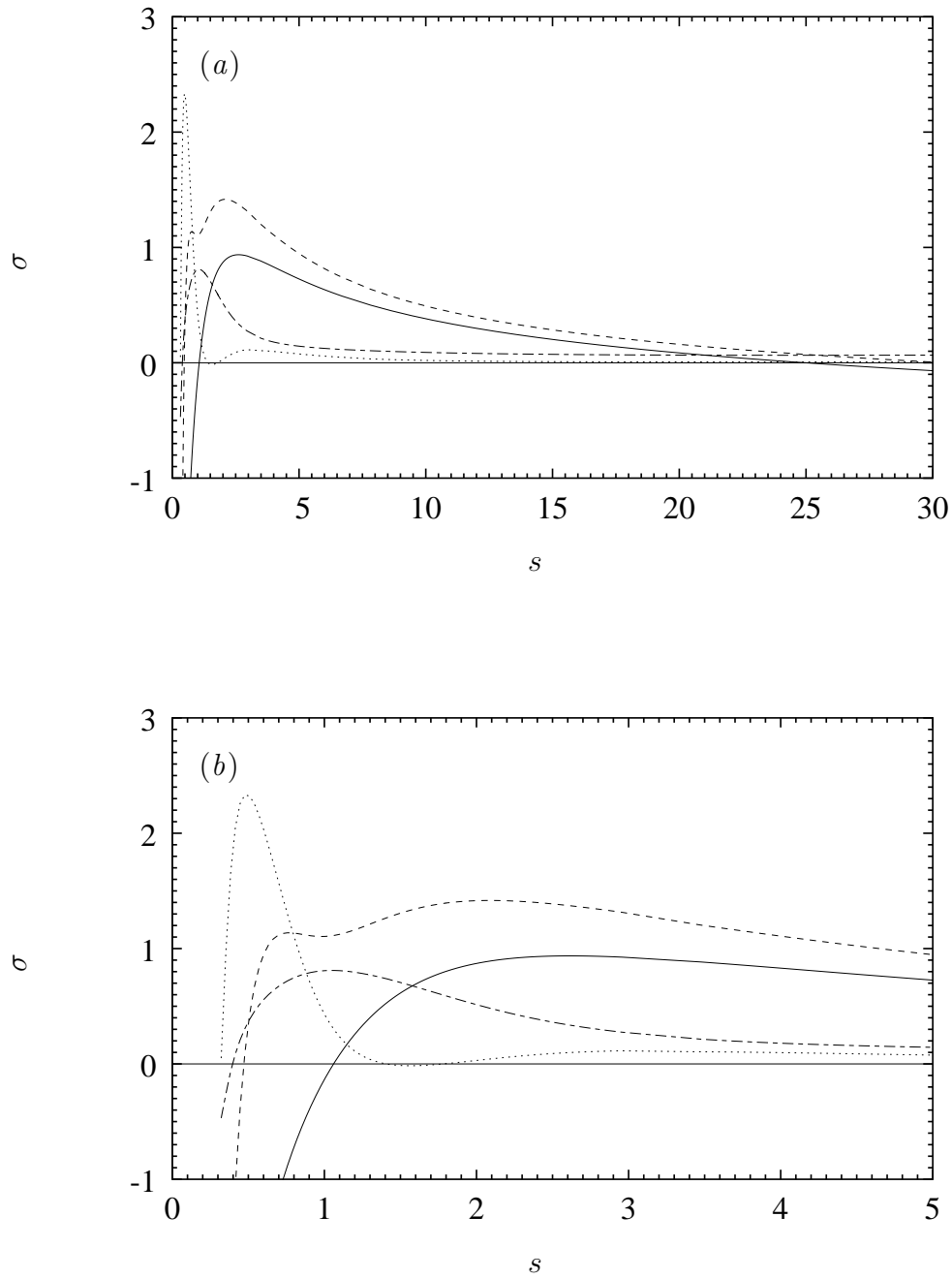
Figure 5.31: Terms contributing to the nonparallel growth-rate: —— QPWC, - - - - NPWC, ········ nonparallel meanflow, —·— eigenfunction distortion. Frame (a) shows the entire unstable region, (b) is a closeup near the leading-edge. Flow parameters: $\beta = 35$, $\mathsf{M} = 0.8$, $\mathsf{Re} = 1 \times 10^5$, $\theta = 35°$.
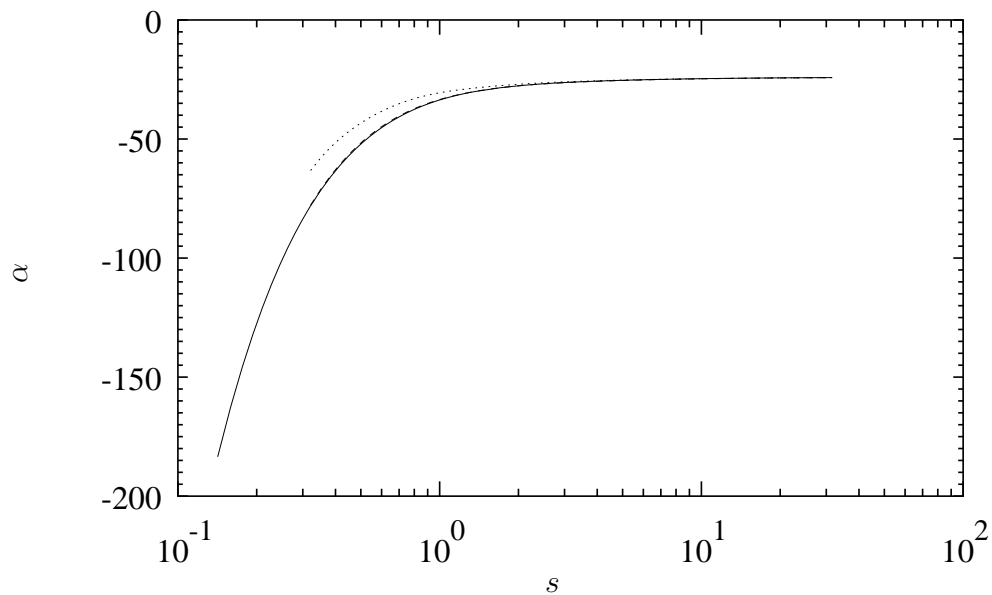
Figure 5.32: Comparison of wavenumber predictions: —— QPNC, - - - - QPWC, ········ NPWC. Flow parameters: $\beta = 35$, $\mathsf{M} = 0.8$, $\mathsf{Re} = 1 \times 10^5$, $\theta = 35°$.
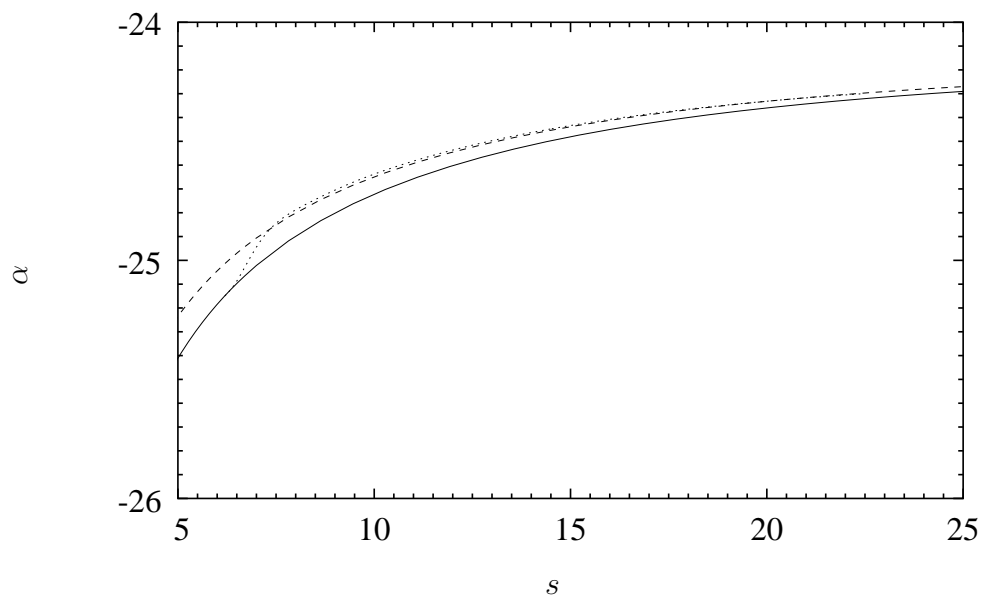
Figure 5.33: Comparison of wavenumber predictions: —— QPWC, - - - - NPWC, ········ LNS. Flow parameters: $\beta = 35$, $\mathsf{M} = 0.8$, $\mathsf{Re} = 1 \times 10^5$, $\theta = 35°$.
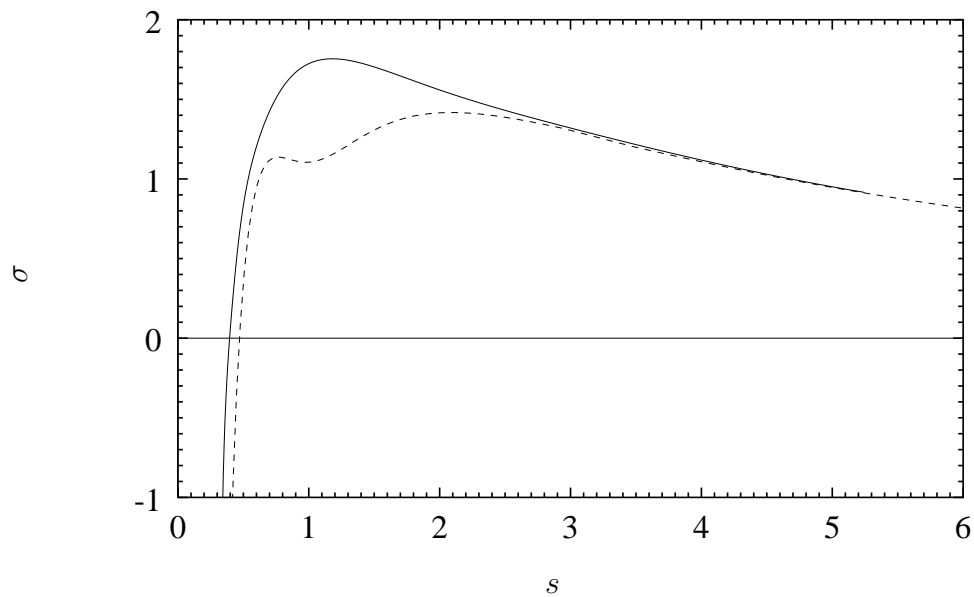
Figure 5.34: Comparison of NPWC and LNS growth-rates near the leading-edge: —— LNS, - - - - NPWC. Flow parameters: $\beta = 35$, $\mathsf{M} = 0.8$, $\mathsf{Re} = 1 \times 10^5$, $\theta = 35°$.
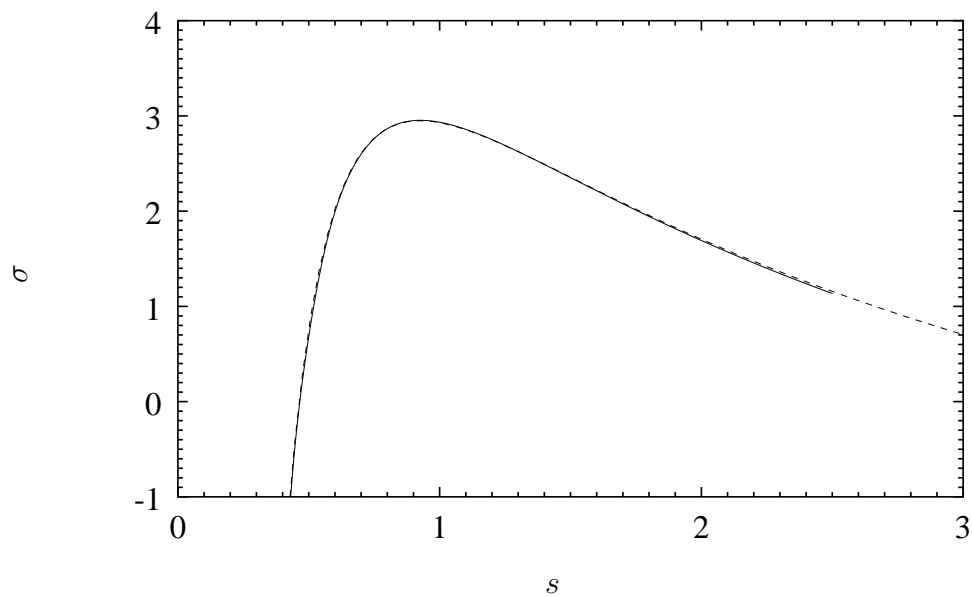
Figure 5.35: Comparison of —— LNS and - - - - NPWC growth-rates for $\beta = 100$, $\mathsf{M} = 0.8$, $\mathsf{Re} = 1 \times 10^5$, and $\theta = 35°$.
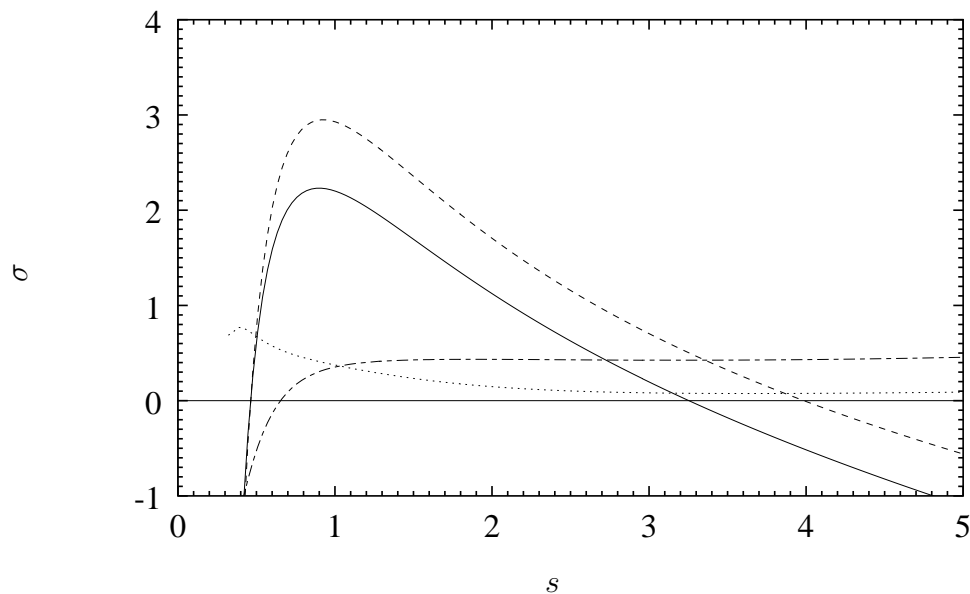
Figure 5.36: Contributions to nonparallel growth-rate: —— QPWC, - - - - NPWC, ········ nonparallel meanflow term, and —·— eigenfunction distortion term for $\beta = 100$, $M = 0.8$, $Re = 1 \times 10^5$, and $\theta = 35°$.
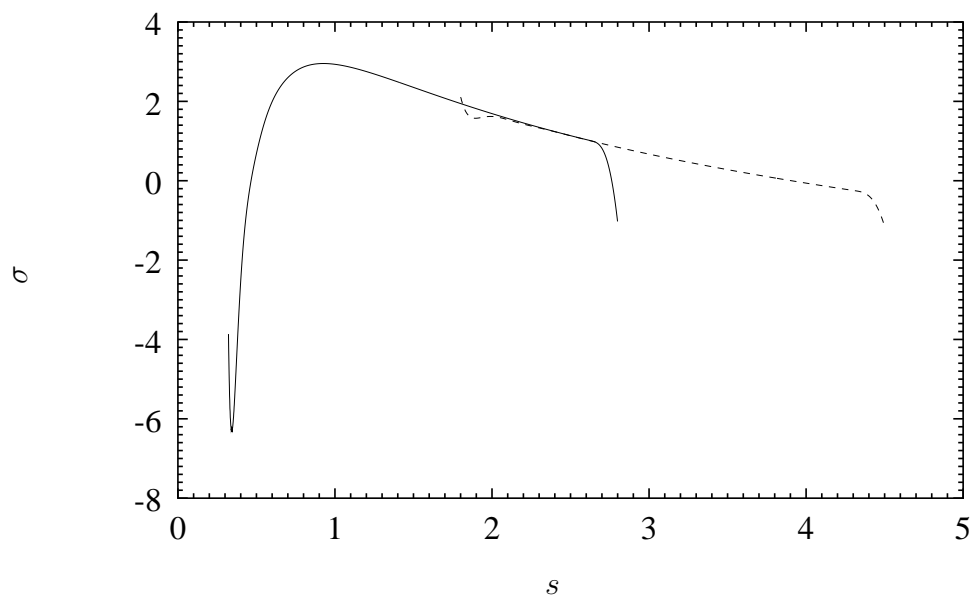
Figure 5.37: Growth-rate from two overlapping domains for $\beta = 100$: —— is domain for $s \in [0.32, 3.18]$ while - - - - is for $s \in [1.78, 5.12]$. The flow conditions are $M = 0.8$, $Re = 1 \times 10^5$, and $\theta = 35°$.
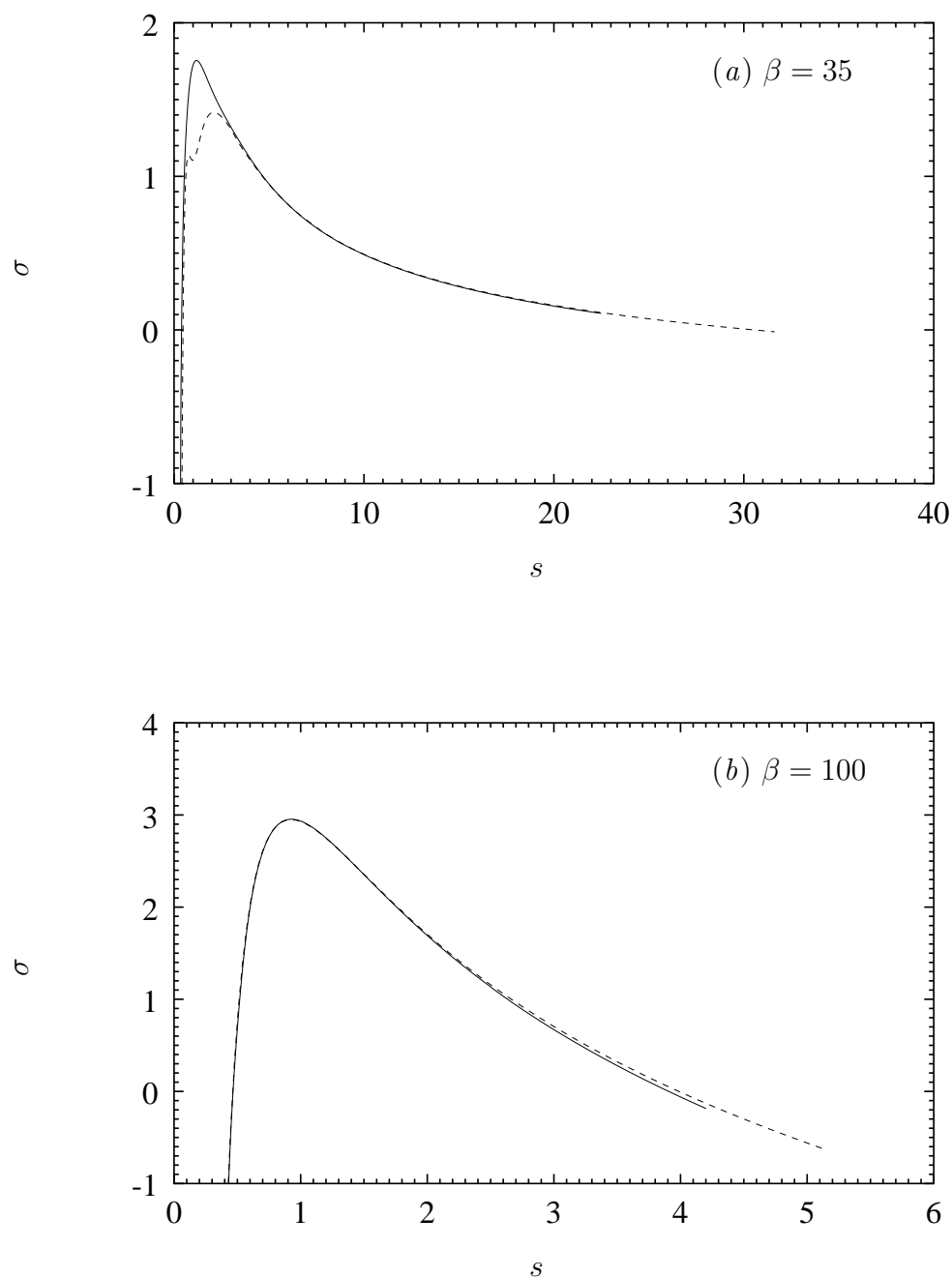
Figure 5.38: LNS growth-rate, based on E'_k, for (a) $\beta = 35$ and (b) $\beta = 100$ compared to NPWC: —— is LNS while - - - - is NPWC. The flow conditions are $\mathsf{M} = 0.8$, $\mathsf{Re} = 1 \times 10^5$, and $\theta = 35°$.
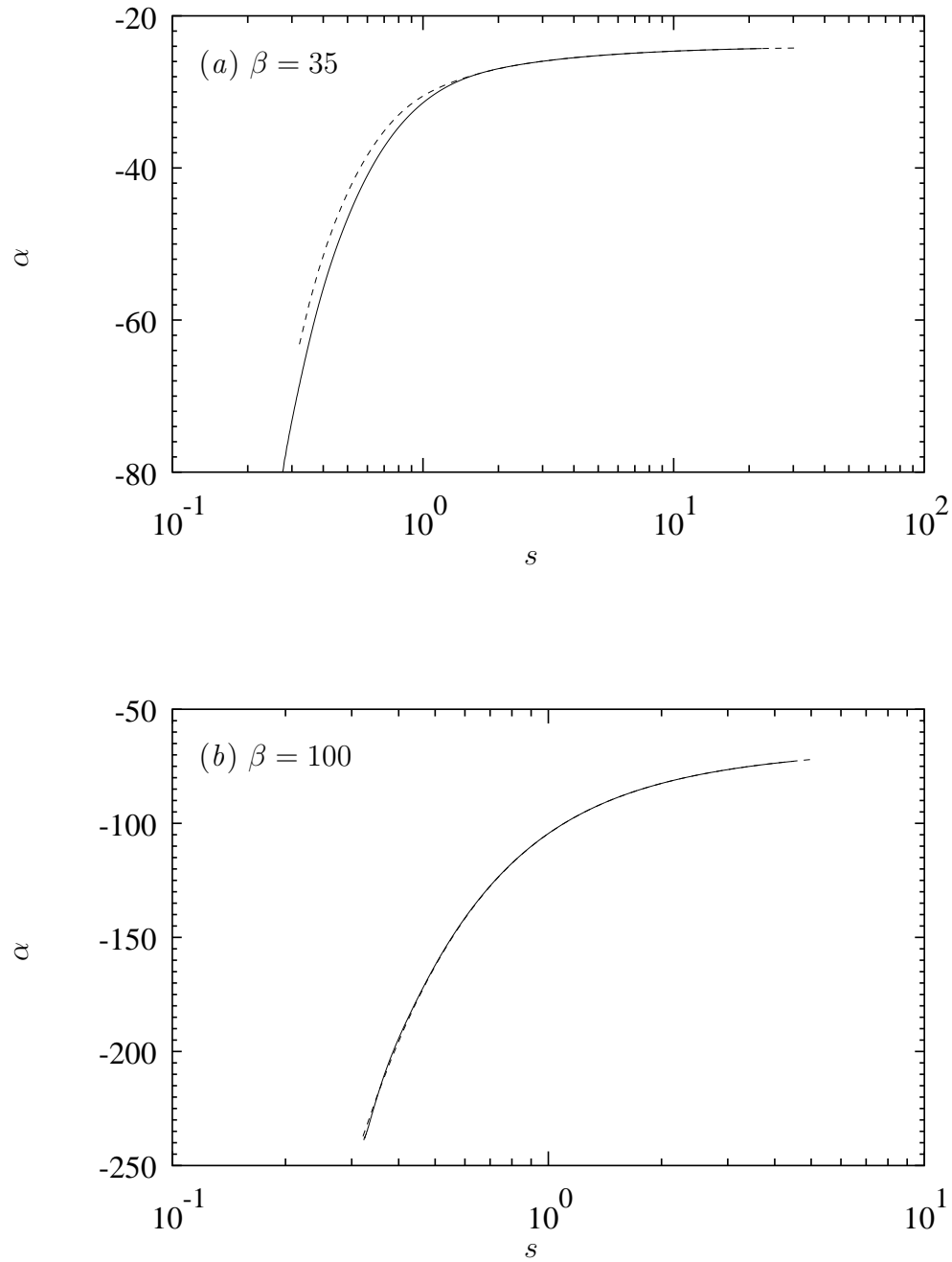
Figure 5.39: LNS wavenumber, based on $|\hat{v}_s|_{max}$, for (a) $\beta = 35$ and (b) $\beta = 100$ compared to NPWC: ——— is LNS while - - - - is NPWC. The flow conditions are $\mathsf{M} = 0.8$, $\mathsf{Re} = 1 \times 10^5$, and $\theta = 35°$.
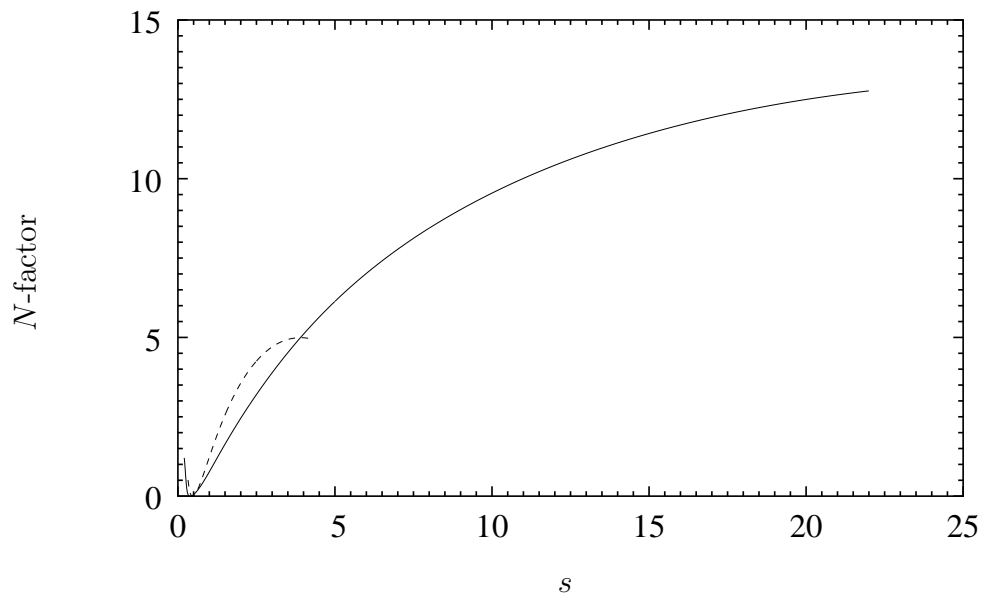
Figure 5.40: Evolution of the N-factor for ——— $\beta = 35$ and - - - - $\beta = 100$ with the flow conditions $\mathsf{M} = 0.8$, $\mathsf{Re} = 1 \times 10^5$, and $\theta = 35°$.
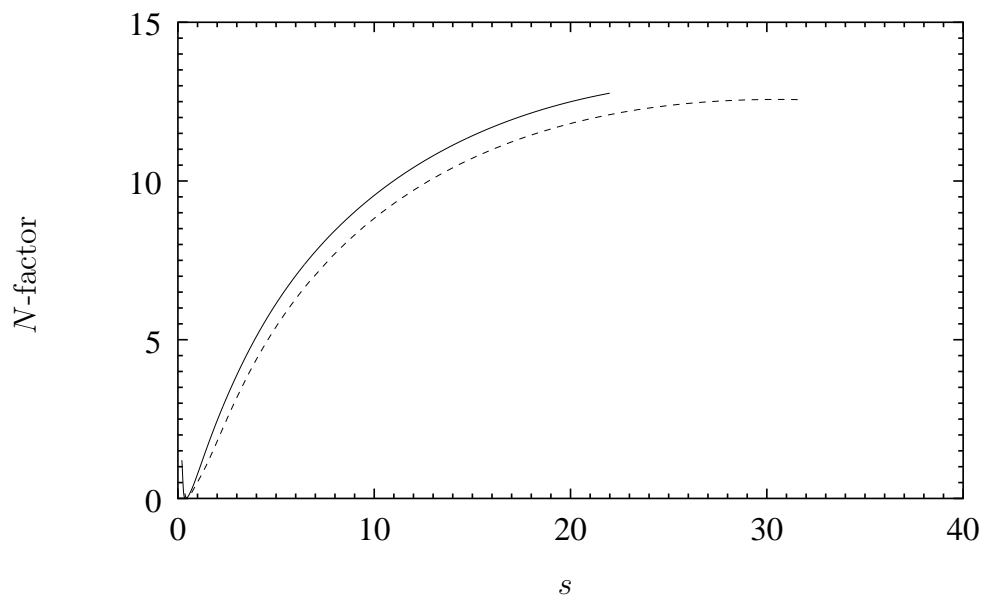
Figure 5.41: Comparison of the N-factor for $\beta = 35$: ——— is LNS and - - - - is NPWC. The flow conditions are $\mathsf{M} = 0.8$, $\mathsf{Re} = 1 \times 10^5$, and $\theta = 35°$.
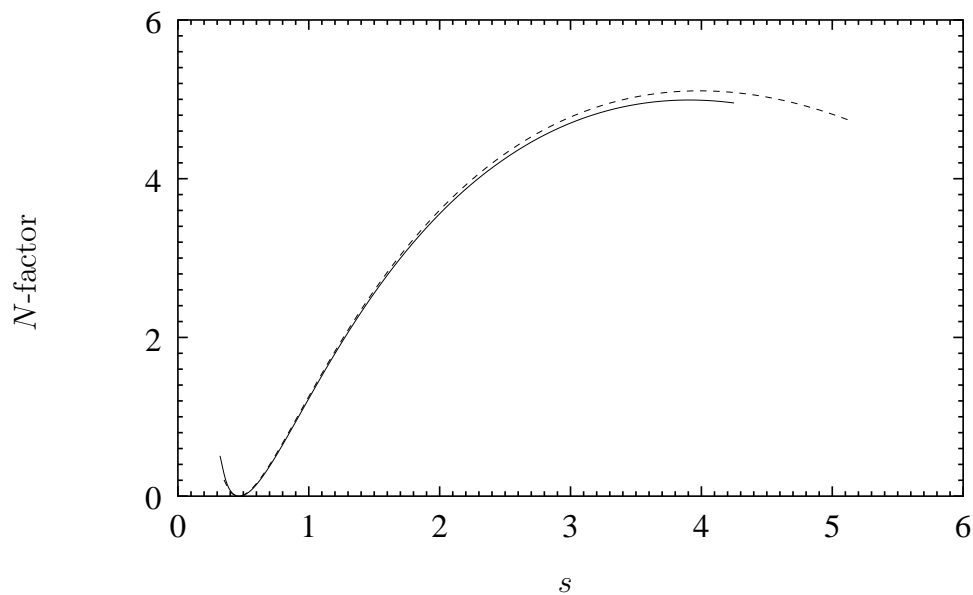
Figure 5.42: Comparison of the N-factor for $\beta = 100$: —— is LNS and - - - - is NPWC. The flow conditions are $\mathsf{M} = 0.8$, $\mathsf{Re} = 1 \times 10^5$, and $\theta = 35°$.
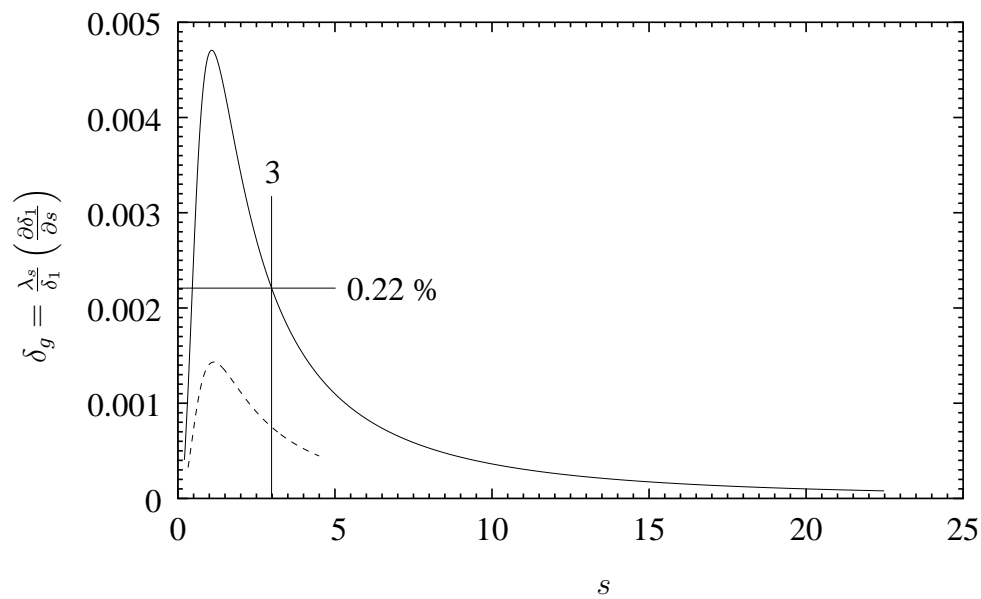
Figure 5.43: Approximate criterion for the failure of nonparallel linear stability theory: —— $\beta = 35$, - - - - $\beta = 100$.
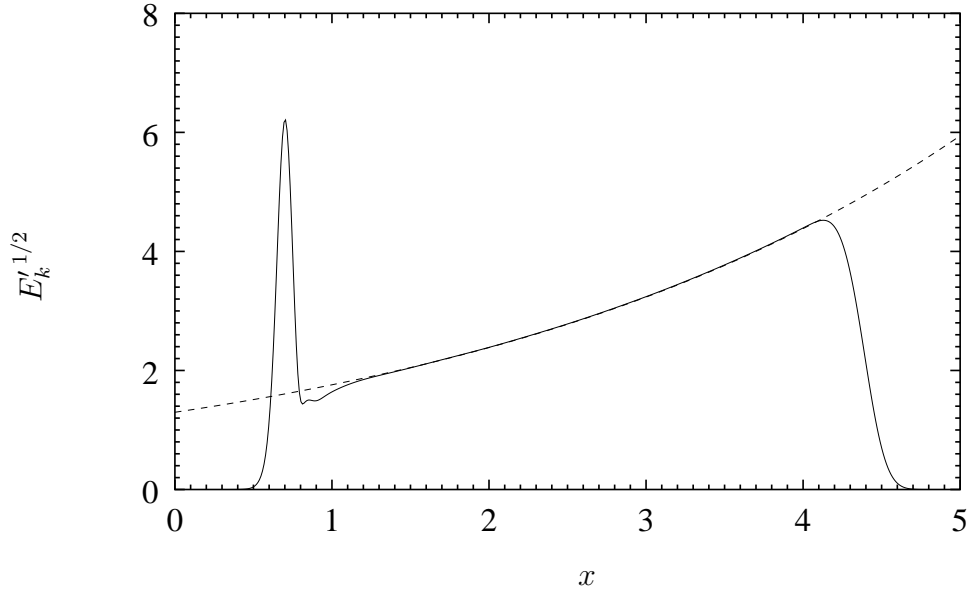
Figure 5.44: Evolution of $E_k'^{1/2}$ on a flat plate with parallel FSC profile downstream of a bump at $x_w = 0.7$ with $\sigma_w = 0.05$: —— LNS and ---- FRNT for the flow conditions $\beta = 35$, $\mathsf{M}_e = 0.657$, $\mathsf{Re} = 1 \times 10^5$, and $\theta_e = 54.5°$.
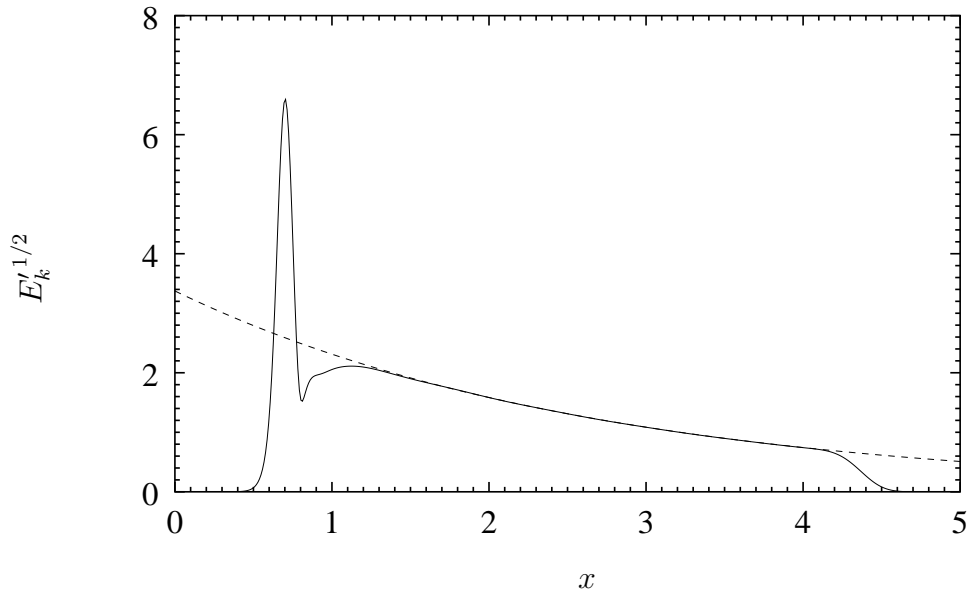
Figure 5.45: Evolution of $E_k'^{1/2}$ on a flat plate with parallel FSC profile downstream of a bump at $x_w = 0.7$ with $\sigma_w = 0.05$: —— LNS and ---- FRNT for the flow conditions $\beta = 30$, $\mathsf{M}_e = 0.657$, $\mathsf{Re} = 1 \times 10^5$, and $\theta_e = 54.5°$.
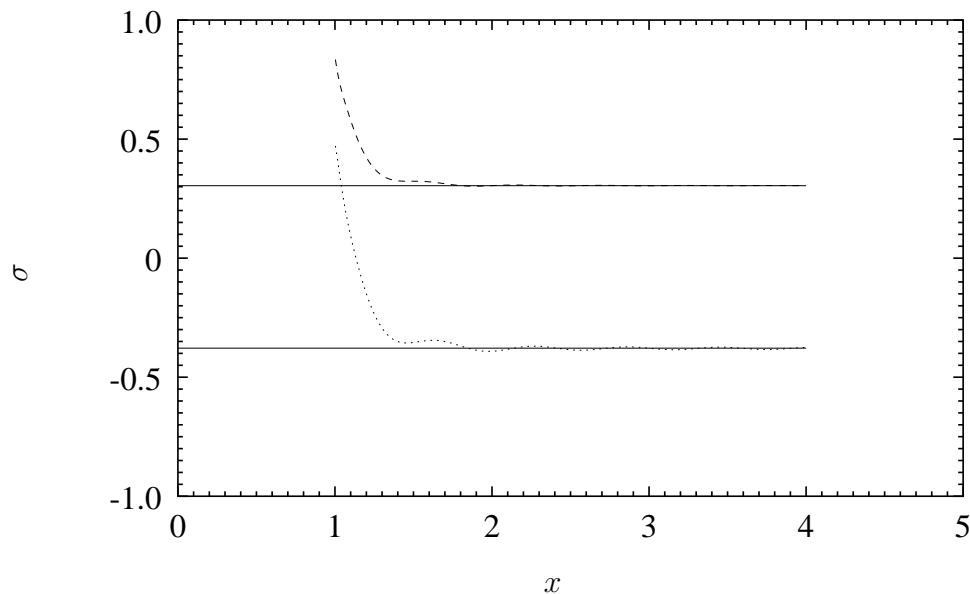
Figure 5.46: Evolution of the growth-rate for a flat plate with parallel FSC profile downstream of a bump at $x_w = 0.7$ with $\sigma_w = 0.05$: —— LST, - - - - LNS with $\beta = 35$ and ⋯⋯ LNS with $\beta = 30$ for the flow conditions $\mathsf{M}_e = 0.657$, $\mathsf{Re} = 1 \times 10^5$, and $\theta_e = 54.5°$.
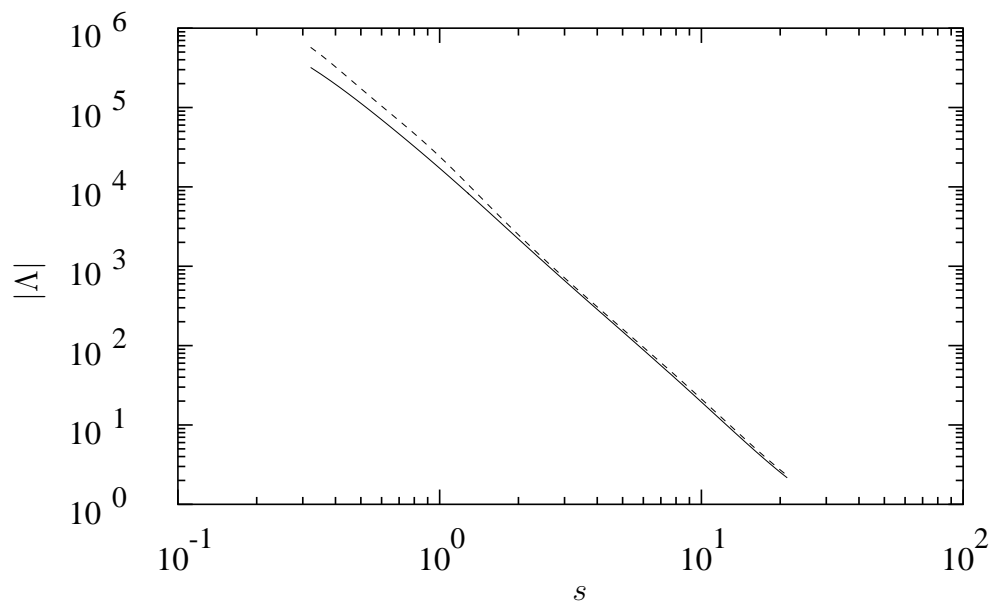
Figure 5.47: Magnitude of the efficiency function for $\beta = 35$: —— no curvature and - - - - with curvature for the flow conditions $\mathsf{M} = 0.8$, $\mathsf{Re} = 1 \times 10^5$, and $\theta = 35°$.
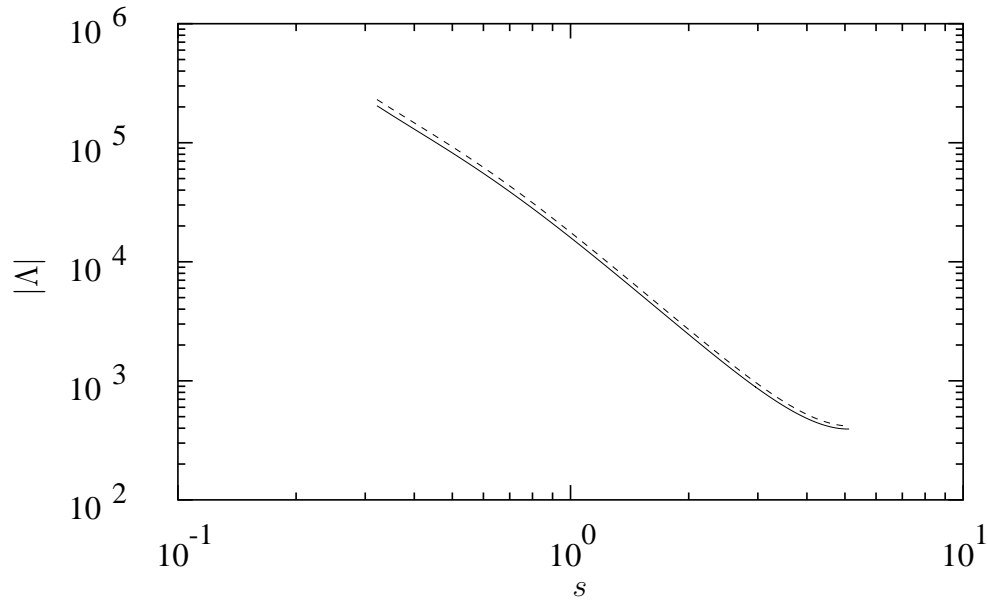
Figure 5.48: Magnitude of the efficiency function for $\beta = 100$: —— no curvature and ---- with curvature for the flow conditions $\mathsf{M} = 0.8$, $\mathsf{Re} = 1 \times 10^5$, and $\theta = 35°$.
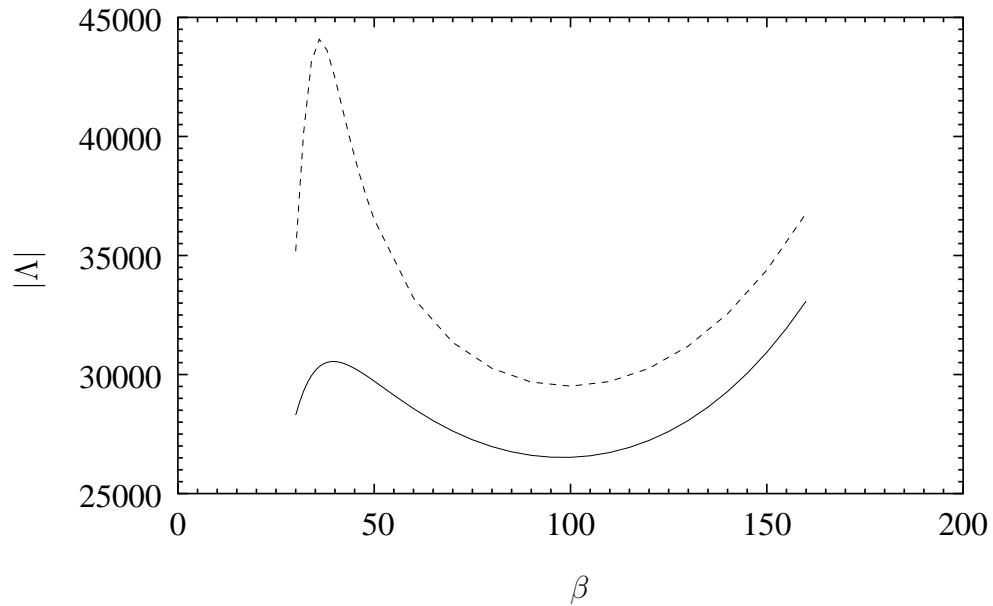
Figure 5.49: Variation of the magnitude of the receptivity efficiency for $s = 0.804$: —— no curvature and ---- with curvature for the flow conditions $\mathsf{M} = 0.8$, $\mathsf{Re} = 1 \times 10^5$, and $\theta = 35°$.
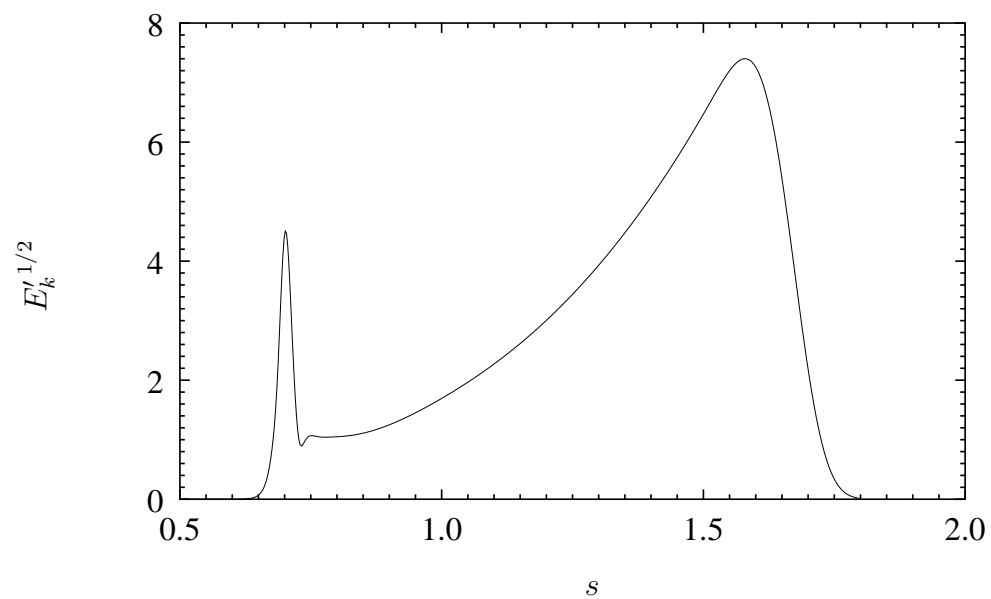
Figure 5.50: Evolution of $E_k'^{1/2}$ for $\beta = 100$, case 3.
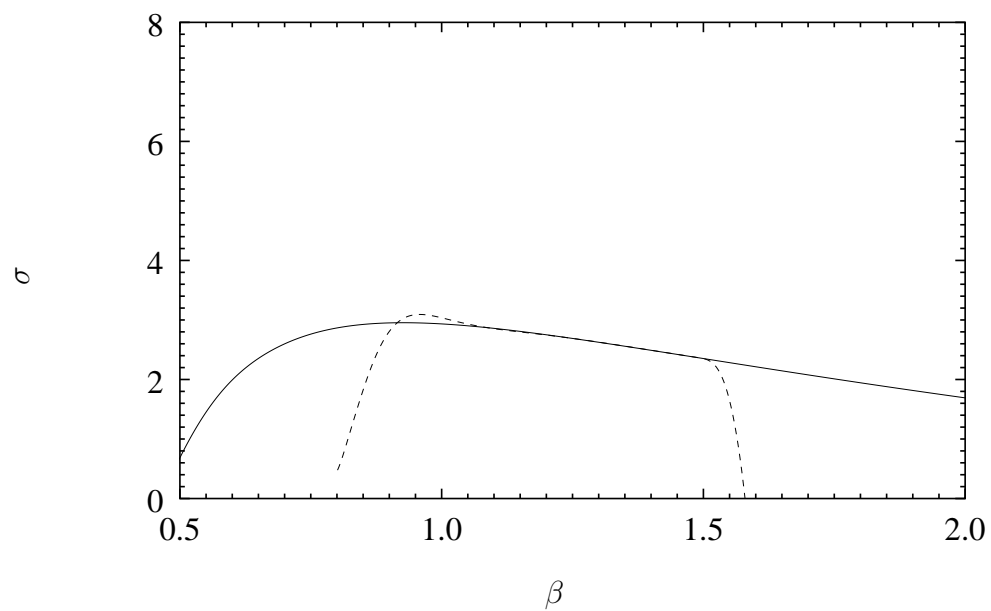
Figure 5.51: Growth rate based on E_k' for $\beta = 100$, - - - - case3, compared to ——— LNS stability result.
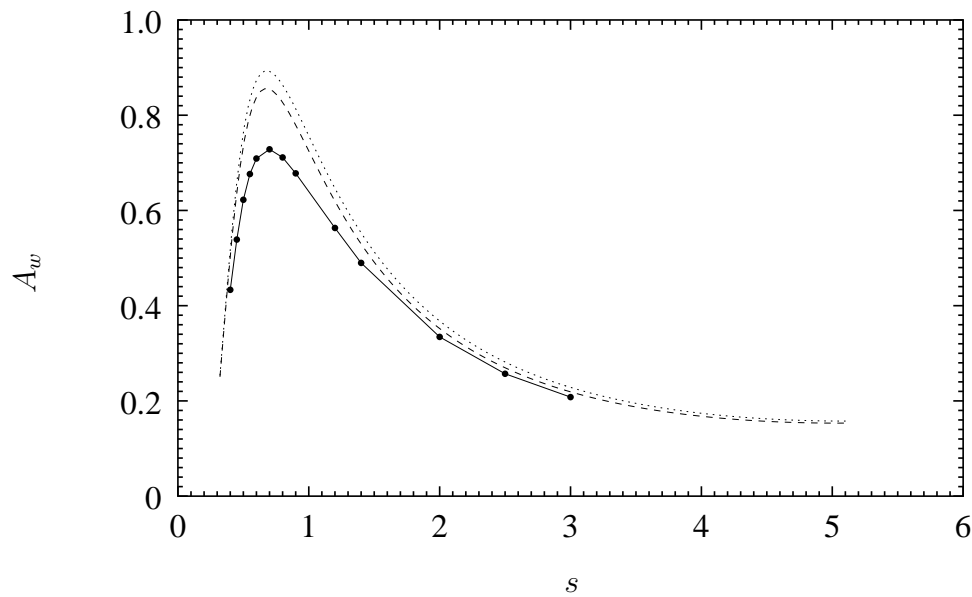
Figure 5.52: Effective amplitude at the bump location for $\beta = 100$ and $\sigma_w = 0.01$. —•— LNS, ---- FRNT no curvature, and ········ FRNT with curvature.
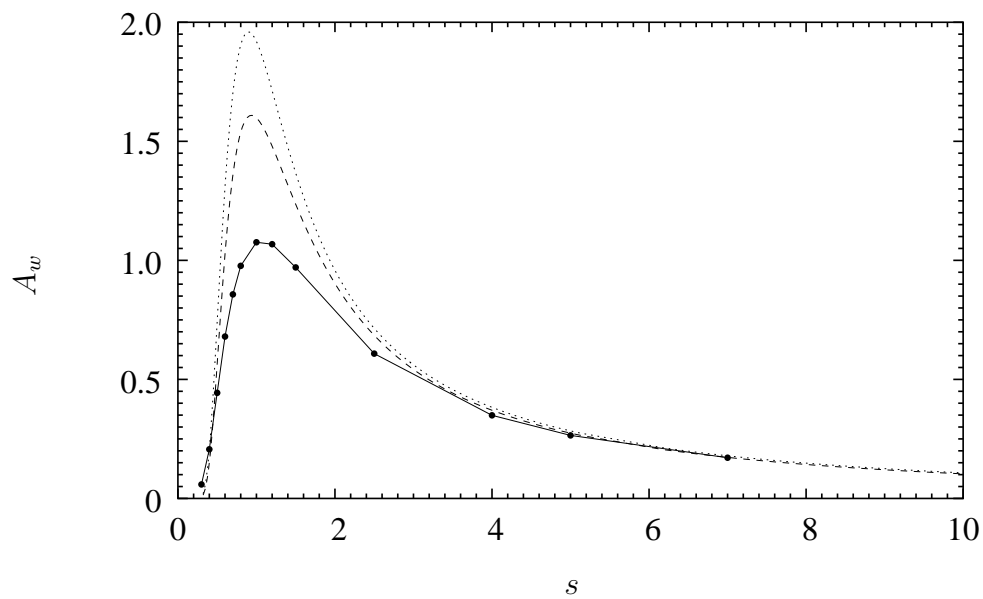
Figure 5.53: Effective amplitude at the bump location for $\beta = 35$ and $\sigma_w = 0.05$. —•— LNS, ---- FRNT no curvature, and ········ FRNT with curvature.
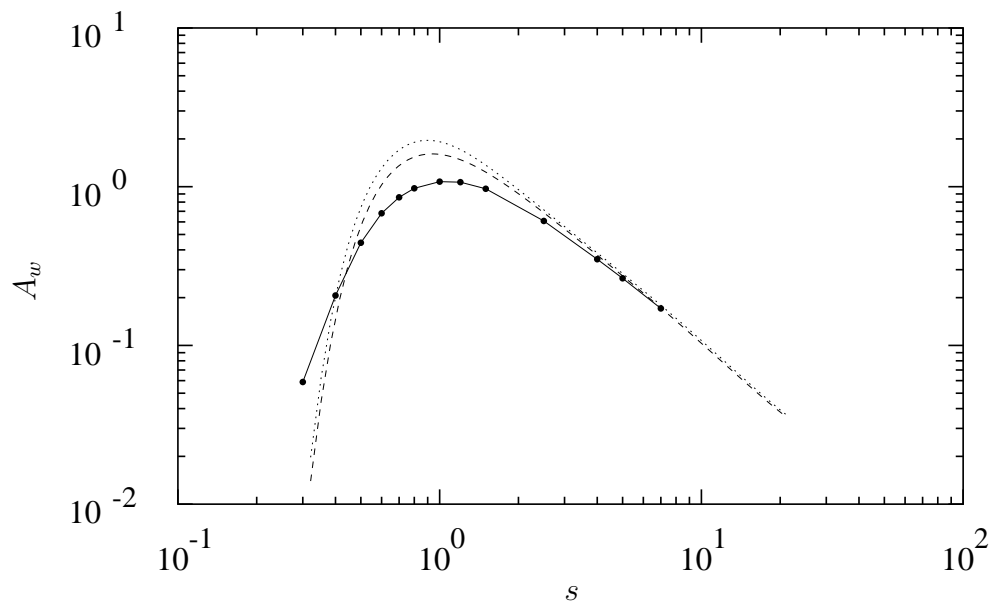
Figure 5.54: Effective amplitude at the bump location for $\beta = 35$ and $\sigma_w = 0.05$. —•— LNS, ---- FRNT no curvature, and ········ FRNT with curvature.
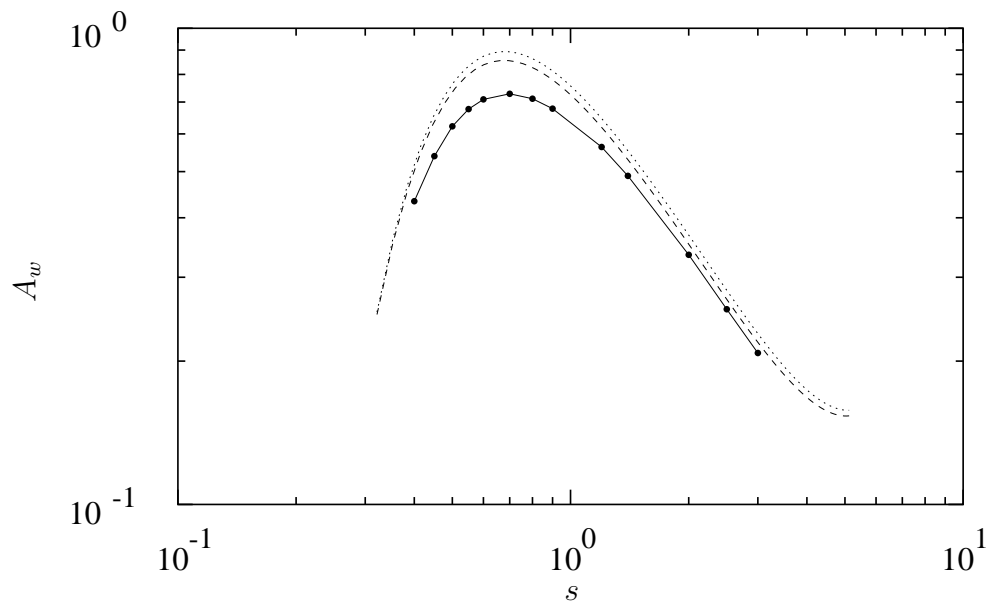
Figure 5.55: Effective amplitude at the bump location for $\beta = 100$ and $\sigma_w = 0.01$. —•— LNS, ---- FRNT no curvature, and ········ FRNT with curavture.
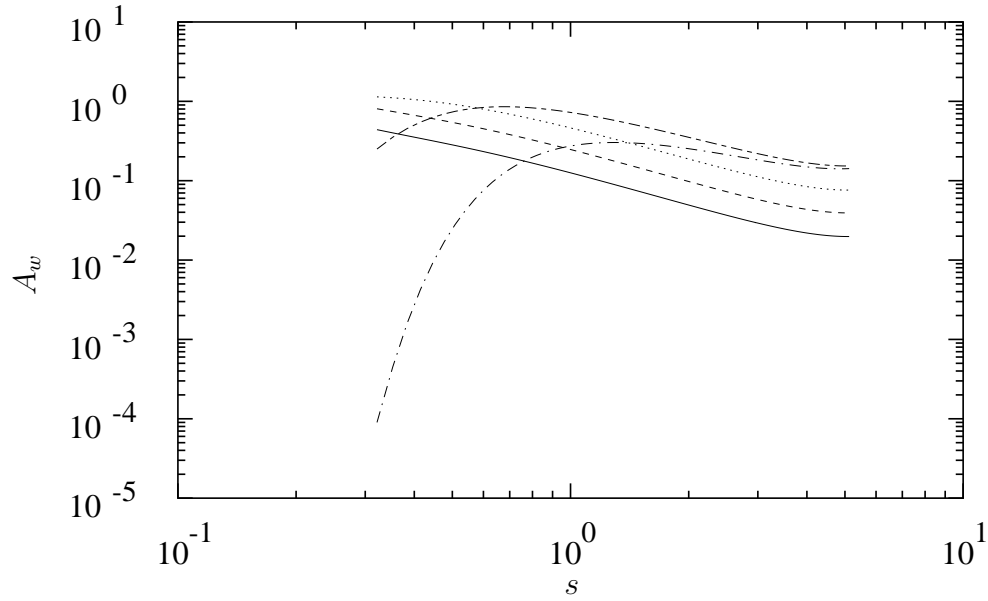
Figure 5.56: The effect of σ_w on the FRNT predicted amplitude, A_w, for $\beta = 100$ without curvature: ——— $\sigma_w = 0.001$, ---- 0.002, ········· 0.004, —–— 0.01, —·— 0.02 .
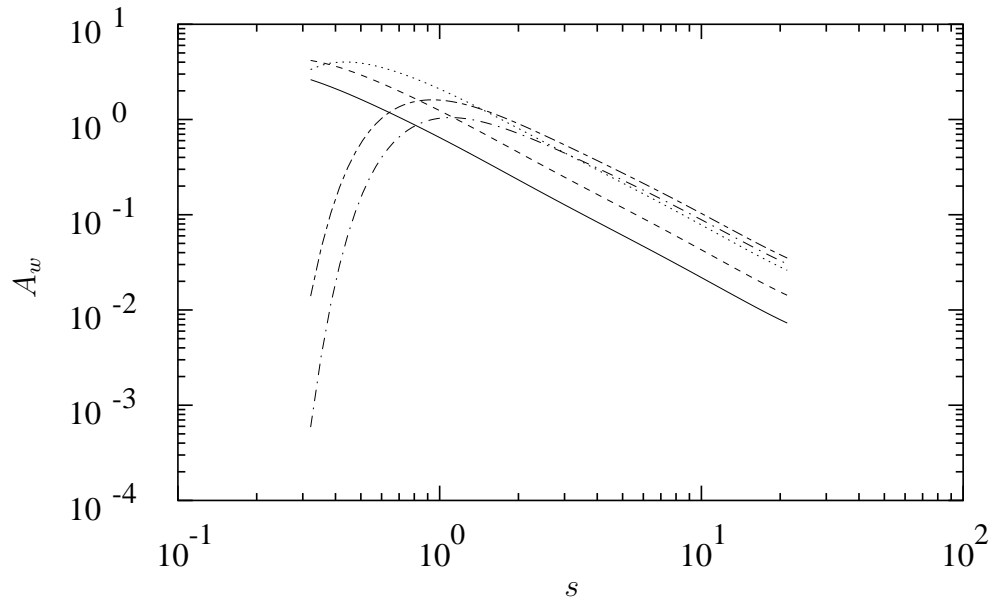
Figure 5.57: The effect of σ_w on the FRNT predicted amplitude, A_w, for $\beta = 35$ without curvature: ——— $\sigma_w = 0.005$, ---- 0.01, ········· 0.02, —–— 0.05, —·— 0.06 .
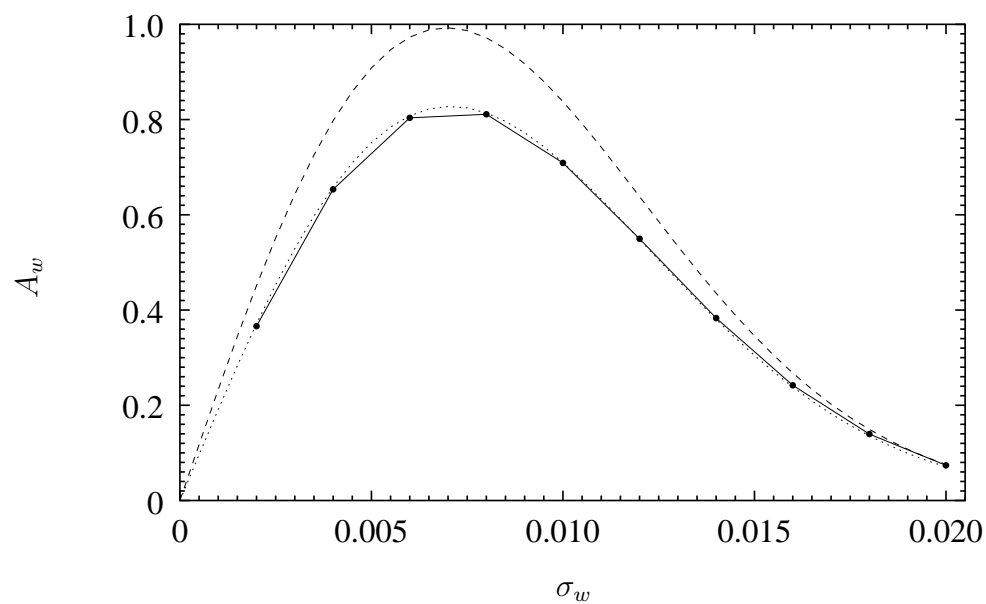
Figure 5.58: Variation of A_w with σ_w at $s = 0.6$, $\beta = 100$. —•— LNS; ---- FRNT no curvature, ········ is a curve fitted to the LNS results using $|\Lambda| = 193$, $\alpha = -141.5$.
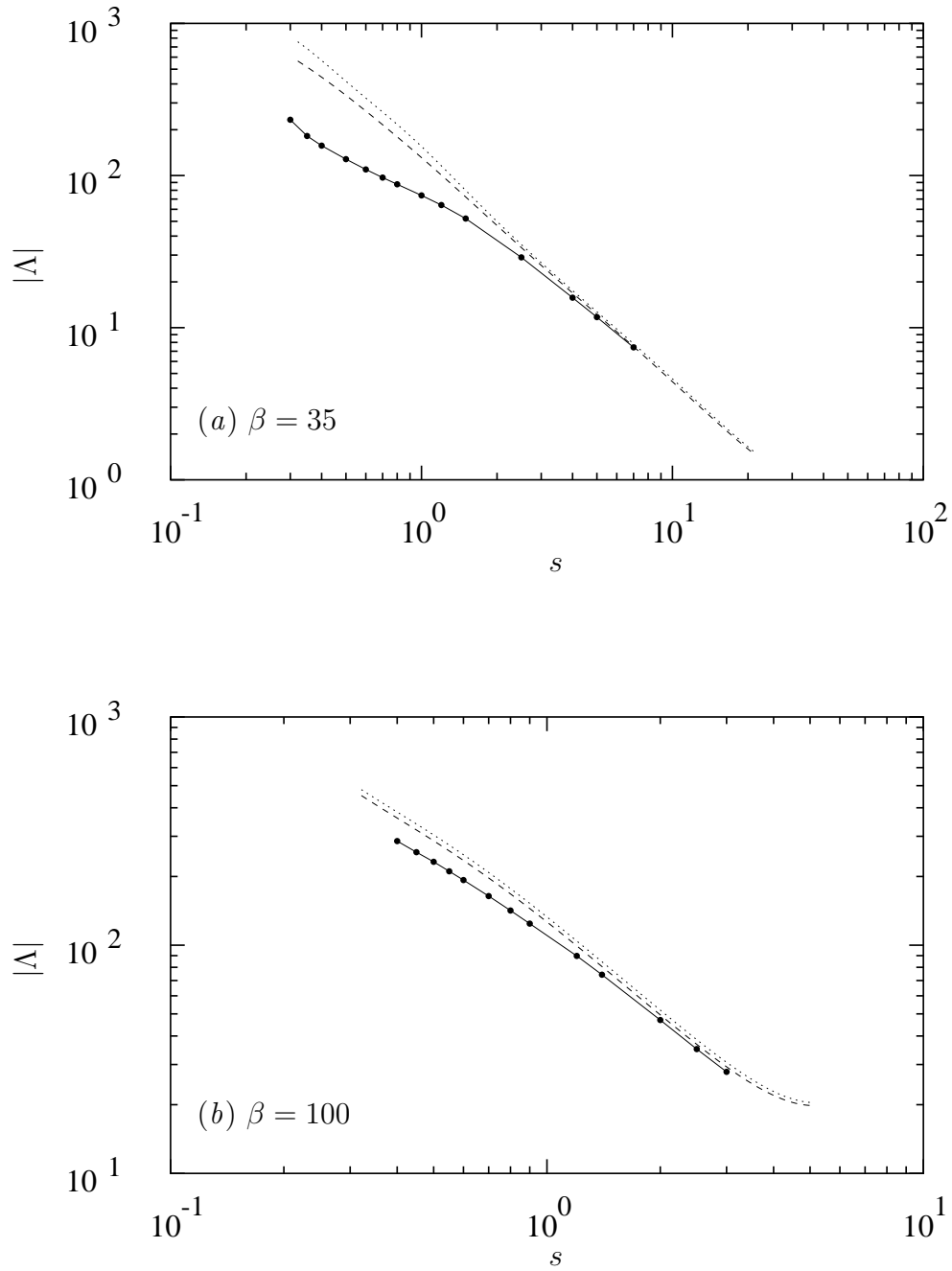
Figure 5.59: Receptivity efficiency function extracted from LNS for (*a*) $\beta = 35$ and (*b*) $\beta = 100$ compared to FRNT: —•— is LNS, ---- is FRNT no curvature, and ········ is FRNT with curvature. The flow conditions are $\mathsf{M} = 0.8$, $\mathsf{Re} = 1 \times 10^5$, and $\theta = 35°$.

Chapter 6

Conclusions and Recommendations

6.1   Conclusions

The receptivity of the three-dimensional boundary-layer on a high-speed, swept, parabolic-cylinder with surface roughness has been investigated using numerical simulation. Taking advantage of the linearity of the receptivity process, a numerical method is developed to accurately and efficiently solve receptivity problems near a swept leading-edge. In this method, the Navier–Stokes equations are written in terms of a nonlinear meanflow solution and a linear disturbance about the meanflow. Equations are developed for both the meanflow and disturbances and these equations are solved in terms of primitive variables using a generalized coordinate system to represent an arbitrary, infinite-span, leading-edge geometry. Spatial derivatives in the plane of the leading-edge are approximated with a fourth-order central-difference scheme. For the linearized disturbance equations, a single Fourier mode is used in the spanwise direction. Due to the high spatial resolution required near the leading edge and in the boundary layer, a fully implicit time-advancement scheme is implemented. To improve efficiency for unsteady disturbances, the linearized equations are solved in the frequency domain. The implicit equations are solved at every iteration using approximate factorization with a specially optimized block-penta-diagonal matrix solver. All boundary conditions are implemented fully implicitly to preserve convergence of the iterative solver.

The numerical method has been extensively validated for model problems that represent the physical phenomena expected in receptivity calculations. These include Tollmien-Schlichting waves in a parallel boundary-layer, crossflow vortices in a parallel boundary-layer, and acoustic scattering from a circular cylinder. Exact solutions are available for each of these problems and the current numerical solutions are shown to converge to the exact solutions. In performing these model calculations, the resolution required to adequately resolve each physical phenomena is established. As a further test of the method, the problem of leading-edge receptivity to sound is investigated

for a flat-plate with a super-ellipse leading-edge. The geometry and flow conditions are modeled after an incompressible calculation performed by Lin [63]. Our meanflow solution at $M = 0.1$ is shown to be in very good agreement with the incompressible solution. Furthermore, our acoustic receptivity results qualitatively agree with Lin's solution, and the amplitude of the Tollmien-Schlichting wave at the first neutral-point is within 10% of Lin's value.

With the computational method validated, the receptivity of a three-dimensional boundary-layer on a swept, infinite-span parabolic-cylinder subject to surface roughness is investigated. This geometry serves as a first-order approximation to the leading-edge of a swept-wing. Both two- and three-dimensional mean solutions are obtained. The two-dimensional solutions at low Mach numbers compare well with the reference incompressible solutions of Davis [31]. The three-dimensional meanflow over a swept parabolic cylinder is obtained for conditions which are modeled after a transonic commercial airliner in cruise condition. In particular, the Reynolds number, when converted to an equivalent wing-chord takes the value of 10^7, which is in the realm of flight Reynolds numbers. The characteristics of this three-dimensional boundary-layer are documented including linear stability predictions incorporating curvature and nonparallel effects. The linear stability code solves the full, compressible, stability-equations in curvilinear coordinates. Unlike recent stability analyses for swept circular cylinders, we allow for chordwise variations of the surface curvature in our formulation. Nonparallel effects are accounted for using a perturbation approach by allowing the solution to vary slowly in the chordwise direction. By including compressibility, curvature, and nonparallel effects our linear-stability-code represents the current "state-of-the-art" in local stability analysis.

The stability analysis for the swept parabolic-cylinder shows that convex surface curvature reduces the growth-rate, while nonparallel effects increase the growth-rate of stationary crossflow vortices. These results are in qualitative agreement with recent analysis for a swept circular-cylinder [76]. Stability calculations performed using the full Linearized Navier–Stokes (LNS) equations are used to provide reference solutions which have an exact account of nonparallel effects. Comparing the nonparallel stability results to the LNS solutions shows that for short wavelength modes, $\beta = 100$, the nonparallel theory agrees well with the LNS solutions. However, for longer wavelengths, $\beta = 35$, the nonparallel theory breaks down near the leading-edge causing

qualitative, as well as quantitative, errors in the stability characteristics.

Receptivity to surface roughness is investigated by modeling a roughness element as a spanwise periodic, linear perturbation of the wall boundary with a Gaussian distribution in the chordwise direction. Receptivity results are obtained both from LNS solutions with surface-roughness boundary-conditions and from Finite Reynolds Number Theory (FRNT) predictions. The theoretical predictions are determined both with and without surface curvature to identify the effect of curvature on receptivity. Based on the theoretical predictions, curvature is shown to enhance the receptivity efficiency over the entire unstable region and the curvature effect is greatest near the lower branch of the neutral curve. The impact of nonparallel flow on the receptivity of crossflow vortices is established by a series of LNS calculations with surface roughness placed at various locations on the wall. Comparison to the FRNT shows that nonparallel flow significantly attenuates the initial amplitude of stationary crossflow vortices downstream of a roughness element near the leading-edge. The effect is most severe for the long wavelength $\beta = 35$ case, where FRNT over-predicts the amplitude of the crossflow mode by as much as 77%. For the shorter wavelength case, $\beta = 100$, the maximum error in the FRNT prediction is 29%. Sufficiently far from the leading-edge, the theoretical predictions approach the LNS solution and are within 5% of the LNS solution at the furthest downstream stations considered here.

By considering a range of bump widths, we have verified the FRNT result that the receptivity amplitude can be written as the product of the Fourier coefficient of the chordwise roughness distribution at the local crossflow wavenumber and a function representing the efficiency of the receptivity process. Based on this form of the solution, the receptivity efficiency function is extracted from the linearized Navier–Stokes solutions. The results indicate conclusively that nonparallel effects dramatically reduce receptivity near the leading-edge. For the cases considered here, the FRNT over-predicts the efficiency function by as much as a factor of 3 near the first neutral point. These results clearly indicate that the prediction of crossflow receptivity near a realistic leading-edge must account for the strongly nonparallel flow near the upstream neutral point.

6.2   Recommendations for Future Research

The most pressing need for future research is in the addition of nonparallel corrections to the FRNT receptivity predictions. Based on the current results, the inclusion of nonparallel effects is vital for the accurate prediction of crossflow receptivity for realistic geometries. The current solutions provide a basis upon which enhanced theories can be evaluated.

Another area for future research is the investigation of nonlinear receptivity mechanisms for surface roughness in a three-dimensional boundary layer. A recent theoretical investigation by Choudhari & Duck [18] suggests that receptivity is likely to become nonlinear even before the stability characteristics of the boundary layer are modified by the surface roughness. This early nonlinear effect may be partially responsible for the extreme sensitivity to surface roughness observed by Radeztsky *et al.* [86] in their experiments. Numerical simulations of nonlinear receptivity due to surface roughness would provide valuable information on this relatively unexplored phenomenon including: the critical bump height for the onset of nonlinearity receptivity; the possibly nonlinear wavelength selection processes; and the early onset of nonlinear, modal interactions.

The application of Parabolized Stability Equations (PSE) to the study of receptivity is also an avenue for future research. Recent work with the PSE method for the prediction of receptivity [52] has involved the imposition of inhomogeneous boundary conditions on the initial condition for the PSE marching procedure. Unfortunately, this method appears to rely on the approximate transient behavior during the startup of PSE marching. Therefore, the relationship of the boundary condition to the final instability waves downstream is unclear. Comparisons to linearized Navier–Stokes solutions, such as those presented here, are required to determine the capabilities and limitations of PSE for receptivity investigations. A related area for research involves the coupling of PSE to the LNS calculations performed here. This offers the advantage of computing LNS solutions on short domains to capture the receptivity process, and then feeding the established boundary layer disturbances into a PSE code for subsequent linear and nonlinear evolution.

Finally, recent research by Lingwood [66, 65] on the nature of the crossflow instability on the rotating disk has shown that absolute instability is possible for this flow.

However, the absolute/convective nature of the crossflow instability for the infinite-span swept-wing is currently unknown, although all current evidence indicates that it is purely convective. As suggested by Tobak [107], the absolute/convective nature of this flow can be investigated using the techniques developed in this thesis by performing a transient calculation where the surface roughness boundary condition is applied impulsively at the start of the calculation. The development of the resulting wave packet can then be tracked similar to that done in the experiments of Lingwood [65].

Appendix A

Matrix Definitions

A.1 Matrices for the Linearized Navier–Stokes Equations

The following appendix lists the nonzero elements of the matrices defined in section 2.3 for the linearized Navier–Stokes equations. All terms are evaluated at the base-flow condition, $\mathbf{U} = \bar{\mathbf{U}}$.

$\boxed{\mathbf{A}\ \text{matrix}}$

$$A_{11} = u_1 \tag{A.1}$$

$$A_{12} = \rho \tag{A.2}$$

$$A_{21} = \frac{T}{\rho \gamma \mathsf{M}^2} \tag{A.3}$$

$$A_{22} = u_1 - \frac{1}{\rho \mathsf{Re}} \left(\lambda_{,1} + 2\mu_{,1} \right) \tag{A.4}$$

$$A_{23} = -\frac{1}{\rho \mathsf{Re}} \left(\mu_{,2} \right) \tag{A.5}$$

$$A_{24} = -\frac{1}{\rho \mathsf{Re}} \left(\mu_{,3} \right) \tag{A.6}$$

$$A_{25} = \frac{1}{\gamma \mathsf{M}^2} - \frac{1}{\rho \mathsf{Re}} \left(\lambda_{,T} u_{i,i} + 2\mu_{,T} S_{11} \right) \tag{A.7}$$

$$A_{32} = -\frac{1}{\rho \mathsf{Re}} \lambda_{,2} \tag{A.8}$$

$$A_{33} = u_1 - \frac{1}{\rho \mathsf{Re}} \mu_{,1} \tag{A.9}$$

$$A_{35} = -2\frac{1}{\rho \mathsf{Re}} \mu_{,T} S_{21} \tag{A.10}$$

$$A_{42} = -\frac{1}{\rho \mathsf{Re}} \lambda_{,3} \tag{A.11}$$

$$A_{44} = u_1 - \frac{1}{\rho \mathsf{Re}} \mu_{,1} \tag{A.12}$$

$$A_{45} = -2\frac{1}{\rho\mathsf{Re}}\mu_{,T}S_{31} \tag{A.13}$$

$$A_{52} = (\gamma - 1)T - \frac{\gamma(\gamma - 1)\mathsf{M}^2}{\rho\mathsf{Re}}\left(2\lambda u_{i,i} + 4\mu S_{11}\right) \tag{A.14}$$

$$A_{53} = -\frac{\gamma(\gamma - 1)\mathsf{M}^2}{\rho\mathsf{Re}}\left(4\mu S_{21}\right) \tag{A.15}$$

$$A_{54} = -\frac{\gamma(\gamma - 1)\mathsf{M}^2}{\rho\mathsf{Re}}\left(4\mu S_{31}\right) \tag{A.16}$$

$$A_{55} = u_1 - \frac{\gamma}{\rho\mathsf{PrRe}}\left(\kappa_{,1} + \kappa_{,T}T_{,1}\right) \tag{A.17}$$

$\boxed{\mathbf{B} \text{ matrix}}$

$$B_{11} = u_2 \tag{A.18}$$

$$B_{13} = \rho \tag{A.19}$$

$$B_{22} = u_2 - \frac{1}{\rho\mathsf{Re}}\mu_{,2} \tag{A.20}$$

$$B_{23} = -\frac{1}{\rho\mathsf{Re}}\lambda_{,1} \tag{A.21}$$

$$B_{25} = -2\frac{1}{\rho\mathsf{Re}}\mu_{,T}S_{12} \tag{A.22}$$

$$B_{31} = \frac{T}{\rho\gamma\mathsf{M}^2} \tag{A.23}$$

$$B_{32} = -\frac{1}{\rho\mathsf{Re}}\left(\mu_{,1}\right) \tag{A.24}$$

$$B_{33} = u_2 - \frac{1}{\rho\mathsf{Re}}\left(\lambda_{,2} + 2\mu_{,2}\right) \tag{A.25}$$

$$B_{34} = -\frac{1}{\rho\mathsf{Re}}\left(\mu_{,3}\right) \tag{A.26}$$

$$B_{35} = \frac{1}{\gamma\mathsf{M}^2} - \frac{1}{\rho\mathsf{Re}}\left(\lambda_{,T}u_{i,i} + 2\mu_{,T}S_{22}\right) \tag{A.27}$$

$$B_{43} = -\frac{1}{\rho\mathsf{Re}}\lambda_{,3} \tag{A.28}$$

$$B_{44} = u_2 - \frac{1}{\rho\mathsf{Re}}\mu_{,2} \tag{A.29}$$

$$B_{45} = -2\frac{1}{\rho\mathsf{Re}}\mu_{,T}S_{32} \tag{A.30}$$

$$B_{52} = -\frac{\gamma(\gamma - 1)\mathsf{M}^2}{\rho\mathsf{Re}}\left(4\mu S_{12}\right) \tag{A.31}$$

$$B_{53} = (\gamma - 1)T - \frac{\gamma(\gamma - 1)\mathsf{M}^2}{\rho\mathsf{Re}}(2\lambda u_{i,i} + 4\mu S_{22}) \tag{A.32}$$

$$B_{54} = -\frac{\gamma(\gamma - 1)\mathsf{M}^2}{\rho\mathsf{Re}}(4\mu S_{32}) \tag{A.33}$$

$$B_{55} = u_2 - \frac{\gamma}{\rho\mathsf{PrRe}}(\kappa_{,2} + \kappa_{,T}T_{,2}) \tag{A.34}$$

$\boxed{\mathbf{C}\text{ matrix}}$

$$C_{11} = u_3 \tag{A.35}$$

$$C_{13} = \rho \tag{A.36}$$

$$C_{22} = u_3 - \frac{1}{\rho\mathsf{Re}}\mu_{,3} \tag{A.37}$$

$$C_{24} = -\frac{1}{\rho\mathsf{Re}}\lambda_{,1} \tag{A.38}$$

$$C_{25} = -2\frac{1}{\rho\mathsf{Re}}\mu_{,T}S_{13} \tag{A.39}$$

$$C_{33} = u_3 - \frac{1}{\rho\mathsf{Re}}\mu_{,3} \tag{A.40}$$

$$C_{34} = -\frac{1}{\rho\mathsf{Re}}\lambda_{,2} \tag{A.41}$$

$$C_{35} = -2\frac{1}{\rho\mathsf{Re}}\mu_{,T}S_{23} \tag{A.42}$$

$$C_{41} = \frac{T}{\rho\gamma\mathsf{M}^2} \tag{A.43}$$

$$C_{42} = -\frac{1}{\rho\mathsf{Re}}(\mu_{,1}) \tag{A.44}$$

$$C_{43} = -\frac{1}{\rho\mathsf{Re}}(\mu_{,2}) \tag{A.45}$$

$$C_{44} = u_3 - \frac{1}{\rho\mathsf{Re}}(\lambda_{,3} + 2\mu_{,3}) \tag{A.46}$$

$$C_{45} = \frac{1}{\gamma\mathsf{M}^2} - \frac{1}{\rho\mathsf{Re}}(\lambda_{,T}u_{i,i} + 2\mu_{,T}S_{33}) \tag{A.47}$$

$$C_{52} = -\frac{\gamma(\gamma - 1)\mathsf{M}^2}{\rho\mathsf{Re}}(4\mu S_{13}) \tag{A.48}$$

$$C_{53} = -\frac{\gamma(\gamma - 1)\mathsf{M}^2}{\rho\mathsf{Re}}(4\mu S_{23}) \tag{A.49}$$

$$C_{54} = (\gamma - 1)T - \frac{\gamma(\gamma - 1)\mathsf{M}^2}{\rho\mathsf{Re}}(2\lambda u_{i,i} + 4\mu S_{33}) \tag{A.50}$$

$$C_{55} = u_3 - \frac{\gamma}{\rho \mathsf{Pr} \mathsf{Re}} \left(\kappa_{,3} + \kappa_{,T} T_{,3} \right) \tag{A.51}$$

$\boxed{\mathbf{D} \text{ matrix}}$

$$D_{11} = u_{i,i} \tag{A.52}$$

$$D_{12} = \rho_{,1} \tag{A.53}$$

$$D_{13} = \rho_{,2} \tag{A.54}$$

$$D_{14} = \rho_{,3} \tag{A.55}$$

$$D_{21} = \frac{1}{\rho} \left[u_i u_{1,i} + \frac{T_{,1}}{\gamma \mathsf{M}^2} \right] \tag{A.56}$$

$$D_{22} = u_{1,1} \tag{A.57}$$

$$D_{23} = u_{1,2} \tag{A.58}$$

$$D_{24} = u_{1,3} \tag{A.59}$$

$$D_{25} = \frac{\rho_{,1}}{\rho \gamma \mathsf{M}^2} - \frac{1}{\rho \mathsf{Re}} \left\{ [\lambda_{,T}]_{,1} u_{i,i} + \lambda_{,T} u_{i,i1} + \right.$$
$$\left. 2 [\mu_{,T}]_{,i} S_{1i} + 2\mu_{,T} S_{1i,i} \right\} \tag{A.60}$$

$$D_{31} = \frac{1}{\rho} \left[u_i u_{2,i} + \frac{T_{,2}}{\gamma \mathsf{M}^2} \right] \tag{A.61}$$

$$D_{32} = u_{2,1} \tag{A.62}$$

$$D_{33} = u_{2,2} \tag{A.63}$$

$$D_{34} = u_{2,3} \tag{A.64}$$

$$D_{35} = \frac{\rho_{,2}}{\rho \gamma \mathsf{M}^2} - \frac{1}{\rho \mathsf{Re}} \left\{ [\lambda_{,T}]_{,2} u_{i,i} + \lambda_{,T} u_{i,i2} + \right.$$
$$\left. 2 [\mu_{,T}]_{,i} S_{2i} + 2\mu_{,T} S_{2i,i} \right\} \tag{A.65}$$

$$D_{41} = \frac{1}{\rho} \left[u_i u_{3,i} + \frac{T_{,3}}{\gamma \mathsf{M}^2} \right] \tag{A.66}$$

$$D_{42} = u_{3,1} \tag{A.67}$$

$$D_{43} = u_{3,2} \tag{A.68}$$

$$D_{44} = u_{3,3} \tag{A.69}$$

$$D_{45} = \frac{\rho_{,3}}{\rho \gamma \mathsf{M}^2} - \frac{1}{\rho \mathsf{Re}} \left\{ [\lambda_{,T}]_{,3} u_{i,i} + \lambda_{,T} u_{i,i3} + \right.$$

$$2\left[\mu_{,T}\right]_{,i}S_{3i} + 2\mu_{,T}S_{3i,i}\bigg\} \tag{A.70}$$

$$D_{51} = \frac{1}{\rho}\left(u_iT_{,i} + (\gamma - 1)Tu_{i,i}\right) \tag{A.71}$$

$$D_{52} = T_{,1} \tag{A.72}$$

$$D_{53} = T_{,2} \tag{A.73}$$

$$D_{54} = T_{,3} \tag{A.74}$$

$$D_{55} = (\gamma - 1)u_{i,i} - \frac{\gamma}{\rho\mathsf{Pr}\mathsf{Re}}\left\{\left[\kappa_{,T}\right]_{,i}T_{,i} + \kappa_{,T}T_{,ii}\right\} -$$

$$\frac{\gamma(\gamma - 1)\mathsf{M}^2}{\rho\mathsf{Re}}\left\{\lambda_{,T}u_{i,i}u_{j,j} + 2\mu_{,T}S_{ij}S_{ij}\right\} \tag{A.75}$$

$\boxed{\mathbf{V}_{11}\text{ matrix}}$

$$V_{22} = (\lambda + 2\mu)/(\rho\mathsf{Re}) \tag{A.76}$$

$$V_{33} = \mu/(\rho\mathsf{Re}) \tag{A.77}$$

$$V_{44} = \mu/(\rho\mathsf{Re}) \tag{A.78}$$

$$V_{55} = \gamma\kappa/(\rho\mathsf{Pr}\mathsf{Re}) \tag{A.79}$$

$\boxed{\mathbf{V}_{12}\text{ matrix}}$

$$V_{23} = (\lambda + \mu)/(\rho\mathsf{Re}) \tag{A.80}$$

$$V_{32} = (\lambda + \mu)/(\rho\mathsf{Re}) \tag{A.81}$$

$\boxed{\mathbf{V}_{13}\text{ matrix}}$

$$V_{24} = (\lambda + \mu)/(\rho\mathsf{Re}) \tag{A.82}$$

$$V_{42} = (\lambda + \mu)/(\rho\mathsf{Re}) \tag{A.83}$$

$\boxed{\mathbf{V}_{22} \text{ matrix}}$

$$V_{22} = \mu/(\rho\text{Re}) \tag{A.84}$$

$$V_{33} = (\lambda + 2\mu)/(\rho\text{Re}) \tag{A.85}$$

$$V_{44} = \mu/(\rho\text{Re}) \tag{A.86}$$

$$V_{55} = \gamma\kappa/(\rho\text{PrRe}) \tag{A.87}$$

$\boxed{\mathbf{V}_{23} \text{ matrix}}$

$$V_{34} = (\lambda + \mu)/(\rho\text{Re}) \tag{A.88}$$

$$V_{43} = (\lambda + \mu)/(\rho\text{Re}) \tag{A.89}$$

$\boxed{\mathbf{V}_{33} \text{ matrix}}$

$$V_{22} = \mu/(\rho\text{Re}) \tag{A.90}$$

$$V_{33} = \mu/(\rho\text{Re}) \tag{A.91}$$

$$V_{44} = (\lambda + 2\mu)/(\rho\text{Re}) \tag{A.92}$$

$$V_{55} = \gamma\kappa/(\rho\text{PrRe}) \tag{A.93}$$

A.2 Matrices for the Nonlinear Navier–Stokes Equations

When forming the LHS for the nonlinear solver, the matrices are the same as given in Appendix A.1 except that instead of evaluating them at $\bar{\mathbf{U}}$, they are evaluated at the previous iteration, $\mathbf{U}_i$. In addition, since the nonlinear solver is linearized at each iteration about an unsteady flow field the unsteady terms must be retained in the LHS. These terms only influence the definition of the $\mathbf{D}$ matrix and the altered terms are

Nonlinear $\mathbf{D}$ matrix

$$D_{21} = \frac{1}{\rho}\left[\frac{T_{,1}}{\gamma\mathsf{M}^2} - \frac{p_{,1}}{\rho} + \frac{1}{\rho\mathsf{Re}}(\lambda_{,1}u_{i,i} + \lambda u_{i,i1} + 2\mu_{,1}S_{1i} + 2\mu S_{1i,i})\right] \quad (A.94)$$

$$D_{31} = \frac{1}{\rho}\left[\frac{T_{,2}}{\gamma\mathsf{M}^2} - \frac{p_{,2}}{\rho} + \frac{1}{\rho\mathsf{Re}}(\lambda_{,2}u_{i,i} + \lambda u_{i,i2} + 2\mu_{,2}S_{2i} + 2\mu S_{2i,i})\right] \quad (A.95)$$

$$D_{41} = \frac{1}{\rho}\left[\frac{T_{,3}}{\gamma\mathsf{M}^2} - \frac{p_{,3}}{\rho} + \frac{1}{\rho\mathsf{Re}}(\lambda_{,3}u_{i,i} + \lambda u_{i,i3} + 2\mu_{,3}S_{3i} + 2\mu S_{3i,i})\right] \quad (A.96)$$

$$D_{51} = \frac{\gamma}{\rho\mathsf{Pr}\mathsf{Re}}(\kappa_{,i}T_{,i} + \kappa T_{,ii}) + \frac{\gamma(\gamma-1)\mathsf{M}^2}{\rho^2\mathsf{Re}}(\lambda u_{i,i}u_{j,j} + 2\mu S_{ij}S_{ij}) \quad (A.97)$$

A.3   Matrices for the Linearized Navier–Stokes Equations with Surface Curvature

This appendix lists the nonzero elements of the matrices defined in equation (D.6) for the linearized Navier–Stokes equations in a body-fitted coordinate system. These matrices are used in Appendices D and E to construct a linear stability theory and receptivity theory which account for surface curvature. We begin by defining the values of several operators which appear in the linearized Navier–Stokes equations for the case where the only nontrivial metric, $h(s,n)$, is in the s-direction. These operators are defined with reference to Appendix A of Sherman [99].

The divergence operator can be written as

$$\nabla \cdot \mathbf{u} = \frac{1}{h}(v_{s,s} + v_n h_{,n}) + v_{n,n} + w_{,z}\,. \tag{A.98}$$

The strain-rate tensor, required for the viscous terms, is given by

$$\mathbf{S} = \frac{1}{2}\begin{bmatrix} \frac{2}{h}(v_{s,s} + v_n h_{,n}) & \frac{1}{h}(v_{n,s} - v_s h_{,n}) + v_{s,n} & \frac{w_{,sn}}{h} + v_{s,z} \\ & 2v_{n,n} & w_{,n} + v_{n,z} \\ \text{sym} & & 2w_{,z} \end{bmatrix}\,. \tag{A.99}$$

The convective derivative in the body-fitted coordinate system is given by the vector

$$\mathbf{c} = (\mathbf{u} \cdot \nabla)\mathbf{u} = \left\{ \begin{array}{c} \frac{v_s}{h}(v_{s,s} + v_n h_{,n}) + v_n v_{s,n} + w v_{s,z} \\ \frac{v_s}{h}(v_{n,s} - v_s h_{,n}) + v_n v_{n,n} + w v_{n,z} \\ \frac{v_s w_{,s}}{h} + v_n w_{,n} + w w_{,z} \end{array} \right\}\,. \tag{A.100}$$

The gradient of the divergence is required for the viscous terms, and the three components are

$$\begin{aligned} \nabla_s(\nabla \cdot \mathbf{u}) &= -\frac{h_{,s}}{h^3}(v_{s,s} + v_n h_{,n}) + \frac{1}{h^2}(v_{s,ss} + v_{n,s}h_{,n} + v_n h_{,sn}) + \\ &\quad \frac{1}{h}(v_{n,sn} + w_{,sz})\,, \end{aligned} \tag{A.101}$$

$$\nabla_n(\nabla \cdot \mathbf{u}) = -\frac{h_{,n}}{h^2}(v_{s,s} + v_n h_{,n}) + \frac{1}{h}(v_{s,sn} + v_{n,n}h_{,n} + v_n h_{,nn}) +$$

$$(v_{n,nn} + w_{,nz}) , \tag{A.102}$$

$$\nabla_z(\nabla \cdot \mathbf{u}) = \frac{1}{h}(v_{s,sz} + v_{n,z}h_{,n}) + (v_{n,nz} + w_{,zz}) . \tag{A.103}$$

The Laplacian of the temperature is required in the energy equation, and can be written as

$$\nabla^2 T = \frac{1}{h^3}\left[-h_{,s}T_{,s} + hT_{,ss} + h^2 T_{,n}h_{,n} + h^3(T_{,nn} + T_{,zz})\right] . \tag{A.104}$$

The final quantity required is the divergence of the strain-rate tensor, which is a vector with components

$$
\begin{aligned}
(\nabla \cdot \mathbf{S})_s \;=\;& \frac{v_{s,nn} + v_{s,zz}}{2} + \frac{v_{n,sn} + v_{n,sz} + v_{s,n}h_{,n}}{2h} + \\
& \frac{3h_{,n}v_{n,s} - v_s(h_{,n}^2 + h_{,nn}h) + 2v_{s,ss}}{2h^2} + \\
& \frac{v_n(hh_{,sn} - h_{,n}h_{,s}) - h_{,s}v_{s,s}}{h^3} ,
\end{aligned}
\tag{A.105}
$$

$$
\begin{aligned}
(\nabla \cdot \mathbf{S})_n \;=\;& \frac{v_{n,zz} + w_{,nz} + 2v_{n,nn}}{2} + \frac{v_{s,sn} + 2h_{,n}v_{n,n}}{2h} + \\
& \frac{v_{n,ss} - 3h_{,n}v_{s,s} - 2v_n h_{,n}^2}{2h^2} + \\
& \frac{v_s(h_{,n}h_{,s} - hh_{,sn}) - h_{,s}v_{n,s}}{2h^3} ,
\end{aligned}
\tag{A.106}
$$

$$
\begin{aligned}
(\nabla \cdot \mathbf{S})_z \;=\;& \frac{2w_{,zz} + v_{n,nz} + w_{,nn}}{2} + \frac{v_{s,sz} + h_{,n}v_{n,z} + h_{,n}w_{,n}}{2h} + \\
& \frac{w_{,ss}}{2h^2} - \frac{h_{,s}w_{,s}}{2h^3} .
\end{aligned}
\tag{A.107}
$$

With these definitions, the matrix operators for the linearized Navier–Stokes equations are listed below, where all terms are evaluated at the base-flow condition, $\mathbf{U} = \bar{\mathbf{U}}$.

$\boxed{\mathbf{A} \text{ matrix}}$

$$A_{11} = v_s/h \tag{A.108}$$

$$A_{12} = \rho/h \tag{A.109}$$

$$A_{21} = \frac{T}{\rho\gamma\mathsf{M}^2 h} \tag{A.110}$$

$$A_{22} = \frac{v_s}{h} - \frac{1}{\rho h \mathsf{Re}}\left(\frac{\lambda_{,s} + 2\mu_{,s}}{h} - \frac{(\lambda + 2\mu)h_{,s}}{h^2}\right) \tag{A.111}$$

$$A_{23} = -\frac{1}{\rho h \mathsf{Re}}\left(\mu_{,n} + \frac{(\lambda + 3\mu)h_{,n}}{h}\right) \tag{A.112}$$

$$A_{24} = -\frac{1}{\rho h \mathsf{Re}}\left(\mu_{,z}\right) \tag{A.113}$$

$$A_{25} = \frac{1}{\gamma h \mathsf{M}^2} - \frac{1}{\rho h \mathsf{Re}}\left(\lambda_{,T}\nabla \cdot \mathbf{u} + 2\mu_{,T}S_{11}\right) \tag{A.114}$$

$$A_{32} = -\frac{1}{\rho h \mathsf{Re}}\left(\lambda_{,n} - \frac{(\lambda + 3\mu)h_{,n}}{h}\right) \tag{A.115}$$

$$A_{33} = v_s/h - \frac{1}{\rho h \mathsf{Re}}\left(\frac{\mu_{,s}}{h} - \frac{\mu h_{,s}}{h^2}\right) \tag{A.116}$$

$$A_{35} = -2\frac{1}{\rho h \mathsf{Re}}\mu_{,T}S_{21} \tag{A.117}$$

$$A_{42} = -\frac{1}{\rho h \mathsf{Re}}\lambda_{,z} \tag{A.118}$$

$$A_{44} = v_s/h - \frac{1}{\rho h \mathsf{Re}}\left(\frac{\mu_{,s}}{h} - \frac{\mu h_{,s}}{h^2}\right) \tag{A.119}$$

$$A_{45} = -2\frac{1}{\rho h \mathsf{Re}}\mu_{,T}S_{31} \tag{A.120}$$

$$A_{52} = (\gamma - 1)T/h - \frac{\gamma(\gamma - 1)\mathsf{M}^2}{\rho h \mathsf{Re}}\left(2\lambda\nabla \cdot \mathbf{u} + 4\mu S_{11}\right) \tag{A.121}$$

$$A_{53} = -\frac{\gamma(\gamma - 1)\mathsf{M}^2}{\rho h \mathsf{Re}}\left(4\mu S_{21}\right) \tag{A.122}$$

$$A_{54} = -\frac{\gamma(\gamma - 1)\mathsf{M}^2}{\rho h \mathsf{Re}}\left(4\mu S_{31}\right) \tag{A.123}$$

$$A_{55} = v_s/h - \frac{\gamma}{\rho h \mathsf{Pr}\mathsf{Re}}\left(\frac{\kappa_{,s} + \kappa_{,T}T_{,s}}{h} - \frac{\kappa h_{,s}}{h^2}\right) \tag{A.124}$$

$\boxed{\mathbf{B} \text{ matrix}}$

$$B_{11} = v_n \tag{A.125}$$

$$B_{13} = \rho \tag{A.126}$$

$$B_{22} = v_n - \frac{1}{\rho h \mathsf{Re}} \left(h\mu_{,n} + \mu h_{,n} \right) \tag{A.127}$$

$$B_{23} = -\frac{1}{\rho \mathsf{Re}} \frac{\lambda_{,s}}{h} \tag{A.128}$$

$$B_{25} = -2\frac{1}{\rho \mathsf{Re}} \mu_{,T} S_{12} \tag{A.129}$$

$$B_{31} = \frac{T}{\rho \gamma \mathsf{M}^2} \tag{A.130}$$

$$B_{32} = -\frac{1}{\rho h \mathsf{Re}} \mu_{,s} \tag{A.131}$$

$$B_{33} = v_n - \frac{1}{\rho \mathsf{Re}} \left(\lambda_{,n} + \frac{\lambda h_{,n}}{h} + 2\mu_{,n} + \frac{2\mu h_{,n}}{h} \right) \tag{A.132}$$

$$B_{34} = -\frac{1}{\rho \mathsf{Re}} \mu_{,z} \tag{A.133}$$

$$B_{35} = \frac{1}{\gamma \mathsf{M}^2} - \frac{1}{\rho \mathsf{Re}} \left(\lambda_{,T} \nabla \cdot \mathbf{u} + 2\mu_{,T} S_{22} \right) \tag{A.134}$$

$$B_{43} = -\frac{1}{\rho \mathsf{Re}} \lambda_{,z} \tag{A.135}$$

$$B_{44} = v_n - \frac{1}{\rho \mathsf{Re}} \left(\mu_{,n} + \frac{\mu h_{,n}}{h} \right) \tag{A.136}$$

$$B_{45} = -2\frac{1}{\rho \mathsf{Re}} \mu_{,T} S_{32} \tag{A.137}$$

$$B_{52} = -\frac{\gamma(\gamma-1)\mathsf{M}^2}{\rho \mathsf{Re}} \left(4\mu S_{12} \right) \tag{A.138}$$

$$B_{53} = (\gamma-1)T - \frac{\gamma(\gamma-1)\mathsf{M}^2}{\rho \mathsf{Re}} \left(2\lambda \nabla \cdot \mathbf{u} + 4\mu S_{22} \right) \tag{A.139}$$

$$B_{54} = -\frac{\gamma(\gamma-1)\mathsf{M}^2}{\rho \mathsf{Re}} \left(4\mu S_{32} \right) \tag{A.140}$$

$$B_{55} = v_n - \frac{\gamma}{\rho \mathsf{Pr} \mathsf{Re}} \left(\kappa_{,n} + \kappa_{,T} T_{,n} + \frac{\kappa h_{,n}}{h} \right) \tag{A.141}$$

$\boxed{\mathbf{C} \text{ matrix}}$

$$C_{11} \;=\; w \tag{A.142}$$

$$C_{13} \;=\; \rho \tag{A.143}$$

$$C_{22} \;=\; w - \frac{1}{\rho \mathsf{Re}}\mu_{,z} \tag{A.144}$$

$$C_{24} \;=\; -\frac{1}{\rho h \mathsf{Re}}\lambda_{,s} \tag{A.145}$$

$$C_{25} \;=\; -2\frac{1}{\rho \mathsf{Re}}\mu_{,T}S_{13} \tag{A.146}$$

$$C_{33} \;=\; w - \frac{1}{\rho \mathsf{Re}}\mu_{,z} \tag{A.147}$$

$$C_{34} \;=\; -\frac{1}{\rho \mathsf{Re}}\lambda_{,n} \tag{A.148}$$

$$C_{35} \;=\; -2\frac{1}{\rho \mathsf{Re}}\mu_{,T}S_{23} \tag{A.149}$$

$$C_{41} \;=\; \frac{T}{\rho \gamma \mathsf{M}^2} \tag{A.150}$$

$$C_{42} \;=\; -\frac{1}{\rho h \mathsf{Re}}\left(\mu_{,s}\right) \tag{A.151}$$

$$C_{43} \;=\; -\frac{1}{\rho \mathsf{Re}}\left(\frac{(\lambda + \mu)h_{,n}}{h} + \mu_{,n}\right) \tag{A.152}$$

$$C_{44} \;=\; w - \frac{1}{\rho \mathsf{Re}}\left(\lambda_{,z} + 2\mu_{,z}\right) \tag{A.153}$$

$$C_{45} \;=\; \frac{1}{\gamma \mathsf{M}^2} - \frac{1}{\rho \mathsf{Re}}\left(\lambda_{,T}\nabla \cdot \mathbf{u} + 2\mu_{,T}S_{33}\right) \tag{A.154}$$

$$C_{52} \;=\; -\frac{\gamma(\gamma - 1)\mathsf{M}^2}{\rho \mathsf{Re}}\left(4\mu S_{13}\right) \tag{A.155}$$

$$C_{53} \;=\; -\frac{\gamma(\gamma - 1)\mathsf{M}^2}{\rho \mathsf{Re}}\left(4\mu S_{23}\right) \tag{A.156}$$

$$C_{54} \;=\; (\gamma - 1)T - \frac{\gamma(\gamma - 1)\mathsf{M}^2}{\rho \mathsf{Re}}\left(2\lambda\nabla \cdot \mathbf{u} + 4\mu S_{33}\right) \tag{A.157}$$

$$C_{55} \;=\; w - \frac{\gamma}{\rho \mathsf{Pr}\mathsf{Re}}\left(\kappa_{,z} + \kappa_{,T}T_{,z}\right) \tag{A.158}$$

$\boxed{\mathbf{D} \text{ matrix}}$

$$D_{11} = \nabla \cdot \mathbf{u} \tag{A.159}$$

$$D_{12} = \rho_{,s}/h \tag{A.160}$$

$$D_{13} = \rho_{,n} + \rho h_{,n}/h \tag{A.161}$$

$$D_{14} = \rho_{,z} \tag{A.162}$$

$$D_{21} = \frac{1}{\rho}\left[\mathbf{c}_1 + \frac{T_{,s}}{\gamma h \mathsf{M}^2}\right] \tag{A.163}$$

$$D_{22} = \frac{v_{s,s} + v_n h_{,n}}{h} + \frac{1}{\rho h \mathsf{Re}}\left(\mu_n h_{,n} + \frac{\mu}{h}(h_{,n}^2 + h_{,nn}h)\right) \tag{A.164}$$

$$D_{23} = v_{s,n} + \frac{v_s h_{,n}}{h} - \frac{1}{\rho h \mathsf{Re}}\left\{\frac{(\lambda_{,s} + 2\mu_{,s})h_{,n}}{h} - \frac{(\lambda + 2\mu)h_{,s}h_{,n}}{h^2} + \right.$$
$$\left. \frac{(\lambda + 2\mu)h_{,sn}}{h}\right\} \tag{A.165}$$

$$D_{24} = v_{s,z} \tag{A.166}$$

$$D_{25} = \frac{\rho_{,s}}{\rho h \gamma \mathsf{M}^2} - \frac{1}{\rho \mathsf{Re}}\left\{\frac{[\lambda_{,T}]_{,s}\,\nabla \cdot \mathbf{u}}{h} + \lambda_{,T}\nabla_s(\nabla \cdot \mathbf{u}) + \right.$$
$$\left. \frac{2}{h}[\mu_{,T}]_{,s} S_{11} + 2[\mu_{,T}]_{,n} S_{12} + 2[\mu_{,T}]_{,z} S_{13} + 2\mu_{,T}(\nabla \cdot \mathbf{S})_s\right\} \tag{A.167}$$

$$D_{31} = \frac{1}{\rho}\left[\mathbf{c}_2 + \frac{T_{,n}}{\gamma \mathsf{M}^2}\right] \tag{A.168}$$

$$D_{32} = (v_{n,s} - 2v_s h_{,n})/h - \frac{1}{\rho h \mathsf{Re}}\left\{\frac{\mu}{h^2}(h_{,s}h_{,n} - hh_{,sn}) - \mu_{,s}\frac{h_{,n}}{h}\right\} \tag{A.169}$$

$$D_{33} = v_{n,n} - \frac{1}{\rho h \mathsf{Re}}\left\{\lambda_{,n}h_{,n} - \lambda\left(\frac{h_{,n}^2}{h} - h_{,nn}\right) - 2\mu\frac{h_{,n}^2}{h}\right\} \tag{A.170}$$

$$D_{34} = v_{n,z} \tag{A.171}$$

$$D_{35} = \frac{\rho_{,n}}{\rho \gamma \mathsf{M}^2} - \frac{1}{\rho \mathsf{Re}}\left\{[\lambda_{,T}]_{,n}\,\nabla \cdot \mathbf{u} + \lambda_{,T}\nabla_n(\nabla \cdot \mathbf{u}) + \right.$$
$$\left. \frac{2}{h}[\mu_{,T}]_{,s} S_{21} + 2[\mu_{,T}]_{,n} S_{22} + 2[\mu_{,T}]_{,z} S_{23} + 2\mu_{,T}(\nabla \cdot \mathbf{S})_n\right\} \tag{A.172}$$

$$D_{41} = \frac{1}{\rho}\left[\mathbf{c}_3 + \frac{T_{,z}}{\gamma \mathsf{M}^2}\right] \tag{A.173}$$

$$D_{42} = w_{,s}/h \tag{A.174}$$

$$D_{43} = w_{,n} - \frac{1}{\rho h \mathsf{Re}}\{\lambda_{,n}h_{,n}\} \tag{A.175}$$

$$D_{44} = w_{,z} \tag{A.176}$$

$$
D_{45} = \frac{\rho_{,z}}{\rho \gamma \mathsf{M}^2} - \frac{1}{\rho \mathsf{Re}} \left\{ [\lambda_{,T}]_{,z} \, \nabla \cdot \mathbf{u} + \lambda_{,T} \nabla_z (\nabla \cdot \mathbf{u}) + \right.
$$

$$
\left. \frac{2}{h} [\mu_{,T}]_{,s} \, S_{31} + 2 [\mu_{,T}]_{,n} \, S_{32} + 2 [\mu_{,T}]_{,z} \, S_{33} + 2\mu_{,T} (\nabla \cdot \mathbf{S})_z \right\} \qquad (A.177)
$$

$$
D_{51} = \frac{1}{\rho} \left(\frac{v_s T_{,s}}{h} + v_n T_{,n} + w T_{,z} + (\gamma - 1) T \nabla \cdot \mathbf{u} \right) \qquad (A.178)
$$

$$
D_{52} = T_{,s}/h + \frac{\gamma(\gamma - 1)\mathsf{M}^2}{\rho \mathsf{Re}} \left\{ 4\mu S_{21} \frac{h_{,n}}{h} \right\} \qquad (A.179)
$$

$$
D_{53} = T_{,n} + \rho(\gamma - 1)T \frac{h_{,n}}{h} - \frac{\gamma(\gamma - 1)\mathsf{M}^2}{\rho \mathsf{Re}} \left\{ (2\lambda \nabla \cdot \mathbf{u} + 4\mu S_{11}) \frac{h_{,n}}{h} \right\} \quad (A.180)
$$

$$
D_{54} = T_{,z} \qquad (A.181)
$$

$$
D_{55} = (\gamma - 1)\nabla \cdot \mathbf{u} - \frac{\gamma}{\rho \mathsf{Pr}\mathsf{Re}} \left\{ [\kappa_{,T}]_{,s} \frac{T_{,s}}{h^2} + [\kappa_{,T}]_{,n} T_{,n} + [\kappa_{,T}]_{,z} T_{,z} + \right.
$$

$$
\left. \kappa_{,T} \nabla^2 T \right\} - \frac{\gamma(\gamma - 1)\mathsf{M}^2}{\rho \mathsf{Re}} \left\{ \lambda_{,T} (\nabla \cdot \mathbf{u})^2 + 2\mu_{,T} S_{ij} S_{ij} \right\} \qquad (A.182)
$$

$\boxed{\mathbf{V}_{ss} \text{ matrix}}$

$$
V_{22} = (\lambda + 2\mu)/(\rho h^2 \mathsf{Re}) \qquad (A.183)
$$

$$
V_{33} = \mu/(\rho h^2 \mathsf{Re}) \qquad (A.184)
$$

$$
V_{44} = \mu/(\rho h^2 \mathsf{Re}) \qquad (A.185)
$$

$$
V_{55} = \gamma \kappa/(\rho h^2 \mathsf{Pr}\mathsf{Re}) \qquad (A.186)
$$

$\boxed{\mathbf{V}_{sn} \text{ matrix}}$

$$
V_{23} = (\lambda + \mu)/(\rho h \mathsf{Re}) \qquad (A.187)
$$

$$
V_{32} = (\lambda + \mu)/(\rho h \mathsf{Re}) \qquad (A.188)
$$

$\boxed{\mathbf{V}_{sz} \text{ matrix}}$

$$
V_{24} = (\lambda + \mu)/(\rho h \mathsf{Re}) \qquad (A.189)
$$

$$
V_{42} = (\lambda + \mu)/(\rho h \mathsf{Re}) \qquad (A.190)
$$

$\boxed{\mathbf{V}_{nn} \text{ matrix}}$

$$V_{22} = \mu/(\rho\mathsf{Re}) \tag{A.191}$$

$$V_{33} = (\lambda + 2\mu)/(\rho\mathsf{Re}) \tag{A.192}$$

$$V_{44} = \mu/(\rho\mathsf{Re}) \tag{A.193}$$

$$V_{55} = \gamma\kappa/(\rho\mathsf{PrRe}) \tag{A.194}$$

$\boxed{\mathbf{V}_{nz} \text{ matrix}}$

$$V_{34} = (\lambda + \mu)/(\rho\mathsf{Re}) \tag{A.195}$$

$$V_{43} = (\lambda + \mu)/(\rho\mathsf{Re}) \tag{A.196}$$

$\boxed{\mathbf{V}_{zz} \text{ matrix}}$

$$V_{22} = \mu/(\rho\mathsf{Re}) \tag{A.197}$$

$$V_{33} = \mu/(\rho\mathsf{Re}) \tag{A.198}$$

$$V_{44} = (\lambda + 2\mu)/(\rho\mathsf{Re}) \tag{A.199}$$

$$V_{55} = \gamma\kappa/(\rho\mathsf{PrRe}) \tag{A.200}$$

A.4   Matrices for the Nonparallel Stability Analysis

To perform the nonparallel stability analysis in Appendix D.3, it is convenient to convert equation (D.29) to a system of first-order ordinary differential equations of the form given by equation (D.32). To accomplish this, the continuity equation is used to remove the explicit dependence on $v'_{n,nn}$ (see Mack [68]). This results in changes to the definitions of the matrices ($\mathbf{A}$, $\mathbf{B}$, *etc.*) and in the following expressions, a tilde is used to indicate the modified matrices. The new (tilde) matrices are identical to the matrices defined in Appendix A.3 except for the following modifications:

$\boxed{\tilde{\mathbf{A}} \text{ matrix}}$

$$\tilde{A}_{31} = A_{31} + \frac{\lambda + 2\mu}{\rho\mathsf{Re}} \left[\frac{v_{s,n}}{h} - \frac{v_s h_{,n}}{h^2} \right] \tag{A.201}$$

$$\tilde{A}_{32} \;=\; A_{32} + \frac{\lambda + 2\mu}{\rho\mathsf{Re}}\left[\frac{\rho_{,n}}{h} - \frac{\rho h_{,n}}{h^2}\right] \tag{A.202}$$

$\boxed{\tilde{\mathbf{B}} \text{ matrix}}$

$$\tilde{B}_{31} \;=\; B_{31} + \frac{\lambda + 2\mu}{\rho\mathsf{Re}}\left[\nabla\cdot\mathbf{u} + v_{n,n} - i\omega\right] \tag{A.203}$$

$$\tilde{B}_{32} \;=\; B_{32} + \frac{\lambda + 2\mu}{\rho\mathsf{Re}}\frac{\rho_{,s}}{h} \tag{A.204}$$

$$\tilde{B}_{33} \;=\; B_{33} + \frac{\lambda + 2\mu}{\rho\mathsf{Re}}\left[2\rho_{,n} + \frac{\rho h_{,n}}{h}\right] \tag{A.205}$$

$$\tilde{B}_{34} \;=\; B_{34} + \frac{\lambda + 2\mu}{\rho\mathsf{Re}}\rho_{,z} \tag{A.206}$$

$\boxed{\tilde{\mathbf{C}} \text{ matrix}}$

$$\tilde{C}_{31} \;=\; C_{31} + \frac{\lambda + 2\mu}{\rho\mathsf{Re}}w_{,n} \tag{A.207}$$

$$\tilde{C}_{34} \;=\; C_{34} + \frac{\lambda + 2\mu}{\rho\mathsf{Re}}\rho_{,n} \tag{A.208}$$

$\boxed{\tilde{\mathbf{D}} \text{ matrix}}$

$$\tilde{D}_{31} \;=\; D_{31} + \frac{\lambda + 2\mu}{\rho\mathsf{Re}}\nabla_n(\nabla\cdot\mathbf{u}) \tag{A.209}$$

$$\tilde{D}_{32} \;=\; D_{32} + \frac{\lambda + 2\mu}{\rho\mathsf{Re}}\left[\frac{\rho_{,sn}}{h} - \frac{\rho_{,s}h_{,n}}{h^2}\right] \tag{A.210}$$

$$\tilde{D}_{33} \;=\; D_{33} + \frac{\lambda + 2\mu}{\rho\mathsf{Re}}\left[\frac{\rho_{,n}h_{,n}}{h} - \rho\left(\frac{h_{,n}^2}{h^2} + \frac{h_{,nn}}{h}\right) + \rho_{,nn}\right] \tag{A.211}$$

$$\tilde{D}_{34} \;=\; D_{34} + \frac{\lambda + 2\mu}{\rho\mathsf{Re}}\rho_{,nz} \tag{A.212}$$

$\boxed{\tilde{\mathbf{V}}_{sn} \text{ matrix}}$

$$\tilde{V}_{31} \;=\; -\frac{\lambda + 2\mu}{\rho\mathsf{Re}}\frac{v_s}{h} \tag{A.213}$$

$$\tilde{V}_{32} \;=\; V_{32} - \frac{\lambda + 2\mu}{\rho\mathsf{Re}}\frac{\rho}{h} \tag{A.214}$$

$\boxed{\tilde{\mathbf{V}}_{nn} \text{ matrix}}$

$$\tilde{V}_{31} = -\frac{\lambda + 2\mu}{\rho \mathrm{Re}} v_n \tag{A.215}$$

$\boxed{\tilde{\mathbf{V}}_{nz} \text{ matrix}}$

$$\tilde{V}_{31} = -\frac{\lambda + 2\mu}{\rho \mathrm{Re}} w \tag{A.216}$$

$$\tilde{V}_{34} = V_{34} - \frac{\lambda + 2\mu}{\rho \mathrm{Re}} \rho \tag{A.217}$$

Using these new matrices, we can define the matrix operators used in equation (D.32). Toward that goal, equation (D.32) is written in a slightly different form

$$\tilde{\mathbf{E}} \hat{\mathbf{Q}}_{,n} + \tilde{\mathbf{F}} \hat{\mathbf{Q}} = \tilde{\mathbf{G}} \frac{dA}{ds_1} + \tilde{\mathbf{H}} A \,. \tag{A.218}$$

The $\tilde{\mathbf{E}}$ matrix is given by

$$\tilde{\mathbf{E}} = \left[\begin{array}{cc} \tilde{\mathbf{E}}_{11} & \tilde{\mathbf{E}}_{12} \\ \tilde{\mathbf{E}}_{21} & \mathbf{0} \end{array} \right] \tag{A.219}$$

where $\mathbf{0}$ is the null matrix,

$$\tilde{\mathbf{E}}_{11} = \tilde{\mathbf{B}}_0 - ik_s \tilde{\mathbf{V}}_{sn} - ik_z \tilde{\mathbf{V}}_{nz} \,, \tag{A.220}$$

$$\tilde{\mathbf{E}}_{12} = \left[\begin{array}{ccc} 0 & 0 & 0 \\ -\tilde{\mathbf{V}}_{nn}(2,2) & 0 & 0 \\ 0 & 0 & 0 \\ 0 & -\tilde{\mathbf{V}}_{nn}(4,4) & 0 \\ 0 & 0 & -\tilde{\mathbf{V}}_{nn}(5,5) \end{array} \right] \,, \tag{A.221}$$

and

$$\tilde{\mathbf{E}}_{21} = \left[\begin{array}{ccccc} 0 & 1 & 0 & 0 & 0 \\ 0 & 0 & 0 & 1 & 0 \\ 0 & 0 & 0 & 0 & 1 \end{array} \right] \,. \tag{A.222}$$

The $\tilde{\mathbf{F}}$ matrix can be written as

$$\tilde{\mathbf{F}} = \begin{bmatrix} \tilde{\mathbf{F}}_{11} & \mathbf{0} \\ \mathbf{0} & -\mathbf{I} \end{bmatrix} \tag{A.223}$$

where $\mathbf{I}$ is the identity matrix and

$$\tilde{\mathbf{F}}_{11} = \tilde{\mathbf{D}}_0 + ik_s\tilde{\mathbf{A}}_0 + ik_z\tilde{\mathbf{C}}_0 + k_s^2\tilde{\mathbf{V}}_{ss} + k_sk_z\tilde{\mathbf{V}}_{sz} + k_z^2\tilde{\mathbf{V}}_{zz} - i\omega\,. \tag{A.224}$$

Beginning with $\tilde{\mathbf{G}}$, the vectors on the RHS of equation (A.218) are given by

$$\tilde{\mathbf{G}} = \left\{ \begin{array}{c} \tilde{\mathbf{G}}_1 \\ \mathbf{0} \end{array} \right\} \tag{A.225}$$

where

$$\tilde{\mathbf{G}}_1 = (2ik_s\tilde{\mathbf{V}}_{ss} + ik_z\tilde{\mathbf{V}}_{sz} - \tilde{\mathbf{A}}_0)\hat{\mathbf{U}}_0 + \tilde{\mathbf{V}}_{sn}\hat{\mathbf{U}}_{0,n}\,. \tag{A.226}$$

Finally, the $\tilde{\mathbf{H}}$ vector is given by

$$\tilde{\mathbf{H}} = \left\{ \begin{array}{c} \tilde{\mathbf{H}}_1 \\ \mathbf{0} \end{array} \right\} \tag{A.227}$$

where

$$\begin{aligned} \tilde{\mathbf{H}}_1 &= \tilde{\mathbf{V}}_{ss}\left(-\frac{dk_s}{ds_1}\hat{\mathbf{U}}_0 + 2ik_s\hat{\mathbf{U}}_{0,s_1} \right) + \tilde{\mathbf{V}}_{sn}\hat{\mathbf{U}}_{0,s_1 n} + \\ &\quad (ik_z\tilde{\mathbf{V}}_{sz} - \tilde{\mathbf{A}}_0)\hat{\mathbf{U}}_{0,s_1} - \mathcal{L}_1(\hat{\mathbf{U}}_0)\,. \end{aligned} \tag{A.228}$$

As long as $\mathsf{Re} \neq 0$, the matrix $\tilde{\mathbf{E}}^{-1}$ can be inverted. Multiplying through by $\tilde{\mathbf{E}}^{-1}$, equation (A.218) can be converted to

$$\hat{\mathbf{Q}}_{,n} + \tilde{\mathbf{E}}^{-1}\tilde{\mathbf{F}}\hat{\mathbf{Q}} = \tilde{\mathbf{E}}^{-1}\tilde{\mathbf{G}}\frac{dA}{ds_1} + \tilde{\mathbf{E}}^{-1}\tilde{\mathbf{H}}A \tag{A.229}$$

which is of the form given by equation (D.32).

Appendix B

Computation of Mesh Metrics

For generality, we assume that there are two levels of mapping used to transform physical space to computational space. These mapping can be written abstractly as

$$(x, y) \mapsto (\tilde{\xi}, \tilde{\eta}) \mapsto (\xi, \eta) \tag{B.1}$$

An example of such a mapping is presented in Chapter 5 where a conformal mapping transforms physical space to parabolic coordinates with an additional mapping used to transform to a uniform computational space. The metric terms required by the flow solver (see section 3.3) to convert derivatives in computational space to derivatives in physical space are computed using the derivatives of the mapping functions along with the chain rule.

For example, to compute the first derivative metrics [see equation (3.1)], the chain rule is used to obtain

$$
\begin{align}
x_{,\xi} &= x_{,\tilde{\xi}}\, \tilde{\xi}_{,\xi} + x_{,\tilde{\eta}}\, \tilde{\eta}_{,\xi}\,, \tag{B.2}\\
y_{,\xi} &= y_{,\tilde{\xi}}\, \tilde{\xi}_{,\xi} + y_{,\tilde{\eta}}\, \tilde{\eta}_{,\xi}\,, \tag{B.3}\\
x_{,\eta} &= x_{,\tilde{\xi}}\, \tilde{\xi}_{,\eta} + x_{,\tilde{\eta}}\, \tilde{\eta}_{,\eta}\,, \tag{B.4}\\
y_{,\eta} &= y_{,\tilde{\xi}}\, \tilde{\xi}_{,\eta} + y_{,\tilde{\eta}}\, \tilde{\eta}_{,\eta}\,. \tag{B.5}
\end{align}
$$

The right-hand-sides of equations (B.2)–(B.5) are known from the definitions of the mapping functions. Thus, the inverse Jacobian is given by

$$\mathbf{J}^{-1} = \begin{bmatrix} x_{,\xi} & y_{,\xi} \\ x_{,\eta} & y_{,\eta} \end{bmatrix} \tag{B.6}$$

and the determinant of the Jacobian is

$$|\mathbf{J}| = \frac{1}{x_{,\xi}\, y_{,\eta} - x_{,\eta}\, y_{,\xi}}. \tag{B.7}$$

Taking the inverse, the Jacobian is obtained

$$\mathbf{J} \equiv \begin{bmatrix} \xi_{,x} & \eta_{,x} \\ \xi_{,y} & \eta_{,y} \end{bmatrix} = |\mathbf{J}| \begin{bmatrix} y_{,\eta} & -y_{,\xi} \\ -x_{,\eta} & x_{,\xi} \end{bmatrix}. \tag{B.8}$$

A similar procedure is used to determine the second derivative metrics [see equation (3.3)] using the second derivatives of the mapping functions along with the chain rule. The results are

$$x_{,\xi\xi} = x_{,\tilde{\xi}\tilde{\xi}}\tilde{\xi}_{,\xi}^2 + x_{,\tilde{\xi}}\tilde{\xi}_{,\xi\xi} + 2x_{,\tilde{\xi}\tilde{\eta}}\tilde{\eta}_{,\xi}\tilde{\xi}_{,\xi} + x_{,\tilde{\eta}\tilde{\eta}}\tilde{\eta}_{,\xi}^2 + x_{,\tilde{\eta}}\tilde{\eta}_{,\xi\xi} \tag{B.9}$$

$$x_{,\xi\eta} = x_{,\tilde{\xi}\tilde{\xi}}\tilde{\xi}_{,\eta}\tilde{\xi}_{,\xi} + x_{,\tilde{\xi}}\tilde{\xi}_{,\xi\eta} + x_{,\tilde{\xi}\tilde{\eta}}\tilde{\eta}_{,\eta}\tilde{\xi}_{,\xi} + x_{,\tilde{\xi}\tilde{\eta}}\tilde{\eta}_{,\xi}\tilde{\xi}_{,\eta} + x_{,\tilde{\eta}\tilde{\eta}}\tilde{\eta}_{,\eta}\tilde{\eta}_{,\xi} + x_{,\tilde{\eta}}\tilde{\eta}_{,\xi\eta} \tag{B.10}$$

$$x_{,\eta\eta} = x_{,\tilde{\xi}\tilde{\xi}}\tilde{\xi}_{,\eta}^2 + x_{,\tilde{\xi}}\tilde{\xi}_{,\eta\eta} + 2x_{,\tilde{\xi}\tilde{\eta}}\tilde{\eta}_{,\eta}\tilde{\xi}_{,\eta} + x_{,\tilde{\eta}\tilde{\eta}}\tilde{\eta}_{,\eta}^2 + x_{,\tilde{\eta}}\tilde{\eta}_{,\eta\eta} \tag{B.11}$$

$$y_{,\xi\xi} = y_{,\tilde{\xi}\tilde{\xi}}\tilde{\xi}_{,\xi}^2 + y_{,\tilde{\xi}}\tilde{\xi}_{,\xi\xi} + 2y_{,\tilde{\xi}\tilde{\eta}}\tilde{\eta}_{,\xi}\tilde{\xi}_{,\xi} + y_{,\tilde{\eta}\tilde{\eta}}\tilde{\eta}_{,\xi}^2 + y_{,\tilde{\eta}}\tilde{\eta}_{,\xi\xi} \tag{B.12}$$

$$y_{,\xi\eta} = y_{,\tilde{\xi}\tilde{\xi}}\tilde{\xi}_{,\eta}\tilde{\xi}_{,\xi} + y_{,\tilde{\xi}}\tilde{\xi}_{,\xi\eta} + y_{,\tilde{\xi}\tilde{\eta}}\tilde{\eta}_{,\eta}\tilde{\xi}_{,\xi} + y_{,\tilde{\xi}\tilde{\eta}}\tilde{\eta}_{,\xi}\tilde{\xi}_{,\eta} + y_{,\tilde{\eta}\tilde{\eta}}\tilde{\eta}_{,\eta}\tilde{\eta}_{,\xi} + y_{,\tilde{\eta}}\tilde{\eta}_{,\xi\eta} \tag{B.13}$$

$$y_{,\eta\eta} = y_{,\tilde{\xi}\tilde{\xi}}\tilde{\xi}_{,\eta}^2 + y_{,\tilde{\xi}}\tilde{\xi}_{,\eta\eta} + 2y_{,\tilde{\xi}\tilde{\eta}}\tilde{\eta}_{,\eta}\tilde{\xi}_{,\eta} + y_{,\tilde{\eta}\tilde{\eta}}\tilde{\eta}_{,\eta}^2 + y_{,\tilde{\eta}}\tilde{\eta}_{,\eta\eta} \tag{B.14}$$

$$|\mathbf{J}|_{,\xi} = -\left(x_{,\xi\xi}y_{,\eta} + x_{,\xi}y_{,\xi\eta} - x_{,\xi\eta}y_{,\xi} - x_{,\eta}y_{,\xi\xi}\right)|\mathbf{J}|^2 \tag{B.15}$$

$$|\mathbf{J}|_{,\eta} = -\left(x_{,\xi\eta}y_{,\eta} + x_{,\xi}y_{,\eta\eta} - x_{,\eta\eta}y_{,\xi} - x_{,\eta}y_{,\xi\eta}\right)|\mathbf{J}|^2 \tag{B.16}$$

$$\xi_{,xx} = \left(|\mathbf{J}|_{,\xi}y_{,\eta} + y_{,\xi\eta}|\mathbf{J}|\right)\xi_{,x} + \left(|\mathbf{J}|_{,\eta}y_{,\eta} + y_{,\eta\eta}|\mathbf{J}|\right)\eta_{,x} \tag{B.17}$$

$$\xi_{,xy} = \left(|\mathbf{J}|_{,\xi}y_{,\eta} + y_{,\xi\eta}|\mathbf{J}|\right)\xi_{,y} + \left(|\mathbf{J}|_{,\eta}y_{,\eta} + y_{,\eta\eta}|\mathbf{J}|\right)\eta_{,y} \tag{B.18}$$

$$\xi_{,yy} = -\left(|\mathbf{J}|_{,\xi}x_{,\eta} + x_{,\xi\eta}|\mathbf{J}|\right)\xi_{,y} - \left(|\mathbf{J}|_{,\eta}x_{,\eta} + x_{,\eta\eta}|\mathbf{J}|\right)\eta_{,y} \tag{B.19}$$

$$\eta_{,xx} = -\left(|\mathbf{J}|_{,\xi}y_{,\xi} + y_{,\xi\xi}|\mathbf{J}|\right)\xi_{,x} - \left(|\mathbf{J}|_{,\eta}y_{,\xi} + y_{,\xi\eta}|\mathbf{J}|\right)\eta_{,x} \tag{B.20}$$

$$\eta_{,xy} = -\left(|\mathbf{J}|_{,\xi}y_{,\xi} + y_{,\xi\xi}|\mathbf{J}|\right)\xi_{,y} - \left(|\mathbf{J}|_{,\eta}y_{,\xi} + y_{,\xi\eta}|\mathbf{J}|\right)\eta_{,y} \tag{B.21}$$

$$\eta_{,yy} = \left(|\mathbf{J}|_{,\xi}x_{,\xi} + x_{,\xi\xi}|\mathbf{J}|\right)\xi_{,y} + \left(|\mathbf{J}|_{,\eta}x_{,\xi} + x_{,\xi\eta}|\mathbf{J}|\right)\eta_{,y} \tag{B.22}$$

Appendix C

Compressible Falkner–Skan–Cooke Solutions

Considerable research into the stability and receptivity characteristics of three-dimensional boundary layers has been conducted for the family of incompressible yawed-wedge flows, often referred to as Falkner–Skan–Cooke (FSC) flows [25]. Under suitable assumptions, an analogous family of self-similar compressible, three-dimensional boundary layers flows are possible. These flows were first studied by Reshotko & Beckwith [91] as a model of the flow near the stagnation-line of a yawed cylinder. In this appendix, we summarize the derivation of the compressible FSC equations and present solutions in a form useful for stability/receptivity calculations.

Using the Stewartson transformation along with a linear viscosity-temperature relation and $\mathsf{Pr} = 1$, the compressible boundary layer equations (subject to isothermal, no-slip wall boundary conditions and edge conditions at infinity) reduce to a system of two, ordinary differential equations. The details of the derivation are presented by Reshotko & Beckwith [91] in the context of the stagnation-line flow and here we only summarize the derivation with suitable changes to consider more general three-dimensional boundary layers. In the following, velocities are nondimensionalized by the free-stream speed-of-sound, c_∞^*, lengths by a convenient length scale L^* (defined explicitly below), and all other quantities are nondimensionalized by their freestream values. Consider the following Falkner-Skan distributions of inviscid slip velocities

$$u_e \equiv \frac{u_e^*}{c_\infty^*} = \mathsf{M}_\infty c_e(\tilde{x})\, \tilde{x}^m \cos\theta\,, \tag{C.1}$$

$$w_e \equiv \frac{w_e^*}{c_\infty^*} = \mathsf{M}_\infty \sin\theta \tag{C.2}$$

where $c_e(\tilde{x}) \equiv c_e^*/c_\infty^*$ is the local speed-of-sound at the boundary layer edge. The tilde denotes that x has been transformed to account for variable viscosity and density

effects using the Stewartson transformation [104] which is defined as

$$\tilde{x} \equiv \frac{\tilde{x}^*}{L^*} = \int_0^x \frac{\mu_w T_0}{\mu_0 T_w} \left(\frac{c_e}{c_0}\right)^{\frac{3\gamma-1}{\gamma-1}} dx \,, \tag{C.3}$$

$$\tilde{y} \equiv \frac{\tilde{y}^*}{L^*} = \frac{c_e}{c_0} \int_0^y \frac{\rho}{\rho_e} dy \,, \tag{C.4}$$

where the subscript "0" denotes freestream stagnation quantities while subscript "w" denotes conditions at the wall. Note that the quantity $(\mu_w T_0)/(\mu_0 T_w)$ can be determined from Sutherland's law given T_0/T_w and for the special case of $T_0/T_w = 1$, $(\mu_w T_0)/(\mu_0 T_w) = 1$. Note that Sutherland's law is only used once to determine the ratio μ_w/μ_0 given T_0/T_w. The viscosity is then given by the linear relationship

$$\frac{\mu}{\mu_0} = \left(\frac{\mu_w T_o}{\mu_0 T_w}\right) \frac{T}{T_0} \,. \tag{C.5}$$

To convert the equations to a set of ordinary differential equations, a similarity transformation is applied:

$$\xi = \tilde{x}, \tag{C.6}$$

$$\eta = \tilde{y} \sqrt{\frac{m+1}{2} \mathsf{Re}_c \left(\frac{c_0}{c_e}\right)^{\frac{2\gamma}{\gamma-1}} \tilde{x}^{m-1}} \,, \tag{C.7}$$

$$u(\xi, \eta) = f'(\eta)\, u_e(\xi) \,, \tag{C.8}$$

$$w(\eta) = g(\eta)\, w_e \,, \tag{C.9}$$

$$\frac{H - H_w}{H_e - H_w} = \phi(\eta) \,, \tag{C.10}$$

where H is the total enthalpy. In equation (C.7)

$$\mathsf{Re}_c = \frac{u_e^*(\tilde{x}^* = L^*)\, L^*}{\nu_e^*(\tilde{x}^* = L^*)} \tag{C.11}$$

is the chordwise Reynolds number, based on edge quantities at $\tilde{x}^* = L^*$.

When $\mathsf{Pr} = 1$, the similarity transformation converts the boundary layer equations into the following system of ordinary differential equations

$$f''' + f f'' = \beta_h \left[f'^2 - 1 - \left(\frac{T_0}{T_{N0}} - 1\right)(1 - g^2) - \left(\frac{T_w}{T_0} - 1\right)\left(\frac{T_0}{T_{N0}}\right)(1 - \phi) \right] \,, \tag{C.12}$$

$$g'' + fg' = 0 \,, \tag{C.13}$$

$$\phi'' + f\phi' = 0 \,, \tag{C.14}$$

where primes denote differentiation with respect to η, the pressure gradient (*i.e.* Hartree) parameter is given by $\beta_h = \frac{2m}{m+1}$, and the ratio T_0/T_{N0}, which combines the effects of sweep-angle and Mach number (see [91]), is defined as

$$\frac{T_0}{T_{N0}} = \frac{1 + \frac{\gamma-1}{2}\mathsf{M}_\infty^2}{1 + \frac{\gamma-1}{2}\mathsf{M}_\infty^2 \cos^2\theta} \,. \tag{C.15}$$

The above equations are solved subject to isothermal, no-slip wall boundary conditions with edge conditions enforced at infinity. After the Stewartson and similarity transformations, these boundary conditions become

$$f(0) = 0, \quad f'(0) = 0, \quad g(0) = 0, \quad \phi(0) = 0,$$
$$f(\infty) = 1, \quad g(\infty) = 1, \quad \phi(\infty) = 1 \,. \tag{C.16}$$

We note that when $\mathsf{Pr} = 1$ the spanwise momentum equation and the energy equation (along with their boundary conditions) are identical such that one equation can be dropped. However, unlike the incompressible case, the chordwise momentum and spanwise momentum (or energy) equations are coupled for compressible flow and must be solved simultaneously. In order for a similarity solution to exist, the coefficients in equations (C.12) must be independent of ξ. This occurs when β_h is constant and the wall is isothermal (*i.e.* T_w/T_0 is constant) and the solutions presented below satisfy both of these requirements. See [91] for a discussion of similarity when $\mathsf{Pr} \neq 1$.

Returning to the definitions of the local edge-velocities (C.1,C.2) we see that the local sweep-angle is given by

$$\theta_e = \tan^{-1}\left(\frac{\tan\theta}{\tilde{x}^{-m}c_e}\right) \tag{C.17}$$

and, since

$$c_e = \frac{1 + \frac{\gamma-1}{2}\mathsf{M}_\infty^2 \cos^2\theta}{1 + \frac{\gamma-1}{2}\mathsf{M}_\infty^2 \tilde{x}^{2m}\cos^2\theta} \tag{C.18}$$

the local sweep-angle is equal to the freestream sweep-angle, θ, when $\tilde{x} = 1$. This, in fact, is what motivates the specific form of the edge velocities given in equations (C.1)

and (C.2). Thus, the length scale L^* can now be identified as the chordwise location where the local sweep-angle equals the freestream sweep-angle and, the chordwise Reynolds number can be explicitly evaluated as

$$\mathsf{Re}_c = \frac{(U_\infty^* \cos \theta) L^*}{\nu_\infty^*} \tag{C.19}$$

since $U_e^* = U_\infty^*$ when $\tilde{x}^* = L^*$.

Once the ODE's have been solved for $f(\eta)$ and $g(\eta)$, the primitive variables at $\tilde{x} = 1$, nondimensionalized by edge quantities, are given by

$$\frac{T}{T_e} = \left(1 + \frac{\gamma - 1}{2} \mathsf{M}_\infty^2\right) \left[1 + \left(\frac{T_w}{T_0} - 1\right)(1 - \phi) - \right. \tag{C.20}$$
$$\left. \left(\frac{\frac{\gamma-1}{2}\mathsf{M}_\infty^2 \cos^2 \theta}{1 + \frac{\gamma-1}{2}\mathsf{M}_\infty^2}\right) f'^2 - \left(1 - \frac{T_{N0}}{T_0}\right) g^2\right],$$

$$\frac{u}{U_e} = f' \cos \theta, \tag{C.21}$$

$$\frac{w}{U_e} = g \sin \theta, \tag{C.22}$$

$$\frac{\rho}{\rho_e} = \frac{T_e}{T}. \tag{C.23}$$

For stability calculations, it is useful to rotate the velocities to the local streamline coordinates:

$$\frac{u_s}{U_e} = f' \cos^2 \theta + g \sin^2 \theta, \tag{C.24}$$

$$\frac{w_s}{U_e} = (g - f') \cos \theta \sin \theta. \tag{C.25}$$

Given the temperature profile, the physical y coordinate is obtained from

$$y \equiv \frac{y^*}{L^*} = \frac{\Psi}{\mathsf{Re}_c^{1/2}} \int_0^\eta \frac{T}{T_e} d\eta \tag{C.26}$$

where

$$\Psi = \left(1 + \frac{\gamma - 1}{2} \mathsf{M}_\infty^2\right)^{\frac{1}{2-2\gamma}} \sqrt{\frac{2}{m+1}}. \tag{C.27}$$

The displacement thickness of the streamwise velocity component is computed from

the definition

$$\delta_1 \equiv \int_0^\infty \left(1 - \frac{\rho u_s}{\rho_e U_e}\right) dy \tag{C.28}$$

which, when converted to an η integral, yields

$$\delta_1 \equiv \frac{\delta_1^*}{L^*} = \frac{\Psi}{\mathsf{Re}_c^{1/2}} \int_0^\infty \left(\frac{T}{T_e} - \frac{u_s}{U_e}\right) d\eta. \tag{C.29}$$

The momentum thickness of the streamwise profile is computed in a similar fashion using the definition

$$\delta_2 \equiv \int_0^\infty \frac{\rho u_s}{\rho_e U_e} \left(1 - \frac{u_s}{U_e}\right) dy \tag{C.30}$$

leading to

$$\delta_2 \equiv \frac{\delta_2^*}{L^*} = \frac{\Psi}{\mathsf{Re}_c^{1/2}} \int_0^\infty \frac{u_s}{U_e} \left(1 - \frac{u_s}{U_e}\right) d\eta. \tag{C.31}$$

The factors δ_1^*/L^* and δ_2^*/L^* are useful in converting solutions to the thickness length-scales commonly used in stability/receptivity analysis. For example, if δ_1^* is the desired length-scale, then

$$\frac{y^*}{\delta_1^*} = \frac{y^*}{L^*}\frac{L^*}{\delta_1^*} = \frac{\int_0^\eta \frac{T}{T_e} d\eta}{\int_0^\infty \left(\frac{T}{T_e} - \frac{u_s}{U_e}\right) d\eta}. \tag{C.32}$$

In order to obtain solutions for $\tilde{x} = 1$, the following parameters must be specified: M_e, T_w/T_0, θ_e, and β_h. Then equations (C.12) and (C.13) are solved using fourth-order accurate Runge-Kutta integration with a fixed step-size. The integration is started from the wall using assumed values of $f''(0)$ and $g'(0)$. Then a Newton iteration is performed to determine $f''(0)$ and $g'(0)$ such that the edge boundary conditions are satisfied. The infinite domain in η is truncated to $\eta = 20$ which is over 5 boundary layer thicknesses above the wall.

Our motivation in computing FSC profiles is to provide a convenient analytical set of boundary-layer profiles that can be used to model the profiles obtained from full NS calculations. As an example of matching a FSC solution to a boundary-layer profile from a NS solution, we consider the flow over a parabolic cylinder with the conditions $\mathsf{M} = 0.8$, $Re = 1 \times 10^5$, $\theta = 35°$, $T_w/T_0 = 1$ and extract the boundary-layer profile at the point of maximum crossflow, $s^*/r_n^* = 0.804$, where $\delta_1^*/r_n^* = 3.842 \times 10^{-3}$. At this location, the solution is projected to the body-normal coordinate-system, (s, n, z), and the local edge-conditions are determined to be: $\mathsf{M}_e = 0.657$, $\theta_e = 54.4°$, and $\beta_h = 0.766$ with $\delta_1^*/r_n^* = 3.842 \times 10^{-3}$. Using these parameters, a FSC profile is computed

and converted to the coordinate system used for the parabolic cylinder. In figure C.1 velocity profiles from the NS and FSC solutions are compared demonstrating very good agreement. The maximum crossflow for the NS profile is -0.107 while the FSC predicts a value of -0.103 which is within 4% of the NS solution. Figure C.2 compares the density and temperature profiles from the NS and FSC solutions and again the agreement is good. Also in good agreement is the shape factor, $H \equiv \delta_1/\delta_2$, which is equal to 2.67 for the FSC profile as compared to the measured value of 2.66 for the NS profile.

Using the linear stability solver discussed in Appendix D, the chordwise wavenumber and growth-rates for a stationary cross-flow instability have been computed for both the NS and FSC profile as a function of spanwise wavenumber. Figure C.3 shows that predicted wavenumbers for both profiles are in good agreement with a slight deviation at higher spanwise wavenumbers. The predicted grow-rates are shown in figure C.4 where it is seen that the FSC profile has a lower peak growth-rate (by $\approx 2\%$), and the unstable range is shifted slightly to higher spanwise wavenumbers. The reduction in peak grow-rate is not surprising given the slightly reduced level of crossflow in the FSC profile. It is, of course, possible to construct a FSC profile that better matches the NS solution by tweaking some of the parameters (θ_e in particular). The advantage of the current approach is that it provides an unambiguous definition of the parameters required to compute FSC profiles, based solely on boundary-layer edge quantities and the displacement thickness.

In summary, we have presented the derivation of the compressible FSC similarity equations and have obtained solutions in a form suitable for stability and receptivity analysis of infinite-span swept-wings. It has also been demonstrated that when boundary-layer edge-conditions and displacement thickness are matched to a local NS solution, FSC solutions are obtained which possess similar stability characteristics.
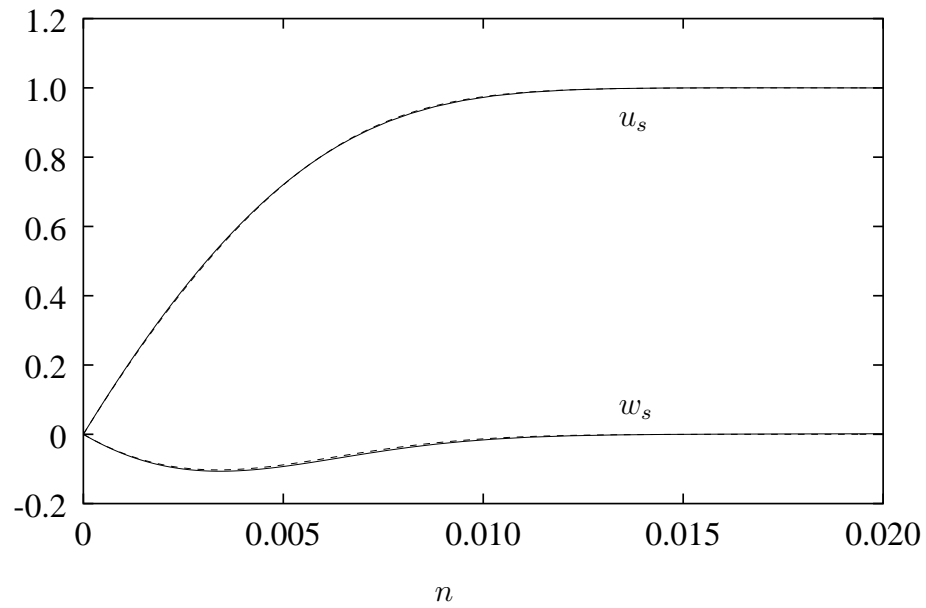
Figure C.1: Comparison of FSC —— and NS ---- boundary layer profiles for the local streamwise and crossflow velocities at s_{max}. Recall that $n = n^*/r_n^*$ is the wall-normal coordinate nondimensionalized by the nose radius of the parabolic cylinder.
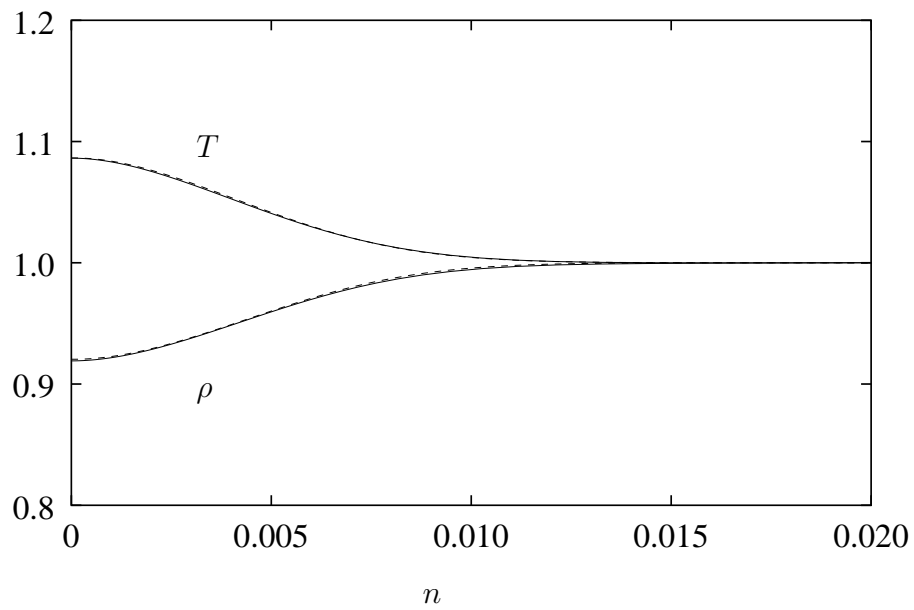
Figure C.2: Comparison of FSC —— and NS ---- boundary layer profiles for the temperature and density at s_{max}.
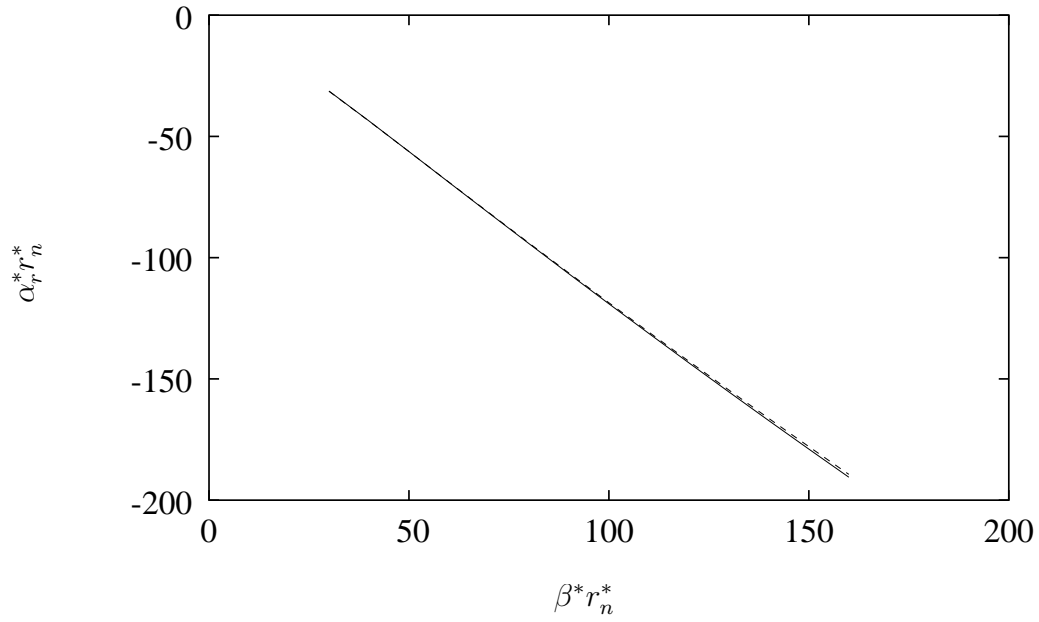
Figure C.3: Comparison of LST wavenumber predictions for the FSC —— and NS
---- boundary layer profiles.
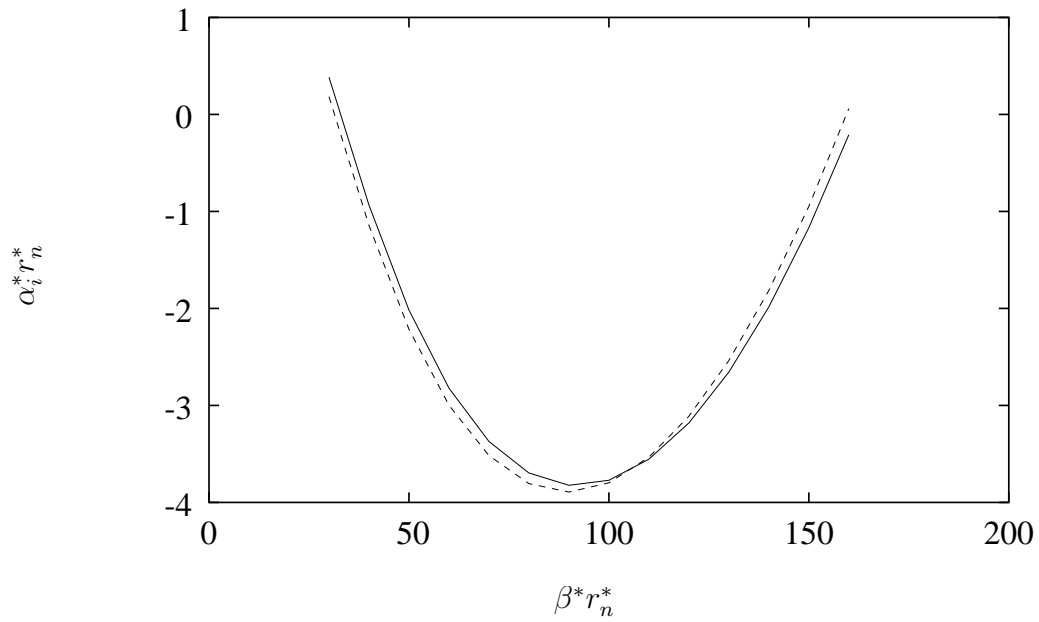
Figure C.4: Comparison of LST growth-rate predictions for the FSC —— and NS
---- boundary layer profiles.

Appendix D

Compressible Stability Solver

The Linear Stability Theory (LST) solver described in this appendix is based on the compressible, linearized-disturbance-equations developed in Chapter 2. Here, these equations are extended to account for surface curvature in the context of an infinite-span swept-wing. The quasi-parallel assumption is then used to form the stability equations and the numerical methods utilized to obtain the eigensolutions to the stability equations are presented. Finally, a perturbation method is introduced to correct the stability results for nonparallel effects and the numerical method implemented to solve for the nonparallel correction is discussed. With both surface curvature and nonparallel effects included, the stability solver described in this appendix represents the state-of-the-art in local linear stability analysis.

For further information on linear stability, the reader is referred to the very thorough review of the compressible stability equations and their solution by Mack [68]. Another useful review of stability analysis, especially as applied to three-dimensional boundary layers, is given by Malik [75].

D.1 Disturbance Equations on a Curved Surface

Recent stability analyses [76, 72] have shown that surface curvature has a significant quantitative effect on the growth-rates of stationary crossflow vortices. To account for this effect, we introduce the body-fitted, orthogonal coordinate system where, s is the coordinate tangent to the body, n is normal to the body, and z is the spanwise coordinate. The disturbance equations (2.22)–(2.24) corresponding to the linearized Navier–Stokes (LNS) equations are then rewritten using coordinate-system independent, vector notation

$$\rho'_{,t} + \nabla\bar{\rho} \cdot \mathbf{u}' + \nabla\rho' \cdot \bar{\mathbf{u}} + \bar{\rho}\nabla \cdot \mathbf{u}' + \rho'\nabla \cdot \bar{\mathbf{u}} = 0\,, \qquad\qquad \text{(D.1)}$$

$$\bar{\rho}\mathbf{u}'_{,t} + \rho'(\bar{\mathbf{u}} \cdot \nabla)\bar{\mathbf{u}} + \bar{\rho}(\mathbf{u}' \cdot \nabla)\bar{\mathbf{u}} + \bar{\rho}(\bar{\mathbf{u}} \cdot \nabla)\mathbf{u}' + \nabla p' = \tag{D.2}$$
$$\frac{1}{\mathsf{Re}}\left[\nabla(\bar{\lambda}\nabla \cdot \mathbf{u}' + \lambda'\nabla \cdot \bar{\mathbf{u}}) + 2\nabla \cdot (\bar{\mu}\mathbf{S}' + \mu'\bar{\mathbf{S}})\right],$$

$$\bar{\rho}T'_{,t} + \rho'(\bar{\mathbf{u}} \cdot \nabla)\bar{T} + \bar{\rho}(\mathbf{u}' \cdot \nabla)\bar{T} + \bar{\rho}(\bar{\mathbf{u}} \cdot \nabla)T' + \tag{D.3}$$
$$\bar{\rho}(\gamma - 1)\bar{T}\nabla \cdot \mathbf{u}' + \bar{\rho}(\gamma - 1)T'\nabla \cdot \bar{\mathbf{u}} + \rho'(\gamma - 1)\bar{T}\nabla \cdot \bar{\mathbf{u}} =$$
$$\frac{\gamma}{\mathsf{PrRe}}\left[\nabla\bar{\kappa} \cdot \nabla T' + \nabla\kappa' \cdot \nabla\bar{T} + \bar{\kappa}\nabla^2 T' + \kappa'\nabla^2\bar{T}\right] +$$
$$\frac{\gamma(\gamma - 1)\mathsf{M}^2}{\mathsf{Re}}\left[(2\bar{\lambda}\nabla \cdot \bar{\mathbf{u}})\nabla \cdot \mathbf{u}' + \lambda'(\nabla \cdot \bar{\mathbf{u}})^2 + 2\mu'\bar{\mathbf{S}} \cdot \bar{\mathbf{S}} + 4\bar{\mu}\bar{\mathbf{S}} \cdot \mathbf{S}'\right],$$

where $\mathbf{u}$ denotes the velocity vector $\{v_s, v_n, w\}^{\mathrm{T}}$ (in the body-fitted coordinate system), and ∇ is the generalized gradient operator. Differential distances in the s-direction are given by $h(s,n)ds$ where $h(s,n)$ is the coordinate system metric and metrics in the other coordinate directions are unity. Each of the differential operators in equations (D.1)–(D.3) can be written as a combination of partial derivatives with respect to (s,n,z) and additional terms involving the metric and its derivatives. For example, the gradient of a scalar function, f, is given by

$$\nabla f = \frac{1}{h}f_{,s}\hat{s} + f_{,n}\hat{n} + f_{,z}\hat{z} \tag{D.4}$$

where $\hat{s}$, $\hat{n}$, $\hat{z}$ are unit vectors in the coordinate directions. Likewise, the divergence of a vector is written as

$$\nabla \cdot \mathbf{u} = \frac{1}{h}(v_{s,s} + v_n h_{,n}) + v_{n,n} + u_{z,z}. \tag{D.5}$$

A complete description of all the generalized, differential operators required for the Navier–Stokes equations is given in Appendix A of Sherman [99]. Using these expressions, the LNS equations can be converted to a compact matrix form, analogous to equation (2.28),

$$\mathbf{U}'_{,t} + \mathbf{A}\mathbf{U}'_{,s} + \mathbf{B}\mathbf{U}'_{,n} + \mathbf{C}\mathbf{U}'_{,z} + \mathbf{D}\mathbf{U}' = \mathbf{V}_{ss}\mathbf{U}'_{,ss} + \mathbf{V}_{sn}\mathbf{U}'_{,sn} +$$
$$\mathbf{V}_{sz}\mathbf{U}'_{,sz} + \mathbf{V}_{nn}\mathbf{U}'_{,nn} + \mathbf{V}_{nz}\mathbf{U}'_{,nz} + \mathbf{V}_{zz}\mathbf{U}'_{,zz}. \tag{D.6}$$

The matrices appearing in equation (D.6) are defined in Appendix A.3. When curvature is removed, by setting $h = 1$, there is a direct correspondence between (s, n, z)

and (x, y, z) and equations (D.6) and (2.28) are equivalent. The reader should note that unlike recent stability analysis of the flow over the circular cylinder [76], our formulation allows for the mesh metric, h, to vary in both n and s, not just n. This greatly complicates the structure of the matrices given in Appendix A.3 but with the benefit that arbitrary two-dimensional bodies can be analyzed.

D.2 Quasi-Parallel Stability Analysis for an Infinite-Span Swept-Wing

Given the body-fitted coordinate system described in the previous section, additional coordinate systems used for stability analysis of an infinite-span swept-wing are shown in figure D.1 where it is assumed that all quantities are nondimensionalized as in section 2.2. The external freestream velocity makes an angle θ with the s-axis. The coordinate system aligned with the local edge-velocity is called the streamline coordinates, (s_s, n, z_s), and the local streamwise direction, s_s, makes an angle θ_e with the chordwise direction. The angle between the local streamwise direction and the freestream velocity is $\theta_p = \theta_e - \theta$.

For an infinite-span swept-wing, all mean z-gradients are zero by definition. By further making the parallel flow assumption, all mean s-derivatives are neglected and the disturbance solution can be written in terms of normal modes

$$\mathbf{U}'(s, n, z, t) = \hat{\mathbf{U}}(n)\, e^{i(k_s s + k_z z - \omega t)} \tag{D.7}$$

where $\hat{\mathbf{U}}(n) = \{\hat{\rho}, \hat{v}_s, \hat{v}_n, \hat{w}, \hat{T}\}^{\mathrm{T}}$ is the complex valued eigenfunction which is a function only of the wall normal coordinate, k_s is the chordwise wavenumber, k_z is the spanwise wavenumber, and ω is the angular frequency. In writing equation (D.7) it is understood that the actual solution is given by the real part of the left-hand-side. Substituting the normal-mode expression into the LNS equations (D.6) results in the following ordinary differential equation

$$-i\omega\hat{\mathbf{U}} + ik_s\mathbf{A}\hat{\mathbf{U}} + \mathbf{B}\hat{\mathbf{U}}_{,n} + ik_z\mathbf{C}\hat{\mathbf{U}} + \mathbf{D}\hat{\mathbf{U}}k_s^2\mathbf{V}_{ss}\hat{\mathbf{U}} -$$
$$ik_s\mathbf{V}_{sn}\hat{\mathbf{U}}_{,n} + k_sk_z\mathbf{V}_{sz}\hat{\mathbf{U}} - \mathbf{V}_{nn}\hat{\mathbf{U}}_{,nn} - ik_z\mathbf{V}_{nz}\hat{\mathbf{U}}_{,n} + k_z^2\mathbf{V}_{33}\hat{\mathbf{U}} = 0. \tag{D.8}$$

Given a mean-flow profile $\bar{\mathbf{U}}(n) = \{\bar{\rho}, \bar{v}_s, \bar{v}_n, \bar{w}, \bar{T}\}^{\mathrm{T}}$, and its first and second deriva-
tives in the wall-normal direction, $\bar{\mathbf{U}}_{,n}$, $\bar{\mathbf{U}}_{,nn}$, the matrices in equation (D.8) are de-
termined with the streamwise and spanwise derivatives of the mean flow set explicitly
to zero. Equation (D.8) is solved subject to the homogeneous boundary conditions

$$\hat{v}_s(0) = 0\,, \quad \hat{v}_n(0) = 0\,, \quad \hat{w}(0) = 0\,, \tag{D.9}$$

$$\hat{T}(0) = 0 \quad \text{or} \quad \hat{T}_{,n}(0) = 0\,, \tag{D.10}$$

$$\hat{v}_s, \hat{v}_n, \hat{w}, \hat{T} \to 0 \quad \text{as} \quad n \to \infty\,. \tag{D.11}$$

The wavenumbers and frequency, (k_s, k_z, ω), form a set of six real parameters
since they are complex quantities in general. With the homogeneous boundary con-
ditions (also mapped to computational space), equation (D.8) reduces to an eigenvalue
problem for any two of the six parameters, given the other four. Typically the eigen-
problems are formulated in either a temporal or spatial approach. For the temporal
problem the wavenumbers are specified real values and the eigenvalue is the complex
frequency, ω. Thus a temporal eigenmode has fixed spatial wavelengths and evolves
in time with the growth rate, σ, given by the imaginary part of ω:

$$\sigma = \mathrm{Im}(\omega)\,. \tag{D.12}$$

In the spatial problem, the frequency and one of the wavenumbers (k_z herein) are
specified real values and the other wavenumber (k_s) is the eigenvalue. In this case,
the waves evolve in space with the growth-rate given by

$$\sigma = -\mathrm{Im}(k_s) \tag{D.13}$$

and the local chordwise wavenumber is given by $\alpha = \mathrm{Re}(k_s)$.

Before proceeding, the reader should note that fixing k_z is a natural and reasonable
constraint for the problems at hand. This is because we are interested in comparing
the LST predictions with LNS solutions which have a value of k_z prescribed through
a receptivity process (either direct or indirect). The instability waves that result from
this receptivity process will have fixed k_z and grow only in the chordwise direction.
This approach is in contrast to the methods used in transition prediction where the
value of k_z (possibly complex) varies in the downstream direction in such a way as to

maximize the growth-rate [71, 81].

With the real parts of the spatial wavenumbers denoted by $\alpha = \mathrm{Re}(k_s)$ and $\beta = \mathrm{Re}(k_z)$ some useful relations can be summarized. The magnitude of the wavenumber vector is

$$k = \sqrt{\alpha^2 + \beta^2}\,, \tag{D.14}$$

the angle between the s-axis and the wave-vector is given by

$$\psi = \tan^{-1}\left(\frac{\beta}{\alpha}\right)\,, \tag{D.15}$$

and the phase velocity is

$$c_p = \frac{\omega}{k}\,. \tag{D.16}$$

Before solving, equation (D.8) is converted to computational space using the mapping $n \mapsto \eta$ which yields

$$
\begin{aligned}
\Big[(\mathbf{B} - ik_s\mathbf{V}_{sn} - ik_z\mathbf{V}_{nz})\eta_{,n}\Delta_\eta + ik_s\mathbf{A} + ik_z\mathbf{C} + \mathbf{D} + \\
k_s^2\mathbf{V}_{ss} + k_z^2\mathbf{V}_{33} - i\omega - \mathbf{V}_{nn}(\eta_{,n}^2\Delta_{\eta\eta} + \eta_{,nn}\Delta_\eta)\Big]\hat{\mathbf{U}} &= 0\,,
\end{aligned}
\tag{D.17}
$$

where the derivatives in η have been replaced with discrete approximations. We have implemented two different discretizations for the wall normal derivatives: fourth-order accurate finite differences and spectrally accurate Chebyshev collocation.

The finite difference operators are the same fourth-order accurate approximations described in section 3.4 for the LNS solver. This method is useful when a LST solution is desired using the same or similar mesh as used in a NS calculation. Usually when using the finite difference method the infinite domain in n is truncated to a finite domain and the far-field boundary condition is enforced at the finite domain boundary. This is only an approximation, but we have found that when the boundary is at least $25\delta_1$ above the wall, the eigensolutions are not adversely affected. The finite domain in n is then mapped to uniform computational space using the algebraic mapping function defined by

$$a = \frac{(n_{max}n_s)}{(n_{max} - 2n_s)}\,, \tag{D.18}$$

$$b = 1 + \frac{a}{n_{max}}\,, \tag{D.19}$$

$$n(\eta) = \frac{a\eta}{b - \eta}\,.$$

<div align="right">(D.20)</div>

In these expressions, n_{max} is the maximum vertical distance above the wall and n_s controls the minimum node spacing at the wall. As a general rule for subsonic mean boundary-layer profiles, we have found that $n_s \approx 2.5\delta_1$ provides an adequate point distribution when $n_{max} \approx 40\delta_1$. In practice, the actual values of n_s and n_{max} are set to ensure that the eigenfunction is adequately resolved since the quality of the solution is rather sensitive to the value of n_s.

Equation (D.17) can also be discretized using the spectrally accurate Chebyshev collocation operators (see Canuto *et al.* [12] on page 69). This method is used to provide reference eigensolutions for comparison with LNS calculations (see Chapter 4) and also to provide accurate solutions which are more economical then the FD method since fewer points are required for the same level of accuracy. Typically the Chebyshev solutions are obtained by mapping the semi-infinite domain in n to a finite domain in η using the transformation

$$n(\eta) = n_s \frac{1 + \eta}{1 - \eta}\,,$$

<div align="right">(D.21)</div>

where n_s again controls the minimum node spacing at the wall and a typical value of $n_s = 2\delta_1$. Unlike the FD method, the Chebyshev solutions are not particularly sensitive to the value of n_s which makes this method more robust.

Regardless of the particular discretization, the boundary conditions are applied to the discrete equations in the same manner. At the wall, the momentum equations are replaced with equations (D.9) and for the case of an isothermal wall, the energy equation is replaced with $\hat{T}(0) = 0$. If, instead, an adiabatic wall is used, the energy equation is modified by explicitly setting the wall-normal derivative of both the mean and disturbance temperature to zero. For the disturbances, this amounts to removing terms which multiply $\hat{T}_{,n}$ at the wall. Although this "weak" formulation for the adiabatic constraint does not guarantee that $\hat{T}_{,n}$ is strictly zero, the deviation from zero will be on the order of the truncation error of the scheme. In all cases, the discrete continuity equation is used at the wall to obtain density. At the far-field boundary, all disturbance quantities are set to zero by replacing the equations of motion with the constraint $\hat{\mathbf{U}} = 0$.

With the boundary conditions applied to the discrete equation (D.17) and the appropriate parameters set, the resulting problem is reduced to a matrix eigenvalue

problem. If the temporal approach is used then the eigenvalue problem can be written as

$$\mathbf{M}\hat{\mathbf{U}} = \omega\hat{\mathbf{U}} \tag{D.22}$$

which is a $(5N_\eta \times 5N_\eta)$ regular, complex eigenvalue problem that is solved using the IMSL routine `EVCCG` [54].

For the spatial problem, the eigenvalue, k_s, appears nonlinearly and the eigenvalue problem can be written in the form

$$(\mathbf{C}_0 + k_s\mathbf{C}_1 + k_s^2\mathbf{C}_2)\hat{\mathbf{U}} = 0. \tag{D.23}$$

Bridges & Morris [11] show that this can be converted to the following extended problem

$$\begin{bmatrix} -\mathbf{C}_0^{-1}\mathbf{C}_1 & -\mathbf{C}_0^{-1}\mathbf{C}_2 \\ \mathbf{I} & \mathbf{0} \end{bmatrix} \left\{ \begin{array}{c} \hat{\mathbf{U}}_1 \\ \hat{\mathbf{U}} \end{array} \right\} = k_s \left\{ \begin{array}{c} \hat{\mathbf{U}}_1 \\ \hat{\mathbf{U}} \end{array} \right\} \tag{D.24}$$

where $\hat{\mathbf{U}}_1 = k_s\hat{\mathbf{U}}$. In practice, the inverse $\mathbf{C}_0^{-1}$ is not directly computed. Instead, the *LU*-factorization of $\mathbf{C}_0$ is computed using the LAPACK routine `CGETRF` [3], and the products, $\mathbf{C}_0^{-1}\mathbf{C}_1$ and $\mathbf{C}_0^{-1}\mathbf{C}_2$, are obtained by forward-solve and back-substitution using the routine `CGETRS` [3].

Equation D.24 is a $(10N_\eta \times 10N_\eta)$ regular, complex eigenvalue problem which is again solved using the `EVCCG` routine [54]. The computational expense of the QR algorithm, which is the basis of IMSL eigenvalue routine, is on the order of N^3, where N is the dimension of the matrix [45]. Thus the spatial eigensystem is eight times as expensive to solve as the temporal eigensystem and this fact motivates the need for high-order accurate spatial differencing.

D.3   Nonparallel Effects

Along with surface curvature, nonparallel effects are also found to have a significant impact on the stability characteristics of stationary crossflow vortices [76]. We have included nonparallelism in our stability calculations using a perturbation approach, pioneered by Ling & Reynolds [64] and Saric & Nayfeh [93]. Here, we follow the approach of Saric & Nayfeh [93] applied to the compressible linear stability equations in curvilinear coordinates.

For high Reynolds numbers, the mean boundary layer flow, $\bar{\mathbf{U}}$, can be considered a slowly varying function of the streamwise coordinate, s. Defining a slow coordinate, $s_1 = \varepsilon s$, the base flow can be written as an expansion in the parameter ε

$$\bar{\mathbf{U}}(s,n) = \bar{\mathbf{U}}_0(s_1,n) + \varepsilon\bar{\mathbf{U}}_1(s_1,n) + \ldots \qquad (D.25)$$

where ε is a small dimensionless parameter representing the nonparallelism of the base flow. Here, $\bar{\mathbf{U}}_0(s_1,n)$ is the quasi-parallel base flow, and $\bar{\mathbf{U}}_1(s_1,n)$ is the first-order nonparallel correction which, for the class of flows considered here, consists only of the scaled, wall-normal velocity, $\bar{\mathbf{U}}_1 = \{0,0,\bar{v}_n/\varepsilon,0,0\}^{\mathrm{T}}$.

Utilizing the method of multiple scales, linear disturbances about the base flow can be expanded in ε as

$$\mathbf{U}'(s,n,z,t) = \left\{A(s_1)\hat{\mathbf{U}}_0(s_1,n) + \varepsilon\hat{\mathbf{U}}_1(s_1,n) + \ldots\right\}$$
$$\exp\left(\int ik_s(s_1)ds + ik_z z - i\omega t\right). \qquad (D.26)$$

From the following analysis, we will show that $\hat{\mathbf{U}}_0(s_1,n)$ is the same quasi-parallel eigenfunction discussed is section D.2, $A(s_1)$ is the local wave amplitude, and $\hat{\mathbf{U}}_1(s_1,n)$ is the nonparallel correction at $\mathcal{O}(\varepsilon)$.

Equations (D.25) and (D.26) are substituted into the linearized Navier–Stokes equations in curvilinear coordinates (D.6) and terms are grouped in powers of ε. In so doing, we note that the matrices ($\mathbf{A}$, $\mathbf{B}$, $\mathbf{C}$, $\mathbf{D}$) can be split into parallel and nonparallel portions, *i.e.*

$$\mathbf{A}(\bar{\mathbf{U}}) = \mathbf{A}_0(\bar{\mathbf{U}}_0) + \varepsilon\mathbf{A}_1\left(\frac{\partial\bar{\mathbf{U}}_0}{\partial s_1},\bar{\mathbf{U}}_1\right) + \ldots, \qquad (D.27)$$

whereas, the matrices due to viscous effects ($\mathbf{V}_{ss}$, $\mathbf{V}_{sn}$, *etc.*) only contain parallel flow contributions. To $\mathcal{O}(\varepsilon^0)$ we obtain the parallel linear stability equations (D.8)

$$\begin{aligned}
\mathcal{L}_0(\hat{\mathbf{U}}_0) &= -i\omega\hat{\mathbf{U}}_0 + ik_s\mathbf{A}_0\hat{\mathbf{U}}_0 + \mathbf{B}_0\hat{\mathbf{U}}_{0,n} + ik_z\mathbf{C}_0\hat{\mathbf{U}}_0 + \mathbf{D}_0\hat{\mathbf{U}}_0 + \\
&\quad k_s^2\mathbf{V}_{ss}\hat{\mathbf{U}}_0 - ik_s\mathbf{V}_{sn}\hat{\mathbf{U}}_{0,n} + k_s k_z\mathbf{V}_{sz}\hat{\mathbf{U}}_0 - \mathbf{V}_{nn}\hat{\mathbf{U}}_{0,nn} - \qquad (D.28)\\
&\quad ik_z\mathbf{V}_{nz}\hat{\mathbf{U}}_{0,n} + k_z^2\mathbf{V}_{33}\hat{\mathbf{U}}_0 \\
&= 0\,.
\end{aligned}$$

This equation is subject to the homogeneous boundary conditions (D.9)–(D.11) leading to an eigenvalue problem for $(k_s, \hat{\mathbf{U}}_0)$ which is identical to that discussed in section D.2.

At $\mathcal{O}(\varepsilon^1)$ the following equation is obtained

$$
\mathcal{L}_0(\hat{\mathbf{U}}_1) = \left\{ (2ik_s\mathbf{V}_{ss} + ik_z\mathbf{V}_{sz} - \mathbf{A}_0)\hat{\mathbf{U}}_0 + \mathbf{V}_{sn}\hat{\mathbf{U}}_{0,n} \right\}\frac{dA}{ds_1} +
$$

$$
\left\{ \mathbf{V}_{ss}\left(-\frac{dk_s}{ds_1}\hat{\mathbf{U}}_0 + 2ik_s\hat{\mathbf{U}}_{0,s_1} \right) + \mathbf{V}_{sn}\hat{\mathbf{U}}_{0,s_1 n} + \right. \tag{D.29}
$$

$$
\left. (ik_z\mathbf{V}_{sz} - \mathbf{A}_0)\hat{\mathbf{U}}_{0,s_1} - \mathcal{L}_1(\hat{\mathbf{U}}_0) \right\}A\,. \tag{D.30}
$$

Here, $\mathcal{L}_0$ is the parallel-flow operator introduced in equation (D.28) and $\mathcal{L}_1$ an operator due to the nonparallel meanflow which takes the form

$$
\mathcal{L}_1(\hat{\mathbf{U}}_0) = ik_s\mathbf{A}_1\hat{\mathbf{U}}_0 + \mathbf{B}_1\hat{\mathbf{U}}_{0,n} + ik_z\mathbf{C}_1\hat{\mathbf{U}}_0 + \mathbf{D}_1\hat{\mathbf{U}}_0\,. \tag{D.31}
$$

Equation (D.29) is also subject to the homogeneous boundary conditions (D.9)–(D.11) which are now written in terms of the $\hat{\mathbf{U}}_1$ variables. Thus, the equations at $\mathcal{O}(\varepsilon^1)$ for $\hat{\mathbf{U}}_1$ are an inhomogeneous version of the parallel-flow stability equations where the RHS forcing term depends on the eigensolution to the homogeneous problem (D.28) and an as-yet undetermined amplitude function $A(s_1)$. Since the homogeneous problem given by $\mathcal{L}_0(\hat{\mathbf{U}}_1) = 0$ has a nontrivial solution (*i.e.* the quasi-parallel eigensolutions) the solution to the inhomogeneous problem (D.29) only has a solution if a solvability condition is met [93].

To simplify the construction of the solvability condition, we first convert the equations (D.29) to a system of first-order equations. This is accomplished using the linearized continuity equation to remove the explicit dependence on $v'_{n,nn}$ (see Appendix A.4). Doing so in equation (D.29) and introducing additional unknowns for first-derivatives of $\hat{\mathbf{U}}_1$ in the wall-normal direction, leads to a system of eight, first-order ordinary differential equations of the form

$$
\hat{\mathbf{Q}}_{,n} + \mathbf{F}\hat{\mathbf{Q}} = \mathbf{G}\frac{dA}{ds_1} + \mathbf{H}A \tag{D.32}
$$

where

$$\hat{\mathbf{Q}} = \begin{Bmatrix} \hat{Q}_1 \\ \hat{Q}_2 \\ \hat{Q}_3 \\ \hat{Q}_4 \\ \hat{Q}_5 \\ \hat{Q}_6 \\ \hat{Q}_7 \\ \hat{Q}_8 \end{Bmatrix} = \begin{Bmatrix} \hat{\rho} \\ \hat{v}_s \\ \hat{v}_n \\ \hat{w} \\ \hat{T} \\ \hat{v}_{s,n} \\ \hat{w}_{,n} \\ \hat{T}_{,n} \end{Bmatrix}_1 \tag{D.33}$$

is the extended vector of unknowns (note that we have dropped the subscript 1 on the definition of $\hat{\mathbf{Q}}$ for brevity). The RHS has two vector coefficients, $\mathbf{G}$ and $\mathbf{H}$, where the nonparallel meanflow terms, $\mathcal{L}_1(\hat{\mathbf{U}}_0)$, contribute to $\mathbf{H}$. The definitions of the matrices appearing in equation (D.32) are given in Appendix A.4. The boundary conditions for (D.32) are given by

$$\hat{Q}_2(0) = 0\,, \quad \hat{Q}_3(0) = 0\,, \quad \hat{Q}_4(0) = 0\,, \tag{D.34}$$

$$\hat{Q}_5(0) = 0 \quad \text{or} \quad \hat{Q}_8(0) = 0\,, \tag{D.35}$$

$$\hat{Q}_2, \hat{Q}_3, \hat{Q}_4, \hat{Q}_5 \to 0 \quad \text{as} \quad n \to \infty\,. \tag{D.36}$$

The solvability condition is constructed by multiplying equation (D.32) by the vector $\hat{\mathbf{Z}}^{\mathrm{T}} = \{\hat{Z}_1, \hat{Z}_2, \hat{Z}_3, \hat{Z}_4, \hat{Z}_5, \hat{Z}_6, \hat{Z}_7, \hat{Z}_8\}$ (later identified as the adjoint eigenfunction) and integrating in the normal direction

$$\int_0^\infty \hat{\mathbf{Z}}^{\mathrm{T}} \hat{\mathbf{Q}}_{,n} dn + \int_0^\infty \hat{\mathbf{Z}}^{\mathrm{T}} \mathbf{F} \hat{\mathbf{Q}} dn = \frac{dA}{ds_1} \int_0^\infty \hat{\mathbf{Z}}^{\mathrm{T}} \mathbf{G} dn + A \int_0^\infty \hat{\mathbf{Z}}^{\mathrm{T}} \mathbf{H} dn\,. \tag{D.37}$$

Integrating by parts leads to

$$-\int_0^\infty (\hat{\mathbf{Z}}_{,n}^{\mathrm{T}} - \hat{\mathbf{Z}}^{\mathrm{T}} \mathbf{F}) \hat{\mathbf{Q}} dn + \hat{\mathbf{Z}}^{\mathrm{T}} \hat{\mathbf{Q}} \Big|_0^\infty = \frac{dA}{ds_1} \int_0^\infty \hat{\mathbf{Z}}^{\mathrm{T}} \mathbf{G} dn + A \int_0^\infty \hat{\mathbf{Z}}^{\mathrm{T}} \mathbf{H} dn\,. \tag{D.38}$$

The solvability condition follows by requiring that both terms on the LHS of (D.38) be zero. Thus, we arrive at the adjoint equation (after transposing),

$$\hat{\mathbf{Z}}_{,n} - \mathbf{F}^{\mathrm{T}} \hat{\mathbf{Z}} = 0 \tag{D.39}$$

and the adjoint boundary conditions which follow from

$$\hat{\mathbf{Z}}^{\mathrm{T}}\hat{\mathbf{Q}}\Big|_{0}^{\infty} = 0\,. \tag{D.40}$$

Since each term in (D.40) must be zero, the boundary conditions on $\hat{\mathbf{Q}}$ require that the following conditions be imposed on the adjoint problem

$$\hat{Z}_1(0) = 0\,, \quad \hat{Z}_6(0) = 0\,, \quad \hat{Z}_7(0) = 0 \tag{D.41}$$

$$\hat{Z}_8(0) = 0 \quad \text{or} \quad \hat{Z}_5(0) = 0\,, \tag{D.42}$$

$$\hat{Z}_1, \hat{Z}_6, \hat{Z}_7, \hat{Z}_8 \to 0 \quad \text{as} \quad n \to \infty\,. \tag{D.43}$$

Thus, equations (D.39) and boundary conditions (D.41)–(D.43) constitute the adjoint eigenvalue problem and when these equations are used in equation (D.38) the solvability condition becomes

$$h_1(s_1)\frac{dA}{ds_1} + h_2(s_1)A = 0 \tag{D.44}$$

where

$$h_1(s_1) = \int_0^\infty \hat{\mathbf{Z}}^{\mathrm{T}}\mathbf{G}\,dn \tag{D.45}$$

and

$$h_2(s_1) = \int_0^\infty \hat{\mathbf{Z}}^{\mathrm{T}}\mathbf{H}\,dn\,. \tag{D.46}$$

In practice, before solving equation (D.44), we convert back from the slow variable s_1 to s by multiplying both sides by ε, leading to

$$h_1(s)\frac{dA}{ds} + h_2(s)A = 0\,. \tag{D.47}$$

In transforming back to s, all the terms requiring derivatives with respect to s_1 are converted to derivatives in the physical coordinate s, and the nonparallel meanflow terms are now of the form $\varepsilon\bar{\mathbf{U}}_1 = \{0, 0, \bar{v}_n, 0, 0\}$. Thus, all quantities are returned to their unscaled values and the solution to equation (D.47) is simply

$$\frac{A(s)}{A(s_0)} = \exp\left(-\int_{s_0}^{s}\frac{h_2}{h_1}\,ds\right) \tag{D.48}$$

where s_0 is an arbitrary reference location. Using this result in equation (D.26), yields to lowest order

$$\mathbf{U}'(s, n, z, t) = A(s_0)\hat{\mathbf{U}}_0(s, n) \ \exp\left[\int_{s_0}^{s}\left(ik_s(s) - \frac{h_2}{h_1}\right)ds + ik_z z - i\omega t\right] . \quad \text{(D.49)}$$

The nonparallel growth-rate and chordwise wavenumber are defined as

$$\sigma = \text{Re}\left[\frac{\partial}{\partial s}\ln(U')\right] , \quad \text{(D.50)}$$

$$\alpha = \text{Im}\left[\frac{\partial}{\partial s}\ln(U')\right] \quad \text{(D.51)}$$

where U' is any desired disturbance quantity. Using these expressions, one obtains

$$\sigma = -\text{Im}(k_s) - \text{Re}\left(\frac{h_2}{h_1}\right) + \text{Re}\left(\frac{\partial}{\partial s}\ln(\hat{U})\right) , \quad \text{(D.52)}$$

$$\alpha = \text{Re}(k_s) - \text{Im}\left(\frac{h_2}{h_1}\right) + \text{Im}\left(\frac{\partial}{\partial s}\ln(\hat{U})\right) . \quad \text{(D.53)}$$

Note that $\hat{U}$ is any particular disturbance eigenfunction which can be a function of both s and n. Thus, both σ and α depend on the particular disturbance quantity used and the wall normal coordinate. The three terms which contribute to the nonparallel growth-rate in equation (D.52) are, in order of appearance: the quasi-parallel growth-rate with curvature, the nonparallel meanflow term, and the eigenfunction growth term.

The adjoint eigenfunction must be computed in order to construct the solvability condition and to determine the nonparallel corrections to the growth-rate and wavenumber. Since the eigenvalues for the regular and adjoint problems are the same, the first-step is to solve the regular eigenvalue problem (*i.e.* equation D.28) using the techniques described in section D.2. Given the appropriate eigenvalue, the adjoint eigenfunction is obtained by direct integration of equation (D.39) subject to boundary conditions (D.41)–(D.43) with no iteration required on the eigenvalue. The integration is started at a fixed height above the wall, $n = n_{max}$, and the initial condition at n_{max} is constructed by solving the uniform-flow version of equation (D.39). Mack [68] describes the analytical procedure used to determine the initial condition

for the compressible equations without curvature. For simplicity, we formulate the problem numerically by substituting the uniform-flow conditions at n_{max} into (D.39) and solving the resulting (8×8) eigensystem using the LAPACK routine `CGEEV` [3]. Doing so, one obtains 8 eigensolutions, four that are damped for large n and four that are unbounded for large n. Consistent with the farfield boundary conditions (D.43), the bounded solutions are used as four linearly-independent initial-conditions at n_{max}. Each of these initial conditions are integrated to the wall using standard fourth-order accurate, fixed-step Runge-Kutta integration with the orthonormalization procedure of Conte [24] used to prevent contamination from the undamped solutions. At the wall, a linear superposition is constructed that satisfies the wall boundary conditions. With curvature, the metric terms vary over the entire wall-normal domain so that the initial condition described above is only approximate. However, in practice, $n_{max} \geq 2$ is found to be adequate for cases with and without curvature. Once the adjoint is obtained, h_1 and h_2 are constructed given the full (nonparallel) meanflow, and the parallel eigenfunctions. Note that in determining h_1 and h_2, chordwise derivatives of both the meanflow and the regular eigenfunctions are required. The chordwise derivatives of the meanflow come directly from the full mean solution, while the streamwise derivatives of the eigenfunctions are computed by solving the regular eigensystem over a range in s and forming fourth-order-accurate finite difference approximations (see section 3.4) for the chordwise derivatives.
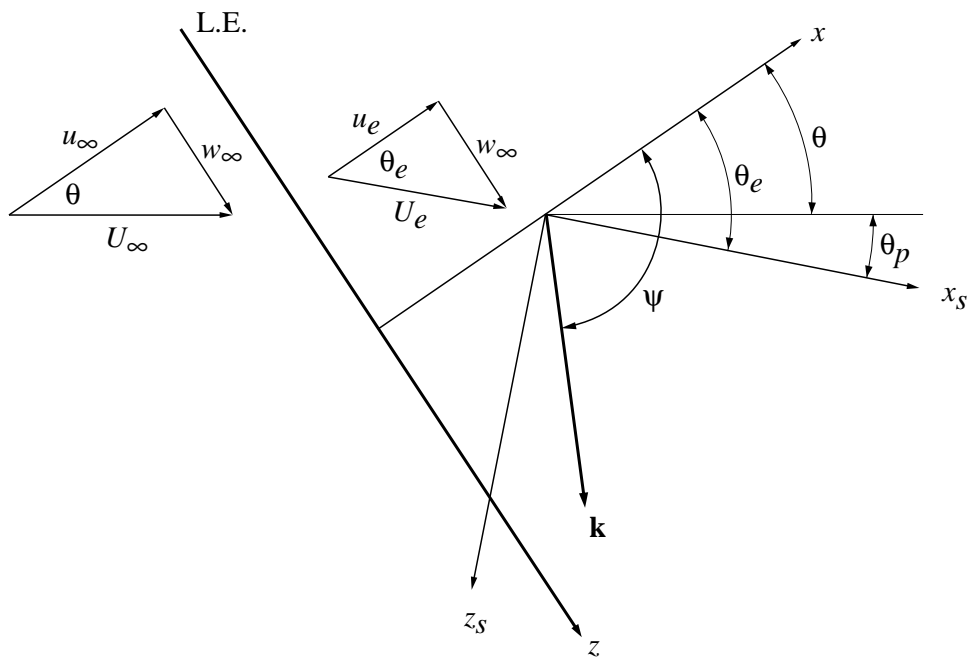
Figure D.1: Coordinate systems for LST analysis of an infinite-span swept wing

Appendix E

Compressible, Finite Reynolds-Number Receptivity Theory

Finite Reynolds-Number Theory (FRNT) is based on the work of Zavol'skii *et al.* [113] who approximated the linearized Navier-Stokes equations locally using the quasi-parallel disturbance equations. This was done within the same receptivity framework used by Goldstein [41] and Ruban [92] (who themselves used high Reynolds number asymptotics). Recently FRNT has been applied by Crouch [27, 28] and Choudhari & Streett [20, 21] to investigate receptivity phenomena under a variety of situations. However, most applications of FRNT have been for incompressible flow with the notable exception of the work of Zhigulev & Fedorov [114] for two-dimensional roughness. In the following, we outline the straightforward extension of FRNT to compressible flow for three-dimensional boundary layers. The development follows the exposition given by Choudhari [17] with appropriate extensions.

In FRNT, the linearized Navier-Stokes equations are approximated by the quasi-parallel disturbance equations. Towards that end, two length scales are defined: l^* corresponding to the streamwise location of the wall disturbance downstream of the leading-edge and L^* which is proportional to the undisturbed boundary layer thickness at $s^* = l^*$. L^* is defined relative to l^* through the relation

$$L^* = \frac{l^*}{\sqrt{\mathsf{Re}_l}}, \tag{E.1}$$

where $\mathsf{Re}_l \equiv U_e^*(s^* = l^*)l^*/\nu^*$ is the Reynolds number based of the local, slip-velocity tangent to the surface at the wall disturbance location. The length-scale L^* is used to scale both the height of the bump and its variations in the streamwise and spanwise directions. With this scaling, the streamwise direction is given by $S = (s^* - l^*)/L^*$, the wall normal direction by $N = n^*/L^*$, and the scaled spanwise direction by $Z = z^*/L^*$.

The global coordinates (s^*, n^*, z^*) when scaled by l^* are denoted as (s, n, z).

Our primary focus is on the generation of stationary cross-flow vortices so that we consider small-amplitude, spanwise periodic wall disturbances (relative to the undisturbed wall, $N = 0$) of the form

$$N_w(S, Z) = \varepsilon_w h_w(S) e^{i\beta_w Z} \tag{E.2}$$

where $\varepsilon_w = \varepsilon_w{}^*/L^* \ll 1$ is the scaled roughness height, $h_w(S)$ is the streamwise shape of the roughness, and $\beta_w = \beta_w{}^* L^*$ is the spanwise wavenumber of the bump. Since the analysis is linear, the current results can be thought of as the response of the boundary layer to a single Fourier mode of a more complicated spanwise distribution.

The flow is denoted by the vector field $\mathbf{U} = \{\rho, u, v, w, T\}^{\mathrm{T}}$ and, if the amplitude of the wall disturbance is sufficiently small, the dependent variables can be expanded as a regular perturbation series in ε_w

$$\mathbf{U}(S, N, Z) = \bar{\mathbf{U}}(N) + \varepsilon_w \mathbf{U}_w(S, N) e^{i\beta_w Z} + \mathcal{O}(\varepsilon_w^2). \tag{E.3}$$

Consistent with FRNT, in writing this expression we utilized the fact that $L^*/l^* \ll 1$ so that the undisturbed mean boundary layer flow $\bar{\mathbf{U}}(s, N)$ can be replaced with the local, quasi-parallel approximation $\bar{\mathbf{U}}(N) \equiv \bar{\mathbf{U}}(s = 1, N)$.

The mean-flow disturbance, $\mathbf{U}_w$, is obtained by solving the Navier-Stokes equations linearized about the parallel mean flow, $\bar{\mathbf{U}}(N)$. The boundary conditions for this problem are the usual no-slip, no-penetration conditions applied at the perturbed wall location, $N(S, Z) = \varepsilon_w h_w(S) e^{i\beta_w Z}$. A detailed derivation of the linearized boundary conditions (transfered to $N = 0$) for compressible flow over curved surfaces is given in Appendix F. In addition, the solutions also satisfy zero-disturbance conditions as $N \to \infty$.

After taking the Fourier transform $(S \to \alpha)$ the linearized Navier-Stokes equations with the quasi-parallel approximation take the form of the compressible stability equations which are the compressible analogue to the Orr-Sommerfeld equation. These equations can be formally written as

$$\mathcal{L}^{(\alpha, \beta_w, \mathsf{Re}, \mathsf{Pr}, \mathsf{M})} \hat{\mathbf{U}}_w = 0 \tag{E.4}$$

where the hat denotes the Fourier transform

$$\hat{\mathbf{U}}_w(\alpha, N) = \frac{1}{\sqrt{2\pi}} \int_{-\infty}^{\infty} \mathbf{U}_w(S, N) e^{-i\alpha S} dS. \tag{E.5}$$

Appendix D presents the compressible stability equations in detail and describes the methods used to obtain eigensolutions for the homogeneous problem. In the present case, we require solutions to the same equations, but with inhomogeneous boundary conditions at the wall. These solutions are obtained with the same Chebyschev spatial discretization used in Appendix D but by including the boundary conditions in the discrete approximation and using Gaussian elimination to solve the resulting linear system.

As discussed in detail by Choudhari [17], the solution of the compressible stability equations in Fourier space can be obtained without regard for causality. However, when the Fourier inversion,

$$\mathbf{U}_w(x, N) = \frac{1}{\sqrt{2\pi}} \int_{\Gamma} \hat{\mathbf{U}}_w(\alpha, N) e^{i\alpha S} d\alpha, \tag{E.6}$$

is performed to return the solution to physical space, causality must be accounted for in choosing the inversion contour, Γ. Herein, we assume that the crossflow instability is convective in nature without applying a rigorous causality condition (*i.e.* the Briggs-Bers criterion [8]). This same assumption has been used by several researchers in the context of FRNT [17, 29].

The contribution of the integral in (E.6) to a particular CF-instability mode is given by the residue of the integrand at the complex streamwise wavenumber of the CF-mode, α_{cf}. The residue theorem states that

$$\int_C f(z) dz = 2\pi i \mathrm{Res}_{z=z_0}[f(z)] = 2\pi i b_1 \tag{E.7}$$

where the function $f(z)$ is analytic in C except at z_0 which is an isolated singular point. If $f(z)$ is written as

$$f(z) = \frac{p(z)}{q(z)} \tag{E.8}$$

where both p and q are analytic at z_0 and

$$p(z_0) \neq 0, \qquad q(z_0) = 0, \qquad \text{and} \qquad q'(z_0) \neq 0 \tag{E.9}$$

then the residue at z_0 is

$$b_1 = \frac{p(z_0)}{q'(z_0)}. \tag{E.10}$$

Returning to equation (E.6), we have

$$p(\alpha) = e^{i\alpha S}, \tag{E.11}$$

$$q(\alpha) = \hat{U}_n^{-1}(\alpha, N) \tag{E.12}$$

Where $\hat{U}_n$ is a particular component of $\hat{\mathbf{U}}_w$. With these expressions, the residue at α_{cf} is given by

$$U_n(S, N) = \frac{i\sqrt{2\pi}}{\frac{\partial \hat{U}_n^{-1}}{\partial \alpha}(\alpha_{cf}, N)} e^{i\alpha_{cf} S}. \tag{E.13}$$

The value of $\frac{\partial \hat{U}_n^{-1}}{\partial \alpha}(\alpha_{cf}, N)$ is determined by computing $\hat{U}_n^{-1}(\alpha, N)$ at $\alpha = \alpha_{cf} \pm \Delta\alpha$ and using a central difference to approximate the derivative.

The form of the perturbation corresponding to the residue at (α_{cf}, β_w) is then given by [41]

$$\mathbf{U}_{cf} = \hat{h}_w(\alpha_{cf}) \, \Lambda(\beta_w, \mathsf{Re}, \mathsf{Pr}, \mathsf{M}) \, \mathbf{E}(N, \beta_w, \mathsf{Re}, \mathsf{Pr}, \mathsf{M}) \, e^{i(\alpha_{cf} S + \beta_w Z)} \tag{E.14}$$

where $\hat{h}_w(\alpha_{cf})$ is the amplitude of the Fourier component of the roughness shape-function which is resonant with the crossflow vortex mode. The factor $\Lambda(\beta_w, \mathsf{Re}, \mathsf{Pr}, \mathsf{M})$ is called the "efficiency" function which characterizes the local receptivity process independent of the geometry of the roughness, and $\mathbf{E}(N, \beta_w, \mathsf{Re}, \mathsf{Pr}, \mathsf{M})$ is the vector of eigenfunctions for the stationary crossflow vortex under consideration. Similar to [17], the eigenfunctions are normalized such that maximum of the eigenfunction for the velocity perturbation in the direction of the local inviscid streamline is unity. Thus, the initial, complex amplitude of the crossflow vortex based on this quantity is

$$A_{cf} = \varepsilon_w \, \hat{h}_w(\alpha_{cf}) \, \Lambda(\beta_w, \mathsf{Re}, \mathsf{Pr}, \mathsf{M}). \tag{E.15}$$

For the purpose of comparing the effectiveness of various parameters on the receptivity of CF vortices, it is sufficient to examine the magnitude of $\Lambda(\beta_w, \mathsf{Re}, \mathsf{Pr}, \mathsf{M})$. However, when directly comparing to the results of experiments or computations, equation (E.15) must be used.

To test our implementation of the FRNT, we have examined the receptivity of the compressible Falkner-Skan-Cooke profile (see Appendix C) to surface roughness. The parameters were chosen to match the incompressible results of Choudhari [17]. We use $\mathsf{M} = 0.1$, $\mathsf{Re}_l = 80,000$, $\theta = 45°$, and $\mathsf{Pr} = 1$ with the isothermal boundary condition, $T_w = T_0$. Under these conditions, the Branch I neutral point for stationary crossflow-vortices is found to be at $\beta_w = 0.1589$, $\alpha_{cf} = -0.1169$. Solving for the residue yields $\Lambda = -0.01955 + 0.03889i$ which has a magnitude of $|\Lambda| = 0.04352$. This value agrees with Choudhari's [17] incompressible result to at least two significant figures.

Appendix F

Linearized Roughness Boundary Condition

Figure F.1 shows a schematic of the geometry under consideration. In this appendix, all lengths are nondimensionalized by a reference length-scale L^* which is the local boundary layer thickness at the roughness location. This scaling leads to a meaningful perturbation expansion for small roughness heights. When using the results of this appendix, care must be taken to properly convert the scaling for the problem at hand. All other quantities, u_j and T, have been nondimensionalized by some convenient reference values.

The smooth wall is denoted by $n(s, z) = 0$, where s is the wall tangent coordinate, n is the wall-normal coordinate, and z is the spanwise coordinate. Note that this is a standard body-fitted coordinate system with n a straight-line coordinate normal to the surface. The rough wall is obtained by adding a small, spanwise-periodic perturbation given by

$$n_w(s, z) = \varepsilon_w h_w(s) e^{i\beta_w z} \tag{F.1}$$

where $\varepsilon_w = \varepsilon_w^*/L^* \ll 1$ is the scaled roughness height, h_w is the streamwise shape function, and $\beta_w = \beta_w^* L^*$ is the spanwise wavenumber of the bump. Note that we have limited the study to spanwise periodic roughness distributions. Since the analysis is linear, the current results can be thought of as the response of the boundary layer to a single Fourier mode of a more complicated spanwise distribution.

The no-slip and isothermal boundary conditions are applied on the perturbed surface

$$u_j(s, n_w, z) = 0, \tag{F.2}$$

$$T(s, n_w, z) = T_w. \tag{F.3}$$

Similar to the expansions used in section 2.3, the flow variables are written as

$$
\begin{aligned}
u_j(x_i) &= \bar{u}_j(x_i) + \varepsilon_w \tilde{u}_j(x_i) + \mathcal{O}({\varepsilon_w}^2), &\text{(F.4)}\\
T(x_i) &= \bar{T}(x_i) + \varepsilon_w \tilde{T}(x_i) + \mathcal{O}({\varepsilon_w}^2), &\text{(F.5)}
\end{aligned}
$$

where perturbations are denoted with a tilde.

Linearized boundary conditions, which can be applied at the unperturbed wall, are derived by expanding equations (F.2) in a Taylor series about the undisturbed wall location. This yields

$$
\begin{aligned}
u_j(s, n_w, z) = 0 &= u_j(s, 0, z) + \varepsilon_w h_w(s) e^{i\beta_w z} \frac{\partial u_j}{\partial n}(s, 0, z) + \mathcal{O}({\varepsilon_w}^2) &\text{(F.6)}\\
T(s, n_w, z) = T_w &= T(s, 0, z) + \varepsilon_w h_w(s) e^{i\beta_w z} \frac{\partial T}{\partial n}(s, 0, z) + \mathcal{O}({\varepsilon_w}^2). &\text{(F.7)}
\end{aligned}
$$

Then using equations (F.4) in equation (F.6) gives

$$
\begin{aligned}
\bar{u}_j(s, 0, z) &= 0, &\text{(F.8)}\\
\bar{T}(s, 0, z) &= T_w, &\text{(F.9)}\\
\tilde{u}_j(s, 0, z) &= -h_w(s) e^{i\beta_w z} \frac{\partial \bar{u}_j}{\partial n}(s, 0, z), &\text{(F.10)}\\
\tilde{T}(s, 0, z) &= -h_w(s) e^{i\beta_w z} \frac{\partial \bar{T}}{\partial n}(s, 0, z), &\text{(F.11)}
\end{aligned}
$$

where only terms of $\mathcal{O}(\varepsilon_w)$ have been retained. The mean flow solution is obtained using homogeneous boundary conditions on the unperturbed surface while the disturbance boundary conditions are inhomogeneous and proportional to the local, mean-flow gradients normal to the surface.

If instead of an isothermal boundary condition, a constant heat-flux condition is used then the derivation of the linearized boundary conditions is substantially more involved. This is due to the fact that the normal direction used in determining the wall-normal temperature gradient must be defined relative to the perturbed surface:

$$
\frac{\partial T}{\partial \tilde{n}}(s, n_w, z) = g_w \tag{F.12}
$$

where $\tilde{n}$ is the perturbed normal direction and g_w is the prescribed, constant heat-flux.

Since we wish to apply these conditions for an infinite-span wing, the derivation

is limited to a two-dimensional cylinder. To derive the proper linearized heat-flux boundary condition we begin by assuming that the unperturbed surface is parametrically described by the arc-length, s. Thus,

$$(x, y) = (f(s), g(s)), \tag{F.13}$$

as shown in figure F.1. The unit tangent and normal vectors are then given, respectively, by

$$\hat{s} = \frac{(f', g')}{\sqrt{f'^2 + g'^2}}, \tag{F.14}$$

$$\hat{n} = \frac{(-g', f')}{\sqrt{f'^2 + g'^2}}, \tag{F.15}$$

where primes denote differentiation with-respect-to s. The perturbed surface is denoted by $(\tilde{x}, \tilde{y})$ where

$$\tilde{x}(s, z) = f(s) - \varepsilon_w h_w(s) e^{i\beta_w z} \frac{g'}{\sqrt{f'^2 + g'^2}}, \tag{F.16}$$

$$\tilde{y}(s, z) = g(s) + \varepsilon_w h_w(s) e^{i\beta_w z} \frac{f'}{\sqrt{f'^2 + g'^2}}. \tag{F.17}$$

To construct the normal to the perturbed surface we begin by defining two vectors which are tangent to the surface. For this, we need derivatives of $\tilde{x}$ and $\tilde{y}$ with respect to s and z.

$$\frac{\partial \tilde{x}}{\partial s} = f' - \frac{\varepsilon_w (e)^{i\beta_w z}}{\sqrt{f'^2 + g'^2}} \left[h'_w g' + h_w \left\{ g'' - \frac{g'(f'f'' + g'g'')}{(f'^2 + g'^2)} \right\} \right], \tag{F.18}$$

$$\frac{\partial \tilde{y}}{\partial s} = g' - \frac{\varepsilon_w (e)^{i\beta_w z}}{\sqrt{f'^2 + g'^2}} \left[h'_w f' + h_w \left\{ f'' - \frac{f'(f'f'' + g'g'')}{(f'^2 + g'^2)} \right\} \right], \tag{F.19}$$

$$\frac{\partial \tilde{x}}{\partial z} = -\varepsilon_w h_w i\beta_w e^{i\beta_w z} \frac{g'}{\sqrt{f'^2 + g'^2}}, \tag{F.20}$$

$$\frac{\partial \tilde{y}}{\partial z} = \varepsilon_w h_w i\beta_w e^{i\beta_w z} \frac{f'}{\sqrt{f'^2 + g'^2}}, \tag{F.21}$$

In the following derivation, these expressions are abbreviated to

$$\tilde{x}_{,s} = f' + \varepsilon_w A, \tag{F.22}$$

$$\tilde{y}_{,s} \;=\; g' + \varepsilon_w B\,, \tag{F.23}$$

$$\tilde{x}_{,z} \;=\; \varepsilon_w C\,, \tag{F.24}$$

$$\tilde{y}_{,z} \;=\; \varepsilon_w D\,, \tag{F.25}$$

where A, B, C, and D are complex functions of (s, z).

Using these abbreviated expressions, two vectors, each tangent to the perturbed surface, can be defined as

$$S_{xy} = \begin{Bmatrix} \tilde{x}_{,s} \\ \tilde{y}_{,s} \\ 0 \end{Bmatrix} \qquad \text{and} \qquad Z_{xy} = \begin{Bmatrix} \tilde{x}_{,z} \\ \tilde{y}_{,z} \\ 1 \end{Bmatrix}. \tag{F.26}$$

The perturbed normal vector is then given by the cross product, $\tilde{n} = S_{xy} \times Z_{xy}$ which is found to be

$$\tilde{n} = \begin{Bmatrix} -\tilde{y}^{\dagger}_{,s} \\ \tilde{x}^{\dagger}_{,s} \\ (\tilde{x}^{\dagger}_{,z}\tilde{y}^{\dagger}_{,s} - \tilde{x}^{\dagger}_{,s}\tilde{y}^{\dagger}_{,z}) \end{Bmatrix}. \tag{F.27}$$

Rewriting the normal vector using equations (F.22-F.25) yields

$$\tilde{n} = \begin{Bmatrix} -(g' + \varepsilon_w B^{\dagger}) \\ (f' + \varepsilon_w A^{\dagger}) \\ \varepsilon_w \left[C^{\dagger}(g' + \varepsilon_w B^{\dagger}) - D^{\dagger}(f' + \varepsilon_w A^{\dagger}) \right] \end{Bmatrix}. \tag{F.28}$$

The normalization of this vector requires the quantity $1/|\tilde{n}|$, which, when expanded for small ε_w, is given by

$$\frac{1}{|\tilde{n}|} = \overbrace{\frac{1}{\sqrt{f'^2 + g'^2}}}^{E} + \varepsilon_w \overbrace{\frac{-(f'A_r + g'B_r)}{(f'^2 + g'^2)^{3/2}}}^{F} + \mathcal{O}(\varepsilon_w^2) \tag{F.29}$$

where the terms E and F have been defined to simplify the notation. Using this expression to normalize $\tilde{n}$ and expanding the result in powers of ε_w leads to

$$\frac{\tilde{n}}{|\tilde{n}|} = \begin{Bmatrix} -g'E - \varepsilon_w(g'F + B^{\dagger}E) \\ f'E + \varepsilon_w(f'F + A^{\dagger}E) \\ \varepsilon_w(C^{\dagger}g' - D^{\dagger}f') \end{Bmatrix} + \mathcal{O}(\varepsilon_w^2)\,. \tag{F.30}$$

Projecting this vector onto the undisturbed tangent and normal vectors yields the following expression

$$
\frac{\tilde{n}}{|\tilde{n}|} = -\varepsilon_w \frac{h_w' e^{-i\beta_w z}}{f'^2 + g'^2} \hat{s} + \left\{ 1 - \varepsilon_w i h_w \sin(\beta_w z) \frac{g'f'' - f'g''}{(f'^2 + g'^2)^{3/2}} \right\} \hat{n} +
$$
$$
\varepsilon_w i h_w \beta_w e^{-i\beta_w z} \hat{z} + \mathcal{O}(\varepsilon_w{}^2). \tag{F.31}
$$

For convenience, this expression is rewritten using the shorthand notation

$$
\frac{\tilde{n}}{|\tilde{n}|} = \varepsilon_w \tilde{n}_s \hat{s} + \left\{ 1 + \varepsilon_w \tilde{n}_n \right\} \hat{n} + \varepsilon_w \tilde{n}_z \hat{z} + \mathcal{O}(\varepsilon_w{}^2). \tag{F.32}
$$

We can now evaluate the temperature gradient in the perturbed normal-direction $\partial T / \partial \tilde{n}$ in terms of the gradients normal and tangent to the original body,

$$
\frac{\partial T}{\partial \tilde{n}} = \varepsilon_w \tilde{n}_s^\dagger \frac{\partial T}{\partial s} + (1 + \varepsilon_w \tilde{n}_n^\dagger) \frac{\partial T}{\partial n} + \varepsilon_w \tilde{n}_z^\dagger \frac{\partial T}{\partial z} + \mathcal{O}(\varepsilon_w{}^2). \tag{F.33}
$$

To evaluate this gradient at $n = n_w$, derivatives are expanded in a Taylor series about $n = 0$. Using equation (F.5) and collecting terms of equal order in ε_w yields

$$
\frac{\partial \bar{T}}{\partial n}(s, 0, z) = q_w, \tag{F.34}
$$

$$
\frac{\partial \tilde{T}}{\partial n}(s, 0, z) = -\tilde{n}_s^\dagger \frac{\partial \bar{T}}{\partial s}(s, 0, z) - \tilde{n}_n^\dagger \frac{\partial \bar{T}}{\partial n}(s, 0, z) -
$$
$$
h_w e^{i\beta_w z} \frac{\partial^2 \bar{T}}{\partial n^2}(s, 0, z) - \tilde{n}_z^\dagger \frac{\partial \bar{T}}{\partial z}(s, 0, z). \tag{F.35}
$$

Writing this expression out in full results in

$$
\frac{\partial \tilde{T}}{\partial n}(s, 0, z) = \frac{h_w' e^{i\beta_w z}}{f'^2 + g'^2} \frac{\partial \bar{T}}{\partial s}(s, 0, z) -
$$
$$
i h_w \sin(\beta_w z) \frac{g'f'' - f'g''}{(f'^2 + g'^2)^{3/2}} \frac{\partial \bar{T}}{\partial n}(s, 0, z) -
$$
$$
h_w e^{i\beta_w z} \frac{\partial^2 \bar{T}}{\partial n^2}(s, 0, z) + i h_w \beta_w e^{i\beta_w z} \frac{\partial \bar{T}}{\partial z}(s, 0, z). \tag{F.36}
$$

Equation (F.36) is valid for any two-dimensional body with a small, spanwise periodic perturbation. For all the cases considered here, $\partial \bar{T} / \partial z = 0$ so that the

last term can be ignored. From the general expression, several special cases follow directly:

Two-dimensional disturbance: $\beta_w = 0$

$$\frac{\partial \tilde{T}}{\partial n}(s,0,z) \;=\; \frac{h'_w}{f'^2 + g'^2}\frac{\partial \bar{T}}{\partial s}(s,0,z) - h_w \frac{\partial^2 \bar{T}}{\partial n^2}(s,0,z)\,, \qquad\qquad \text{(F.37)}$$

Flat Plate

$$\frac{\partial \tilde{T}}{\partial n}(s,0,z) \;=\; h'_w e^{i\beta_w z}\frac{\partial \bar{T}}{\partial s}(s,0,z) - h_w e^{i\beta_w z}\frac{\partial^2 \bar{T}}{\partial n^2}(s,0,z)\,, \qquad\qquad \text{(F.38)}$$

Flat Plate with parallel flow assumption

$$\frac{\partial \tilde{T}}{\partial n}(s,0,z) \;=\; -h_w e^{i\beta_w z}\frac{\partial^2 \bar{T}}{\partial n^2}(s,0,z)\,. \qquad\qquad \text{(F.39)}$$
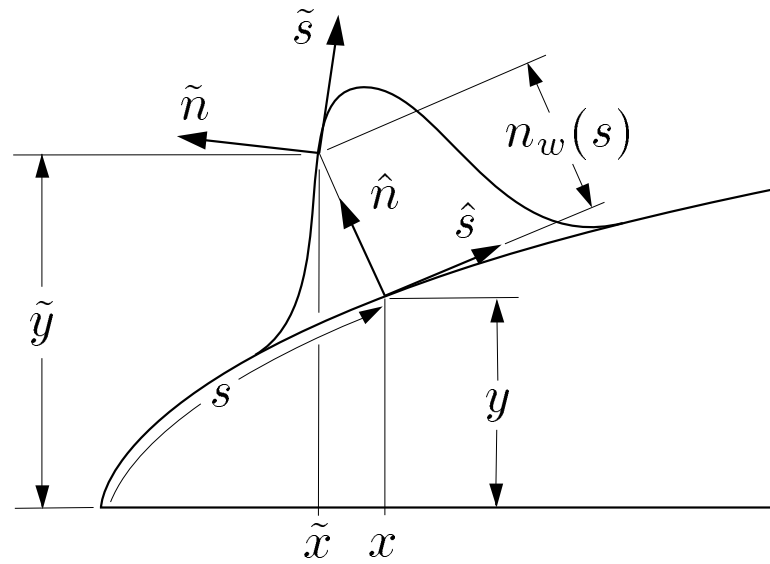
Figure F.1: Schematic of surface roughness geometry. Note that the height of the bump is exaggerated for clarity.

Bibliography

[1] I. H. Abbott and A. E. von Doenhoff. *Theory of Wing Sections.* Dover Publications, 1959.

[2] N. A. Adams. Numerical study of boundary layer interaction with shocks – method and code validation. Center for Turbulence Research, Annual Research Briefs, 1994.

[3] E. Anderson et al. *LAPACK User's Guide.* Society for Industrial and Applied Mathematics, 1992.

[4] A. P. Bassom. Time-dependent inviscid vortices in three-dimensional boundary layers. *Quarterly Journal of Mechanics and Applied Mathematics*, 45(3):339–362, 1992.

[5] A. P. Bassom and P. Hall. Vortex instabilities in three-dimensional boundary layers: the relationship between Görtler and crossflow vortices. *Journal of Fluid Mechanics*, 232:647–680, 1991.

[6] R. M. Beam and R. F. Warming. An implicit finite-difference algorithm for hyperbolic systems in conservation-law form. *Journal of Computational Physics*, 22:87–110, 1976.

[7] P. Beaudan and P. Moin. Numerical experiments on the flow past a circular cylinder at sub-critical Reynolds number. Technical Report TF-62, Thermosciences Division, Department of Mechanical Engineering, Stanford University, December 1994.

[8] A. Bers. *Handbook of Plasma Physics*, Volume I: Basic Plasma Physics, Chapter 3.2: Space-Time Evolution of Plasma Instabilities — Absolute and Convective. North–Holland Publishing Company, 1983.

[9] A. L. Braslow, D. V. Maddalon, D. W. Bartlett, R. D. Wagner, and F. S. Collier Jr. Applied aspects of laminar-flow technology. D. M. Bushnell and J. N. Hefner, editors, *Progress in Aeronautics and Astronautics, Vol. 123*, pages 47–78. American Institute of Aeronautics and Astronautics, 1990.

[10] K. S. Breuer and T. Kuraishi. Bypass transition in two- and three-dimensional boundary layers. *24th Fluid Dynamics Conference*, AIAA 93-3050, 1993.

[11] T. J. Bridges and P. J. Morris. Differential eigenvalue problems in which the parameter appears nonlinearly. *Journal of Computational Physics*, 55:437–460, 1984.

[12] C. Canuto, M. Y. Hussaini, A. Quarteroni, and T. A. Zang. *Spectral Methods in Fluid Dynamics*, page 69. Springer-Verlag, 1988.

[13] C.-L. Chang, M. R. Malik, G. Erlebacher, and M. Y. Hussaini. Linear and nonlinear PSE for compressible boundary layers. Technical Report ICASE-93-70, ICASE, NASA Langley Research Center, Hampton, Virginia, 1993.

[14] C.-L. Chang and C. L. Merkle. The relation between flux vector splitting and parabolized schemes. *Journal of Computational Physics*, 80:344–361, 1989.

[15] M. Choudhari and C. Streett. Boundary layer receptivity phenomena in three-dimensional and high-speed boundary layers. *AIAA Second International Aerospace Planes Conference*, AIAA 90-5258, 1990.

[16] M. Choudhari. Distributed acoustic receptivity in laminar flow control configurations. *Physics of Fluids*, 6(2):489–506, 1993.

[17] M. Choudhari. Roughness-induced generation of crossflow vortices in three-dimensional boundary layers. *Theoretical and Computational Fluid Dynamics*, 6:1–30, 1994.

[18] M. Choudhari and P. W. Duck. Nonlinear excitation of inviscid stationary vortex in a boundary-layer flow. *NASA Contractor Report 198327*, ICASE 96-27, 1996.

[19] M. Choudhari and E. J. Kerschen. Instability wave patterns generated by interaction of sound waves with three-dimensional wall suction or roughness. *28th Aerospace Sciences Meeting*, AIAA 90-0119, 1990.

[20] M. Choudhari and C. L. Streett. A finite Reynolds-number approach for the prediction of boundary-layer receptivity in localized regions. *Physics of Fluids*, 4(11):2495–2514, 1992.

[21] M. Choudhari and C. L. Streett. Theoretical prediction of boundary-layer receptivity. *25th AIAA Fluid Dynamics Conference*, AIAA 94-2223, 1994.

[22] S. S. Collis and S. K. Lele. A computational approach to swept leading-edge receptivity. *AIAA 34th Aerospace Sciences Meeting*, AIAA 96-0180, 1996.

[23] T. Colonius, P. Moin, and S. K. Lele. Direct computation of aerodynamic sound. Technical Report TF-65, Thermoscience Division, Department of Mechanical Engineering, Stanford University, Stanford, CA 94305, June 1995.

[24] S. D. Conte. The numerical solution of linear boundary value problems. *SIAM Review*, pages 309–321, 1966.

[25] J. C. Cooke. The boundary layer of a class of infinite yawed cylinders. *Mathematical Proceedings of the Cambridge Philosophical Society*, 46:645–648, 1950.

[26] T. Corke and O. Haddad. Receptivity to sound on a parabolic leading edge. R. Henkes and J. van Ingen, editors, *Colloquium of the Royal Netherlands Academy of Arts and Sciences on Transitional Boundary Layers in Aeronautics*, 1995.

[27] J. D. Crouch. Localized receptivity of boundary layers. *Physics of Fluids*, 4(7):1408–1414, 1992.

[28] J. D. Crouch. Receptivity of three-dimensional boundary layers. *31th Aerospace Sciences Meeting & Exhibit*, AIAA 93-0074, 1993.

[29] J. D. Crouch. Theoretical studies on the receptivity of boundary layers. *25th AIAA Fluid Dynamics Conference*, AIAA 94-2224, 1994.

[30] J. D. Crouch and P. R. Spalart. A study of non-parallel and nonlinear effects on the localized receptivity of boundary layers. *Journal of Fluid Mechanics*, 290:29–37, 1995.

[31] R. T. Davis. Numerical solution of the Navier–Stokes equations for symmetric laminar incompressible flow past a parabola. *Journal of Fluid Mechanics*, 51(3):417–433, 1972.

[32] H. Deyhle and H. Bippes. Disturbance growth in an unstable three-dimensional boundary layer and its dependence on environmental conditions. *Journal of Fluid Mechanics*, 316:73–113, 1996.

[33] P. G. Drazin and W. Reid. *Hydrodynamic Stability*, pages 69–73. Cambridge University Press, 1981.

[34] H. Fasel and U. Konzelmann. Non-parallel stability of a flat-plate boundary layer using the complete Navier–Stokes equations. *Journal of Fluid Mechanics*, 221:311–347, 1990.

[35] C. C. Fenno Jr., C. L. Streett, and H. A. Hassan. Use of finite volume schemes for transition simulation. *AIAA Journal*, 30(4):1122–1125, 1992.

[36] C. C. Fenno Jr. *Direct Numerical Simulation of Forced and Natural Receptivity Mechanisms Over Flat Plates and Parabolic Cylinders*. Ph.D. thesis, North Carolina State University, 1993.

[37] M. Gaster. A simple device for preventing turbulent contamination on swept leading edges. *Journal of the Royal Aeronautical Society*, 69:788, 1965.

[38] M. B. Giles. Nonreflecting boundary conditions for Euler equation calculations. *AIAA Journal*, 28(12):2050–2058, 1990.

[39] D. Givoli. Non-reflecting boundary conditions. *Journal of Computational Physics*, 94:1–29, 1991.

[40] M. E. Goldstein. The evolution of Tollmien–Schlichting waves near a leading edge. *Journal of Fluid Mechanics*, 127:59–81, 1983.

[41] M. E. Goldstein. Scattering of acoustic waves into Tollmien–Schlichting waves by small streamwise variations in surface geometry. *Journal of Fluid Mechanics*, 154:509–529, 1985.

[42] M. E. Goldstein and L. S. Hultgren. A note on the generation of Tollmien–Schlichting waves by sudden surface-curvature change. *Journal of Fluid Mechanics*, 181:519–525, 1987.

[43] M. E. Goldstein and L. S. Hultgren. Boundary-layer receptivity to long-wave free-stream disturbances. *Annual Reviews of Fluid Mechanics*, 21:137–166, 1989.

[44] M. E. Goldstein, S. J. Leib, and S. J. Cowley. Generation of Tollmien–Schlichting waves on interactive marginally separated flows. *Journal of Fluid Mechanics*, 181:485–517, 1992.

[45] G. H. Golub and C. F. van Loan. *Matrix Computations*, pages 96,380. The Johns Hopkins University Press, second edition, 1989.

[46] Y. Guo and N. A. Adams. A spectral/finite-difference algorithm for direct numerical simulation of spatially growing compressible boundary layer transition. Technical Report IB 221-93 A 26, Institut für Strömungsmechanik, December 1993.

[47] B. Gustafsson. The convergence rate for difference approximations to mixed initial boundary-value problems. *Mathematics of Computation*, 29(130):396–406, 1975.

[48] P. W. Hammerton and E. J. Kerschen. Boundary-layer receptivity for a parabolic leading edge. *Journal of Fluid Mechanics*, 310:243–267, 1996.

[49] C. D. Harris, W. D. Harvey, and C. W. Brooks, Jr. The NASA Langley laminar-flow-control experiment on a swept, supercritical airfoil: Design overview. *NASA Technical Paper 2809*, NAS 1.60:2809, 1988.

[50] T. S. Haynes and H. L. Reed. Computations in nonlinear saturation of stationary crossflow vortices in a swept-wing boundary layer. *34th Aerospace Sciences Meeting*, AIAA 96-0182, 1996.

[51] T. Herbert. Boundary-layer transition—analysis and prediction revisited. *29th Aerospace Sciences Meeting*, AIAA 91-0737, 1991.

[52] T. Herbert and N. Lin. Studies of boundary-layer receptivity with parabolized stability equations. *24th Fluid Dynamics Conference*, AIAA 93-3053, 1993.

[53] C. Hirsch. *Numerical Computation of Internal and External Flows, Vol. II: Computational Methods for Inviscid and Viscous Flows*. Wiley, New York, 1990.

[54] IMSL. International mathematical and statistical library. Version 2.0, 1991.

[55] M. Israeli and S. A. Orszag. Approximation of radiation boundary condition. *Journal of Computational Physics*, 41:115–135, 1981.

[56] N. A. Jaffe, T. T. Okamura, and A. M. O. Smith. Determination of spatial amplification factors and their application to predicting transition. *AIAA Journal*, 8:301–308, 1970.

[57] E. J. Kerschen. Boundary layer receptivity. *12th Aeroacoustics Conference*, AIAA 89-1109, 1989.

[58] J. Kim and P. Moin. Application of a fraction-step method to incompressible Naiver–Stokes equations. *Jounal of Computational Physics*, 59(2):308–23, June 1985.

[59] V. V. Kozlov and O. S. Ryshov. Receptivity of boundary layers: Asymptotic theory and experiment. *Proceedings of the Royal Society of London, Series A*, 429(1877):341–373, 1990.

[60] S. K. Lele. Compact finite difference schemes with spectral-like resolution. *Journal of Computational Physics*, 103(1):16–42, 1992.

[61] N. Lin, H. L. Reed, and W. S. Saric. Boundary-layer receptivity to sound: Navier–Stokes computations. *Bulletin of the American Physical Society*, 35(10):2260, 1990.

[62] N. Lin, H. L. Reed, and W. S. Saric. Effect of leading-edge geometry on boundary-layer receptivity to freestream sound. M. Hussaini, A. Kumar, and C. Streett, editors, *Instability, Transition, and Turbulence*, pages 421–440. Springer-Verlag, 1992.

[63] N. Lin. *Receptivity of the Boundary Layer Over a Flat Plate with Different Leading-Edge Geometries: Numerical Simulations*. Ph.D. thesis, Arizona State University, 1992.

[64] C.-H. Ling and W. C. Reynolds. Non-parallel flow correction for the stability of shear flows. *JFM*, 59(3):571–591, 1973.

[65] R. J. Lingwood. An experimental study of absolute instability of the rotating-disk boundary-layer flow. *Journal of Fluid Mechanics*, 314:373–405, 1996.

[66] R. Lingwood. Absolute instability of the boundary layer on a rotating disk. *Journal of Fluid Mechanics*, 299:17–33, 1995.

[67] R. W. MacCormack. Current status of numerical solutions of the Navier–Stokes equations. AIAA 88-0513, 1988.

[68] L. M. Mack. Boundary layer linear stability theory. *Special Course on Stability and Transition of Laminar Flow*, AGARD-R-709:3.1–3.81, 1984.

[69] K. Mahesh. Personal Communication, May 1996.

[70] K. Mahesh, P. Moin, and S. K. Lele. The interaction of a shock wave with a turbulent shear flow. Technical Report TF-69, Thermosciences Division, Department of Mechanical Engineering, Stanford University, 1996.

[71] M. R. Malik. Numerical methods for hypersonic boundary layer stability. *Journal of Computational Physics*, 86:376–413, 1990.

[72] M. R. Malik and P. Balakumar. Linear stability of three-dimensional boundary layers: Effects of curvature and non-parallelism. *31st Aerospace Sciences Meeting*, AIAA 93-0079, 1993.

[73] M. R. Malik and F. Li. Transition studies for swept wing flows using PSE. *31st Aerospace Sciences Meeting*, AIAA 93-0077, 1993.

[74] M. R. Malik, F. Li, and C.-L. Chang. Cross-flow disturbances in three-dimensional boundary layers: non-linear deveopment, wave interaction and secondary instability. *Journal of Fluid Mechanics*, 268:1–36, 1994.

[75] M. R. Malik. Stability theory for laminar flow control design. D. M. Bushnell and J. N. Hefner, editors, *Viscous Drag Reduction in Boundary Layers, Progress in Aeronautics and Astronautics, Vol. 123*, pages 3–46. American Institute of Aeronautics and Astronautics, 1990.

[76] J. A. Masad and M. R. Malik. Effects of body curvature and nonparallelism on the stability of flow over a swept cylinder. *Physics of Fluids*, 6(7):2363–2379, 1994.

[77] B. E. Mitchell, S. K. Lele, and P. Moin. Direct computation of the sound generated by subsonic and supersonic axisymmetric jets. Technical Report TF-66, Thermoscience Division, Department of Mechanical Engineering, Stanford University, 1996.

[78] M. V. Morkovin. Bypass-transition research: Issues and philosophy. Technical Report AFFDL-TR-68-149, Air Force Flight Dynamics Laboratory, Wright–Paterson Air Force Base, 1969.

[79] P. M. Morse and K. U. Ingard. *Theoretical Acoustics*, pages 400–405. Princeton University Press, 1968.

[80] J. W. Murdock. Tollmien–Schlichting waves generated by unsteady flow over parabolic cylinders. *AIAA 19th Aerospace Sciences Meeting*, AIAA 81-0199, 1981.

[81] A. H. Nayfeh. Stability of three-dimensional boundary layers. *AIAA Journal*, 18:406–416, 1980.

[82] M. Nishioka and M. V. Morkovin. Boundary-layer receptivity to unsteady pressure gradient: experiments and overview. *Journal of Fluid Mechanics*, 171:219–261, 1986.

[83] T. J. Poinsot and S. K. Lele. Boundary conditions for direct simulations of compressible viscous flows. *Journal of Computational Physics*, 101(1):104–128, 1992.

[84] D. I. A. Poll. Some observations of the transition process on the windward face of a long yawed cylinder. *Journal of Fluid Mechanics*, 150:329–356, 1985.

[85] T. H. Pulliam. Solution methods in computational fluid dynamics. http://www.nas.nasa.gov/~pulliam, April 1994.

[86] R. H. Radeztsky Jr., M. S. Reibert, and W. S. Saric. Effect of micron-sized roughness on transition in swept-wing flows. AIAA 93-0076, 1993.

[87] R. H. Radeztsky Jr., M. S. Reibert, and W. S. Saric. Development of stationary crossflow vortices on a swept wing. AIAA 94-2373, 1994.

[88] M. M. Rai and P. Moin. Direct numerical simulation of transition and turbulence in a spatially evolving boundary layer. *Journal of Computational Physics*, 109(2):169–192, 1993.

[89] G. Redeker, K. H. Horstmann, H. Köster, and A. Quast. Investigations on high Reynolds number laminar flow airfoils. *ICAS Proceedings: 15th Congress of the International Council of the Aeronautical Sciences*, ICAS-86-1.1.3:73–85, 1986.

[90] M. S. Reibert, W. S. Saric, R. B. C. Jr., and K. L. Chapman. Experiments in nonlinear saturation of stationary crossflow vortices in a swept-wing boundary layer. *34th Aerospace Sciences Meeting*, AIAA 96-0184, 1996.

[91] E. Reshotko and I. E. Beckwith. Compressible laminar boundary layer over a yawed infinite cylinder with heat transfer and arbitrary Prandtl number. Technical report, NACA - Report 1379, 1958.

[92] A. I. Ruban. On the generation of Tollmien–Schlichting waves by sound. *Fluid Dynamics*, 19(5):709–717, 1984.

[93] W. S. Saric and A. H. Nayfeh. Nonparallel stability of boundary-layer flows. *Physics of Fluids*, 18(8):945–950, 1975.

[94] W. S. Saric, H. L. Reed, and E. J. Kerschen. Leading edge receptivity to sound: Experiments, DNS, and theory. *25th AIAA Fluid Dynamics Conference*, AIAA 94-2222, 1994.

[95] W. S. Saric and H. L. Reed. Stability and transition of three-dimensional boundary layers. *Fluid Dynamics of Three-Dimensional Turbulent Shear Flows and Transition*, AGARD-CP-438, 1989.

[96] W. S. Saric, W. Wei, and B. K. Rasmussen. Effect of leading edge on sound receptivity. *Laminar-Turbulent Transition, Vol. IV*, 1995.

[97] G. B. Schubauer and H. K. Skramstad. Laminar boundary layer oscillations and transitions on a flat plate. *Journal of Aerospace Sciences*, 14:69–79, 1947.

[98] F. Shakib. *Finite Element Analysis of the Compressible Euler and Navier–Stokes Equations.* Ph.D. thesis, Stanford University, Department of Mechanical Engineering, November 1988.

[99] F. S. Sherman. *Viscous Flow*, pages 644–658. McGraw-Hill Publishing Company, 1990.

[100] P. R. Spalart. Direct numerical study of leading-edge contamination. *Fluid Dynamics of Three-Dimensional Turbulent Shear Flows and Transition*, AGARD-CP-438, 1989.

[101] P. R. Spalart, J. D. Crouch, and L. L. Ng. Numerical study of realistic perturbations in three-dimensional boundary layers. *Application of Direct and Large Eddy Simulation to Transition and Turbulence*, AGARD-CP-551, 1994.

[102] J. L. Steger. Implicit finite difference simulation of flow about arbitrary geometries with application to airfoils. *AIAA 10th Fluid & Plasmadynamics Conference*, AIAA 77-665, 1977.

[103] J. L. Steger and R. F. Warming. Flux vector splitting of the inviscid gasdynamics equations with application to finite-difference methods. *Journal of Computational Physics*, 40:263–293, 1981.

[104] K. Stewartson. *The Theory of Laminar Boundary Layers in Compressible Fluids*, Chapter 4, pages 61–98. Oxford Clarendon Press, 1964.

[105] C. K. W. Tam and J. C. Webb. Dispersion-relation-preserving finite difference schemes for computational acoustics. *Journal of Computational Physics*, 107:262–281, 1993.

[106] K. W. Thompson. Time-dependent boundary conditions for hyperbolic systems, II. *Journal of Computational Physics*, 89:439–461, 1990.

[107] M. Tobak. Personal Communication, November 1996.

[108] M. van Dyke. Higher approximations in boundary-layer theory part 3. parabola in uniform stream. *Journal of Fluid Mechanics*, 19:145–159, 1963.

[109] B. van Leer. Towards the ultimate conservative difference scheme. IV. A new approach to numerical convection. *Journal of Computational Physics*, 23:276–299, 1977.

[110] Y. C. Vigneron, J. V. Rakich, and J. C. Tannehill. Calculation of supersonic viscous flow over delta wings with sharp subsonic leading edges. *AIAA 78-1337*, 1978.

[111] F. M. White. *Viscous Fluid Flow*, page 29. McGraw–Hill, Inc., second edition, 1991.

[112] R. W. Wlezien. Measurement of acoustic receptivity. *25th AIAA Fluid Dynamics Conference*, AIAA 94-2221, 1994.

[113] N. A. Zavol'skii, V. P. Reutov, and G. V. Ryboushkina. Generation of Tollmien–Schlichting waves via scattering of acoustic and vortex perturbations in boundary layer on wavy surface. *Journal of Applied Mechanics and Technical Physics*, 24(3):79–86, 1983.

[114] V. N. Zhigulev and A. V. Fedorov. Boundary-layer receptivity to acoustic disturbances. *Journal of Applied Mechanics and Technical Physics*, 28(1):28–34, 1987.

[115] Y. H. Zurigat and M. R. Malik. Effects of cross-flow on Görtler instability in incompressible boundary layers. *Physics of Fluids*, 7(7):1616–1625, 1995.